Contribution to control uncertainties in numerical modelling of dam performances : an application to an RCC dam

Ana Patricia Pimentel Torres Gaspar

ÉCOLE CENTRALE DES ARTS ET MANUFACTURES « ÉCOLE CENTRALE PARIS »

THÈSE

présentée par

Ana Patrícia PIMENTEL TORRES GASPAR

pour l'obtention du

GRADE DE DOCTEUR

Spécialité : Génie Civil, Modélisation numérique

Laboratoire d'accueil : Mécanique des Sols, Structures et Matériaux

Sujet: Contribution to control uncertainties in numerical modelling of dam performances. An application to an RCC dam.

Soutenue le: 3 novembre 2014

devant un jury composée de:

M. BARROS Joaquim	Président
Mme. MODARESSI Arézou	Directrice de Thèse
M. LOPEZ-CABALLERO Fernando	Directeur de Thèse
M. GOMES CORREIA António	Directeur de Thèse
M. LACKNER Roman	Rapporteur
M. CHATEAUNEUF Alaa	Rapporteur
M. TAVARES DE CASTRO António	Examinateur
M. MELLAL Aïssa	Examinateur

2014ECAP0053

Ao meu avô,

Francisco Pimentel Torres.

Acknowledgements

This doctoral thesis was developed in the framework of a double diploma agreement between two institutions' teams of which I am very proud being part of: ISISE center at Universidade do Minho (UM), in Guimarães, Portugal, and MSSMat laboratory at Ecole Centrale Paris (ECP), in Châtenay-Malabry, France. The financial support by the Portuguese Foundation for Science and Technology (FCT) PhD grant (SFRH/BD/63939/2009, QREN POPH - Tipologia 4.1) is here recognized.

This thesis would have not been achieved without the encouragement and support of my three supervisors, whom I would like to acknowledge. As my mentors, they have prepared me in both human and scientific contexts and to each one of them I express here my gratitude. First, I thank Prof. António Gomes Correia for having encouraged me since the beginning, in 2008, when I participated in the Erasmus program at Ecole Nationale des Ponts et Chausées (ENPC), without which I would have probably never attained the place where I stand today; for introduced me to Mme. Arézou Modaressi and M. Fernando Lopez-Caballero at MSSMat; for motivating me to continue with the master degree and finally with the doctoral thesis; for having introduced me to engineers and researchers in Energies of Portugal (EDP) and in the National Civil Engineering Laboratory (LNEC); for having encouraged me to participate in national and international congresses; and finally I also acknowledge his help on finding financial support with FCT. Secondly, to Mme Arézou Modaressi I thank the opportunity she gave me at the time of my final project (PFE, *Projet fin d'études*) in 2009, which has encouraged me to pursuit my academic path towards master and doctoral degrees; for giving me the chance to teach and guide master students in their research works, from which I have learned a lot of pedagogic skills; for the encouragement and the financial support to participate on several congresses and workshops; and for all of the scientific (and artistic!) advices. Last but not least, to M. Fernando Lopez-Caballero I address my deepest gratitude for having constantly encouraged me through all these years; I thank him for all of the discussions, presentations and

late meetings; for having motivated me to participate on international congresses, which gave me more and more confidence in presenting my work and from which I have plenty of good memories; for having introduced me to other engineers and researchers; for all the patience during low motivation periods; and for the financial support for congresses.

I would also like to address my gratitude to the members of the jury committee for the thesis' defense: Roman Lackner and Alaa Chateauneuf thank you for your revision of the manuscript and useful comments about it; António Tavares de Castro and Aïssa Mellal for having accepted to examine my work and for all of the useful discussions we had; and finally Joaquim Barros for being the President of the jury and for his comments about my work.

This thesis also benefits from a partnership with EDP, on which several work meetings were organized. I would like to thank all the engineers I have encountered at EDP, namely to Eng. Armando Camelo, Eng. Domingos Silva Matos and Eng. Celso Lima. A special thanks to Eng. Armando Camelo for all his scientific advice and literature about concrete and dams he kindly gave me.

I would like to address my gratitude to researchers António Tavares de Castro and Noemi Schlar Leitão from LNEC for all the work meetings, the scientific advices and literature about RCC dams. The fruitful discussions we had enlightened several questions and raised another, which have contributed to enrich this work. I also acknowledge LNEC's president, researcher Carlos Pina for his scientific advice at the WCCM2012 congress.

A special thanks is addressed to Miguel Azenha from UM for all of the scientific advices regarding concrete behaviour at early ages.

I would like to specially express here my gratitude to M. Denis Aubry for all his guidance in scientific questions and in particular for his help with the COMSOL Multiphysics® software. I also thank him for all of the fruitful discussions over coffee and lunch, always accompanied with wise advices.

I acknowledge here all the support and companionship of all my colleagues and internship students with whom I have shared many moments at MSSMat, and specially of those with whom I have shared the office: Esteban Saez, Tammam Hammad, Alexandre Foucault, Maryam Tabbakhha, Luís Todo-Bom, Biyu Tian, Ghizlane Benosman, Houda Attia, Nerea Aramendi and Maria Madaffari. I would also like to address my special thanks to Cristian Niéto-Gamboa, Silvana Montoya Noguera, Vinicius Alves Fernandes, Tatiana Okhulkova and Diana Salem for all the moments we have shared and their friendship. To my colleagues at University of Minho I also address my gratitude for their friendship and support: Sandra Cunha, Ana Sofia

Araújo, Joana Andrade, Manuel Parente, Marisa Pinheiro, Ana Teixeira and Joaquim Tinoco. A special thanks to my colleagues from the UJ2CP (association for the PhD students of ECP) team 2012/2013: Laurent Tranchant, Göknur Sirin and Romain Faye. It was a pleasure to share such experience with them.

I would also like to acknowledge here the support of the laboratory staff at MSSMat, and specially: Anne-Sophie Mourovnal, Nadège Ols, Fleur Litoust, Nathalie Langlet, Martine Lavabre, Carol Simon, Francis Armand, Frédéric Douit and Daniel Kervem; and at UM: Maria Rodrigues, Cristiana Maia, Rosário Pereira, Diana Oliveira and Prof. Rosa Vasconcelos. Also, I can not finish without mention the support and kindness of Catherine l'Hôpital, Géraldine Carbonel and Emmanuelle Coplo from the doctoral school at ECP.

To all my friends all over the world I address here my gratitude for their friendship. A special thanks to: Sinda, Mourad, Chloé, Anita, Eli, Laura, Lucie, Mehdi, Ronay, Francesca, Isabel, Sara, Joana, Paulo, Karina, Filipe, Flávia, Cátia, Nuno, Ana Maria, Tó and Valter. Without your support the path would have been much more sinuous. I also address my gratitude to Hélder for all his love, patience and constant encouragement.

Finally, I address all my gratitude and love to all my family, and specially to my parents Alfredo Gaspar and Maria de Fátima Gaspar who have supported me unconditionally and always encouraged me to pursuit; to my brother André Gaspar and sister Joana Gaspar for all your support; to my grandmothers Maria Laurentina Pimentel Torres and Maria Arminda Gaspar for all the prayers and unconditional support; and finally to my truly missed grandfather Francisco Pimentel Torres who has always deposit much faith in me and my future.

Abstract

Contribution to control uncertainties in numerical modelling of dam performances. An application to an RCC dam.

The use of fully probabilistic approaches to account for uncertainties within dam engineering is a recently emerging field on which studies have been mostly done concerning the safety evaluation of dams under service. This thesis arises within this framework as a contribution on moving the process of risk analysis of dams beyond empirical knowledge, applying probabilistic tools on the numerical modelling of a roller compacted concrete (RCC) dam during its construction phase.

The work developed here aims to propose a methodology so as to account for risks related to cracking during construction which may compromise the dam's functional and structural behaviour.

In order to do so, emphasis is given to uncertainties related to the material itself (i.e. strength, water-to-cement ratio, among others) as well as to ambient conditions during the construction phase of RCC dams. A thermo-chemo-mechanical model is used to describe the RCC behaviour. Concerning the probabilistic model, two aspects are studied: how the uncertainties related to the input variables are propagated through the model, and what is the influence of their dispersion on the dispersion of the output, assessed by performing a global sensitivity analysis by means of the RBD-FAST method. Also, spatial variability of some input parameters is accounted for through bi-dimensional random fields.

Furthermore, a coupling between reliability methods and finite element methods is performed in order to evaluate the cracking potential of each casted RCC layer during construction by means of a *cracking density* concept. As an important outcome of this applied research, probability curves for cracking density within each casted layer as functions of both age and boundary conditions are predicted, which is believed to be an original contribution of this thesis.

The proposed methodology may therefore be seen as a contribution to help engineers un-

derstand how uncertainties will affect the dam behaviour during construction and rely on it in the future to improve and support the design phase of the dam project.

Keywords: RCC dams, Thermo-chemo-mechanical behaviour, Uncertainties, Reliability methods, Sensitivity analysis, RBD-FAST, Random fields.

Résumé

Contribution pour le contrôle des incertitudes dans la modélisation numérique de la performance de barrages. Application à un barrage en BCR.

L'application des approches probabilistes pour tenir compte des incertitudes dans le domaine des barrages est un sujet en développement. Cependant, la plupart des études ont été réalisées sur l'évaluation de la sécurité des barrages pendant leur service. Ce travail de thèse vise à appliquer ce type d'approches et à faire une contribution à l'analyse de risque des barrages en béton compacté au rouleau (BCR) dès sa construction, à l'aide d'une simulation numérique.

Les travaux présentés dans ce manuscrit proposent l'application d'une méthodologie qui vise à quantifier la vulnérabilité vis-à-vis de l'apparition de la fissuration pendant la construction du barrage, ce qui peut affecter à long-terme la perméabilité et par conséquent, compromettre son comportement structurel.

Pour ce faire, l'accent est mis sur les incertitudes liées à quelques caractéristiques des matériaux (e.g., résistance, rapport eau-ciment, entre autres) et aux conditions environnementales pendant la phase de construction. Un modèle thermo-chemo-mécanique est utilisé pour décrire le comportement du BCR. En ce qui concerne le modèle probabiliste, deux aspects sont étudiés: i) comment les incertitudes liées aux variables d'entrée sont propagées dans le modèle, et ii) quelle est l'influence de leur dispersion par rapport à la dispersion totale de la sortie. Ce dernier est évalué par l'intermédiaire d'une analyse de sensibilité globale effectuée avec la méthode RBD-FAST. En outre, la variabilité spatiale des paramètres d'entrée est aussi prise en compte à travers des champs aléatoires bidimensionnels.

Par ailleurs, un couplage entre des méthodes de fiabilité et la méthode d'éléments finis est effectué de façon à évaluer le potentiel de fissuration dans chaque couche de BCR lors de sa construction en utilisant un concept de *densité de fissuration*. Comme résultat important issu de ce travail de recherche, des courbes de probabilité pour la densité de fissuration sont obtenues au niveau de chaque couche en fonction de leur âge et des conditions aux limites, ce qui est

considérée comme étant une contribution originale de cette thèse.

La méthodologie proposée peut être utilisé pour aider à comprendre comment les incertitudes vont affecter le comportement du barrage pendant sa construction et servir d'appui dans le futur pour améliorer et soutenir la phase de conception du projet de barrage.

Mots-clés: Barrages BCR, Comportement thermo-chemo-mécanique, Incertitudes, Méthodes de fiabilité, Analyse de sensibilité, RBD-FAST, Champs aléatoires.

Resumo

Contribuição para o controlo de incertezas na modelação numérica do comportamento de barragens. Aplicação a uma barragem BCC.

A aplicação de métodos probabilísticos para o estudo de incertezas no ramo da engenharia de barragens é um campo em crescente ascensão no qual a grande maioria dos estudos realizados se concentra na avaliação da segurança de barragens durante o período de serviço. Este trabalho de tese situa-se neste contexto, pretendento contribuir para a abordagem de análise de risco em barragens em betão compactado com cilindros (BCC) durante a fase de construção.

Assim, é proposta uma metodologia na qual são tidos em conta riscos relacionados com a fissuração do BCC durante a sua construção, o que poderá comprometer o comportamento funcional e estrutural da barragem.

As incertezas consideradas integram algumas propriedades do material (i.e. resistência, rácio água-cimento, entre outras) bem como as condições climatéricas que se observam durante a fase de de construção de barragens em BCC. Para descrever o comportamento do BCC é utilizado um modelo termo-químico-mecânico. O modelo probabilístico considera, por um lado, a propagação das incertezas relacionadas com as variáveis de entrada e, por outro, permite avaliar qual a influência que têm na dispersão da resposta do modelo. Essa influência é avaliada através de uma análise de sensibilidade global, recorrendo ao método RBD-FAST. A variabilidade espacial de alguns parâmetros de entrada é também tida em conta através de campos aleatórios bi-dimensionais.

O acoplamento entre métodos de fiabilidade e elementos finitos permite avaliar o potencial de fissuração de cada camada de BCC durante a construção da barragem. Para tal é introduzido o conceito de *densidade de fissuração*. Esta abordagem constitui uma contribuição original, com a obtenção de curvas de probabilidade para a densidade de fissuração, avaliadas ao nível de cada camada e em função da idade e condições de fronteira.

A metodologia desenvolvida constitui uma contribuição para a compreensão da influência

de determinadas incertezas no comportamento da barragem durante a sua construção, podendo servir no futuro como um importante suporte à fase de projecto de barragens.

Palavras-chave: Barragens BCC, Comportamento termo-químico-mecânico, Incertezas, Métodos de fiabilidade, Análise de sensibilidade, RBD-FAST, Campos aleatórios.

Contents

List of Figures

List of Tables

List of abbreviations and symbols

For the sake of brevity, each symbol is described by its most common meaning in the present thesis. There are symbols allong the text which are not included in this list because they concern single cases.

Abbreviations

AAR	Alcali-aggregate reactions
ACI	American Concrete Institute
ANN	Artificial Neural Network
AST	Average Surface Temperature
BaCaRa	French project about RCC application on dams (BaCaRa, 1996)
CC	Conventional Concrete
CDF	Cumulative Distribution Function
C-S-H	Calcium-Silicate-Hydrates
CH	Calcium Hydroxide
CVC	Conventional Vibrated Concrete
DPL	Double Power Law
EDF	*Eléctricité de France*
EC2	Eurocode 2
FAST	Fourier Amplitude Sensitivity Test
FEM	Finite Element Method
FMEA	Fault Modes Event Trees
FORM	First Order Reliability Method
FOSM	First Order Second Moment method

Continue in the next page ...

ICOLD	International Committee on Large Dams
LHS	Latin Hypercube Sampling method
LNEC	*Laboratório Nacional de Engenharia Civil*
MCS	Monte Carlo Sampling method
RCC	Roller Compacted Concrete
HPRCC	High Performance Roller Compacted Concrete
HPC	High Performance Concrete
OPC	Ordinary Portland Concrete
RBD-FAST	Random Balance Design FAST
RCD	Roller-Compacted Dam
PDE	Partial Derivative Equation
PEM	Point Estimate Method
PVC	Polyvynilchloride
SORM	Second Order Reliability Method
SPANCOLD	Spanish Committee on Large Dams
TSTM	Temperature Stress Testing Machine
USACE	United States Army Corps of Engineers

Latin alphabet

A_f	Constant parameter for the definition of the ageing degree
A_j	Fourier coefficient
A_{xi_0}	Parameter of the affinity function by Cervera et al. (1999a)
$\tilde{A}$	Chemical affinity
$\tilde{A}_m$	Measured chemical affinity
$\tilde{A}_c$	Computed chemical affinity
B	Temperature sensitivity factor
B_f	Constant parameter for the definition of the ageing degree
B_j	Fourier coefficient

Continue in the next page ...

C	Heat capacity per unit volume
C	System's capacity
C_c	Amount of cement per unit volume
C_ε	Volume heat capacity per unit volume
c	Cement content
c	Specific heat
c_{evap}	Specific evaporation heat
$c_{\mu 0}$	Parameter of the creep model
CV	Coefficient of variation
D	System's demand
DM	Damage measures
DV	Decision variables
E	Young's modulus
E	Exposition
E_0	Asymptotic elastic modulus
E_∞	Final Young's modulus
E_a	Activation energy
E_c	Concrete Young's modulus
$E_{cm}(28)$	Elastic modulus of concrete at the age of 28 days
E_{rad}	Actual radiation intensity
f	Daily frequency
f_c	Compressive strength
$f_{c,\infty}$	Final compressive strength
f_t	Tensile strength
$f_{t,\infty}$	Final tensile strength
FS	Factor of safety
F^{-1}	Inverse cumulative distribution function
F_B	Non-Gaussian random field
F_G	Gaussian random field

Continue in the next page ...

H	Relative speed of the hydration reaction
H	Hazard
h	Heat transfer coefficient
h_c	Convection part of the heat transfer coefficient
h_r	Radiation part of the heat transfer coefficient
I_f	Cracking index
$I_{f,lim}$	Limit cracking index
IM	Intensity measures
J	Compliance function
k	Thermal conductivity
k_ξ	Parameter of the affinity function by Cervera et al. (1999a)
l_ξ	Heat of hydration per unit volume
M	Maturity function
m	Shape factor of the Weibull function
$N_{0\leq I_f<I_{f,lim}}$	Number of points on which cracking occurs
N_T	Total number of points
n_T	Material property that controls the sensibility to the curing temperature
P	General mechanical property
P	Period
Pt d	Point located near the downstream face of the dam
Pt lu	Point located near the foundation and upstream face within the dam body
Pt i	Point located in the dam core
Q	Heat of hydration
$\dot{Q}$	Hydration heat rate per unit volume
Q_∞	Cumulated heat at complete hydration
Q^0	Rate of external heat supply provided by conduction
$\underline{q}$	Heat flow vector
q	Heat flux at the surface

Continue in the next page ...

q_c	Convection heat flux
q_r	Long wave radiation heat flux
q_s	Solar radiation heat flux
q_{evap}	Water evaporation heat flux
$q_{max,20}$	Maximum heat production rate at 20°C
R	Universal gas constant
r.v.	Random variable
S	Safety margin
S_i	First order sensitivity index
s/c	Silica fume-to-cement ratio
T	Temperature
T_{ad}	Adiabatic temperature rise
T_{ad}^{∞}	Final temperature under adiabatic conditions
$T_{\alpha,ref}$	Zero-stress reference temperature
$T_{d,m}$	Mean daily ambient temperature
T_{ext}	Ambient temperature
T_{iso}	Temperature of an isothermal test
T_m	Mean annual temperature
T_{max}	Maximum ambient temperature
T_{min}	Minimum ambient temperature
T_{ref}	Reference temperature
T_T	Maximum temperature at which hardening of concrete may occur
T_0	Initial/casting temperature
ΔT_0	Added temperature to casting temperature
t	Time
t_e	Equivalent time
t'	Instant of load application
V	Vulnerability
V	Total variance

Continue in the next page ...

V_i Partial variance

v_w Wind velocity

w/c Water-to-cement ratio

w_i Characteristic integer frequency

Greek alphabet

α Scale factor of the Weibull function

α_T Coefficient of thermal expansion

β Reliability index

$\underline{\varepsilon}^p$ Plastic strain tensor

ε_{cr} Creep strain

ε_{el} Elastic strain

ε_T Thermal strain

ε_{tot} Total strain

ϵ Concrete emissivity

ζ Hardening force

η Dashpot viscosity

η_{ξ_0} Parameter of the affinity function by Cervera et al. (1999a)

$\tilde{\eta}$ Parameter of the affinity function by Cervera et al. (1999a)

θ_x Correlation length, x direction

θ_y Correlation length, y direction

κ Ageing internal variable

$\dot{\kappa}$ Ageing degree rate

λ Formwork heat convection coefficient

λ_{fc} Function that rules the evolution of the ageing degree as function of the hydration degree

λ_{IM} Annual frequency of exceedance of IM

Continue in the next page ...

λ_T	Function that rules the evolution of the ageing degree as function of the temperature
ν	Poisson's ratio
ξ	Hydration degree
ξ_0	Initial hydration degree
ξ_∞	Final hydration degree
ξ_{set}	Hydration degree threshold
$\dot{\xi}$	Hydration degree rate
ρ	Volumetric weight
ρ_f	Cracking density
ρ_{G_i,G_j}	Correlation coefficient between points G_i and G_j
σ	Standard deviation
σ_1	First principal stress
σ_2	Second principal stress
σ_t	Tensile stress
ς	Emissivity of the night sky
τ	Relaxation time of a dashpot
$\tau_{\mu 0}$	Parameter of the creep model
ϕ	Phase
ϕ_y	Annual phase
ϕ_d	Daily phase
χ	Hardening/softening variable

Chapter 1

Introduction

The dam engineering field has recently assisted to an increased use of probabilistic methods applied to the process of risk analysis (Westberg, 2009). As a contribution within this framework, the present thesis aims to account for uncertainties by means of a probabilistic numerical modelling of a roller compacted concrete (RCC) dam.

Moreover, while in the available literature focus is generally given to the service life of the dam (e.g. de Araújo and Awruch, 1998b; Westberg, 2009; Moncada, 2009; Altarejos-García et al., 2012), in the present work emphasis is given to its behaviour during the construction phase.

Hence, a methodology is proposed so as to perform a probabilistic thermo-chemo-mechanical analysis of an RCC dam during its construction phase. This is achieved by performing both uncertainty and sensitivity analysis. In this sense, several aspects related to uncertainties inherent to the construction phase of an RCC dam are addressed in this manuscript. Some of those mentioned aspects are pointed out by Hansen and Forbes (2012) as being delicate steps on the design of dams and often object of several assumptions and variations. Those aspects are: the ambient temperature, the casting temperature, the specific heat, the elasticity modulus, the adiabatic heat rise, the coefficient of thermal expansion and the construction schedule. All of the cited factors are, implicitly or explicitly, accounted for in the present work. Uncertainties related to those aspects are propagated through the model by means of a probabilistic methodology exposed and applied in chapters 5 and 6.

The main goal is to assess the probability of failure, which is here defined as the probability of exceeding a certain pre-defined cracking potential ($P[\rho_f \geq \rho_{f,lim}]$, where ρ_f is the cracking density), assessed in each RCC casted layer, as function of age and boundary conditions. This

methodology is briefly described by means a the schematic representation in Figure 1.1. In the last section of this chapter, further details are given.

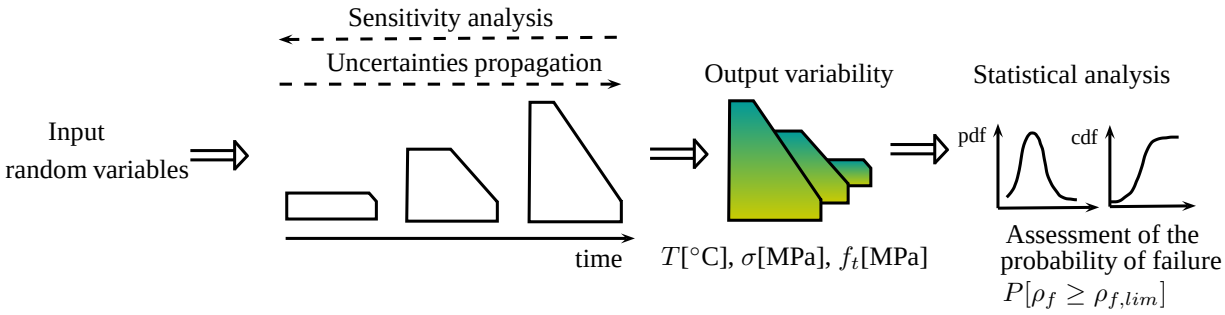

Figure 1.1: Brief scheme of the thesis framework

This introduction chapter intends not only to explain the thesis' objectives, but also to give some introductory concepts which are believed to improve the thesis reading and understand its main goal. Therefore, generalities about the roller compacted concrete technology are firstly presented, followed by the general lines of the thermo-chemo-mechanical behaviour of RCC (analyzed in more detail in chapter 2). Moreover, in order to place the present work within the bigger framework of risk analysis, a brief introduction on the reliability methods applied to dam risk analysis is made, namely a quick introduction to the reliability theory, measures of reliability and common definitions of risk. Finally, are presented the objectives and main contributions of the present work.

1.1 Roller-Compacted Concrete - generalities and applications

The American Concrete Institute (ACI) defines the roller compacted concrete (hereafter denominated RCC) as probably being *"the most important development in concrete dam technology in the past quarter century"* (ACI Committee 207, 1999). The RCC is characterized by its main advantage: rapid construction and consequent reduced cost.

As described in the French BaCaRa project about RCC application on dams, the RCC is a concrete which, as its denomination infer, is compacted by vibratory roller devices. Due to this placing method and to a lower cement content, its behaviour may be divided into two distinct parts: in the first hours after placing, the behaviour is similar to that of a soil; however, several hours later it begins to behave as a hardened concrete; between these two phases the RCC

behaviour is not well known (BaCaRa, 1996). Several authors defend that the RCC assembly the advantages of both domains: those of soil and those of concrete domains (Lackner and Mang, 2004). This construction material is mostly applied in dam and pavement construction, being also used in dam rehabilitation.

The history of RCC goes back to the 1960's, when a high-production no-slump mixture spread with bulldozers was used in Alpe Gere Dam, Italy, and in Manicougan I, Canada (ACI Committee 207, 1999). However, the first RCC dams were constructed later, during the 1980's.

Raphael (1971) presented in his work "The Optimum Gravity Dam", an embankment which was constructed by aggregates enriched with cement and placed using earth moving equipments. With this work, he obtained a better shear strength when compared with a traditional embankment, and was therefore able to design more inclined face slopes.

Between 1972 and 1974, Cannon (1974) performed several experimental studies on a concrete with low cement content, transported by trucks, spread with bulldozers and compacted with vibratory rollers. During this period, also many studies were performed by the U.S. Army Corps of Engineers (ACI Committee 207, 1999).

Figure 1.2: Willow Creek RCC Dam, USA (http://www.nww.usace.army.mil)

All of these early studies during the 1970's have contributed to the construction of an "optimum gravity dam" (ACI Committee 207, 1999). Finally, the first dam in the world to be effectively considered as an RCC dam was constructed in the United States of America. It is the Willow Creek dam (Figure 1.2), with a total RCC volume of 331000 m^3, constructed in 1982 during a period of less than 5 months.

In Japan, in the late 1970's, the RCC technology was developed and referred to as RCD, roller compacted dam. The first Japanese RCD was the Shimajigawa Dam (Figure 1.3), completed in 1981. The RCD technique differs from the RCC one in what concerns the layers' thicknesses: 1m for RCD versus 0.15 to 0.3m for RCC (ACI Committee 207, 1999); and on

the use of bulldozers to spread the mixture in 3 or 4 layers, which are then compacted with vibratory rollers.

Figure 1.3: Shimajigawa RCD Dam, Japan (http://damsroom.web.fc2.com)

Figure 1.4: Pedrógão dam, Portugal (http://cnpgb.inag.pt)

In Portugal, the first (and the only one until now) RCC dam, Pedrógão dam (Figure 1.4), was constructed between April and August 2004. It is located in the Guadiana river, 20km downstream from Alqueva dam (Leitão et al., 2007). The case study of this thesis is inspired from Pedrógão dam's case. For this dam's construction, three different RCC mixtures were previewed, all of them characterized by a high fly ash content. However, for the application in this thesis' work, it was decided to only consider a single RCC mixture in the entire dam body.

The roller compacted concrete is not only applied to gravity dams, but also to arch dams. One example is the Portugues dam in Puerto Rico (Figure 1.5). The case study dealt with in the present thesis is a gravity RCC dam.

Figure 1.5: Portugues dam, Puerto Rico, USA (http://www.dragados-usa.com)

1.1.1 Advantages, disadvantages and particularities

From a construction point of view, and as mentioned before, the main advantage of RCC is the rapid construction and reduced cost. As referred in ACI Committee 207 (1999), the placing method used in the RCC technology is sufficiently rapid to allow higher construction rates. For example, in the case of the Kerrville Ponding Dam in the USA, an RCC dam was rapidly placed downstream of an embankment dam that presented a high risk of failure due to overtopping (ACI Committee 207, 1999). However, the suitability of an RCC dam depends on several conditions, such as the availability of aggregates and a good quality foundation rock. Therefore, if these conditions are not available in the dam construction site, RCC is not a suitable solution. Due to the construction method by superposed layers, this kind of dams have a large number of horizontal/lift joints which, as enhanced by Marques (2008), will increase the structure's susceptibility to percolation and can affect, in an extreme case scenario, its stability and durability. That is why "cold joints" treatment in these structures is of high importance. A "cold joint" is an horizontal joint between two consecutive posed layers which has been exposed to air for more than 4 hours (Ortega et al., 2003). According to Ortega et al. (2003), these joints have to be treated with a bedding mix before the casting of the next RCC layer. This point is further explored in chapters 2 and 4.

There are several differences between roller compacted concrete (RCC) and conventional concrete (CC). The lower cement content which characterizes an RCC will lead to a slower hydration process and a lower hydration heat than for CC (Cervera et al., 2000a). The RCC also presents a lower water content which will lead to less shrinkage. Another main difference between these two concretes is the no-slump consistency of the RCC. When compared with a CC, and because of all the previously cited differences, RCC is characterized by higher density and lower stiffness.

1.1.2 Thermo-chemo-mechanical behaviour of RCC - general lines

As already mentioned, the RCC has a low cement content, which will lead to a lower hydration heat when compared with conventional concrete. Therefore, it is not because of its cement content that significant temperature gradients will occur within the dam body. As previously stated, RCC dams are known by their main advantage: a high construction rate, which on one hand is possible thanks to a lower cement content and, on the other hand, will contribute to greater temperature gradients inside the dam body. Therefore, the higher concreting rate used in RCC dams will lead to significant temperature rises during the first days after casting.

On those early ages, thermal shrinkage will occur, even though less than for conventional concrete thanks to the low water content of RCC. Because of the layered construction method, convection phenomena at the dam faces and foundation rock, and geometrical characteristics such as the distance between transverse joints, the RCC volume changes are restricted and therefore thermally induced stresses will occur.

When concrete starts to cool down and its stiffness has increased, higher thermal gradients will occur due to the concrete's low conductivity (and consequent lower capacity to dissipate the heat generated during the hydration process), to the adopted construction scheme and to the convection and radiation phenomena with the environment. The higher thermal gradients will lead to tensile stresses and since the tensile strength is very low at these early ages, cracking may appear, which will induce a certain damage level, even before the dam's loading (Cervera et al., 1999a).

Numerical models representing the complex behaviour of concrete at early-age are nowadays commonly used in practice (Cervera et al., 1999a,b; De Schutter, 2002). These kind of models allow to better understand the RCC dam behaviour during the construction phase.

In order to take into account all of the phenomena observed in concrete at early ages (hydration, ageing, damage and creep), a coupled thermo-chemo-mechanical model is needed (Cervera et al., 2000a). This model shall be able to predict the hydration degree evolution as well as the associated temperature, the concrete's stiffness, strengths and tensile stresses in order to assess the probability of cracking during the dam's construction phase, on which relies the main purpose of this thesis. However, a coupled thermo-chemo-mechanical model is not easy to manage and many researchers dealing with these problems uses an uncoupled model (i.e. by firstly solving the thermal model and using its solution to solve the mechanical model, such as in Noorzaei et al. (2006)).

Anyway, this kind of models are currently applied on both conventional concrete works (i.e. De Schutter, 2004; Faria et al., 2006; Azenha et al., 2008; Benboudjema and Torrenti, 2008; Azenha, 2009) and RCC dams (Cervera et al., 2000a,b; Luna and Wu, 2000; Lackner and Mang, 2004; Leitão et al., 2007). The coupled thermo-chemo-mechanical model applied in the present thesis is the one developed by Cervera's team (Cervera et al., 1999a,b), formulated based on the theory of porous media by Coussy (1996).

According to Leitão (2011), the thermal analysis of concrete dams in Portugal began in the late 1940's at LNEC (*Laboratório Nacional de Engenharia Civil*) with the beginning of the construction of large dams. In her paper, Leitão (2011) enhances the work developed in Portugal during the last 60 years about this subject, namely the first thesis entitled "Temperatures variations in dams" by Silveira (1961) and the experimental techniques developed by Rocha and Serafim (1958) for the evaluation of the thermal and thermo-mechanical properties of materials. It is during the 1980's and 1990's, with the evolution of numerical techniques and the increasing computers' performances that the numerical thermal analysis of dams emerges. In LNEC it was recently developed home-grown finite element code written in FORTRAN90 that allows the simulations of a dam's construction taking into account the environmental conditions and the hydration heat generation in concrete (Leitão, 2011).

1.2 Reliability methods on dam risk analysis - a brief introduction

No system is 100% safe and to each one of them, a risk is necessarily associated. Socially, the desired safety level, and the inherent risk level, shall be defined based on the balance between two principles: *equity* and *efficiency* (Bowles et al., 2007). While *equity* is related to the *right of individuals and society to be protected*, *efficiency* traduces the *need that society has to distribute and use its available resources in such a way as to gain maximum benefit.* As Harr (1987) stated in his early book about reliability in civil engineering, reliability is the antithesis of failure. While reliability may be defined, quantified, tested and confirmed, failure is highly subjective and qualitative. Moreover, *it is the purpose of reliability-based design to produce an engineered system whose failure would be an event of very low probability* (Harr, 1987).

1.2.1 Reliability theory and measures of reliability

Reliability of a system, or the risk of failure, nowadays known as being probabilistic concepts, were often assessed by a factor of safety. Traditionally, the factor of safety is defined as being the ratio between a system's capacity (C) and its demand (D) (equation 1.1), where the capacity may traduce strength, the loads being described by the demand. However, both strengths and loads are object of uncertainties, and if capacity and demand are uncertain, then the factor of safety will also be uncertain, which is actually the Eurocode philosophy.

$$FS = \frac{C}{D} \tag{1.1}$$

Uncertainties are generally classified into aleatory and epistemic (Paté-Cornell, 1996). Aleatory uncertainties are those who result from natural processes' variability and can only be reduced with the increase of available data. Still, for uncertainties related to natural phenomena, such as wind or seismic loads, their reduction is much more difficult. Epistemic uncertainties result from the lack of knowledge and/or data concerning a given phenomena. This type of uncertainties may either be statistical (lack of data) or modelling (when related to the adopted model to describe a phenomenon). Epistemic uncertainties are usually not accounted for in reliability analysis.

In situ experiments give most of the information on a structure but are also sources of uncertainty related to the chosen inspection method, to the person charged on collecting and interpreting the results or to the inherent spatial variability of the material itself (Malika, 2009). In this sense, reliability theory is a useful tool that leads to a more systematic and consistent use of available information to predict the future behaviour of a given structure.

Another useful measure of reliability is the safety margin (S), defined as being the difference between capacity and demand (equation 1.2). In this sense, for $S < 0$, failure occurs and for $S > 0$ the system is safe. Therefore, boundary $S = 0$ defines the limit state. Actually, the safety margin S is analogous to the commonly used performance function $g(D, C)$, D and C being here the solicitation/demand and resistance/capacity, respectively. If uncertainties are taken into account, the probability of failure (equation 1.3) is given by the grey areas of Figure 1.6. It is enhanced here that the analysis of the failure area in Figure 1.6a is often object of misinterpretations, by considering it as being the total area of superpositions of the demand and capacity curves (Favre, 2004). Actually, the probability of failure is given by the area under the capacity curve where $P(C) < P(D)$ (Figure 1.6a), corresponding to $P(S)$ on Figure 1.6b

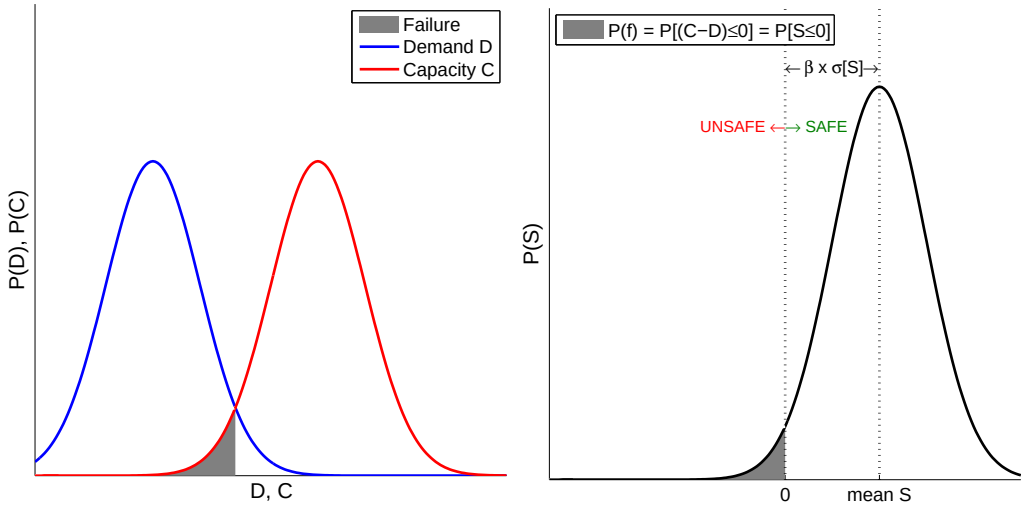

Figure 1.6: Schematic representation of the probability of failure: a) Probability distributions of capacity C and demand D ; b) Probability distributions of safety margin S.

on the *unsafe* zone.

$$S = C - D \tag{1.2}$$

$$P_f = P[(C - D) \leq 0] = P[S \leq 0] \tag{1.3}$$

Finally, a widely applied measure of reliability is the so-called reliability index β (Harr, 1987), given in equation 1.4, where $\bar{S}$, $\sigma[S]$ and $CV[S]$ are the mean value, the standard deviation and the coefficient of variation for the safety margin, respectively.

$$\beta = \frac{\bar{S}}{\sigma[S]} = \frac{1}{CV[S]} \tag{1.4}$$

Reliability analysis/methods are generally classified into the following three categories (Harr, 1987; Haldar and Mahadevan, 2000):

- Level I: in this level, the probability of failure is not calculated and uncertainties are accounted for through the use of (partial) safety factors , applied for different loading conditions; the Point Estimate Method (PEM) presented by Rosenblueth in 1975 is one example of Level I reliability methods (Harr, 1987);

- Level II: in this level, it is sufficient to know the expected/mean values ($E[X]$) and standard deviations ($\sigma[X]$) to characterize uncertainties; first-order, second-moment methods

(FOSM) are an example of Level II reliability methods, and use Taylor series expansion of the functions forms to compute the response's mean and standard deviation;

- Level III: in this level are included the exact methods, on which the probability distribution functions of all uncertain variables must be known from the beginning of the analysis; an example of this Level III reliability method is Monte Carlo Sampling (MCS), and those which are MCS-based, such as Latin Hypercube Sampling (LHS). At this level, the obtained probability of failure is also object of uncertainties and will converge for a large number of computations. Therefore, it is obtained an estimation of the probability, to which an error is associated.

The categorization of reliability methods within these three levels is not uniform amongst the available literature and some other levels may be considered (Teixeira, 2012). For example, Paté-Cornell (1996) presents six levels of complexity on how to account for uncertainties in probabilistic risk analysis. Those levels go from Level 0, which consists on simply identify the hazard (Fault Modes Event Trees FMEA are an example of this level), to Level 5, which leads to the obtention of a family of risk curves by accounting for the probability distribution of several uncertainties as well as for experts' judgement. In between, Level 1 consists on accounting for the worst case scenario; Level 2 adds "plausible upper bounds" to the worst case scenario; Level 3 is the first level on which probabilistic concepts are accounted for, by relying on the central values like the mean, median or mode value; and Level 4 consists on probabilistic risk analysis resulting on a single risk curve, accounting for both epistemic and aleatory uncertainties.

1.2.2 Definition of *Risk*

There are several definitions for *Risk Assessment*. The ICOLD definition divide it into *risk analysis* and *risk evaluation*. According to the ICOLD bulletin 2005, cited in Westberg (2009), there are several limitations to the use of risk assessment in dam engineering, such as the difficulty to estimate the probability of failure with a certain reliability, estimate the dam failure's consequences, the fact that there is not a widely recognised and accepted methodology to evaluate risk and finally, the fact that there is not a good acceptance of the concept of *tolerable risk* by society. *Tolerable risk* is defined as being a risk with whom society is ready to live with in exchange of certain benefits as compensation (Bowles, 2012; SPANCOLD, 2013). This definition meets the previously described balance between *equity* and *efficiency*.

A quick definition of *Risk* may be taken from Economics, on which it is generally defined by the product between the following three concepts: *hazard* (H), *vulnerability* (V) and *exposition* (E) (equation 1.5). On the other hand, the risk related to dam safety is defined by ICOLD (2003) as being the *measure of the probability and severity of an adverse effect to life, health, property, or environment.* Generally, *risk is estimated by the combined impact of all triplets of scenario, probability of occurrence and the associated consequence.* In equation 1.6 is identified the risk related to dam safety (Altarejos-García et al., 2012), where P indicates probability and C consequences, being P[response|loads] the conditional probability of a certain response given a certain load case. Taking the Economics' definition given above, the *hazard* would be the probability of occurrence of a certain load event, the *vulnerability* would be P[response|loads] and the *exposition* would be the consequences resulting from that response.

$$\text{Risk} = \text{H} \times \text{V} \times \text{E} \tag{1.5}$$

$$Risk = \int P[\text{load events}] \times P[\text{response}|\text{loads}] \times C[\text{loads, response}] \tag{1.6}$$

A similar definition of risk is used by seismic engineers, such as equation 1.7 (Cornell and Krawinkler, 2000), on which DM are damage measures, EDP are engineering demand parameters and IM are intensity measures.

$$\lambda_{p_f} = \sum_{k=1}^{N_{\text{DM}}} \sum_{j=1}^{N_{\text{EDP}}} \sum_{i=1}^{N_{\text{IM}}} P[\text{DV}|\text{DM}_k] \cdot P[\text{DM}_k|\text{EDP}_j] \cdot P[\text{EDP}_j|\text{IM}_i] \cdot \Delta\lambda_{\text{IM}_i} \tag{1.7}$$

In the present thesis, the probability of cracking will be analyzed during the construction of an RCC dam. Within this framework, in equation 1.7, DV (decision variables) would be a limit state of cracking, DM (damage measures) would be a measure of the crack extent, EDP (engineering demand parameters) would be the temperature and stresses outputs from the numerical modelling and finally IM (intensity measures) would be, for example, the ambient temperature load, being λ_{IM} the annual frequency of exceeding IM. In the present thesis, the probability analysis focuses on the two conditional probabilities $P[DM_k|EDP_j]$ and $P[EDP_j|IM_i]$ of equation 1.7. By relating this with the definition of equation 1.5, uncertainties will be accounted for related to *vulnerability* and *hazard*, respectively.

1.2.3 Dam safety assessment

In dam engineering, safety analysis is a field that has been evolving during the last decades. In every dam's project, the safety management, conducted through risk assessment and management, is an essential an crucial key to prevent disasters. Mitigation tools and contingency plans are elaborated based on risk analysis.

Even if it is known that the safety of dams is a concept of probabilistic nature, its evaluation has been done in a deterministic manner over the years (Westberg, 2009). In her thesis, Santana (1996) enhances this point by pointing that the classical methods of structural stability analysis, which are based on the concept of the global safety coefficient, are not sufficient to traduce reality. Uncertainties are taken into account in these kind of evaluations by means of a safety coefficient determined empirically, which only has a meaning for each particular case (Santana, 1996; Westberg, 2009). Those evaluations should then take into account uncertain parameters by means of probabilistic tools as a complement to the deterministic classical tools.

The Eurocode approach has motivated the use of semi-probabilistic methods for the safety evaluation of civil engineering structures. Dam engineering is, however, only addressed in a small section of Eurocode 7, dedicated to Geotechnics (CEN, 2004b).

It is known that the partial factors of safety are conservative, which in some cases leads to an over-dimensioning of the structure and consequently over-cost estimation. In this sense, fully probabilistic methods have been studied during the last two decades so that uncertainty can be propagated through the limit state function via a stochastic-oriented methodology. Probabilistic assessment of structures' safety has already been applied to concrete and steel structures since more than 20 years (Ferry-Borges, 1982; Harr, 1987; Keitel and Dimmig-Osburg, 2010). For example, advances in the reinforced concrete domain may be found in literature, with studies that use Level II (FORM) (Chateauneuf et al., 2013) and Level III (MCS and LHS) (Yang, 2007; Hassan et al., 2010; Bastida-Arteaga et al., 2010, 2011) methods to perform reliability analysis. The wide application of those methods goes from the account of uncertainties related to material properties and climatic conditions to study the corrosion of reinforced concrete (Hassan et al., 2010; Bastida-Arteaga et al., 2010, 2011), to uncertainties related with the adopted creep model (Yang, 2007; Keitel and Dimmig-Osburg, 2010; Chateauneuf et al., 2013), among many others.

Efforts have been accomplished towards this direction in the dam engineering field, namely in the works of Westberg (2009), Moncada (2009) and Altarejos-García et al. (2012), among

others. In those works, probabilistic tools are applied to the safety evaluation of concrete dams under service by giving a random character mostly to hydraulic charges (e.g. uplift and headwater). Westberg (2009) also considers uncertainties related to some material parameters such as concrete density and cohesion between dam and rock. Reliability techniques such as FORM/SORM (Level II) and Monte Carlo (Level III) are used on all the three works cited above. An earlier work by de Araújo and Awruch (1998b) deal with uncertainties within the probabilistic numerical modelling of concrete dams, by accounting for random variables on concrete properties and seismic loads via 50 Monte-Carlo simulations. In this work, the safety factors against sliding, crushing and cracking are assessed during the service life of the dam.

In his thesis, Moncada (2009) presents a probabilistic evaluation of a gravity dam's safety and proposes a methodology to define the probabilistic laws describing some parameters' distribution. However, the lack of available measured data, essential to reproduce the variability on material properties and consequent thermo-chemo-mechanical behaviour, is pointed out as being the main constraint.

In Portugal, a thesis was developed by Castro (1998) about backanalysis methods applied to the interpretation of concrete dams' behaviour. Studies were more recently performed about risk analysis applied to embankment dams by Caldeira (2008) and Pimenta (2009). In concrete dams, a work was developed in order to study the application of Artificial Neural Networks (ANN) in dam safety control by Mata et al. (2007).

According to the technical guidelines on dam safety of the Spanish Committe on Large Dams, SPANCOLD (SPANCOLD, 2013), the determination of the failure probability within the context of risk analysis may be performed by reliability methods, experts' judgement and/or specific methodologies to estimate failure probabilities. Often, the lack of data for performing reliability methods is supported by experts' judgement. In Spain, a work has been developed during the past few years related to the application of reliability techniques on the estimation of the probability of failure for concrete dams (Altarejos-García, 2009).

The failure modes identification is one of the most critical steps on dam risk analysis (Westberg, 2009), and may be either structural, hydraulic or related to material degradation. It is the characterization of their interaction that is difficult to assess in order to identify the ultimate failure. One of the most studied failure modes using reliability methods is the sliding failure mode. The examples found in SPANCOLD technical guidelines (SPANCOLD, 2013) concern sliding and overtopping failure modes.

Westberg (2009) presents in her thesis a compilation of existing papers on which structural

reliability analysis is applied to concrete gravity dams. A total of 12 papers were published on this area from 1985 to 2009 (4 of them in 2009). More recently, in 2012, a paper about the estimation of the probability of sliding of concrete dams was presented by Altarejos-García et al. (2012). Moreover, a compilation of works presented in the 3rd International Forum on Risk Analysis, Dam Safety, Dam Security and Critical Infrastructure Management were published in 2012 (Escuder-Bueno et al., 2012), gathering several works related to dam security and safety.

However, very few examples exist on the application of risk analysis and reliability methods to RCC dams, being the work of Moncada (2009) one example. No work about the account for spatial variability of material properties was found within reliability analysis of RCC dams. Moreover, as far as the author is aware, all of the existing works on this area concern the dam long-term behaviour after its construction period, during its service life.

1.3 Objectives and contribution of the thesis

The present thesis aims to be a contribution within the context of probabilistic risk analysis, by applying reliability methods in order to account for uncertainties related to material parameters/characteristics (vulnerability) and loads (hazard) during the construction phase of an RCC dam. In this sense, a coupling between reliability methods and finite element methods is performed in order to achieve the evaluation of the cracking potential of each casted RCC layer during construction. The cracking potential is assessed on each casted layer by means of a cracking density concept, introduced in this thesis. Even if the present work does not aim to compute the response of a real dam case, the geometry and material characteristics were inspired from a real case, Pedrógão dam, located in Portugal. A coupled thermo-chemo-mechanical model (Cervera et al., 1999a,b) is adopted to account for hydration and ageing phenomena at early ages, enabling the consideration of temperature influence on the mechanical properties' evolution.

From the available literature data (e.g. ACI Committee 207, 1999; Conrad, 2006; Noorzaei et al., 2006), it is pointed out that thermo-chemo-mechanical concrete properties are significantly affected by varying intrinsic material parameters such as the aggregates' conductivity, the cement content or the water-to-cement ratio. Therefore, uncertainty associated with these parameters' determination should be considered.

Moreover, and because considering all uncertainties related to the problem is a numerically expensive task, a global sensitivity analysis may be previously performed to quantify the influ-

ence of uncertain input parameters on the response variability of the numerical model output. The first-order sensitivity indices obtained for each studied set of parameters give precious information that help and support the decision of which input uncertainties are worth be considered in the model or which properties must be measured with a good accuracy, establishing a kind of "*hierarchy*" on input parameters. From this point of view, the sensitivity studies are also relevant by giving support to attribute a certain parameter a deterministic character, once that parameter was predefined as uncertain given *in-situ* or experimental measures. This is a very important feature which contributes to lighten the uncertainty analysis.

In addition, even if concrete casting is controlled during construction, some spatial heterogeneity could appear. Spatial heterogeneity shall then be introduced via random fields theory on the most influent parameters. As previously mentioned, no work about the account for spatial variability of material properties within reliability analysis of RCC dams was found in literature.

This thesis' work aims to account for the risk related to cracking during construction which can affect the dam permeability and serviceability at long-term and consequently compromise its structural behaviour. However, those limit states are not modelled in the present thesis, the objective being only to assess the cracking extent (by means of a *cracking density* concept) on each casted layer. It is believed that the presented methodology could be useful in practice to guide some decisions during the design phase of the dam (accounting or not for longitudinal joints, changing the construction scheme, detect the zones more prone to cracking on which it should be considered a different RCC mixture, ...). This analysis is performed in both a deterministic (chapter 4) and probabilistic (chapters 5 and 6) manner.

In figure 1.7 is presented a scheme which intends to give a full framework of the work developed in this thesis and how the main objective is achieved. Basically, each application begins with the definition of the "case scenario" by specifying the adopted parameters and laws to describe the material properties' evolution in time $P(t)$, the ambient temperature evolution $T_{ext}(t)$ and the construction schedule/scheme $Z(t)$ adopted for the layered construction of the RCC dam.

Then, if the computation is deterministic, the "case scenario" is injected in the model and the dam's construction is simulated. In this case, the output will be the temperature, stresses and strengths evolutions in time obtained for that particular case scenario. The cracking index $I_f = f_t/\sigma$ is then computed and, by applying the *cracking density* ρ_f concept (presented in

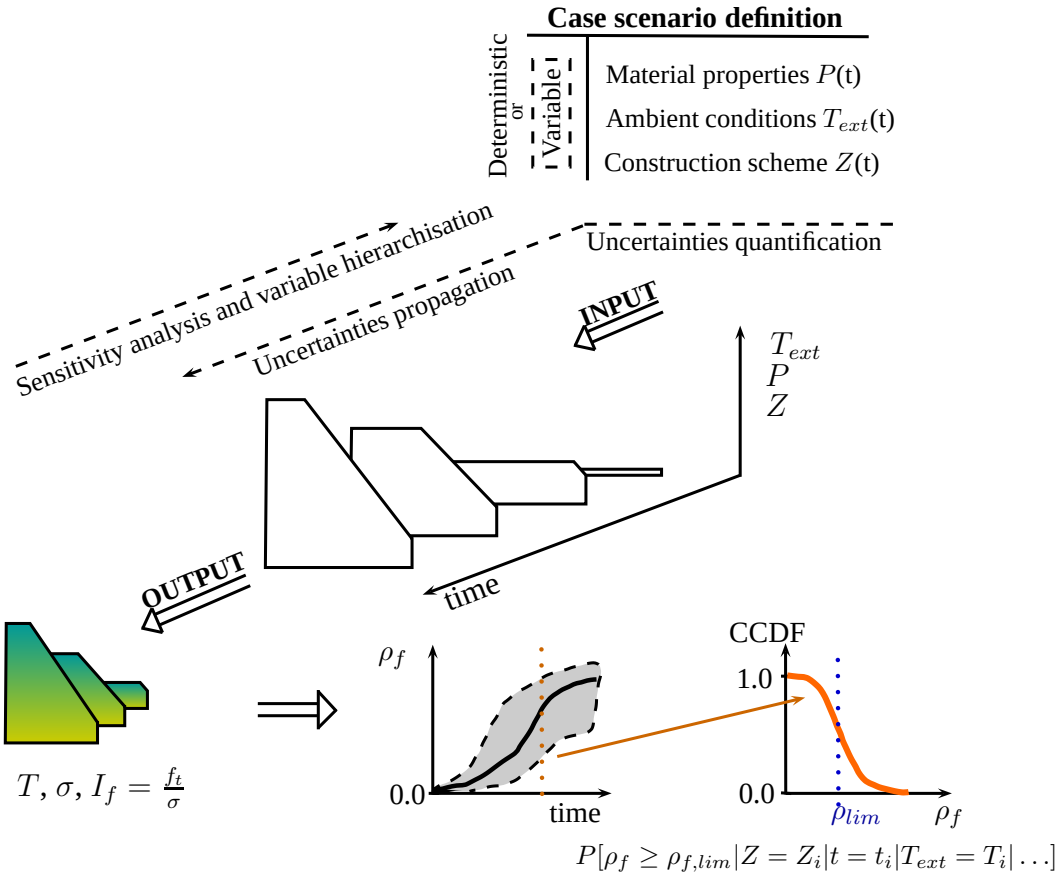

Figure 1.7: Thesis scheme

chapter 3), a measure of the cracking extent on each casted layer is obtained. Since this is a deterministic computation, only one curve for $\rho_f(t)$ is found, and therefore the probability of exceeding a certain damage limit $P[\rho_f \geq \rho_{f,lim}]$ can not be assessed.

On the other hand, if uncertainties related to the "case scenario" are accounted for, then uncertainties' propagation and sensitivity analysis may be performed. Moreover, the output of the model will lead to not one only single curve of $\rho_f(t)$, but to N curves, N being the number of computations. Therefore, in this case, a probabilistic analysis may be performed over the output of $\rho_f(t)$, and the probability of exceeding a certain limit $\rho_{f,lim}$, for a chosen layer and instant in time, may be assessed, and the main goal of this work is finally achieved.

This thesis is organized into seven chapters, being the first and last chapters the introduction and conclusions, respectively.

In **chapter 2** is presented a state of the art concerning the most frequently applied thermo-chemo-mechanical models. Focus is given to hydration models, ageing concept, creep phenomena and cracking at early ages. Firstly, the hydration reaction is described and three hydration

models are presented. Then, the mechanical behaviour of concrete, and more specifically, of RCC is addressed, giving focus to the mechanical properties' evolution at early ages. Afterwards, a brief description of creep phenomena is made and emphasis is given to the model used by Cervera et al. (2002). Because the main goal of this thesis is to assess the probability of exceeding a certain level of damage/cracking, a last section is dedicated to cracking in RCC dams, where concepts like the joint maturity index (JMI) and cracking index (I_f) are introduced. Results found in three literature works concerning cracking of RCC dams during construction are exposed (Cervera et al., 2000b; Lackner and Mang, 2004; Noorzaei et al., 2006).

Chapter 3 concerns the description of the adopted numerical model, its implementation and justification. First of all, details about the coupling of the hydration and ageing degrees are discussed. Then, the validation and verification of the applied thermo-chemo-mechanical model with some elementary tests, namely an adiabatic, an isothermal and cyclic tests, is included. Moreover, details about the dam model are given, namely the cross section geometry, the adopted technique to model the layered construction, the considered boundary conditions, the casting temperature and the zero-stress reference temperature. Finally, the cracking index I_f and density ρ_f concepts are presented and details on their determination are given.

Chapter 4 is the first "applied" chapter, on which the thermo-chemo-mechanical model is applied to simulate the behaviour of the RCC dam during construction in a deterministic manner. In this chapter, parametric studies are carried out by considering different case scenarios, which concern some critical aspects which are often object of unpredicted changes in this kind of analysis, such as the ones cited by Hansen and Forbes (2012): the ambient temperature T_{ext}, the casting temperature T_0 and the construction schedule/scheme "cc". First, a reference/default case is presented. Emphasis is given to the assessment of cracking index and cracking density, two concepts applied in this thesis in order to evaluate the damage extent within the dam body, evaluated at each construction step. The joint maturity index (JMI), a measure of the horizontal joints' quality, is here applied to help the identification of critical layers. The account for cold joints treatment and lateral formwork mechanical and thermal restrains is also studied in the last section of this chapter. Chapter 4 may be seen as an introductory "applied" chapter, on which the fully coupled thermo-chemo-mechanical model is not yet applied using a probabilistic approach, but on which details about the model's performance and the expected dam behaviour can be understood, namely in what concerns the cracking density concept application.

In **chapter 5**, a methodology to perform sensitivity analysis and probabilistic assessment

of the dam's behaviour during construction is presented. An application is done over the case study. As a first approach, an in order to test the proposed probabilistic framework, this chapter is confined to the thermal behaviour of the dam during construction, meaning that any stress state assessment is performed and the cracking index and density are not evaluated either. A description about the adopted probabilistic tools is made. Uncertainties related to both the material parameters and environmental conditions are accounted for, in a first manner by means of random variables and secondly by accounting for the space variability of some material properties by means of random fields. This last point is something that was not found within the available literature and consists therefore in a novel application of random fields to account for spatial variability on some material properties within a thermal analysis of an RCC dam during construction. A global sensitivity analysis is performed by means of the Random Balanced Design FAST (RBD-FAST) test, on which the first-order sensitivity indexes are assessed and give information about the influence of the input variability on the variability of the output. The work presented and discussed in this chapter was published in *Engineering Structures* (Gaspar et al., 2014) and gives a good basis for the comprehension of the sensitivity analysis performed over the full thermo-chemo-mechanical behaviour of the dam discussed in the next chapter.

Finally, in **chapter 6** are gathered the concepts and methodologies presented in the last two chapters. Basically, it concerns the application of the methodology proposed in chapter 5 to the full thermo-chemo-mechanical model applied in chapter 4. The considered uncertainties are related to both the thermal and mechanical behaviour, and two case scenarios concerning the ambient temperature are addressed: winter and summer. The cracking index and density concepts are applied within a probabilistic framework and the probability of exceeding a chosen limit $\rho_{f,lim}$ is assessed on each casted layer. Different approaches are used to evaluate the probability of "failure", namely by using the reliability index β, by applying the First Order Second Moment method (FOSM, a Level II reliability method), and finally by applying a Monte-Carlo based method (a Level III reliability method) on which uncertainties are propagated by means on the basis of the randomization procedure characteristic of the RBD-FAST method. The last section of chapter 6 concerns the sensitivity analysis' results obtained using RBD-FAST. Moreover, by applying the Bayes' theorem, a naive Bayesian approach adopted in order to perform a kind of sensitivity analysis over the cracking density results.

In order to lighten the manuscript's reading and ensure that each chapter can be read independently, a brief description of the dam thermo-chemo-mechanical model is made within

each “applied” chapter (i.e. chapters 4, 5 and 6).

This manuscript ends with a chapter dedicated to the conclusions of the presented work. Here, the main conclusions of each “applied” chapter are gathered. Some recommendations for future research are also added at the end of chapter 7. To this manuscript are also joined two appendices intending to give more details about the adopted methodologies and applied probabilistic tools.

Chapter 2

Thermo-chemo-mechanical behaviour of roller compacted concrete (RCC)

Concrete is a composite construction material known as being a mixed paste of the following three parts: cement, water and aggregates. Its mechanical properties will evolve during curing due to the formation of a binder paste that will bond all the aggregates, giving consistency to the skeleton. The binder paste results from the chemical reaction that occurs between cement and water (and eventual additives). Due to the exothermic and thermally activated character of the chemical reaction, a thermo-chemo-mechanical model is needed in order to simulate the behaviour of concrete at early ages. The objective of this chapter is to review some of the existing models and to compare their performances, emphasizing their application to roller-compacted concrete (RCC). Firstly is presented the hydration reaction, with emphasis on three hydration models. Then, the mechanical properties' evolution of concrete at early ages is discussed, followed by a brief description of creep phenomena and viscoelastic models. The described models are organized in the following approaches: maturity concept, equivalent time and hydration degree. At the end, a section is dedicated to cracking in RCC dams.

2.1 Hydration reaction

The hydration reaction in concrete occurs due to the chemical reaction between cement and water. This reaction is highly exothermic and thermally activated, characteristic of the hardening phase of concrete and accompanied by an increase of its volume. The main purpose of a hydration model is to assess the heat of hydration evolution in order to predict temperature distribution in a concrete structure at early ages.

From the hydration reaction result hydration products, which will, in turn, contribute to the stiffening/hardening of concrete. This reaction can be divided into three main phases: dissolution, precipitation and diffusion. During the precipitation phase, low density C-S-H (calcium silicate hydrates) hydrates are produced, while high density ones are formed during the diffusion phase. The physical and chemical mechanisms inherent to this reaction are not yet fully understood. It is however known that the hydration rates are quite different for each mineral component (calcium silicates, calcium aluminates, etc).

In a simplified way, there exist three different types of hydration models according to the scale level they use to traduce the hydration of cement: micro, meso and macro-models. According to Ji (2008), a microscopic model is able to simulate the hydration of each chemical component of cement, point by point, within the model. An example of a microscopic model is the one of Bentz et al. (1998). A meso-model predicts the evolution of the hydration reaction by a growth of the cement particles forming a skeleton. An example of a meso-model is the one developed by van Breugel (1991). For engineering purposes, a macroscopic description of the hydration reaction is usually adopted (Cervera et al., 1999a).

From a macroscopic point of view, concrete's stiffening can be seen as a variation of the Young's modulus in time (Ulm and Coussy, 1996). Actually, during hydration, the thermal and mechanical properties of concrete are continuously changing (De Schutter, 2002), such as depicted in Figure 2.1 (HPC stands for High Performance Concrete and OC for Ordinary Concrete) where the hydration degree traduces the hydration reaction evolution from 0 to 1. This evolution, generally called "ageing", will influence the crack threshold and, consequently, the cracking of concrete at early ages (Ulm and Coussy, 1996).

The increase of the Young's modulus will be accompanied by increased stresses induced by restrained thermal and chemical shrinkage. If those stresses reach the concrete strength developed so far, then cracking will occur, with further consequences on the durability of the structure. This behaviour is observed in a concrete specimen tested in the Temperature Stress Testing Machine (TSTM) such as in Figure 2.2 by Ji (2008). In this schematic representation of the TSTM, TD is referring to the thermal deformation, while AD corresponds to the autogenous shrinkage due to self-desiccation, the two main causes of volume changes in concrete at early-ages (Ji, 2008). In this case, cracking would occur around 168 hours of age, when the stress value attains the tensile stress developed so far.

Concluding, the material properties should be related to the evolution of the hydration reaction, which can be achieved by performing a thermo-chemo-mechanical model, enabling the

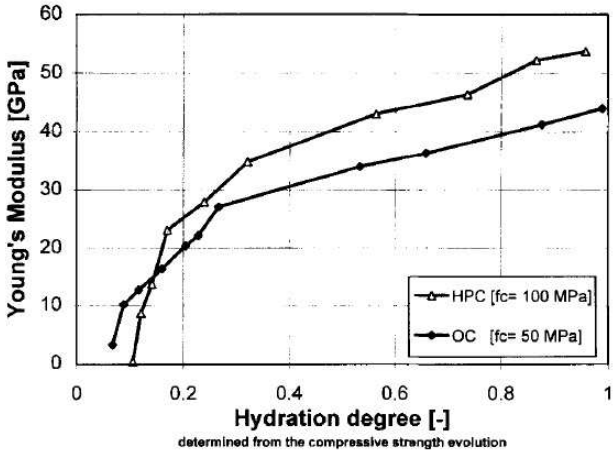

Figure 2.1: Young's modulus evolution as function of the hydration degree (Ulm and Coussy, 1996), experimental values from Laplante (1993)

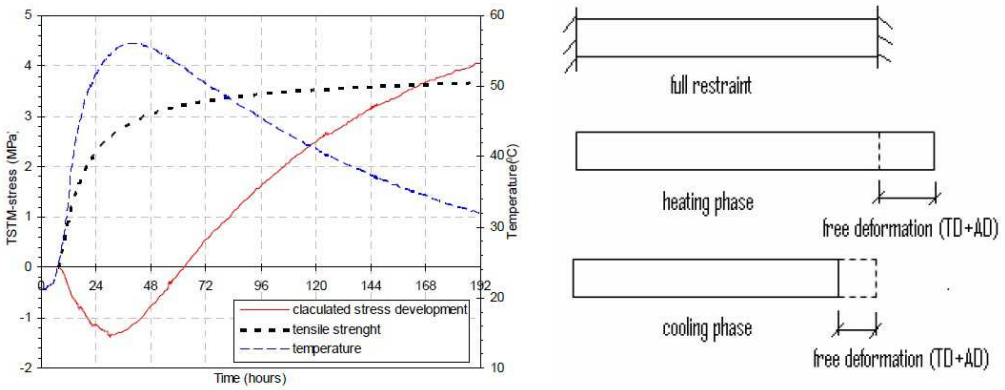

Figure 2.2: Temperature, stress and tensile strength development of a concrete specimen testes in TSTM (Ji, 2008)

prediction of the rate of hydration and heat production, estimating the evolution of mechanical properties in time. Material laws based on the evolution of the hydration reaction should then be incorporated in this model (Cervera et al., 1999a; De Schutter, 2002). This point will be further discussed in section 2.3.1.

The general heat transfer problem is described by equation 2.1, where ρ [kg/m^3] is the volumetric weight, c[J/(kg·°C)] is the specific heat, T[°C] is the temperature ($\dot{T}$ being its first derivate), $\underline{q}$ is the heat flow vector described by the Fourier law (equation 2.2, where k[W/(m·°C)] is the thermal conductivity), and $\dot{Q}$[W/m^3] is the rate of heat generation per unit volume.

$$\rho \cdot c \cdot \dot{T} = -div(\underline{q}) + \dot{Q} \tag{2.1}$$

$$\underline{q} = -\underline{\underline{k}} \cdot \underline{grad(T)} \tag{2.2}$$

The rate of heat generation per unit volume results from the temperature evolution within the concrete mass that occurs due to the hydration reaction between cement and water, which in turn will affect the mechanical properties' evolution. The definition of this hydration heat by means of a hydration model varies among researchers.

The hydration heat is commonly described as a function of time, such as in equation 2.3, where $q(t)$ is the hydration heat production rate at time t. Experimental tests such as the adiabatic (no heat exchanges between the sample and the environment), semi-adiabatic (almost constant ambient temperature, heat losses through the sample faces) and isothermal ones (constant ambient temperature) are used to evaluate the hydration heat of cement pastes and concrete. The cumulative hydration heat $Q(t)$ and the rate of hydration heat $q(t)$ may be compared in Figure 2.3 by Conrad (2006).

$$Q(t) = \int_0^t q(t)dt \tag{2.3}$$

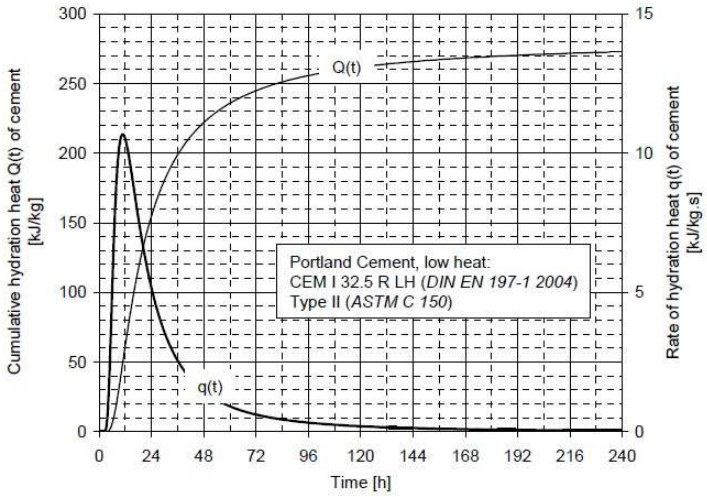

Figure 2.3: Adiabatic hydration heat of a Portland cement (Conrad, 2006)

The main idea of the hydration model is to define the concrete's ageing mechanism by means of a certain time variable, so that it can be possible to compute the mechanical properties of concrete as functions of that variable. Because the hydration reaction is also exothermic and thermally activated, that ageing variable shall be able to take into account both the effects of

time and temperature. This was exactly the purpose of the maturity concept introduced by Nurse (1949).

According to Carino and Lew (2001), the origins of the maturity method go back to 1949 in a work developed by Nurse (1949), who defined the maturity function $M[°C·h]$ (currently called *temperature-time factor*) as in equation 2.4, commonly known as the *Nurse-Saul maturity function*. In this equation, T is the mean temperature during time interval Δt and T_0 is the *datum temperature*, which is the temperature below which the mechanical properties evolution stops, usually taken equal to $-10°C$.

$$M = \sum_{0}^{t} (T - T_0)\,\Delta t \tag{2.4}$$

From this method, Saul (1951) formulated the *maturity rule*, which states that concrete from the same mixture and at the same maturity level presents the same strength properties independently from the temperature history that it has been subjected to, meaning that for a certain concrete mix there exists one only strength-maturity curve. This method was widely accepted and applied in the past and consists on one of the first documented methods to account for the dual effect of time and temperature on the strength evolution of concrete. However, an assumption is inherent to this method: the initial strength rate (right after casting, at early-ages) development is considered to vary linearly with temperature, which is known not to be valid (Carino and Lew, 2001).

The maturity method was studied and its applicability tested by various authors, and it was found that the maturity rule is not always valid, such as it may be concluded by Figure 2.4, reported by Carino and Lew (2001) as a "crossover effect". These results showed that concrete from the same mix cured at lower temperatures develop lower strength at early ages but will attain higher strength values later in time, when compared with a concrete cured at higher temperatures, which means that it can not be fully characterized by one only strength-maturity curve. This motivated research for more complex hydration models accounting for both time and temperature effects in concrete's mechanical behaviour at early ages.

For the thermal analysis of concrete massive structures it is common practice to adopt an adiabatic hydration model. This kind of models is of easiest application and allows the estimation of the thermal behaviour of the structure's core. One example is the model developed

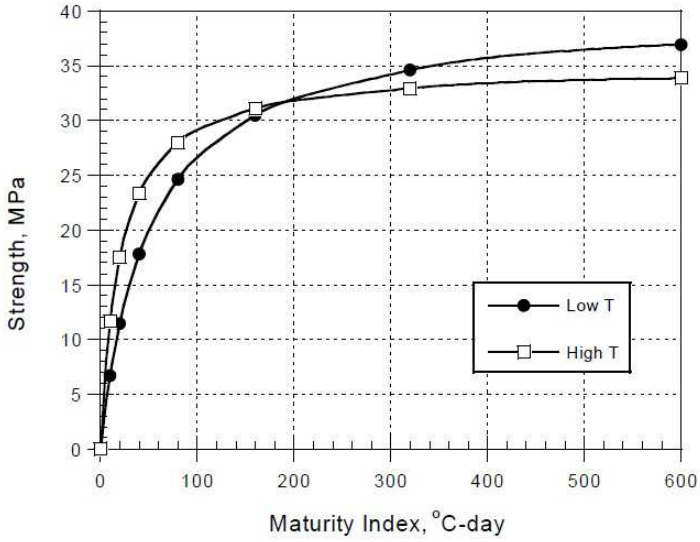

Figure 2.4: Strength evolution in concrete as function of the maturity index for two different curing temperatures (Carino and Lew, 2001)

and presented by Tanabe et al. (1985) and applied by several authors, such as Noorzaei et al. (2006) and Jaafar et al. (2007) to RCC dam's modelling. This model quantifies the hydration heat by means of the temperature evolution measured during an adiabatic test. Since under adiabatic conditions there are no heat exchanges with the surrounding environment, the heat transfer problem of equation 2.1 is reduced to equation 2.5. In the hydration model used by the previously cited authors, the adiabatic temperature T_{ad} is given in equation 2.6, where T_{ad}^{∞} is the maximum temperature of concrete under adiabatic conditions and $\alpha[s^{-1}]$ is a parameter that represents the heat generation rate. Finally, the rate of hydration heat may be described by equation 2.7.

$$\rho \cdot c \cdot \dot{T_{ad}} = \dot{Q} \tag{2.5}$$

$$T_{ad} = T_{ad}^{\infty} \cdot (1 - \exp(-\alpha \cdot t)) \tag{2.6}$$

$$\dot{Q} = \rho \cdot c \cdot T_{ad}^{\infty} \cdot \alpha \cdot \exp(-\alpha \cdot t) \tag{2.7}$$

This hydration model is of easy application since it only requires the results from an adiabatic test. However, it can only be applied to massive concrete structures and one must be aware that it can only reproduce the temperature evolution under adiabatic conditions, that is, without considering the heat exchanges with the surrounding environment. Therefore, this shall be a useful model in the sense that it allows the computation of the hydration heat in the center of massive concrete structures, at least during the first hours or even days after casting, giving an

idea of the early age thermal behaviour of that structure.

The adiabatic hydration model may also be formulated based on the hydration degree concept. The hydration degree ξ describes the evolution of the hydration reaction and varies from $\xi = 0$ when the reaction as not yet begun, and $\xi = 1.0$ when the reaction has finished. Giesecke et al. (2002), cited by Khan (2011), propose an adiabatic hydration model, here given by equation 2.8, that used the hydration degree concept ξ (equation 2.9).

$$\dot{Q} = \rho \cdot c \cdot T_{ad}^{\infty} \cdot \dot{\xi} \tag{2.8}$$

$$\xi = \frac{T_{ad}}{T_{ad}^{\infty}} \tag{2.9}$$

Furthermore, other methods have raised, namely based on the equivalent time concept, presented hereafter.

Another widely used model, presented by Rastrup (1954), is based on the equivalent time concept. The equivalent time concept (at that time called *time-temperature function* by Rastrup, which is actually equivalent to the maturity concept presented above), is introduced to allow the comparison between a heat transfer process at a given established reference temperature (generally under isothermal conditions with a (reference) temperature of $T_{ref} = 20°C$) and a process that occurs at any temperature. In other words, the equivalent time is the time during which a concrete specimen would have to be cured under that reference temperature in order to achieve the strength of a concrete specimen cured under other conditions (De Schutter, 2004).

Rastrup (1954) defines a time-temperature function such as in equation 2.10, where $T_{ref}[°C]$ is a constant reference temperature and B is the commonly called temperature sensitivity factor (taken by Rastrup equal to 0.1). This formulation consists actually on the equivalent time. The hydration heat is then described by means of equation 2.11, on which A, b, D and n are model parameters obtained by regression analysis of experimental data.

$$t_e = \int_0^t 2^{B(T-T_{ref})} dt \tag{2.10}$$

$$Q = A + D \cdot \exp(-b \cdot [t_e]^n) \tag{2.11}$$

The equivalent time approach has been widely applied since. However, an assumption is (still) implicit here: linear dependency between the initial/early-age rate of strength develop-

ment and temperature, which is a limitation of this method.

In order to overcome that limitation, Hansen and Pedersen (1977) proposed the definition of the equivalent time concept by means of an Arrhenius-type function such as equation 2.12, which assumes a non-linear relationship between strength development and curing temperature achieved by the introduction of the activation energy E_a[J/mol].

$$t_e = \int_0^t \exp\left(-\frac{E_a}{R}\left(\frac{1}{T} - \frac{1}{T_{ref}}\right)\right) dt \tag{2.12}$$

Carino (1982) and Byfors (1980) have compared these two methods and came up with the conclusion that the maturity function based on the equivalent time concept is more powerful than the Nurse-Saul one because it leads to a reduction on the obtained differences on the strength-maturity curves while adopting different curing temperatures. The same conclusions were achieved in a more recent study by Ballim and Graham (2003).

Even if comparative studies made by several authors point that the equivalent time method using an Arrhenius-type model gives better results, it still presents a limitation: lack of ability to take into consideration the effects of the early-age temperature on the long-term strength (Carino and Lew, 2001).

Another difficulty of the Arrhenius-type model is that it implies the determination of the activation energy E_a, considered by Carino and Lew (2001) as being the key parameter of this equation. Generally the ratio E_a/R is assumed as being constant, even if this assumption may be object of several discussions because of the activation energy evolution during the hydration reaction. That evolution has been reported in the work of Azenha (2009). However, Lura and Van Breugel (2001) reported that the temperature evolution and cracking risk evaluated in a 0.4m thick wall is not significantly affected by changes in E_a/R. Carino (1984) developed a procedure to study the activation energy by evaluating the effect of the curing temperature on the strength development, which resulted in the following conclusions: for a water-to-cement ratio of 0.45, 30[kJ/mol] $\leq E_a \leq$ 64[kJ/mol] (that is 3600[K] $\leq E_a/R \leq$ 7700[K]); for a water-to-cement ratio of 0.6, 30[kJ/mol]$\leq E_a \leq$ 56[kJ/mol] (that is 3700[K] $\leq E_a/R \leq$ 6700[K]).

Pinto and Hover (1999) proposed a new method to determine the activation energy by measuring the setting times at different temperatures and then transforming them into the natural logarithm of the inverse of time versus the inverse of temperature. The slope of that linear relationship is the factor $-E_a/R$ of the Arrhenius function. Concerning fly ashes and silica fume, Waller (1999) concluded that the activation energy may be assumed as a constant value

independently of the type of fly ashes or silica fume. Furthermore, Buffo-Lacarrière (2007) has presented in her thesis a sensitivity study that has shown that the ratio E_a/R does not significantly affect the temperature and hydration degree's evolutions.

At the image of the maturity method, the equivalent time concept also allows the evaluation of the strength evolution of a certain concrete specimen, subjected to an arbitrary temperature history, from its evolution obtained under adiabatic conditions (T_{ref}).

Another well-known hydration model is the one developed by Ulm and Coussy (1996), also used by Cervera and his work team (Cervera et al. (1999a,b, 2000a,b, 2002)) and Lackner and Mang (2004). This model uses the concept of hydration degree ξ, introduced by Byfors (1980) in his work of 1980.

The hydration degree ξ describes the evolution of the chemical reaction. For that reason, it is considered as being the fundamental parameter in the description of concrete behaviour at early ages. It is traditionally defined by the relative amount of cement that has already reacted and it varies from 0 (or a value close to zero) to 1 (when the reaction is completed) under ideal conditions. Those ideal conditions are characterized by an adequate water-to-cement ratio (w/c), that guarantees a full hydration and a perfect contact between the cement grains (Cervera et al., 1999a). However, those ideal conditions are generally not obtained in practice, and so, the final hydration degree never reaches 1.0 and it is defined by the empirical equation 2.13 defined by Pantazopoulo and Mills (1995), where ξ_∞ is the final hydration degree.

$$\xi_\infty = \frac{1.031 \cdot w/c}{0.194 + w/c} \tag{2.13}$$

In a hydration model an assumption is generally made: there are no water transfers between the environment and the system and therefore this is a closed chemical system. In this case, according to Cervera et al. (1999a), the chemical reaction will come to an end either when: i) assuming there is an adequate initial water content in the mixture, all of the unhydrated cement has reacted; or ii) assuming an insufficient initial water content (which is generally observed in practice), all of the free water has already been consumed. In this last situation a realistic value of the actual hydration degree is observed.

There are several ways to describe the hydration degree's evolution in literature: based on the rate of temperature evolution under adiabatic conditions (equation 2.14, where T_0 is the temperature for $t = 0$), by being the rate of hydration heat generated (equation 2.15, where

Q_∞ is the cumulated heat at complete hydration and $\dot{Q}$ is the heat production rate), by means of an Arrhenius-type law (equation 2.16, where $\tilde{A}$ is the chemical affinity, E_a is the activation energy, R is the universal gas constant ($R = 0.00831$kJ/mol) and T[K] is the temperature), and finally by means of a Rastrup-type function (equation 2.17 (Sabbagh-Yazdi et al., 2007)).

$$\xi(t) = \frac{T_{ad}(t) - T_0}{T_{ad}^{\infty} - T_0} \tag{2.14}$$

$$\xi(t) = \frac{1}{Q_\infty} \int_0^t \dot{Q}(t)dt \tag{2.15}$$

$$\dot{\xi} = \tilde{A} \cdot \exp\left(-\frac{E_a}{RT}\right) \tag{2.16}$$

$$\dot{\xi} = \tilde{A} \cdot 2^{(T/10)} \tag{2.17}$$

In Figure 2.5 is plotted the temperature evolution of an adiabatic test and its corresponding (normalized) chemical affinity $\tilde{A}$ evolution as function of the hydration degree.

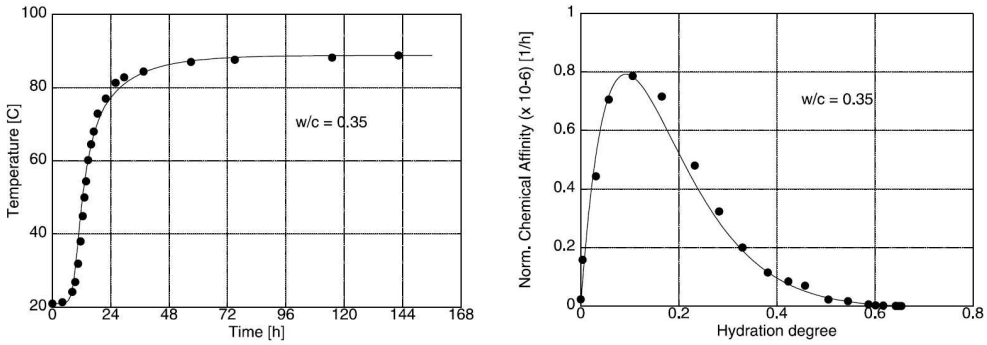

(a) (b)

Figure 2.5: Adiabatic test (Cervera et al., 2002), experimental measures from Bentz et al. (1998): a) Temperature evolution; b) Normalized chemical affinity evolution.

Even though different approaches are available in literature, it is nowadays widely accepted that the maturity/hydration degree evolution in concrete at early ages can be accurately modeled by means of an Arrhenius-type function. Therefore, it is the Arrhenius-type function that will be adopted in the present work.

2.2 Three hydration models review

In this section, three hydration models that use the hydration degree concept are analyzed in more detail.

Cervera and his team based their thermo-chemo-mechanical model on the work of Ulm and Coussy (1996) and came up with a hydration heat evolution of the Arrhenius-type form of equation 2.18.

$$\dot{Q} = l_\xi \cdot \tilde{A}(\xi) \cdot \exp\left(-\frac{E_a}{R \cdot T}\right) \tag{2.18}$$

In this model, l_ξ [J/m^3] is the heat of hydration per unit volume and $\tilde{A}(\xi)$ is the chemical affinity introduced by Ulm and Coussy (1996) and it fully characterizes the macroscopic hydration kinetics for a given concrete. According to Coussy (1996), the chemical affinity is the driving force of the reaction and it measures the difference of potential between the reactants and the products. When the chemical affinity is higher than zero, the chemical reaction only occurs from the reactants towards the products. The reaction stops when the chemical affinity reaches its equilibrium ($\tilde{A} = 0$).

The evaluation of $\tilde{A}(\xi)$ may be performed either by means of adiabatic calorimetric or isothermal strength evolution tests. For instance, Cervera et al. (1999a) use adiabatic calorimetric test results (such as in Figure 2.5), while Lackner and Mang (2004) also uses isothermal compressive strength test results, as depicted in Figure 2.6 (where a linear relationship is assumed between the compressive strength f_c and the hydration degree ξ).

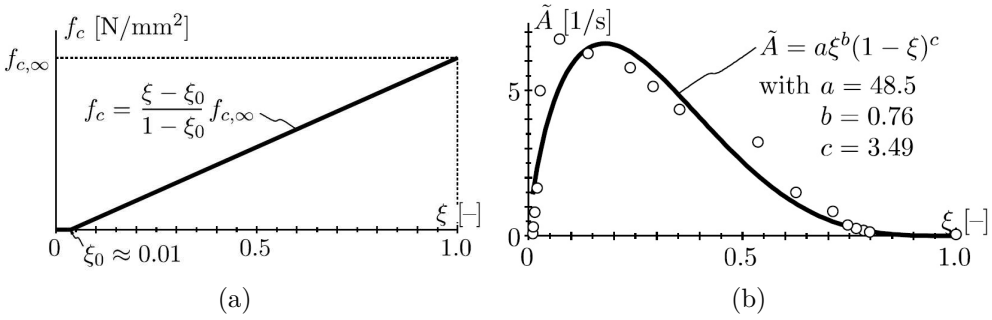

Figure 2.6: Isothermal test (Lackner and Mang, 2004): a) Compressive strength evolution; b) Chemical affinity evolution.

It was demonstrated by Ulm and Coussy (1996) that both procedures lead to the same chemical affinity evolution, as shown in Figure 2.7.

As previously exposed, under adiabatic conditions the field equation reduces to equation 2.5 and the hydration degree may be described by equation 2.14. Considering equation 2.18, then l_ξ may be evaluated by equation 2.19 given in Cervera et al. (1999a). On its turn, the chemical affinity under adiabatic conditions, given equations 2.5 and 2.14, is given by equation 2.20.

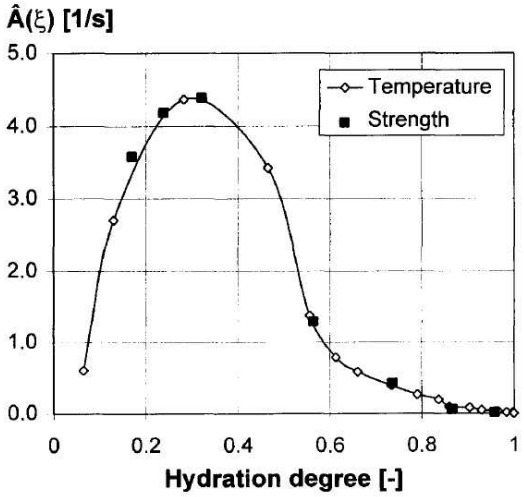

Figure 2.7: Chemical affinity evolution of a HPC determined from adiabatic temperature elevation ("Temperature" curve) and from isothermal strength evolution ("Strength" squared points) (Ulm and Coussy, 1996)

$$l_\xi = \frac{\rho \cdot c}{\xi_\infty} \cdot (T_{ad}^\infty - T_0) \tag{2.19}$$

$$\tilde{A}(\xi) = \frac{\xi_\infty}{T_{ad}^\infty - T_0} \cdot \dot{T}_{ad} \cdot \exp\left(-\frac{E_a}{R \cdot T_{ad}}\right) \tag{2.20}$$

Cervera et al. (1999a), based on the thermodynamic framework of Ulm and Coussy's model, finally came up with a definition of the chemical affinity that involves several parameters (equation 2.21) which are obtained by calibrating the results of equation 2.20.

$$\tilde{A}(\xi) = \frac{k_\xi}{\eta_{\xi 0}} \left(\frac{A_{\xi 0}}{k_\xi \xi_\infty} + \xi\right)(\xi_\infty - \xi) \exp\left(-\overline{\eta}\frac{\xi}{\xi_\infty}\right) \tag{2.21}$$

As recalled before, Lackner and Mang (2004) used isothermal compressive strength test's results to evaluate the chemical affinity evolution (Figure 2.6) by assuming a linear relationship between the hydration degree and the compressive strength of the form of equation 2.22 (adopting $a = 1.0$) given by De Schutter and Taerwe (1996). Here, it was assumed that the final degree of hydration is equal to 1.0, which was already mentioned not to be realistic.

$$\frac{f_c(\xi)}{f_c(\xi_\infty = 1)} = \left(\frac{\xi - \xi_0}{1 - \xi_0}\right)^a \tag{2.22}$$

Lackner and Mang (2004) have finally defined the chemical affinity evolution by regression analysis from the compressive strength test's results such as given in equation 2.24 where a, b and c are constant parameters, which seems much more simpler than the one presented by

Cervera's team (equation 2.21).

$$\tilde{A}(\xi) = \frac{1-\xi_0}{f_{c,\infty}} \cdot \frac{df_c(t)}{dt} \cdot \exp\left(-\frac{E_a}{R \cdot T}\right) \tag{2.23}$$

$$\tilde{A}(\xi) = a \cdot \xi^b \cdot (1-\xi)^c \tag{2.24}$$

On their turn, De Schutter and Taerwe (1995) describe the heat production rate by means of two functions $\tilde{A}(\xi)$ and $g(T)$. $\tilde{A}(\xi)$ describes the influence of the hydration degree ξ, while $g(T)$ describes the influence of temperature. In equation 2.25, $q_{max,20}$ is the maximum heat production rate at 20°C. In equation 2.26 a_{st}, b_{st} and c_{st} are constant parameters.

$$q(\xi, T) = q_{max,20} \cdot \tilde{A}(\xi) \cdot g(T) \tag{2.25}$$

$$\tilde{A}(\xi) = c_{st} \cdot [\sin(\xi\pi)]^{a_{st}} \cdot \exp(-b_{st}\xi) \tag{2.26}$$

$$g(T) = \exp\left[\frac{E_a}{R}\left(\frac{1}{293} - \frac{1}{273+T}\right)\right] \tag{2.27}$$

Concluding, the three hydration models described in this section are as follows:

- Cervera et al. (2000a) (5 parameters):

$$\tilde{A}_\xi(\xi) = \frac{k_\xi}{\eta_{\xi 0}}\left(\frac{A_{\xi 0}}{k_\xi \xi_\infty} + \xi\right)(\xi_\infty - \xi) \cdot \exp\left(-\tilde{\eta}\frac{\xi}{\xi_\infty}\right) \tag{2.28}$$

- Lackner and Mang (2004) (3 parameters):

$$\tilde{A} = a \cdot \xi^b \cdot (1-\xi)^c \tag{2.29}$$

- De Schutter and Taerwe (1995) (3 parameters):

$$\tilde{A} = c_{st} \cdot [\sin(\xi\pi)]^{a_{st}} \cdot \exp(-b_{st}\xi) \tag{2.30}$$

These three hydration models will be applied and compared hereafter. The characteristics of different concrete materials studied by each author are given in Table 2.1. These characteristics concern the type of cement, the water-to-cement ratio (w/c) and the silica fume-to-cement ratio (s/c). Tables 2.2 and 2.3 present each model's parameters.

Figure 2.8 gives the evolution of the normalized chemical affinity obtained with equation 2.30 (De Schutter and Taerwe, 1995). This curve represents a typical response of a hydration model,

with the hydration degree (ξ) varying from 0 to 1.0 and a chemical affinity which presents a unique peak value. The first part of the curve, from zero to the peak, corresponds to the first two stages of the hydration reaction: dissolution and precipitation; while the second part of the curve, from the peak to the final hydration degree, corresponds to the third stage: diffusion.

In what concerns the results of the chemical affinity obtained with the hydration model of Lackner and Mang (2004) and plotted in Figure 2.9a, it may be concluded that the maximum value of the chemical affinity is attained at a lower hydration degree for RCC when compared with the CC. This is even more evident while analyzing Figure 2.9b, where it can be noted that

Table 2.1: Material properties for each model

Material	Cement content c	w/c	s/c
De Schutter and Taerwe (1995)	Portland cement CEM I 52.5		
Lackner and Mang (2004)			
CC (Conventional Concrete)	315kg PZ35(F)/m^3	0.54	-
RCC90 (Roller Compacted Concrete)	90kg/m^3	1.0	-
Cervera et al. (1999b)			
C-30		0.50	–
C-100		0.25	0.09
L(OPC)		0.50	–
L(HPC)		0.30	0.1

Table 2.2: Chemical affinity model parameters (De Schutter and Taerwe, 1995; Lackner and Mang, 2004)

Model	Parameters		
	a_{st}[1/s]	b_{st}[1/s]	c_{st}[1/s]
De Schutter and Taerwe (1995)	0.667	3.0	2.5968
	a[1/s]	b[1/s]	c[1/s]
Lackner and Mang (2004)			
CC	48.5	0.76	3.49
RCC90	57.0	0.75	7.05

Table 2.3: Chemical affinity model parameters (Cervera et al., 1999b)

Cervera et al. (1999b) Parameter	C-30	C-100	L(OPC)	L(HPC)
k_ξ/η_{ξ_0} [1/h]	$0.14 \cdot 10^6$	$4 \cdot 10^6$	$1 \cdot 10^6$	$1 \cdot 10^6$
ξ_∞	0.75	0.58	0.75	0.75
$\tilde{\eta}$	7.5	6.0	7.5	7.5
A_{ξ_0}/k_ξ	$1 \cdot 10^{-4}$	$1 \cdot 10^{-4}$	$1 \cdot 10^{-4}$	$0.01 \cdot 10^{-4}$

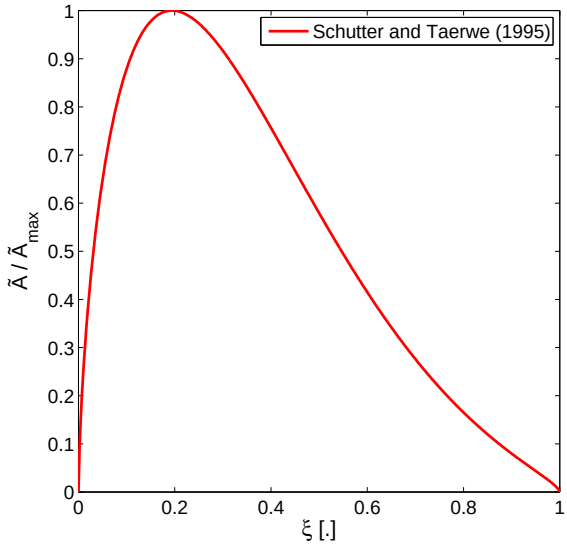

Figure 2.8: Normalized chemical affinity evolution, De Schutter and Taerwe (1995)

the peak of the chemical affinity for RCC is lower than for CC. This means that the heat of hydration of the RCC is lower than for CC and also that RCC maturates earlier than the CC. This fact can be explained by the lower cement content of the RCC paste ($c = 90\text{kg/m}^3$) when compared with the CC ($c = 315\text{kg/m}^3$).

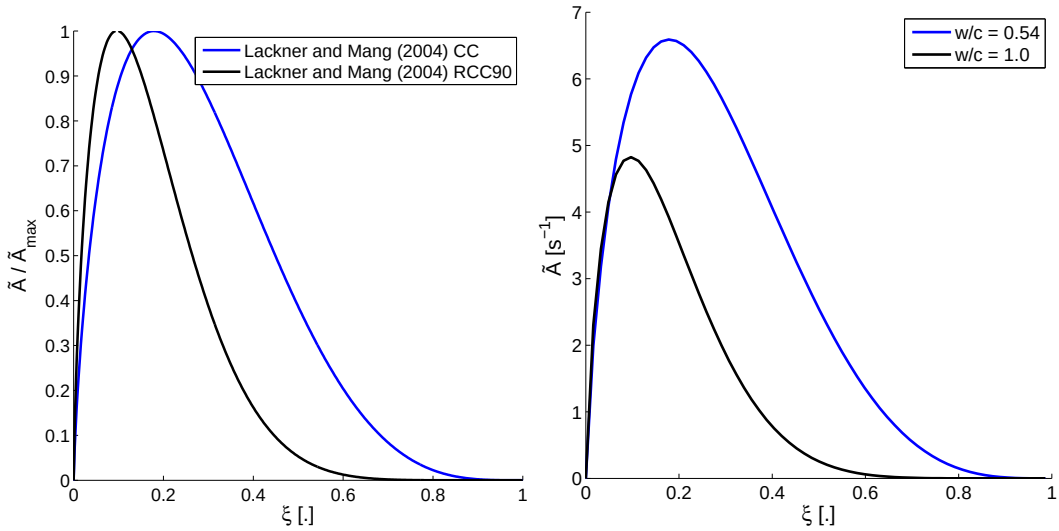

(a) (b)

Figure 2.9: Chemical affinity evolution by Lackner and Mang (2004): a) Normalized chemical affinity evolution ; b) (Non-normalized) Chemical affinity evolution.

Figures 2.10 and 2.11 show the response of Cervera's model (equation 2.28) for four different conventional concrete mixtures described in Table 2.3. In what concerns the normalized evolution of the chemical affinity, it is noted in Figure 2.10 that the difference between the four

responses is not significant. Actually, the behaviour is exactly the same until reaching the peak, diverging afterwards only for mixture C-100, even though not much. However, while analyzing Figure 2.11b, where are plotted the non-normalized responses for mixtures with different water-to-cement (w/c) and silica fume-to-cement (s/c) ratios, it may be seen that their evolutions are very different.

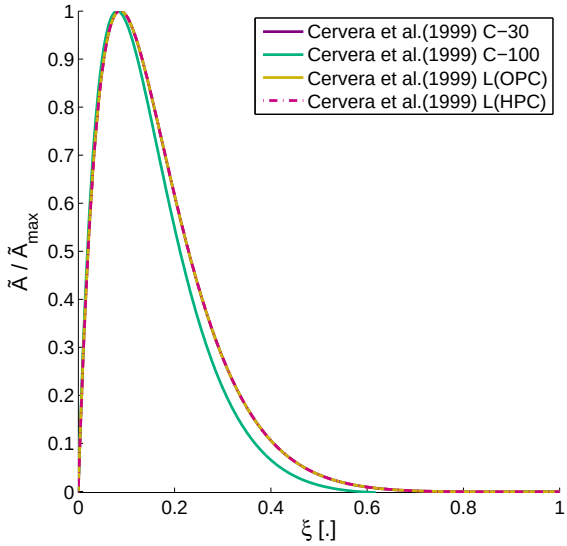

Figure 2.10: Normalized chemical affinity evolution, Cervera et al. (1999b)

However, in Figure 2.11d, the response for the two mixtures is the same, even though their water-to-cement and silica fume-to-cement ratios are different. Actually, the only parameter that changes for these two materials (L(OPC) and L(HPC)) is A_{ξ_0}/k_ξ (Table 2.3), while the others are exactly the same. It can then be concluded that this parameter (A_{ξ_0}/k_ξ) does not influence the evolution of the chemical affinity.

Contrary to the L(OPC) and L(HPC) concretes, the model parameters for C-30 and C-100 concretes are different, with exception to the A_{ξ_0}/k_ξ, which has already been concluded not to influence the results. In Figure 2.11a the influence of the final hydration degree (ξ_∞) is evident: the C-30 curve reaches a chemical affinity of zero for a hydration degree $\xi_\infty = 0.75$, while the C-100 curve reaches it for a hydration degree $\xi_\infty = 0.58$.

Even if there are differences between the parameters used for the four mixtures, it may be noticed that their peak values are attained for the same hydration degree.

Finally, Figure 2.12 shows the normalized chemical affinity evolution for the three previously presented hydration models. The account for a final hydration degree ξ_∞ which is different from the theoretical value of 1.0 is well evidenced in Cervera's model, when compared with the other

two models. In the present work it was decided to apply the hydration model given by Cervera's team.

2.3 Mechanical behaviour

It is known that concrete's mechanical behaviour is very complex and highly non-linear (Cervera et al., 1999b). Some of the existing models to account for this complex behaviour are based on

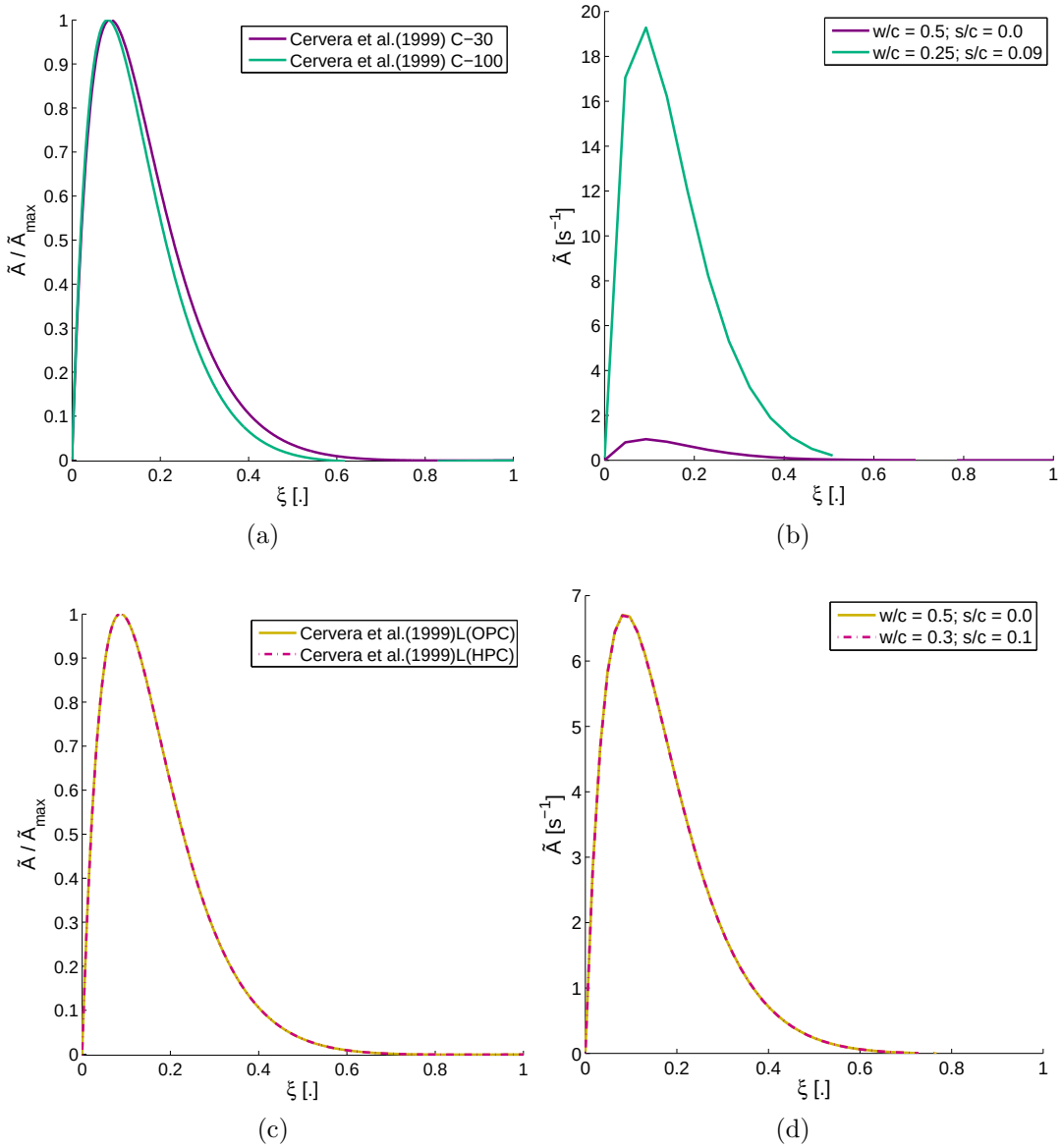

Figure 2.11: Chemical affinity evolution by Cervera et al. (1999b): a) Normalized chemical affinity evolution, C-30 and C-100; b) (Non-normalized) Chemical affinity evolution, C-30 and C-100; c) Normalized chemical affinity evolution, L(OPC) and L(HPC); d) (Non-normalized) Chemical affinity evolution, L(OPC) and L(HPC).

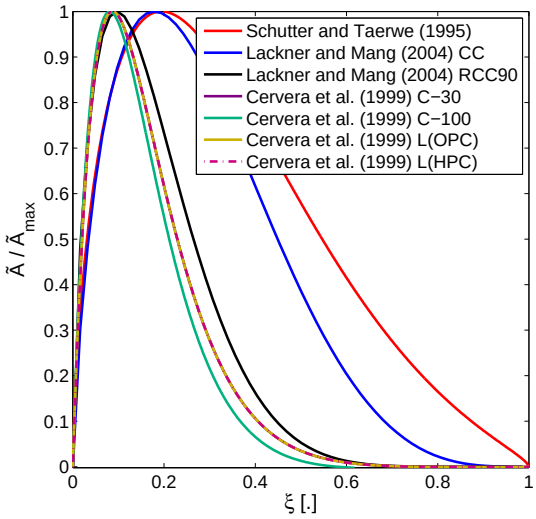

Figure 2.12: Normalized chemical affinity evolution, three different models

several developed theories that accounts either for elastic and/or viscoelastic phenomena only, or are formulated within plasticity framework, or based on fracture mechanics or continuum damage theories. One example of a model based on the continuum damage theory is the one developed by Cervera et al. (1999b), on which an isotropic damage model is developed, accounting for both temperature and ageing effects in a fully coupled problem.

A chemoplastic material model, based on the Rankine criterion formulated in the framework of multisurface chemoplasticity, is developed by Lackner and Mang (2004) and applied to the simulation of early-age cracking in concrete. In this chemoplastic model, the crack healing that occurs at early ages due to the continuous hydrates formation (while hydration reaction is still an ongoing process) is accounted for. The resolution of this model is, however, uncoupled, by solving first the thermal problem, and using its output to solve the chemo-mechanical part of the model.

In the present thesis, the adopted model, even if it is inspired from the Cervera's team one, is within the framework of non-linear viscoelasticity. Therefore, no damage or plastic and healing phenomena are modeled.

2.3.1 Mechanical properties evolution

As previously mentioned, mechanical properties in concrete evolve during the curing process, which occurs due to the hydration reaction between cement and water. During this process, heat production occurs, which is why a thermal framework needs to be established in order to

study concrete's behaviour. Therefore, a thermo-chemo-mechanical model is needed and shall be able to take into account the hydration (chemical) reaction kinetics and the mechanical properties evolution as a function of that kinetics.

The compressive strength is highly dependent on the curing temperature of concrete. If the curing temperature is elevated, the short-term (1 day) compressive strength will develop faster than the long-term one (28 days), fact previously discussed in Figure 2.4. On the contrary, lower curing temperatures will lead to a higher compressive strength at 28 days and a lower one at short-term (Laplante, 1993). This fact, demonstrated by Verbeck and Helmuth (1968) cited by Laplante (1993), is schematically represented in Figure 2.13a. In Figure 2.13b are plotted measured results by Kim et al. (1998) for three different curing temperatures as well as the correspondent isothermal tests simulations performed by the model adopted in this thesis. These results validate the ability of the used finite element software to simulate these kind of problems, and will be object of further discussion in chapter 3.

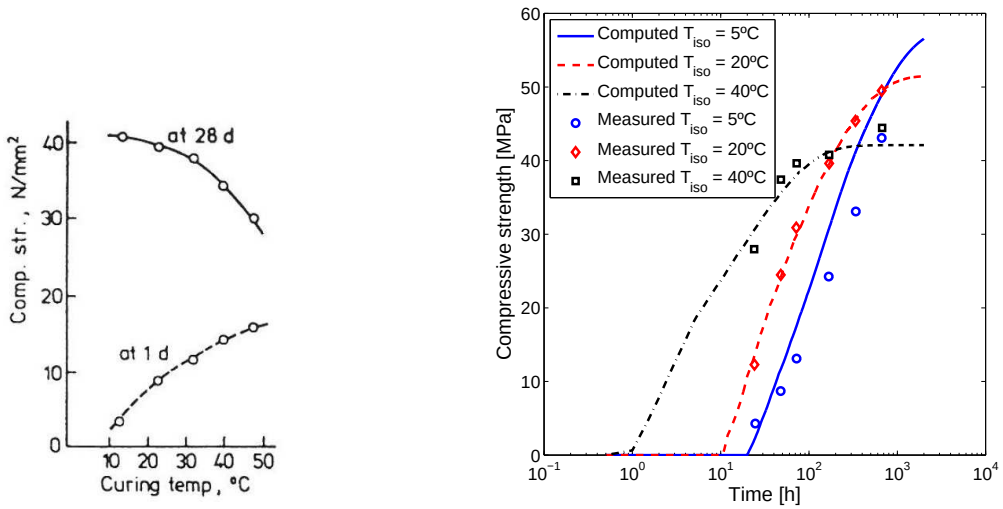

(a) (b)

Figure 2.13: Curing temperature effect on compressive strength evolution at early ages: a) Verbeck and Helmuth (1968) cited by Laplante (1993); b) Measured data from Kim et al. (1998).

According to the work developed by several authors in the 1960's and 1970's cited in Laplante (1993), the decreasing in compressive strength with increasing curing temperatures may be due to both chemical and physical causes. The physical causes occur due to the temperature increase that will lead to a volume increase. Water and air fractions of concrete will suffer a greater volume increase than the solid fraction (Figure 2.14). The volume increase, being restrained by the solid fraction of the cement paste that has already reacted, will lead to internal stresses

which can induce porosity and micro-cracking if the tension strength is not yet sufficiently high (Laplante, 1993).

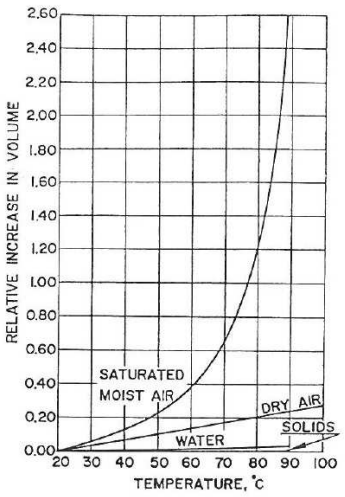

Figure 2.14: Volume increase of water, saturated and dry airs and solid fractions of conventional concrete, Alexandersson (1972) cited by Laplante (1993)

Several authors, namely Byfors (1980), have concluded that there is a linear relationship between hydration degree and compressive strength, such as in Figure 2.15.

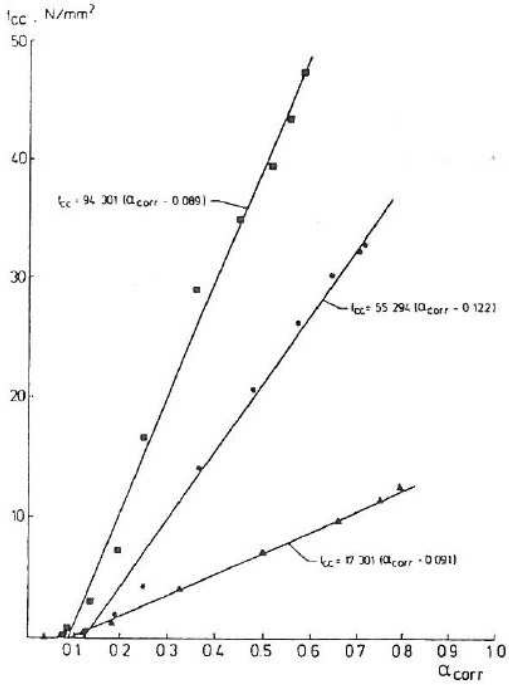

Figure 2.15: Linear relationship between the compressive strength and the hydration degree (Byfors, 1980)

Analyzing these results, Laplante (1993) concluded that the compressive strength evolution

is non linear for low hydration degrees, but that it becomes linear quite rapidly. This was further observed by several authors, such as De Schutter and Taerwe (1996) in Figure 2.16. De Schutter and Taerwe (1996) proposed an exponential relationship between the compressive strength and the hydration degree of the form of the previously discussed equation 2.22.

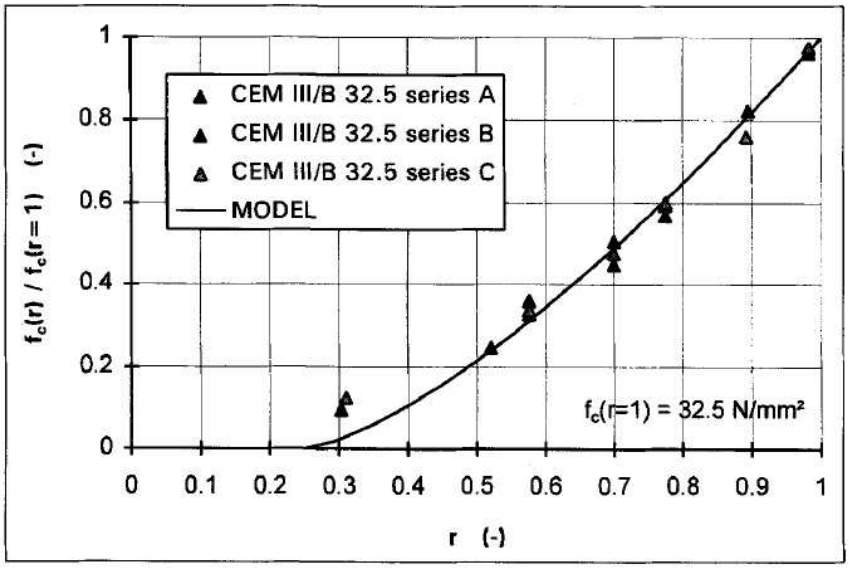

Figure 2.16: Compressive strength evolution as function of the hydration degree (De Schutter and Taerwe, 1996)

De Schutter and Taerwe (1996) presented several relationships that describe the mechanical properties of concrete at early ages, such as the compressive strength and the Young's modulus, as functions of the hydration degree. The compressive strength, tensile strength and Young's modulus evolutions are described by an equation of the form of 2.31, where P is each mechanical property, ξ_0 and a are constant parameters. De Schutter and Taerwe (1996) also made the assumption that below a certain value of the hydration degree (ξ_0) there is no strength development (mechanical percolation threshold), which is analogous to the hydration threshold ξ_{set} of Cervera's model, presented later in this section. They have also described the Poisson's ratio as a function of the hydration degree by means of equation 2.32. According to three different types of cement (CEM I 52.5, CEM III/B 32.5 and CEM III/C 32.5), De Schutter and Taerwe (1996) give different values for $P(\xi = 1)$, ξ_0 and a parameters.

$$P(\xi) = P(\xi = 1) \cdot \left(\frac{\xi - \xi_0}{1 - \xi_0} \right)^a \tag{2.31}$$

$$\nu(\xi) = 0.18 \cdot \sin\left(\frac{\xi \cdot \pi}{2} \right) + 0.5 \cdot \exp(-10 \cdot \xi) \tag{2.32}$$

Faria et al. (2006) also used equation 2.31 to account for the evolution of mechanical properties at early ages. In their work, Faria et al. (2006) first solve the thermal problem and then inject the resulting temperatures and hydration degrees in the mechanical one. This is a one-directional coupling in the sense that only the thermal problem will influence the mechanical problem and the thermal problem properties are constant. This simplification is usually assumed in these kind of problems, as pointed out by De Borst and Van den Boogaard (1994). This model was used to perform the numerical simulation of the construction of a concrete gravity dam in Azenha et al. (2008). The calibration of the heat of hydration model was done through the isothermal calorimeter experimental results. The authors concluded that the comparison between the measured and numerical temperatures and deformations was very satisfactory, which increases the confidence on this model. Azenha et al. (2008) have considered in their simulations the existence of two galleries inside the dam body, which is not usually taken into account in these kind of analysis.

Several authors, like Byfors (1980) and Laplante (1993), have identified a critical hydration degree , below which concrete has not yet developed sufficient resistance to support the developed stresses. That critical hydration degree may therefore be seen as a mechanical (or hydration) threshold. In Figure 2.16 the critical hydration degree would be $\xi = 0.25$. Cervera et al. (1999a) also use this concept (ξ_{set}) to describe the ageing parameter on which mechanical properties will depend.

In what concerns the tensile strength evolution, it was concluded by several authors cited by Laplante (1993) (e.g. Byfors, 1980) that it is influenced by the same factors as the compressive strength. It is therefore useful to define the tensile strength as a function of the compressive strength.

Bertagnoli et al. (2008), following the definitions by De Schutter and Taerwe (1996), used a hydration degree dependent compressive strength and Young's modulus such as described in equations 2.33 and 2.34, where f_t is the tensile strength and λ and α are obtained from experimental results and c is a constant parameter to avoid nil resistances at the beginning of the computation.

$$\frac{f_c(\xi)}{f_c(\xi=1)} = \frac{f_t(\xi)}{f_t(\xi=1)} = \lambda\xi + (1-\lambda)\xi^{\alpha} \geq c \tag{2.33}$$

$$\frac{E_c(\xi)}{E_c(\xi=1)} = \lambda\xi + (1-\lambda)\xi^{\alpha/3} \geq c \tag{2.34}$$

The model presented by De Schutter and Taerwe (1996) is of easy application but still it presents an important limitation if the purpose is to study the mechanical properties' evolution not only at early ages but also at long-term, since the curing temperature history is not considered in the model, as it was recently enhanced by Wang and Lee (2012).

Moreover, the compressive strength also varies with some material properties such as the water-to-cement ratio (or water-to-binder w/B ratio, binder being the cement and added pozzolans and/or fly ashes). In Figure 2.17, from Conrad (2006), are plotted the compressive strengths evaluated at different ages and for different mixtures available from RCC dam's projects by Berga et al. (2003), as well as the regression curves from ACI Committee 207 (1999).

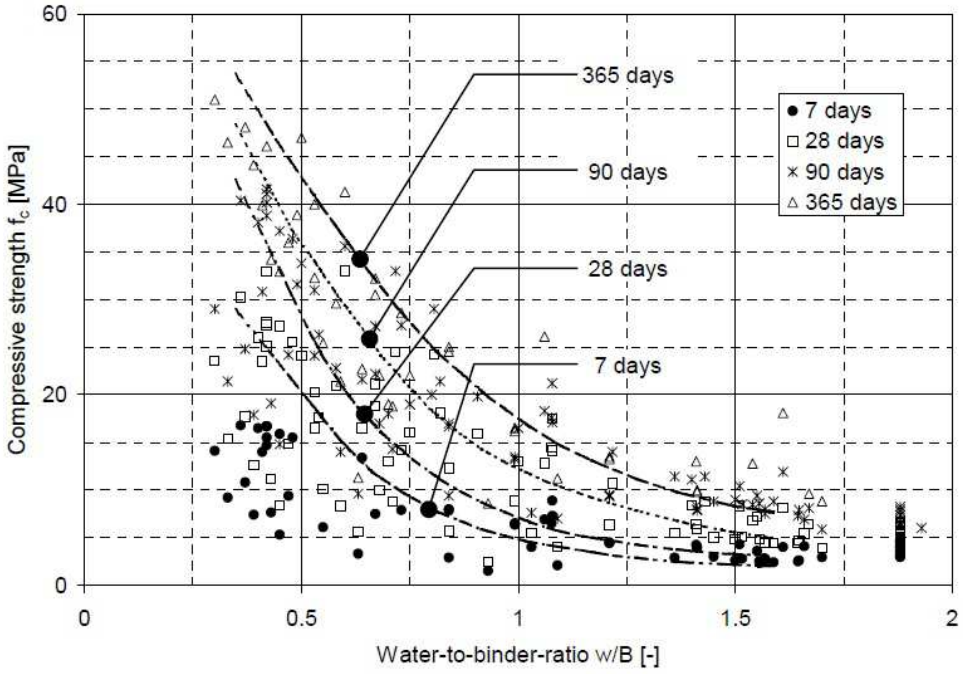

Figure 2.17: RCC compressive strength evolution as function of the water-to-binder ratio (Conrad, 2006)

The compressive strength may also be plotted as function of the cementitious content, such as in Figure 2.18 by the same authors.

Concerning the Young's modulus evolution, studies were carried out by Bettencourt Ribeiro and de Almeida (2000) in order to evaluate the resistance and deformability of a high performance roller compacted concrete (HPRCC). The HPRCC is a RCC made with a high cement dosage, 10% of silica fume, superplasticizer and aggregates that have high mechanical resistance. Several experimental tests were performed in order to evaluate the compressive and tensile split-

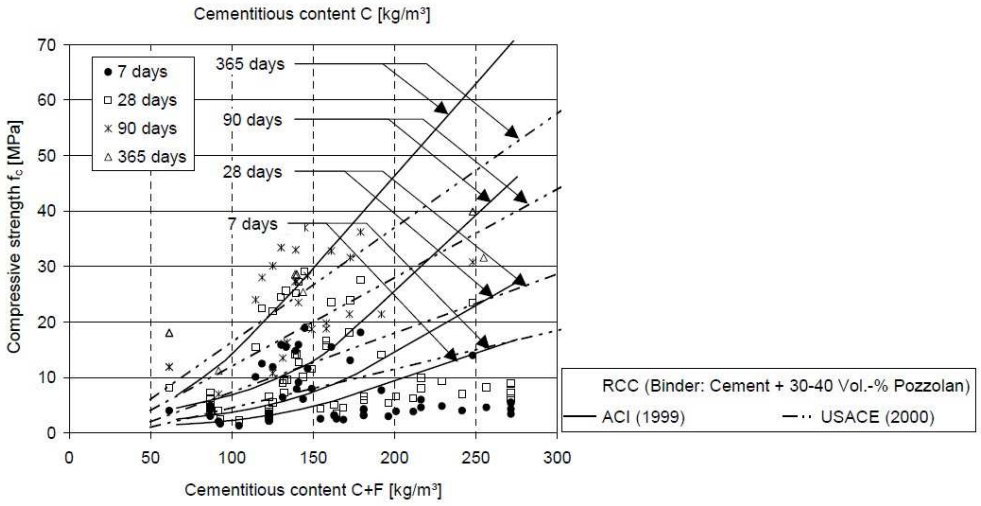

Figure 2.18: RCC compressive strength evolution as function of the cementitious content (Conrad, 2006)

ting strengths, the abrasion resistance and the elasticity modulus. Bettencourt Ribeiro and de Almeida (2000) have concluded that the HPRCC presents a compressive strength which is 4.5 times higher than the one of a normal concrete and that these values are significantly higher than the normal values obtained for a HPC in Portugal. The reasons presented by the authors to these results are based on the following: use of a high resistant basalt rock (increases the concrete's strength); use of a highly powerful superplasticizer (decreases the dosage of mixing water); the high compaction energy used for the RCC production; and the dry consistency of the RCC (decrease of the sand dosage). Bettencourt Ribeiro and de Almeida (2000) have also taken the Eurocode 2 (CEN, 2004a) expression for estimating the modulus of elasticity, given by equation 2.35.

$$E = 9.5 \cdot \sqrt[3]{f_c} \tag{2.35}$$

The results obtained both with the EC2 formula and the experimental measure at 28 days were almost equal (48.5 against 48.6GPa). In this study, the HPRCC presented a high abrasion resistance ($< 0.1mm$ at 28 days) which is a very good result to motivate the use of this material in pavements subjected to high abrasion.

From the experimental measures point of view, a procedure to continuously monitor the concrete's Young's modulus evolution at early ages was proposed by Azenha et al. (2010, 2011). This technique relies on the ambient vibration technique and consists of monitoring the evolution of the first natural frequency of a composite cantilever. The main advantage of this

experiment is that it allows a continuous measurement since the casting of concrete.

In their work about the evaluation of the Young's modulus of early-age RCC, Conrad et al. (2003) conclude that the common approaches used to evaluate the evolution of Young's modulus of conventional concrete are not suitable for RCC mixtures with low cement content. Conrad et al. (2003) performed several uniaxial compressive strength tests on a lean RCC at different ages (from 3 hours to 365 days), and propose equation 2.36 to describe the evolution of the Young's modulus of RCC. It shall be noticed that the age t defined here is the equivalent time/age t_{eq}, and the Young's modulus $E_{c,\infty}$ is evaluated by taking a reference value at curing isothermal conditions of 23°C.

$$E_c(t) = E_{c,\infty} \cdot \exp(a \cdot t^b) \tag{2.36}$$

Conrad (2006) gathered data from Mujib dam, namely results from an isothermal test at 23°C, plotted in Figure 2.19 by the round points. A coefficient of variation $CV = 25.9\%$ was found for the last value of the Young's modulus, at 365 days of age. The RCC used in Mujib dam has low cement content (85kg/m^3), no added pozzolan and a water-to-binder ratio $w/B = 1.61$. Conrad (2006) used an exponential function of the form of equation 2.37 to represent the Young's modulus evolution. In equation 2.37, $k_E(\infty)[.]$ is the multiplier at infinite age, t_e[d] is the effective age, b and c are shape factors, E_C[MPa] is the Young's modulus of the cylinders (with a diameter of 150mm) and t_s[d] is the standard age (28, 90 or 365 days).

$$E_C(t_e) = k_E(\infty) \cdot \exp\left(b \cdot t_e^c\right) \cdot E_C(t_s) \tag{2.37}$$

The model which is applied in this thesis is inspired on the one developed by Cervera's team and will be discussed hereafter. This model was also applied to an RCC dam modelling in Cervera et al. (2000a,b). Cervera et al. (2002) present a thermo-chemo-mechanical model that has undergone some developments and modifications since 1997 (Prato et al., 1997; Cervera et al., 1999a,b, 2000a,b, 2001, 2002).

The thermo-chemo-mechanical model described in Cervera et al. (2002) is based on the Theory of Reactive Porous Media developed by Ulm and Coussy (1996). The thermo-chemo-mechanical model developed by Ulm and Coussy (1996) is based on the theory of reactive porous media by Coussy (1996) and formulated in the framework of the thermodynamics of the irreversible processes, which allows the description of the hydration reaction that occurs in

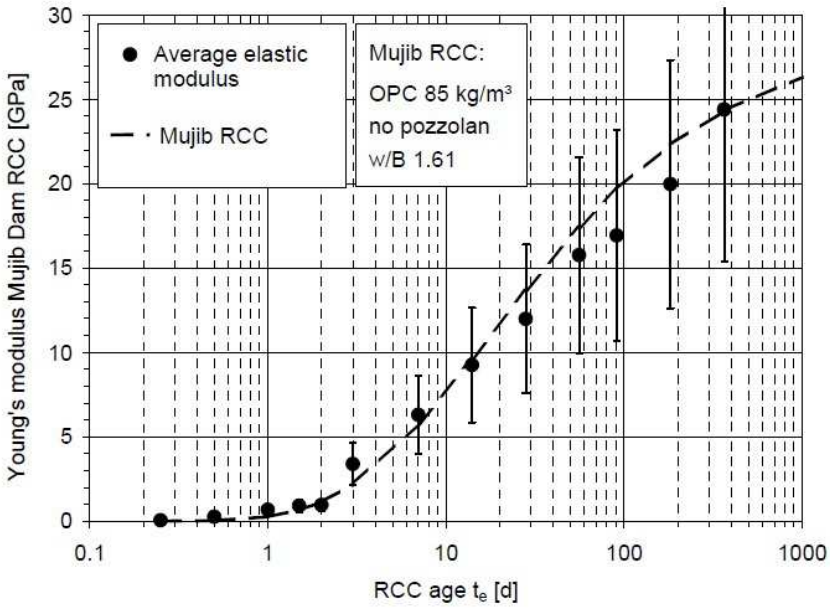

Figure 2.19: RCC Young's modulus, Mujib dam (Conrad, 2006)

concrete at early ages, by means of macroscopic variables. Adopting a closed system (without mass exchanges with the environment), Ulm and Coussy assumed in their model that the dominant mechanism of the reaction kinetics would be the diffusion of water through the layers of hydrates already formed, such as schematically represented in Figure 2.20. Therefore, the concrete is here considered as being a porous medium composed of a skeleton (the reaction products, that is, the hydrates that have already formed) and fluid phases (the reactant phase, that is, the free water). The further explanation of this theory appears to be too exhaustive for the purpose of the present work. For further details please refer to the previous references.

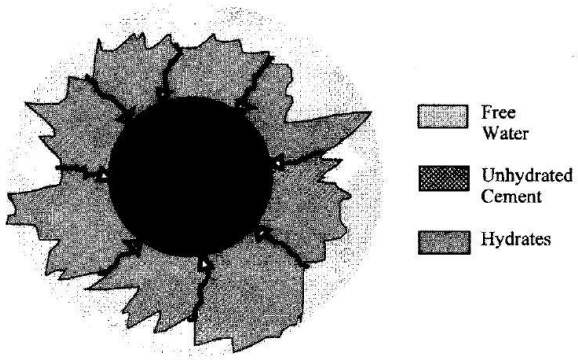

Figure 2.20: Schematic representation of free water microdiffusion through layers of already formed hydrates to unhydrated cement (Ulm and Coussy, 1996)

Therefore, two main hypotheses are taken in Cervera et al. (2001) model: mass conservation

and closed system (there are no water exchanges with the environment).

Cervera et al. (2002) introduce in this model an ageing parameter, which will rule the concrete stiffening during time, right after it has begun to cure. That instant of cure beginning, which marks the transition between a fluid material without strength to a material that begins to gain tensile strength due to the formation of a solid skeleton, is very difficult to determine with precision. The ageing degree κ is function of both temperature and hydration degree (equation 2.38).

$$\dot{\kappa} = \lambda_T(T) \cdot \lambda_{f_c}(\xi) \cdot \dot{\xi} \geq 0 \tag{2.38}$$

The beginning of the curing phase is ruled by the parameter ξ_{set}. Thus, since this parameter enters in the definition of λ_{f_c}, it will also rule the beginning of the ageing degree evolution (equation 2.40).

$$v\lambda_T(T) = \left(\frac{T_T - T}{T_T - T_{ref}} \right)^{n_T} \tag{2.39}$$

$$\lambda_{f_c}(\xi) = A_f \cdot \xi + B_f \quad , \text{for } \xi \geq \xi_{set} \tag{2.40}$$

The percolation threshold ξ_{set} will then define the beginning of the mechanical properties' evolution, which is in agreement with the definition given before: this hydration degree traduces the moment the concrete may have turned into a solid and begun stiffening (Cervera et al., 1999a). In this work, ξ_{set} will be generally called "hydration threshold". In equation 2.39, T_T is the maximum temperature at which hardening of concrete may occur and n_T is a material property that controls the sensibility to the curing temperature.

Concluding, the mechanical properties of concrete such as the compressive strength, tensile strength and elasticity modulus, will be functions of the ageing degree, such as described in equations 2.41 to 2.43, where A_e and A_+ are constants (Cervera et al., 1999a).

$$f_c(\kappa) = \kappa \cdot f_{c,\infty} \tag{2.41}$$

$$E(\kappa) = \kappa^{1/2} \cdot E_\infty \quad , E_\infty = A_e \cdot f_{c,\infty}^{1/2} \tag{2.42}$$

$$f_t(\kappa) = \kappa^{2/3} \cdot f_{t,\infty} \quad , f_{t,\infty} = A_+ \cdot f_{c,\infty}^{2/3} \tag{2.43}$$

Going back to the Cervera's team 1997 paper (Prato et al., 1997), where the concept of ageing degree was not yet introduced, it may be seen that the definition of the compressive

strength (equation 2.44) does not involve the hydration degree rate, but rather the hydration degree itself and it only depends on the λ_{fc} part of the more recent formula.

$$f_c = A_f \cdot \xi^2 + B_f \cdot \xi \tag{2.44}$$

Even if this is the model description found in the more recent papers, there are some parameters that lack more detailed explanation. That is the case, for example, of the A_f and B_f parameters used to define λ_{fc}. Some detailed information about these parameters may be found in an older paper (Prato et al., 1997), where they are defined as in equations 2.45 and 2.47, f_{cr} being a critical compressive strength, that is, the compressive strength at the instant of ξ_{set}.

$$A_f = \frac{1/(Y \cdot \xi_{set}) - 1/\xi_\infty}{\xi_{set} - \xi_\infty} \tag{2.45}$$

$$Y = \frac{f_{c,\infty}}{f_{cr}} \tag{2.46}$$

$$B_f = \frac{1}{\xi_\infty} - \xi_\infty \cdot A_f \tag{2.47}$$

In Prato et al. (1997), the ξ_{set} hydration degree is introduced by a ξ_{cr} hydration degree, which corresponds to the critical hydration degree for f_{cr}, definition that is in agreement with the more recent definition of the ξ_{set} hydration degree, which is essential to maintain the ageing degree as a positive value ($\kappa \geq 0$). Prato et al. (1997) reported Y ratios that are comprised between 10 and 35. The coefficients A_f and B_f may be obtained by means of an adiabatic test. To find n_T it is enough to measure the final compressive strength in an isothermal test carried out at a temperature that is different from the reference one. In this model, the mechanical properties act as internal-like variables and their evolution laws are formulated in terms of the hydration degree and temperature.

As previously mentioned, Cervera et al. (2000a,b) applied the thermo-chemo-mechanical model to the analysis of an RCC dam (Urugua-í dam) behaviour during construction. The data from adiabatic tests performed over the mixtures applied in this RCC dam and the curves obtained with this model are plotted in Figure 2.21a. In Figure 2.21b are plotted experimental data resulting from isothermal tests and the corresponding curves obtained with the thermo-chemo-mechanical model. Four concrete mixtures were applied in Urugua-í dam: H180 and H220 are conventional concrete mixtures with cement contents of 180 and 220kg/m^3 respec-

tively; RCC60 and RCC90 are RCC mixtures with low cement contents of 60 and 90kg/m^3 respectively. All of the applied mixtures had no pozzolan addmixtures.

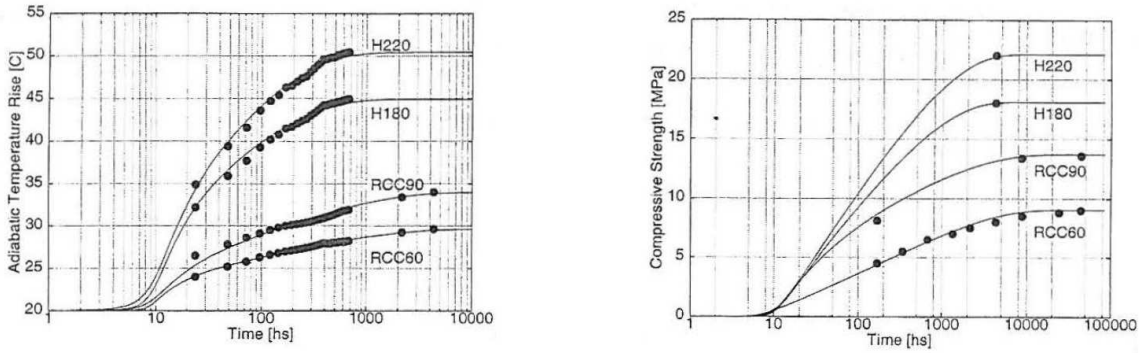

(a) (b)

Figure 2.21: Experimental vs. numerical data (Cervera et al., 2000a) for Urugua-í RCC dam: a) Adiabatic test; b) Isothermal test.

2.3.2 Creep phenomena

Creep phenomena is characteristic of viscoelastic materials. This is a long-term phenomena, related to the material's deformation in time under sustained loads. In concrete, creep is often divided into basic creep (creep phenomena that occurs independently from water losses) and drying creep (creep phenomena occurring at the surface of a concrete structure). The sustained loads are due to thermo-chemical phenomena at early-ages (Cervera et al., 1999b; Aurich, 2008). It is known that the most evident evolutions in concrete's behaviour occur at early ages, fact that has already been mentioned in the previous sections of this thesis. Therefore, creep effects are even more important if the analysis under study includes the simulation of early age behaviour, which is the case in this thesis. Moreover, studies revealed that creep depends on the amount and type of aggregate, the water-to-cement ratio, the age of loading and the duration of loading, among others (Bažant, 1988). In conventional dam design, creep and shrinkage of concrete are usually taken into account as a given thermal contraction (Shaw, 2010).

In what concerns RCC, Andriolo (1998) concluded that it is more prone to creep deformations than conventional vibrated concrete (CVC). However, more recent work by Shaw (2010) indicates that high-paste RCC (i.e. RCC with a paste content greater than 150kg/m^3, typically containing fly ashes at 40 to 60% of the total paste content (Abdo, 2008)) presents lower shrinkage and creep at early ages, specially when applied to an arch RCC dam. Shaw (2010) concludes by giving an ideal RCC mix composition that will minimize creep, characterized by a

paste content of 200kg/m^3 (or greater) and a high fly ash content of approximately 70% of the total paste content. Furthermore, Shaw (2010) concludes that for a high-paste RCC gravity dam, a total shrinkage and creep of approximately 50 microstrain shall be considered against the usually assumed 125 to 200 microstrain for CVC. However, creep is higher for RCC mixtures with low strength and low cementitious content, as proved in the work of Conrad et al. (2003).

As it is also enhanced by Shaw (2010), RCC samples used for laboratory testing are not representative of the exact behaviour of placed and compacted RCC. Compared with the CVC technology which is older and therefore much more studied and experienced, RCC is still a very recent technique and a lot of research and learning shall still arise. Moreover, Shaw (2010) enhances another point about creep tests, which is the fact that for those tests the aggregate >50mm is removed and the induced stress level is up to 40% of the compressive strength, not representing the real (insulated, contained and at low stress) conditions of RCC at the core of a dam. Concerning the presence of fly ashes in an RCC mixture, it was concluded by Grieve (1991) and later by Shaw (2010) that it reduces creep effects in concrete, and the greater the fly ash content, the lower the autogenous shrinkage in cement paste will be.

In the case study of the present thesis, the apdopted RCC mixture has 55kg/m^3 of cement and 165kg/m^3 of fly ash, and may therefore be considered as a high-paste RCC mixture. As previously exposed, according to the findings presented in the PhD thesis by Shaw (2010), for high-paste RCC, creep at early ages will be lower than what would be expected for CVC. An assumption of not considering creep effects could be taken for the case study of this thesis. However, and because most of the available literature uses creep laws to account for basic creep at early ages in the modelling of RCC dams, it was decided to include basic creep effects in the model. Both autogenous and drying shrinkage will be ignored.

Even if there exists a lot of on-going and past research about creep phenomena, there is not a consensus about the "best" theory to describe it. Creep and relaxation phenomena are intended to describe long-term deformations occurring in concrete under sustained loads, which is traduced by a reduction of the rate of elasticity modulus development in time. The consequences of those phenomena consist basically in a reduction of the stress level at long-term. A high creep level is characteristic of a lower strength and less rigid concrete, which will be more prone to "relieve a sustained stress" (Hansen and Reinhardt, 1991).

In linear viscoelasticity, the total strain (ε_{tot}) is proportional to the stress. Ignoring auto-

genous and drying shrinkage, the total strain may then be subdivided into an elastic (ε_{el}), a thermal (ε_T) and a creep parts (ε_{cr}), so that:

$$\varepsilon_{tot} = \varepsilon_{el} + \varepsilon_T + \varepsilon_{cr} \tag{2.48}$$

The linearity between strain and stress in concrete has been observed experimentally within the service stress range (i.e., for a stress level lower than 40% of the strength) by applying different stress levels such as in Figure 2.22a (Bažant, 1988). The total strain may then be expressed as equation 2.49 which introduces the compliance function $J(t, t')$, t' being the instant of loading. By applying the principle of superposition, equation 2.50, the Volterra integral form is obtained. It shall be pointed out that this principle is valid only if some conditions are fulfilled, the more restricting one being as follows: the stress level shall not exceed 40% of the compressive strength so that the behaviour is linear and the principle of superposition applied (Bažant, 1988). An equivalent form of this approach is also often referred to in the literature by using the relaxation modulus (equations 2.51 and 2.52). The compliance curves will have the form of the ones represented in Figure 2.22b, while the relaxation curves will be like the ones represented in Figure 2.22c.

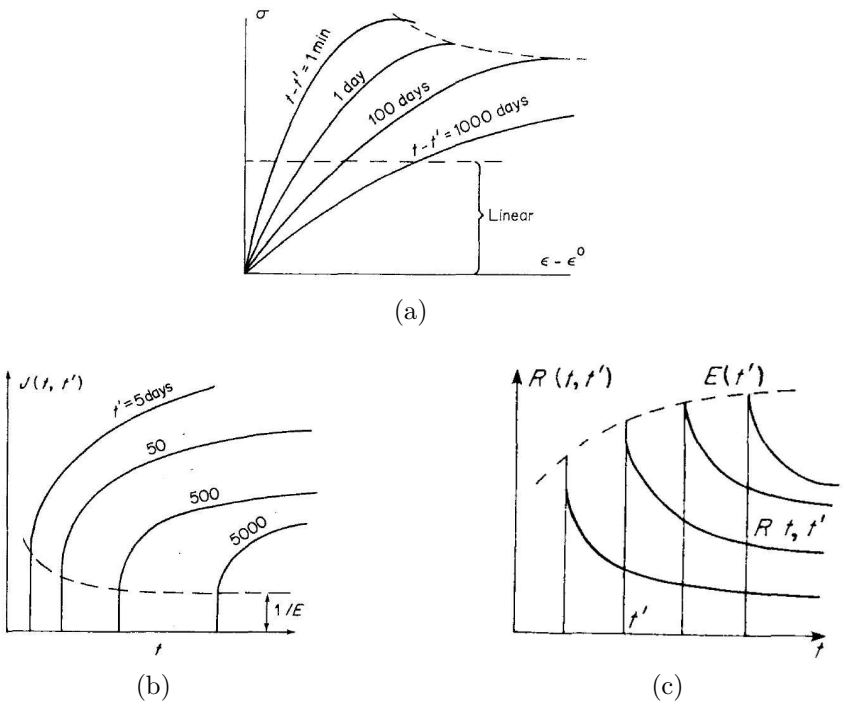

(a) (b) (c)

Figure 2.22: Creep tests (Bažant, 1988): a) Creep isochrones; b) Compliance curves for various ages t' at loading; Relaxation curves for various ages t' at loading.

$$\varepsilon_{tot}(t) = \sigma \cdot \mathbf{J}(t,t') + \sigma_0(t) \tag{2.49}$$

$$\varepsilon_{tot}(t) = \int_0^t \mathbf{J}(t,t') d\sigma(t') + \varepsilon_0(t) \tag{2.50}$$

$$\sigma_{tot}(t) = \varepsilon \cdot \mathbf{R}(t,t') + \varepsilon_0(t) \tag{2.51}$$

$$\sigma_{tot}(t) = \int_0^t \mathbf{R}(t,t') d\varepsilon(t') + \sigma_0(t) \tag{2.52}$$

Generally, creep phenomena in concrete studies is taken into account by a creep law/creep compliance/specific creep, which describes the compliance function $J(t,t')$ or the relaxation function $R(t,t')$ by formulas available in literature. Another way of accounting for creep is to develop the Volterra integrals into a set of linear differential equations via Dirichlet or Taylor series. An analogy may then be made between those series and the well-known Maxwell and Kelvin chains.

Anyway, creep in concrete is most generally accounted by means of a compliance function $J(t,t')$. Several formulas to reproduce the creep curves obtained experimentally are available in literature, the Double Power Law (DPL) being the most applied one. The DPL was originally proposed by Bažant and Osman (1976) and is given here by equation 2.53, where $E_0(t')$ is the asymptotic elastic modulus, t' is the instant of load application, and ϕ_1, m, α and n are material parameters. This formula has proven its adequacy along the years by several studies on concrete at early ages (Ji, 2008).

$$J(t,t') = \frac{1}{E_0(t')} + \frac{\phi_1}{E_0(t')} \cdot (t'+\alpha)^{-m} \cdot (t-t')^n \tag{2.53}$$

For concrete at early-ages, some corrections to equation 2.53 were proposed and adopted in the work of Leitão et al. (2007) applied to Pedrógão RCC dam. The first correction was introduced by Miranda et al. (2000) and consists in adding a retardation parameter to the exponent n with the objective of obtaining physically accepted relaxation curves (Leitão et al., 2007). The second correction, introduced by Emborg (1986), adds an exponential part ($A \cdot e^{-Bt_0}$) in order to improve the elasticity modulus in the first days of age.

$$J(t,t') = \frac{1}{E_0(t')} \left(1 + \phi_1 \left(t_0^{-m} + \alpha\right) \cdot (t-t_0)^{n(1-\exp(-t_0/k))} + A \cdot e^{-Bt_0}\right) \tag{2.54}$$

A different method is presented by De Schutter and Taerwe (2000), called "fictitious degree of hydration method" which relates the creep function to the evolution of the hydration degree,

applied to concrete at early-ages. In this method, the basic creep strain depends directly on the hydration degree ξ, on the hydration degree at loading ξ_b and on the stress level at loading α_b, such as in equation 2.55. This model can be interpreted as a Kelvin chain model with elastic moduli and viscous dashpots depending on the hydration degree. The main advantage of this method is that time does not interfere explicitly.

$$\varepsilon_c(\xi, \xi_b, \alpha_b) = a(\xi_b, \alpha_b) \cdot \left(\frac{\xi - \xi_b}{1 - \xi_b}\right)^{b(\xi_b, \alpha_b)} \tag{2.55}$$

The mechanical component of the thermo-chemo-mechanical model by Buffo-Lacarrière (2007) includes both creep and damage (anisotropic) models that were adapted to account for the dependence of the mechanical properties on the hydration degree (Boutillon et al., 2012) $\sigma = \tilde{\sigma}\,(1 - D)$, D being the damage. This means that only a percentage of the section is able to sustain the load. When $\sigma = \tilde{\sigma}$ (damage $D = 0$), there is no damage and all the section will sustain the load. This model requires some parameters that are not very easy to obtain experimentally (crack energy evolution, creep rate at early ages, etc), which is why this model is a part of the CEOS.fr project, on which numerical and experimental studies are coupled in order to validate the model (Boutillon et al., 2012).

As it was stated before, the Volterra integrals (equations 2.50 and 2.52) may be solved by linear differential equations obtained via Dirichlet or Taylor series, enabling an analogy with the well-known and widely applied Maxwell and Kelvin rheological models.

Such as reported in Cervera et al. (1999b), the resolution of this kind of problem via Dirichlet series, which can be interpreted as a generalized Maxwell chain, has computational advantages, fact that was enhanced by Carol and Bažant (1997). This kind of rheological model will be adopted in the present thesis since it is implemented in the used FEM software.

Cervera et al. (2002) developed a model which combines the use of ageing and viscoelastic and damage models to provide a phenomenological description of the mechanical behaviour of early age concrete. The objective is then to couple a viscoelastic and a damage model. According to Cervera et al. (2000a), the microprestress-solidification theory is one of the most widely accepted theories used to model creep in concrete at early ages. The main idea of this theory is to consider concrete as a viscoelastic material which can be modeled by a series of Kelvin chains. In this rheological model, the elastic moduli of springs vary proportionally in

time and have as limit an attained value of a proposed "solidified fraction". In Cervera et al. (2000b), to model the concrete long-term behaviour, a Maxwell chain is considered with a parallel arrangement, which had already been concluded by Carol and Bažant (1997) as leading to computational advantages when compared with the Kelvin chains series arrangement.

The generalized Maxwell model is described in terms of the elastic moduli of each spring, E_i, and the relaxation times of the dashpots, τ_i, where i is each of the Maxwell chain's elements. The dashpots relaxation times may be characterized by $\tau_i = \eta_i/E_i$, η_i being their viscosities. Generally, the relaxation time of the first dashpot is considered $\tau_1 = +\infty$ in order to obtain an asymptotic elastic modulus E_1. In their work, Cervera et al. (1999b) have assumed that the elastic moduli vary proportionally to the ageing function, according to equation 2.56, and that the relaxation time remains constant. In this way, the evolution of these variables is governed by equation 2.57, $\sigma = \sum_{i=1}^{N} \sigma_{\mathbf{i}}$ being the total stress sustained by the Maxwell chain, where N is the number of branches (Carol and Bažant, 1997; Cervera et al., 1999b). In equation 2.57, E^i_∞ is the final Young's modulus of each spring, ε is the total strain tensor, $\bar{\mathbf{D}} = (1/E)\mathbf{D}$ and $\lambda_E(\kappa) = \kappa^{1/2}$ is the elastic modulus ageing function.

$$E^i(\kappa) = \kappa^{1/2} \cdot E^i_\infty \tag{2.56}$$

$$\dot{\sigma}_{\mathbf{i}} + \frac{\sigma_{\mathbf{i}}}{\tau_i} = \lambda_E(\kappa) E^i_\infty \bar{\mathbf{D}} \dot{\varepsilon}, \quad i = 1, \dots N \tag{2.57}$$

Moreover, based on experimental evidence of the solidification theory by Bažant and Prasannan (1989), Cervera et al. (1999b) added a flow term intended to account for ageing effects related to the long-term creep behaviour (represented by a circular element connected in series with the parallel chains in Figure 2.23). They finally conclude that this is equivalent to adopt ageing elastic moduli in the generalized Maxwell chain. In this way, the governing equation 2.57 becomes equation 2.58, where τ_μ is the relaxation time of the flow term given in equation 2.59. The material properties $\tau_{\mu 0}$ and $c_{\mu 0}$ characterize the flow term, the first one being the initial viscosity and the second one its rate of evolution. In their work, Cervera et al. (1999b) also considered another relaxation time to account for the ageing effect on the elastic modulus. In the present work, this last relaxation time is not going to be accounted for.

$$\dot{\sigma}_{\mathbf{i}} + \left(\frac{1}{\tau_i} + \frac{1}{\tau_\mu} \right) \sigma_{\mathbf{i}} = \lambda_E(\kappa) E^i_\infty \bar{\mathbf{D}} \dot{\varepsilon}, \quad i = 1, \dots N \tag{2.58}$$

$$\tau_\mu = \frac{\tau_{\mu 0}}{\lambda_E \mu} \tag{2.59}$$

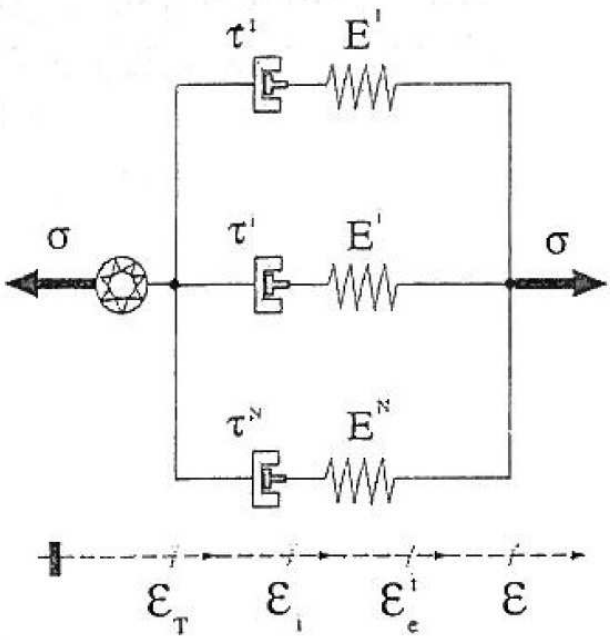

Figure 2.23: Generalized Maxwell model (Cervera et al., 2002)

$$\mu(t) = \frac{1}{1 + c_{\mu 0} t} \tag{2.60}$$

2.4 Cracking in RCC dams

Cracking in concrete at early ages occurs if the structure is subjected to a tensile state greater than the strength developed so far, as stated by Springenschmid and Breitenbucher (1998).

Thermal cracking in RCC dams has been observed during the years and is a great concern amongst designers. Several examples are gathered and reported in Hansen and Forbes (2012), such as the cases of the Upper Stillwater dam (Figure 2.24) constructed in 1985-87 in a site where the annual average temperature is of 2.9°C and with a maximum casting temperature fixed at 10°C. The cost of repair of cracks in this dam was reported by Hansen and Forbes (2012) as to have exceeded $7 million.

According to ACI Committee 207 (1999), cracking in RCC dams may affect structural stability, permeability, durability and visual appearance. To avoid vertical cracking, which is very difficult to repair and control, vertical joints are added to the dam project. Transverse contraction joints may also be included in a dam project, such as waterstops and drains. The contraction joints will then induce a weakened plane through which cracks will propagate (ACI Committee 207, 1999).

Most of the thermal cracking that occurred in RCC dams and reported in Hansen and Forbes (2012) consist on vertical cracking and do not generally affect their structural stability. Moreover, they may have been caused not only by thermal stresses, but also due to differential settlements occurring in the foundation and horizontal movements induced by the reservoir filling (Hansen and Forbes, 2012). These authors also reported that not all the cracks occur at the same time nor they have the same width.

Therefore, cracking in RCC dams shall be prevented, even if their consequences will not generally compromise the stability of the structure. Major cracks can be induced and affect the dam's permeability, their repair being highly expensive. Delays in construction lead often to RCC placing during the warmer season which is not desirable since it induces higher peak

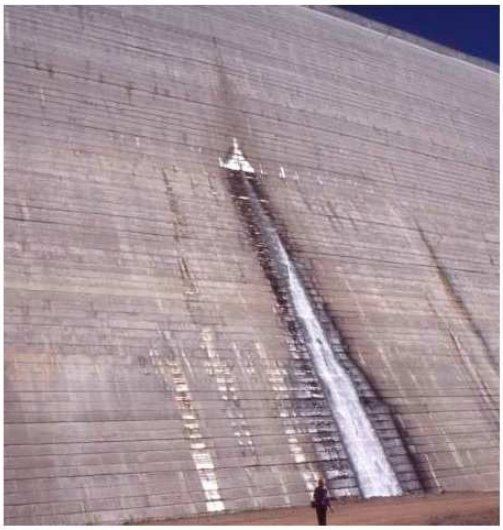

(a)

(b)

Figure 2.24: Cracking in Upper Stillwater dam (Hansen and Forbes, 2012): a) Major crack; b) Aerial view.

temperatures in the dam's core than what was predicted during the design phase. A maximum casting temperature is usually fixed and cooling measures are applied in order to stay below that maximum temperature. If the construction is pushed towards the hot season, those measures will need to be more extreme (i.e., use of ice or liquid nitrogen in the mixture) and consequently more costly.

In order to avoid cracking near the dam up and downstream faces, several mitigation measures are adopted in practice. For example in Pedrógão dam a coverage of the downstream face with a steepest spillway built with reinforced concrete was applied as a mitigation measure (Leitão et al., 2007). Other solutions may consist on the use of higher cement content mixtures near the dam faces and/or the application of impervious materials such as small conventional concrete slabs or PVC membranes on the dam faces in order to guarantee the impermeabilization of the dam body. Moreover, in some cases of dams built with lower cement contents, the structural and hydraulic functions are sometimes separated and a certain level of cracking is assumed not to affect the structural stability.

Another practical aspect of RCC dams' construction that should be object of attention concerning cracking at early ages is related to the horizontal/lift joints. The layered construction of RCC dams implies a great number of those joints which is a major concern in these kind of structures. Because they increase the dam's susceptibility to percolation and may affect, in extreme cases, its stability and durability, horizontal joints shall be object of careful care during construction.

According to the time delay on constructing two consecutive layers, horizontal joints may be classified as follows: hot joints, cold joints and warm joints (BaCaRa, 1996). Hot joints are of less concern since they are characteristic of shorter time delays between the casting of two layers (as their name indicates, the material has not begun to cool down yet). On the other hand, cold joints are of major concert because the surface of a casted layer has already begun to gain resistance and its moist condition is very different from the fresh layer to be casted afterwards. These joints are characteristic of bigger time delays between the casting of two layers. Warmer joints are those between the other two, whose definition and identification is harder to do.

Several aspects may decrease the quality of a cold joint, such as the contamination by dirt, the compaction level used on the subsequent layer, the weather conditions (rain, hot or freezing temperatures), inadequate amount of water at the surface, among others. The consequences

of the factors influencing a joint quality will increase proportionally to the time delay between the construction of two consecutive layers.

In practice, several techniques are used to overcome those consequences, such as using high pressure water jets to clean the surface (if it has already hardened). This will remove a superficial layer, along with all the contamination (i.e. dust) that may have occurred. After the thin layer removal, aggregates that had been segregated during compaction will eventually "emerge" at surface, which will increase the roughness of the surface and, consequently, facilitate the adherence of the upper layer (Bettencourt Ribeiro et al., 2001). Also, cold joints may be treated with a bedding mix right before casting of the next RCC layer (Ortega et al., 2003). If weather conditions are worse (rain, snow, freezing temperatures), it is useful to protect the layer surface by covering it with plastic or insulating mats, so that the humidity conditions are maintained ACI Committee 207 (1999).

In what concerns the tensile strength of the lift joints, Bettencourt Ribeiro et al. (2001) developed a work where the influence of different parameters on the tensile strength is analyzed. The joint's quality is usually evaluated by the "joint maturity index" (JMI) (BaCaRa, 1996; ACI Committee 207, 1999; Bettencourt Ribeiro et al., 2001), here given in equation 2.61, where AST[°C] is the average surface temperature and TE[h] is the time of exposure (time delay between the construction of two layers).

$$\mathrm{JMI} = \mathrm{AST} \cdot \mathrm{TE} \tag{2.61}$$

The conclusions drawn by Bettencourt Ribeiro et al. (2001) accentuate the need to perform the joint's treatment before posing the upper layer, which needs to be compacted before the initial setting time of the lower layer. A continuous decrease of the joint quality with the time of exposure was identified.

Even if the JMI may have been object of critics (in, for example, BaCaRa (1996)) because of its inadequate use due to a direct transposition of °F to °C which leads to erroneous conclusions, it is a useful tool to help understand some results found within this thesis, included and discussed in chapter 5.

As stated by de Araújo and Awruch (1998a), there are two different model formulations generally used to the cracking analysis of concrete structures: the non-linear fracture theory

and the continuum damage theory. While in the former discrete cracks are considered and when cracking begins a stress-crack width relationship is considered, in the latter the cracked material is considered as a continuum media and cracking begins when the maximum principal stress is greater than the tensile strength, the cracking growth leading to a descent in the stress-strain diagram.

Moreover, crack opening and growth is a research domain in current development, either in concrete or in other materials (i.e. steel and welded joints). The Fatigue Crack Growth (FCG) is an extensively studied domain on which probabilistic approaches have been increasingly applied. For example, Sain and Kishen (2008) performed a probabilistic assessment of FCG in a concrete beam subjected to cyclic loading. Moreover, Riahi et al. (2010, 2013) presents the Stochastic Response Suface Method (SRSM) to perform reliability analysis on structures subjected to fatigue crack growth.

In the beginning, cracking of concrete at early ages was only accounted for by limiting temperature gradients that occur in a structure. In the past two decades, efforts have been made in order to understand concrete cracking sensitivity by accounting for thermal and other early age stresses (Springenschmid and Breitenbucher, 1998). These authors point out two important parameters worth being considered in a cracking analysis: the concrete cracking sensitivity (dependent on the concrete constituents, composition and casting temperature) and the boundary conditions (structure dimensions, degree of restraint and temperatures).

Several authors performed cracking analysis in concrete at early ages, either by accounting or not crack width or even crack healing that occurs due to the continuous hydrates formation, such as in the work of Lackner and Mang (2004). In most of the available studies, cracking is evaluated by comparing stresses and strengths. Emborg (1998) defined a maximum stress level η_{max} equal to 0.7 to avoid early age cracking (equation 2.62, where σ_t is the tensile stress and f_{ct}^* the tensile failure strength). This leads to a safety factor of $FS = 1/\eta_{max} = 1.4$.

$$\eta_{max} = max\left(\frac{\sigma_t(t)}{f_{ct}^*(t)}\right) \tag{2.62}$$

Concerning crack analysis over RCC dams, some studies may also be found in the available literature, such as in Jaafar et al. (2007) which prevent thermal cracking by fixing an allowable temperature drop ΔT (equation 2.63, where K_R and K_f are the structure and restraint factors defined in function of the restrain level of the structure, α is the coefficient of thermal expansion, W_b is the block width and ε_c is the tensile strain capacity) which depends on a given admissible

crack width (W_p) of 2.0mm. Noorzaei et al. (2006) evaluated the cracking risk of RCC Kinta dam by applying a limit of 1.0 to the cracking index (equation 2.64). The cracking index definition is actually analogous to the factor of safety FS presented before. Therefore, if $I_f \geq 1.0$, the structure is safe. These authors computed the cracking index on three points located at two elevations: 1.5 and 12.9m. The results are plotted in function of the time since RCC placing in Figures 2.25a and 2.25b, respectively. It may be observed that all of the three analyzed points located at 1.5m elevation present I_f lower than the allowable limit of 1.0 at early ages, meaning that the tensile strength f_t is lower than the tensile stress σ and therefore those points are cracked. It is observed also that points "a" and "b" pass to the "safe" zone after 25 days, while point "c" remains with $I_f < 1.0$. Moreover, a cracking index greater than 1.0 is found for point "c", but at the end values lower than the allowable limit of 1.0 are found again. For points located in elevation 12.9m, it is concluded that point "a" and "c" are safe, with $I_f > 1.0$, while point "b" is cracked at early ages. Noorzaei et al. (2006) concluded that the dam is safe against cracking for points "a" and "b" because even if these points present cracking indexes below the allowable limit of 1.0, that happens while the concrete is still young (age below 30 days). Concerning point "c", they concluded that it should be object of special attention in the first 75 days after casting.

$$\Delta T = \frac{1}{K_R K_f \alpha_T} \left[\frac{W_p}{W_b} + \varepsilon_c \right] \tag{2.63}$$

$$I_f = \frac{f_t(t)}{\sigma(t)} \geq 1.0 \tag{2.64}$$

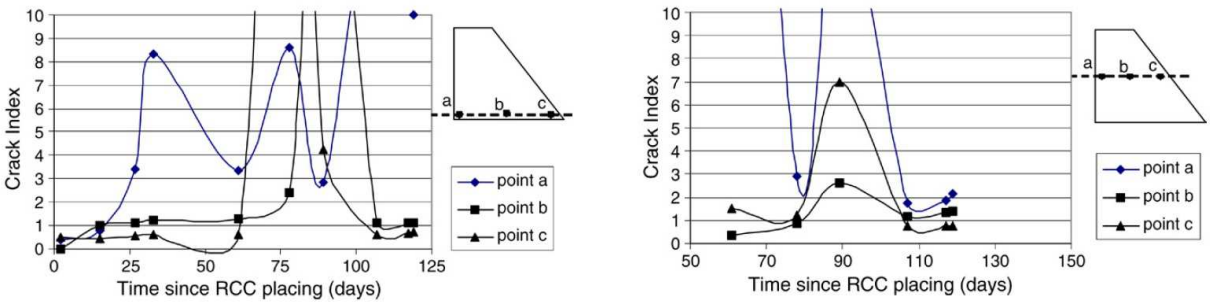

(a) (b)

Figure 2.25: Cracking index $I_f = f_t/\sigma$ (Noorzaei et al., 2006): a) Elevation 1.5m; b) Elevation 12.9m.

It shall be stressed that the model applied by Noorzaei et al. (2006) does not account

for plastic deformations and early-age self healing of concrete. An assumption is made while analyzing the results: it is assumed that for ages below 30 days, concrete is still fresh and even if it presents cracking indexes below the allowable limit, that is not a problem since its resistance will still evolve afterwards. Even if this approximation could be a good one in practice, it lacks of clarity. By not defining a percolation threshold above which concrete begins to stiff, this assumption may be neglecting important early-age cracking. Furthermore, it is observed that the obtained cracking indexes oscillate in time, which could happen if the model accounted for plastic deformations, but it is not the case here. Therefore, the cracking index should increase monotonically during the analysis.

Cervera et al. (2000b) performed a thermo-chemo-mechanical analysis on Urugua-í RCC dam and computed the tensile ratio (such as η of equation 2.62), defined as the ratio between the tensile stress by the tensile strength, during construction. In Figure 2.26 is plotted the tensile ratio η surface obtained at the end of construction. It is observed that the areas more prone to cracking (where the tensile ratio is closer to 1.0) are located near the foundation and near the up and downstream faces of the dam.

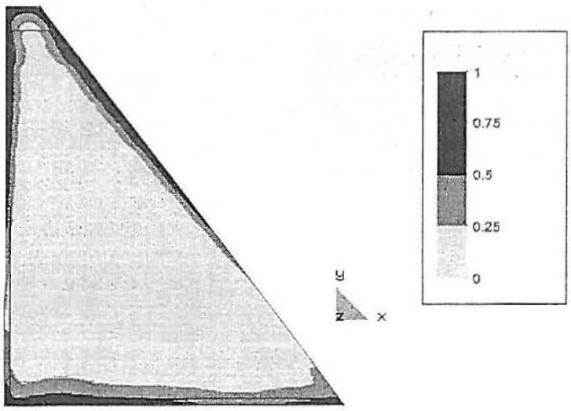

Figure 2.26: Tensile ratio $\eta = \frac{\sigma}{f_t}$ at the end of construction (Cervera et al., 2000b)

As previously discussed in section 2.3, Lackner and Mang (2004) propose a model for the simulation of the early-age cracking of a RCC dam, which is based on the Rankine criterion and in the theory of chemoplasticity. This model accounts for the early-age self-healing occurring due to the continuous formation of hydrates during the hydration reaction at early ages. Lackner and Mang (2004) have also applied their model to the analysis of an RCC dam construction. However, these authors have not accounted for creep effects. In a first analysis, Lackner and Mang (2004) obtained the tensile ratio η surface plotted in Figure 2.27, on which the maximum registered value of 0.91 occurred at the bottom downstream corner of the dam's cross section.

It is concluded that cracking did not occurred.

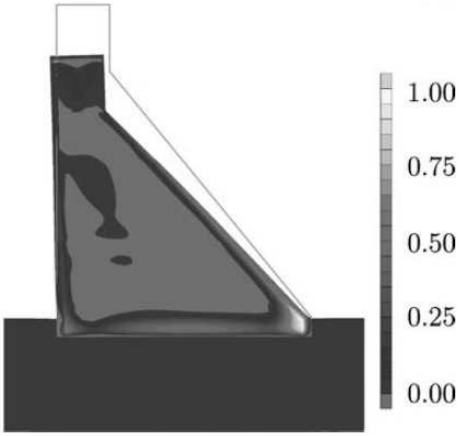

Figure 2.27: Tensile ratio $\eta = \frac{\sigma}{f_t}$ at the end of construction (Lackner and Mang, 2004)

In order to observe the performance of their model to predict cracking, Lackner and Mang (2004) have changed some conditions of the application, such as the ambient temperature by decreasing it from 15 to 5°C and the amount of heat released by the RCC from 45000kJ/m^3 to 100000kJ/m^3. Under these conditions, they have computed higher temperatures within the dam body which have resulted, associated with a lower ambient temperature, in higher temperature gradients. Therefore, cracking has occurred this time, here plotted in Figure 2.28a characterized by the hardening variable $\chi > 0$ (the hardening variable χ accounts for the decrease of strength as a consequence of plastic deformations). It is observed that cracking occurs in the bottom part of the dam, near the foundation, as well as on the up and downstream faces (even if it is not quite visible in Figure 2.28a). It is also observed that a great part in the dam's core suffers cracking as well, which is concluded by Lackner and Mang (2004) as being a consequence of unequal settlements of the dam. These authors complement their analysis by computing a cracking indicator C which is given by equation 2.65, where W^f is the energy released in consequence of cracking and G^f is the fracture energy. The cracking indicator surface is plotted in Figure 2.28b showing low levels of C, leading to the conclusion that most of the cracks have opened at early ages and were therefore healed during the hydration reaction. Lackner and Mang (2004) finish by concluding that it is expected that cracking will most likely occur in the downstream face of the dam.

$$C = \frac{W^f}{G^f} \quad , \quad 0 \leq C \leq 1 \tag{2.65}$$

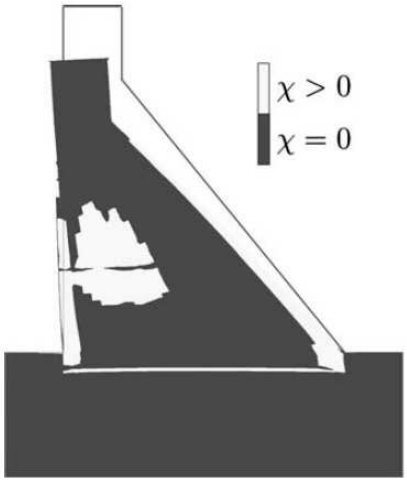

(a)

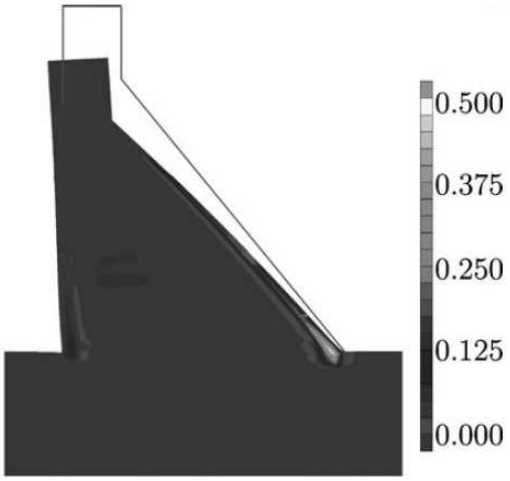

(b)

Figure 2.28: Cracking in RCC (Lackner and Mang, 2004): a) $\chi > 0$; b) Cracking indicator C.

In this thesis, a cracking index and density concepts are introduced and evaluated during the simulation of the dam construction, at each construction step. The cracking index I_f is here considered as being the ratio between the tensile strength f_t[MPa] and the first principal stress σ_1[MPa] (such as in equation 2.64). The cracking density concept will be further described in chapter 3.

2.5 Summary

A thermo-chemo-mechanical framework needs to be considered in the modelling of concrete's behaviour in order to account for the temperature and the hydration reaction evolution during the hardening of the material. The thermo-chemo-mechanical analysis of concrete structures

is often done in a one-direction coupled manner, by first solving the thermal problem and using its output to solve the mechanical one. Then, some existing models allows the fully coupling between thermal and mechanical phenomena, such as the thermo-chemo-mechanical model developed by Cervera et al. (1999a) and Cervera et al. (1999b). In this model, an ageing degree κ, which depends on both temperature and hydration degree, will rule the mechanical properties' evolution. The beginning of the mechanical properties' evolution is ruled by a mechanical/hydration threshold ξ_{set}, below which the RCC is considered not to have developed any strength. This model has been successfully applied during the years and was also applied to the modelling of an RCC dam construction (Cervera et al., 2000a,b).

Considering creep effects in concrete, a lot of on-going research and discussion exists in this domain. For the case of RCC, it is believed that creep and shrinkage effects are more important for mixtures using a low cement content. It is reported by Shaw (2010) that, however, those creep and shrinkage effects are reduced when compared with conventional concrete, if the mixture has a high cement content and, moreover, a high fly ash admixtures content. Creep is often modeled by means of a double power law on which the Young's modulus is affected by a compliance function. In the thermo-chemo-mechanical model of Cervera's team, creep is accounted for by means of a generalized Maxwell chain, on which each spring's Young's modulus is dependent on the ageing degree κ.

Early age cracking has been identify in RCC dams during the years. Causes are often attributed to high thermal gradients that occur due to unpredicted delays during construction, pushing it trough the warmer months for which the design was not adapted. There exist some cracking analysis of RCC dams in literature using very different models and hypothesis, three of them being reported here.

In this thesis, a thermo-chemo-mechanical model is used. In the next chapter are included some validation and verification tests such as an adiabatic, an isothermal and a cyclic test, performed over different mixtures. A proposal to account for cracking extent within each casted layer during construction is also presented in the next chapter by introducing the *cracking density* concept.

Chapter 3

Implementation and justification of the numerical model

This chapter intends to present and justify the hypotheses and choices for the numerical model of this thesis. Firstly, details about the coupling of hydration and ageing degrees are discussed. Then, the validation and verification of the adopted thermo-chemo-mechanical model is done by simulating adiabatic, isothermal and cyclic tests and comparing the obtained results with measures from the available literature. Moreover, are given the details of the application to an RCC dam construction, namely about the geometry and mesh, the procedure to model the dam layered construction, the boundary conditions, the casting temperature and the zero-stress reference temperature. Finally, are presented the details about the adopted procedure to account for cracking in an RCC dam during construction. All of the computations performed in this thesis used the COMSOL Multiphysics® software (version 4.2) to solve the numerical problem and Matlab to perform the results' post-treatment.

3.1 Coupling of hydration and ageing degrees

In the present work, a hydration model which follows the Arrhenius-type function is adopted to describe the hydration degree rate, such as in equation 3.1. In this hydration model, the hydration degree rate is dependent on both the hydration degree itself and on temperature. These two dependent variables need to be coupled. Two approaches can be used here: the first one by considering equation 3.1 as a *material behaviour model*, which would lead to an implicit integration scheme within each integration point; the second one would be to consider the hydration degree as a degree of freedom, meaning that the problem would have two degrees

of freedom, one for the hydration degree and another for temperature. The second approach strongly couples the heat transfer and the hydration reaction phenomena. In this work, the second approach is chosen. Moreover, because the hydration degree is independent from one layer to the next one, it will need to be defined locally at each casted layer level. This is achieved by modelling equation 3.1 through a PDE (partial derivative equation) for each casted layer. The hydration degree will therefore be discontinuous, while temperature is continuous inside all of the domain.

$$\dot{\xi} = \tilde{A}(\xi) \cdot \exp\left(-\frac{E_a}{R \cdot T}\right) \tag{3.1}$$

Another coupling issue related to the thermo-chemo-mechanical model is the ageing degree coupling with the dependent variables hydration degree and temperature. As previously exposed and discussed in chapter 2, the ageing degree evolution will rule the RCC mechanical properties evolution such as the compressive and tensile strengths or the Young's modulus. The ageing degree evolution is described by equation 3.2.

$$\dot{\kappa} = \lambda_T(T) \cdot \lambda_{f_c}(\xi) \cdot \dot{\xi} \tag{3.2}$$

$$\lambda_T = \left(\frac{T_T - T}{T_T - T_{ref}}\right)^{n_T} \tag{3.3}$$

$$\lambda_{f_c} = A_f \cdot \xi + B_f, \quad \text{for} \quad \xi \geq \xi_{set} \tag{3.4}$$

The same logic as the second approach presented for the hydration model could be applied, by modelling equation 3.2 by means of a PDE module. Another hypothesis would be to model the ageing degree directly as a variable, by approximating its integral as in equation 3.5, where $\langle\rangle$ are the Macaulay brackets ($\xi - \xi_{set} = \xi - \xi_{set}$ if $\xi - \xi_{set} \geq 0$, and $\xi - \xi_{set} = 0$ if $\xi - \xi_{set} < 0$).

$$\kappa = \lambda_T(T) \cdot \lambda_{f_c}(\xi) \cdot \langle \xi - \xi_{set} \rangle \tag{3.5}$$

The two approaches are here applied to a beam model, such as the one depicted in Figure 3.1. The model parameters are described in Table 3.1. Table 3.2 gives the A_f and B_f values optimized for both approaches. Heat transfer with the environment only occurs on the top surface, and all of the other boundaries are insulated. The lower boundary is mechanically blocked in both horizontal and vertical directions, while the lateral boundaries are only blocked horizontally. The results are analyzed on three points inside the beam, placed at the bottom,

center and top.

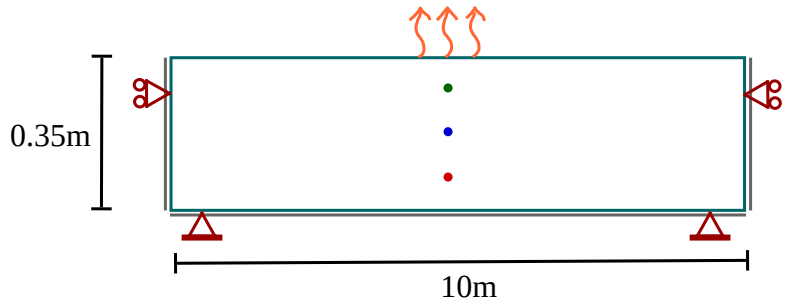

Figure 3.1: Beam model

Table 3.1: Beam model parameters

ρ[kg/m^3]	C[J/(m^3∘C)]	k[W/(m·°C)]	h[W/(m^2·°C)]	T_0[°C]	α_T[1/°C]	$T_{\alpha,ref}$[°C]
2400	$2.07 \cdot 10^6$	6.11	14.4	21	$8.33 \cdot 10^{-6}$	20
ξ_∞[.]	E_a/R[K]	k_ξ/η_{ξ_0}[1/h]	A_{ξ_0}/k_ξ[.]	$\bar{\eta}$[.]	l_ξ[J/m^3]	
0.75	4000	$0.14 \cdot 10^7$	$1 \cdot 10^{-4}$	7	$1.58 \cdot 10^8$	
ξ_{set}[.]	n_T[.]	T_T[°C]	T_{ref}[°C]	ν[.]	$f_{c,\infty}$[MPa]	E_∞[GPa]
0.2	0.42	100	20	0.2	34.5	29.6

Table 3.2: 1PDE and 2PDE parameters

	A_f[.]	B_f[.]
1 PDE	0.2	1.3
2 PDE	1.22	0.81

The results obtained with the two approaches are presented in Figures 3.2 to 3.5. It is observed that both approaches lead to very similar results.

The approach that uses 1 PDE revealed to be less numerically expensive and leading to accurate results, provided that A_f and B_f parameters are well optimized to match isothermal tests results for each approach. Since the objective of this thesis is to perform uncertainty analysis by means of probabilistic studies, reducing computation time is of extreme importance, and the 1 PDE approach is therefore chosen in this work.

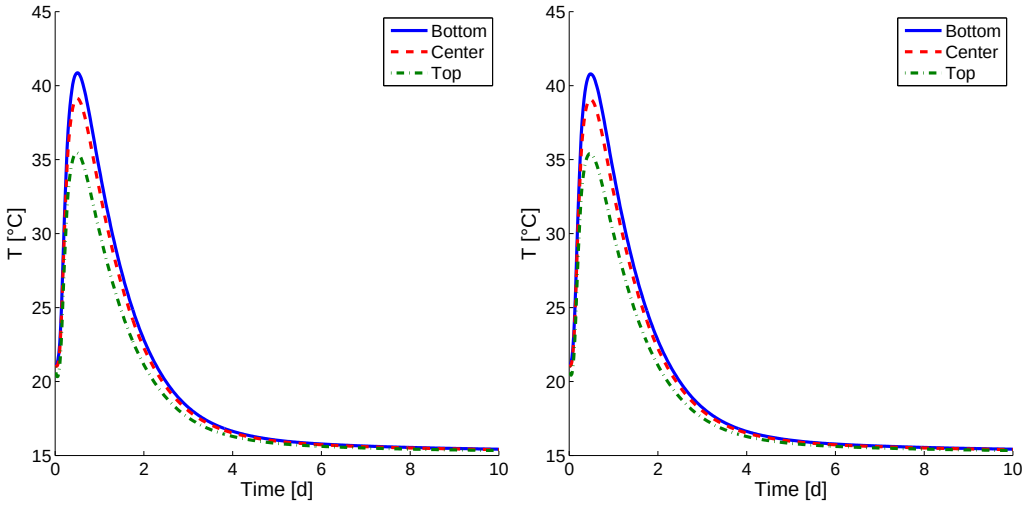

Figure 3.2: Temperature in the beam model: a) 1 PDE; b) 2 PDE.

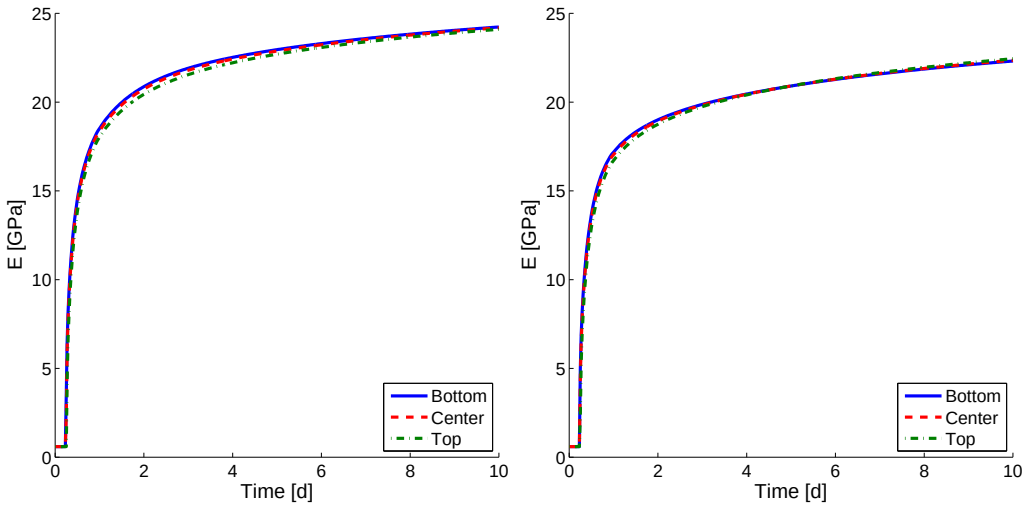

Figure 3.3: Young's modulus in the beam model: a) 1 PDE; b) 2 PDE.

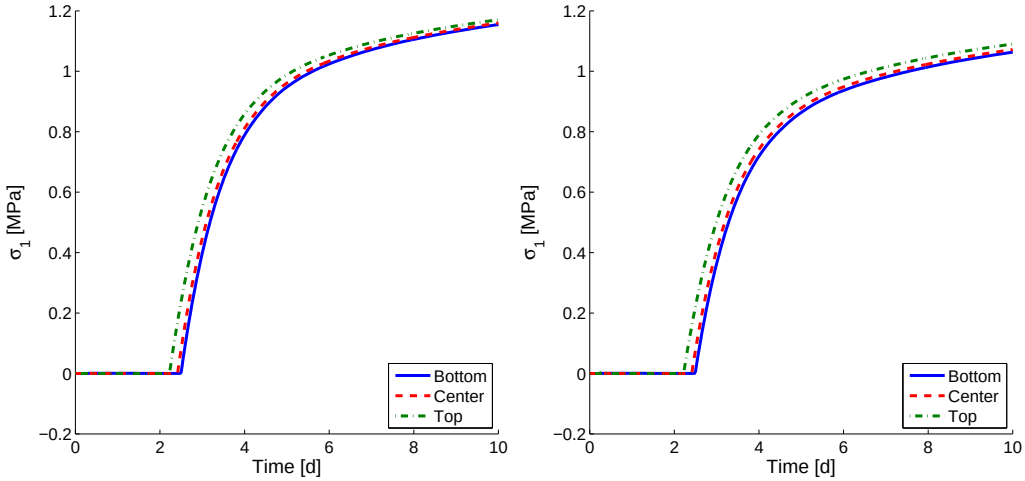

Figure 3.4: First principal stress in the beam model: a) 1 PDE; b) 2 PDE.

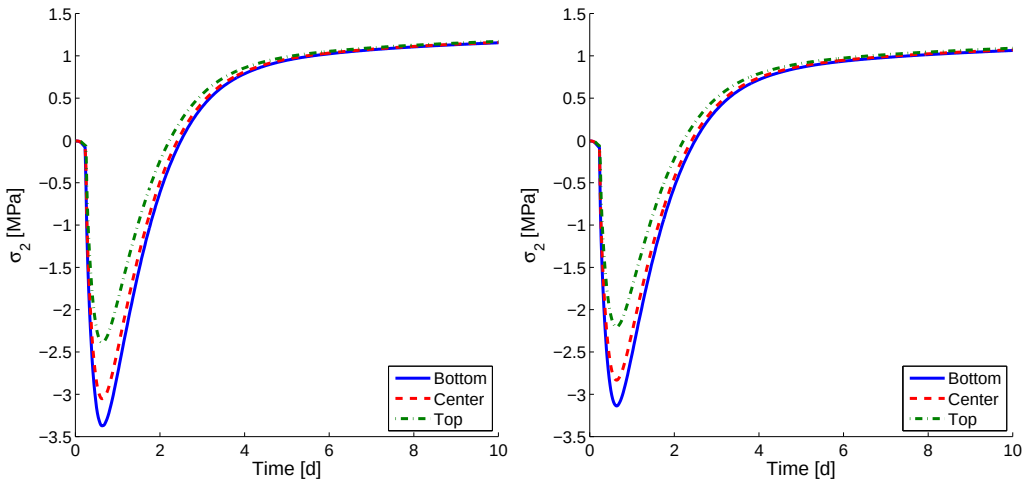

Figure 3.5: Second principal stress in the beam model: a) 1 PDE; b) 2 PDE.

3.2 Thermo-chemo-mechanical model validation and verification

This section intends to present and discuss some elementary tests that were performed in order to validate and verify the performance of the adopted thermo-chemo-mechanical model. Three different RCC mixtures taken from the available literature are studied. First, adiabatic and isothermal tests are simulated for the three RCC mixtures, evaluating the chemical affinity curve, temperature and compressive strength evolution which are compared with available experimental measures. Finally some tests are performed using the coupled thermo-chemo-mechanical model in viscoelasticity, applying the available data and model parameters of Cervera et al. (1999b) (ordinary Portland concrete (OPC) from Laplante (1993)) to account for creep effects.

Each RCC mixture characteristics and the correspondent model parameters are summarized in Table 3.3. The three mixtures are inspired from the literature, and for RCC1 and RCC3 some model parameters needed to be optimized in order to match measured values.

3.2.1 Adiabatic tests

An adiabatic test is simulated for each RCC mixture described in Table 3.3. Only the thermo-chemical part of the model is solved in this application. The adiabatic 2D numerical model consists of a 1m-side square, discretized by a triangular mesh of 480 elements, and a time-step of 0.5 hours. For each mixture, the computation is carried on until the last available experimental measure. On all of the model boundaries, Neumann condition are applied (zero flux), that is, all of the four boundaries are insulated. The hydration model described by Cervera et al. (1999b) (please refer to section 2.2 for further details) is adopted here. The chemical affinity is therefore described by equation 3.6. The temperature is measured in the center of the 1m-side square.

$$\tilde{A}_\xi(\xi) = \frac{k_\xi}{\eta_{\xi 0}} \left(\frac{A_{\xi 0}}{k_\xi \xi_\infty} + \xi \right) (\xi_\infty - \xi) \cdot \exp\left(-\tilde{\eta} \frac{\xi}{\xi_\infty} \right) \tag{3.6}$$

As it may be concluded by the results plotted in Figures 3.6, 3.7 and 3.8, the considered model is able to reproduce experimental measures for adiabatic tests.

Table 3.3: Properties for each RCC mixture used in the elementary tests

Property	RCC1 (Leitão et al., 2007)	RCC2 (Cervera et al., 2001)	RCC3 (Lackner and Mang, 2004)
$c+f[\mathrm{kg/m^3}]$	220	195	90
$w/(c+f)[.]$	0.6	0.4	1.0
$\rho[\mathrm{kg/m^3}]$	2400	2500	2500
$C[\mathrm{J/(m^3{\cdot}°C)}]$	$2.21\cdot10^6$	$2.44\cdot10^6$	$2.5\cdot10^6$
$k[\mathrm{W/(m{\cdot}°C)}]$	2.3	1.97	1.7
$T_0[°\mathrm{C}]$	21	21	20
$f_{c,\infty}[\mathrm{MPa}]$	18	40	13.6
$\xi_\infty[.]$	0.779	0.69	1.0
$E_a/R[\mathrm{K}]$	5000	5000	4000
$k_\xi/\eta_{\xi_0}[1/\mathrm{s}]$	2500	19444	129⋆
$A_{\xi_0}/k_\xi[.]$	0.005	0.0001	0.0043⋆
$\overline{\eta}[.]$	8.1	10.5	9.02⋆
$l_\xi[\mathrm{J/m^3}]$	$6.24\cdot10^7$	$7.0\cdot10^7$	$4.5\cdot10^7$
$\xi_{set}[.]$	0.25⋆	0.1	0.01⋆
$A_f[.]$	4.2⋆	3.47	−0.04⋆
$B_f[.]$	−1.05⋆	−0.76	1.05⋆
$n_T[.]$	0.12⋆	0.0	0.0⋆
$T_T[°\mathrm{C}]$	100⋆⋆	100	100⋆⋆
$T_{ref}[°\mathrm{C}]$	20⋆⋆	20	20⋆⋆

⋆ optimized to match measured values

⋆⋆ hypothesis

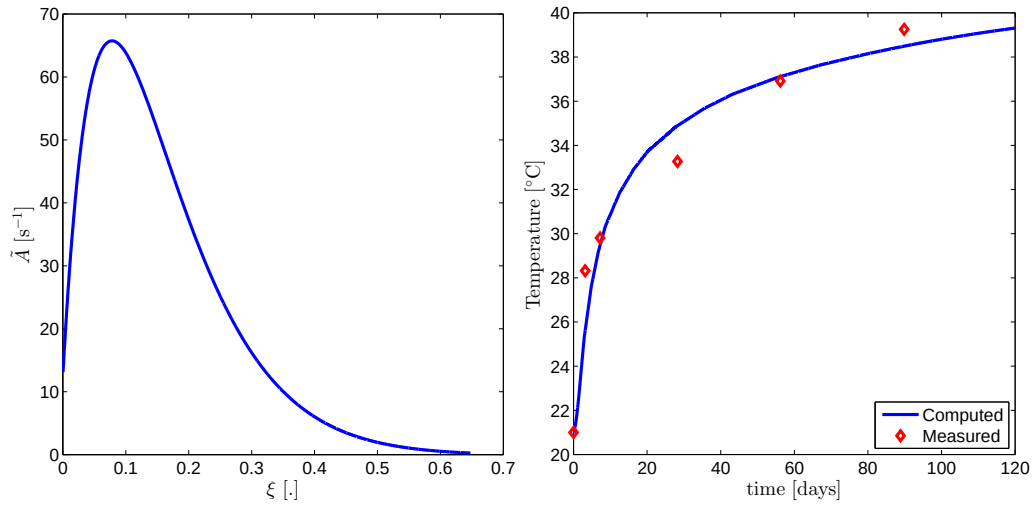

(a) (b)

Figure 3.6: Adiabatic tests, RCC1 mixture: a) Chemical affinity function; b) Temperature evolution, measured values from Leitão et al. (2007).

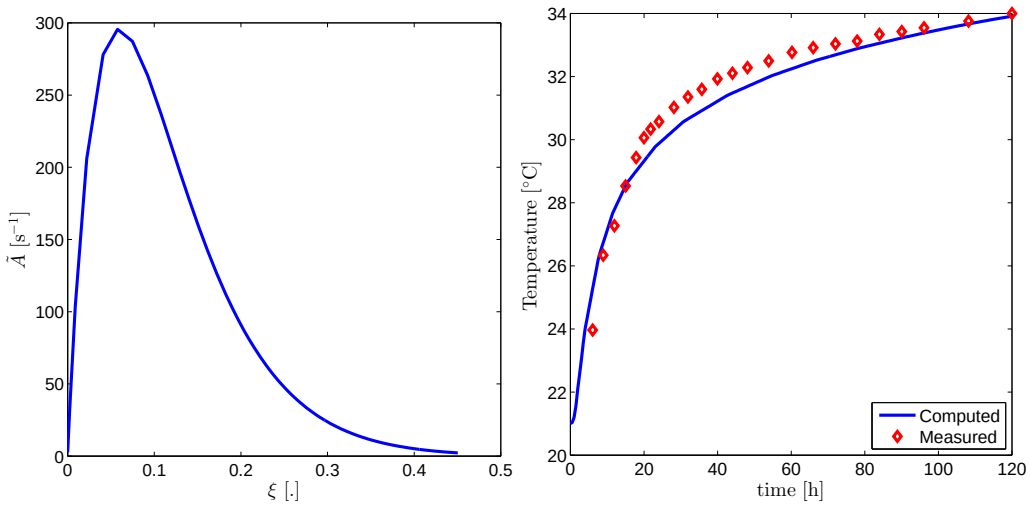

(a) (b)

Figure 3.7: Adiabatic tests, RCC2 mixture: a) Chemical affinity function; b) Temperature evolution, measured values from Cervera et al. (2001).

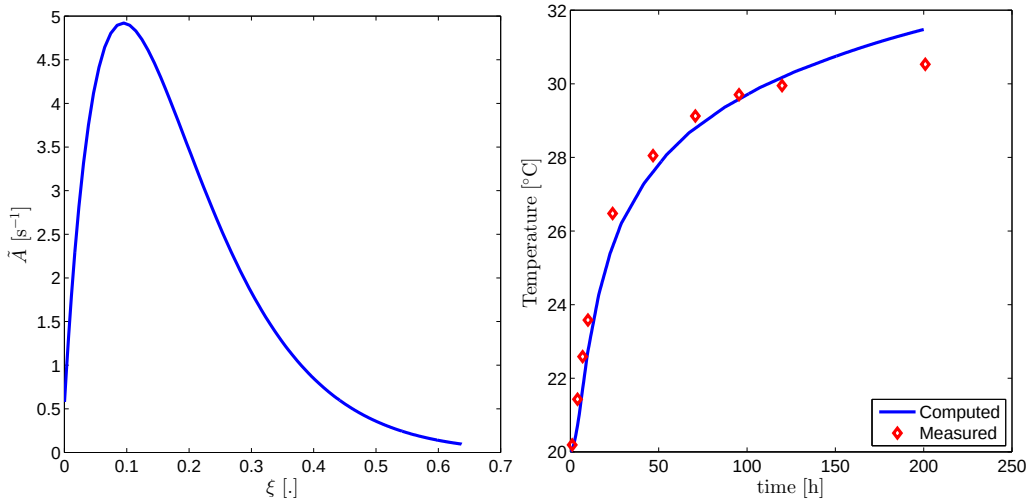

(a) (b)

Figure 3.8: Adiabatic tests, RCC3 mixture: a) Chemical affinity function; b) Temperature evolution, measured values from Lackner and Mang (2004).

3.2.2 Isothermal tests

An isothermal test is simulated for each RCC mixture described in Table 3.3. This time, the full thermo-chemo-mechanical model is solved. The isothermal numerical model consists of a 0.1x0.2m^2 rectangle, discretized by a triangular mesh of 314 elements, and a time-step of 0.5 hours. For each mixture, the computation is carried on until the last available experimental measure. The boundaries of the model are Dirichlet condition type, which means that on all

boundaries a constant temperature (called T_{iso}) is imposed during the simulation.

As previously described in section 2.3.1, the compressive strength is obtained via an ageing function $\kappa(\xi)$ (equations 3.7 to 3.10).

$$f_c(\kappa) = \kappa \cdot f_{c,\infty} \tag{3.7}$$

$$\kappa = \lambda_T \cdot \lambda_{f_c} \cdot \dot{\xi} \tag{3.8}$$

$$\lambda_T = \left(\frac{T_T - T}{T_T - T_{ref}} \right)^{n_T} \tag{3.9}$$

$$\lambda_{f_c} = A_f \cdot \xi + B_f \tag{3.10}$$

In Figure 3.9 are plotted the compressive strength evolutions during an isothermal test at $T_{iso} = 20°C$ for the three studied RCC mixtures.

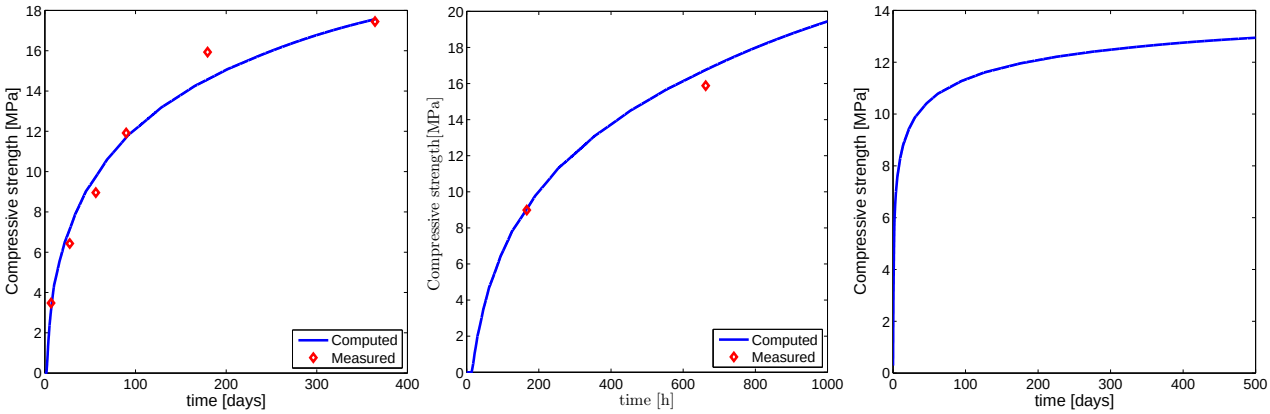

Figure 3.9: Isothermal tests at 20°C: a) Compressive strength evolution, RCC1, measured data from Leitão et al. (2007); b) Compressive strength evolution, RCC2, measured data from Cervera et al. (2001); c) Compressive strength evolution, RCC3.

The influence of the isothermal temperature boundary condition may be understood by comparing the obtained compressive strength evolutions of three isothermal tests using RCC1 mixture at $T_{iso} = 5$, 20 and 40°C (Figure 3.10). The surrounding temperature influence is here reproduced thanks to the n_T parameter of equation 3.9, which for RCC1 has a non-zero value. A similar test was previously plotted in section 2.3.1, Figure 2.13b, using data from Kim et al. (1998).

The results of Figures 3.9 and 3.10 lead to the conclusion that the adopted model is able to reproduce measured mechanical properties' evolution under isothermal conditions and also

account for the influence of different isothermal temperatures. The latter conclusion is useful if the aim is to simulate the RCC behaviour under varying ambient temperature.

3.2.3 Cyclic tests

The results presented in this subsection intend to demonstrate the ability of the model to account for creep effects. The viscoelastic behaviour of RCC is simulated via a generalized Maxwell model such as the one presented in section 2.3.2. Because of the lack of available data concerning creep of RCC, it was decided to verify this model with the available data for an ordinary Portland concrete (OPC) (Laplante, 1993; Cervera et al., 1999b). The Maxwell chain is composed of two branches, characterized by two elastic springs and one dashpot such as in Figure 3.11. In Table 3.4 are described the model parameters used in the following verification tests. It shall be enhanced here that the aim of the test described in this subsection is not to obtain the exact response found in Cervera et al. (1999b), but only to verify if the used numerical code is able to model the described phenomena.

A cyclic (loading and unloading) test is performed over a 2D geometry of 0.3x1.2m^2 rectangle, discretized by a mesh of 158 triangular elements, and a time-step of 0.5 hours. The top and bottom boundaries of the model are considered insulated (Neumann boundary conditions) and on the lateral boundaries heat flux is considered (equation 3.11, where h[W/m^2·°C] is the heat transfer coefficient, T_{ext}[°C] is the ambient temperature and $\underline{n}$ is the normal vector to the surface). The lower boundary is mechanically blocked, while the other remain free. The loading path applied at the top face of the model as well as a geometric sketch of the cyclic test are

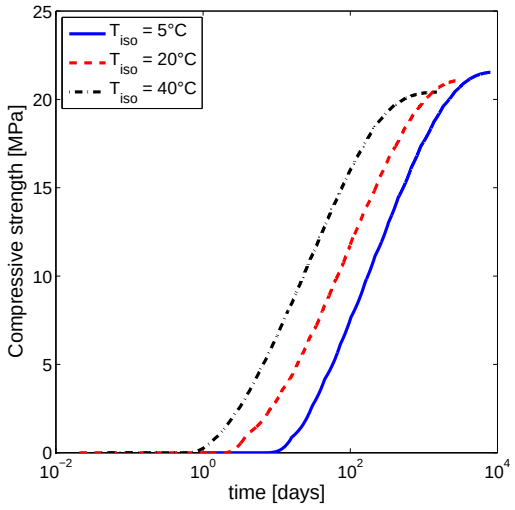

Figure 3.10: Compressive strength evolution at different isothermal temperature

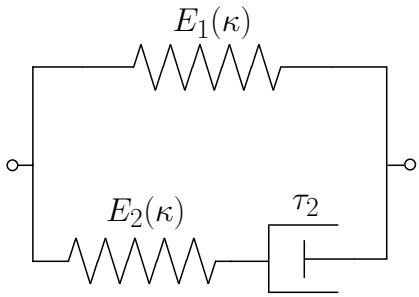

Figure 3.11: Generalized Maxwell chain with two branches

depicted in Figure 3.12. The Young's modulus is a function of the ageing degree κ such as in equation 3.12.

$$\frac{\partial T}{\partial \underline{n}} = \begin{cases} \frac{h}{k} \cdot (T_{ext} - T) \\ 0 \text{ if insulated surface} \end{cases} \tag{3.11}$$

$$E(\kappa) = \kappa^{1/2} \cdot E_\infty \tag{3.12}$$

The obtained results for the cyclic test are considered as being representative of the loading and unloading paths. Even if there exist a slight overestimation of the creep deformation when the loading is stopped, the elastic deformation at the loading instants is well reproduced (Figure 3.13b). Moreover, the applied model parameters may be object of several uncertainties due to lack of some data, which is why the obtained results are not exactly the same as the measured ones. So as to demonstrate the influence of a certain hypothesis made on the adopted model parameters, it was decided to change the hydration heat l_ξ[J/m^3]. It was then observed that l_ξ changes significantly the viscoelastic behaviour (Figure 3.14b). It is also observed that the

Table 3.4: Properties of OPC mixture

Property	OPC	Property	OPC	Property	OPC
ρ[kg/m^3]	2370	ξ_∞[.]	0.75	n_T[.]	0.0
C[J/(m^3·°C)]	$2.45 \cdot 10^6$	E_a/R[K]	4000	T_T[°C]	100
k[W/(m·°C)]	1.6	k_ξ/η_{ξ_0}[1/s]	333	T_{ref}[°C]	20
h[W/(m^2·°C)]	4.44	A_{ξ_0}/k_ξ[.]	$1 \cdot 10^{-4}$	$E_1 : E_2$	3 : 1
T_0[°C]	20	$\overline{\eta}$[.]	6.0	τ_1[h]	$+\infty$
$f_{c,\infty}$[MPa]	35.2	l_ξ[J/m^3]	$1.05 \cdot 10^{8\star}$	τ_2[h]	15
E_∞[GPa]	38.5	ξ_{set}[.]	0.1	$\tau_{\mu 0}$[10^3h]	0.7
ν[.]	0.2*	A_f[.]	2.56	$c_{\mu 0}$[10^{-3}1/h]	6.0
α_T[1/°C]	$1.2 \cdot 10^{-5}$	B_f[.]	0.37		

* hypothesis

increasing of the relaxation time τ_2 leads to a decrease in the creep deformation (Figure 3.15).

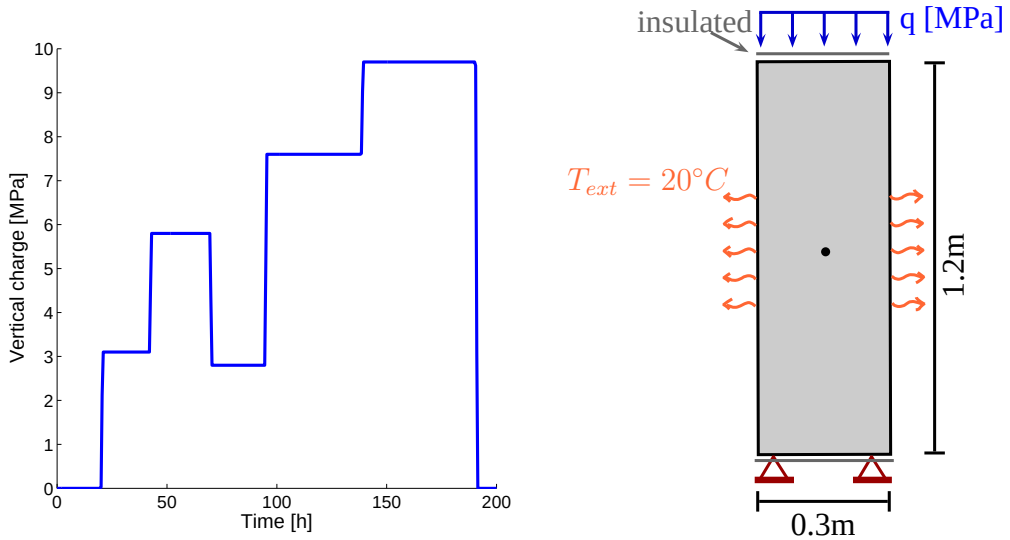

(a) (b)

Figure 3.12: Cyclic test: a) Loading path; b) Test sketch.

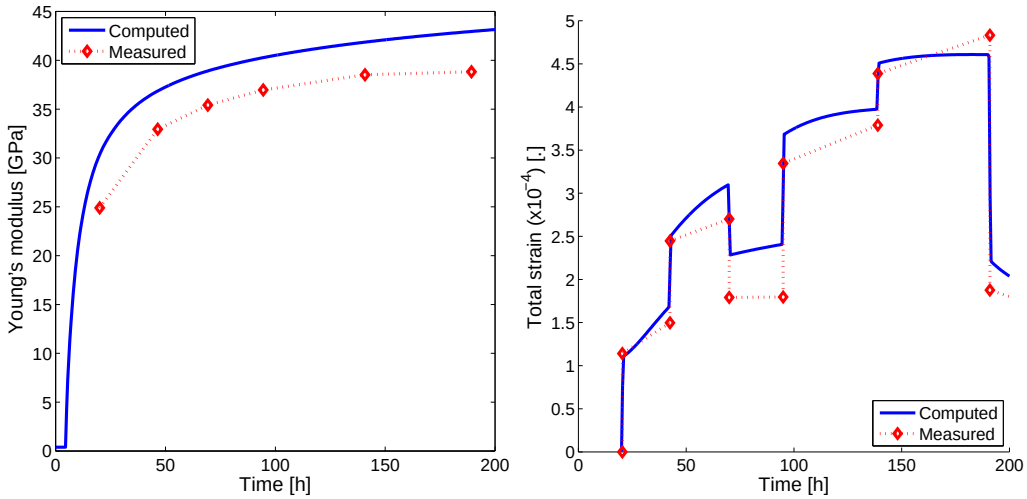

(a) (b)

Figure 3.13: Computed vs. measured (Cervera et al., 1999b) results of the cyclic test: a) Young's modulus evolution; b)Total strain evolution.

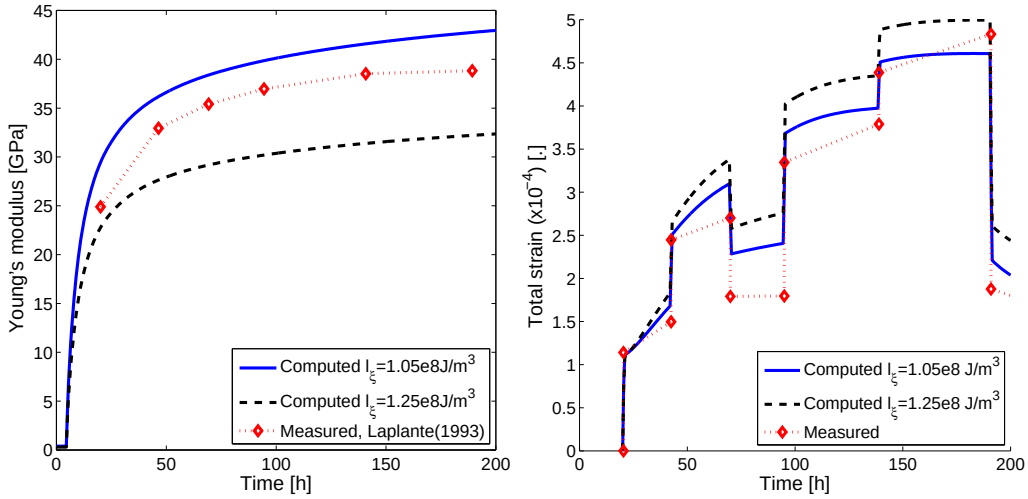

(a) (b)

Figure 3.14: Influence of l_ξ[J/m^3]: a) Young's modulus evolution; b) Total strain evolution.

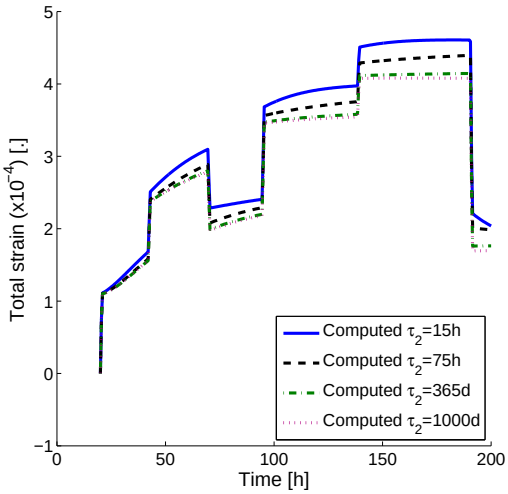

Figure 3.15: Influence of τ_2

3.3 Application to an RCC dam

The model geometry used in the present work consists of a gravity RCC dam placed on a rock foundation. This model is inspired from a real case, Pedrógão dam, the only RCC gravity dam constructed in Portugal, until now. The dam body is 28.2m high, 30m wide at its base level and with a downstream slope of 0.8. A scheme of the geometry is presented in Figure 3.16. The dimensions of the foundation rock are not directly specified in the scheme because two cases are adopted in the present work: for modelling only the thermal behaviour, a 5m deep foundation is used and considered sufficient to model the thermal restrain imposed by the foundation rock; while modelling the thermo-mechanical behaviour of the dam, a deeper and wider foundation is adopted to represent the mechanical restrain imposed by the foundation rock. The foundation dimensions are specified in Table 3.5. In the adopted geometry, each RCC layer is 0.6m high.

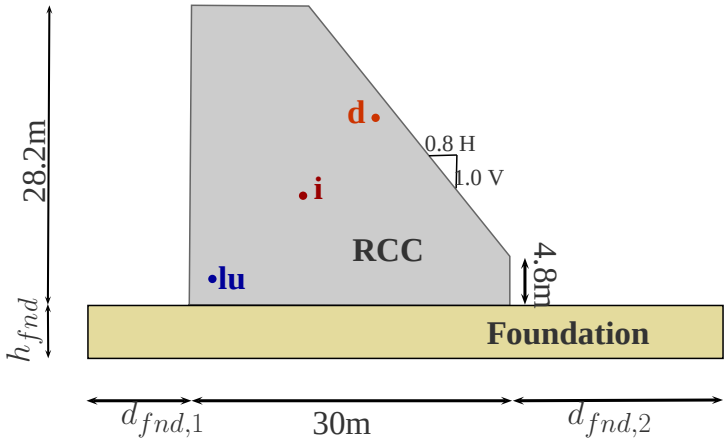

Figure 3.16: Dam geometry scheme

Moreover, three points are discretized in the dam body, on which results are assessed in more detail in the applied chapters 4, 5 and 6. Their denomination intend to represent their emplacement within the dam body: "point lu", placed at (2.1,2.1)m, stands for "**l**ow **u**pstream", "point i", placed at (12.6,11)m, stands for "**i**nterior" and "point d", placed at (18.4,17.9)m, stands for "**d**ownstream".

Table 3.5: Foundation rock dimensions

	$h_{fnd}[m]$	$d_{fnd,1}[m]$	$d_{fnd,2}[m]$
Thermal behaviour	5	5	20
Thermo-mechanical behaviour	20	20	50

Concerning the mesh discretization, quadratic triangular elements are adopted in this work. The mesh is automatically generated by the numerical software and is composed of 3721 elements with an average element quality of 0.88. In Figure 3.17 is represented the adopted mesh in this work. The more refined areas within the dam body correspond, in this case, to point "lu" and "i".

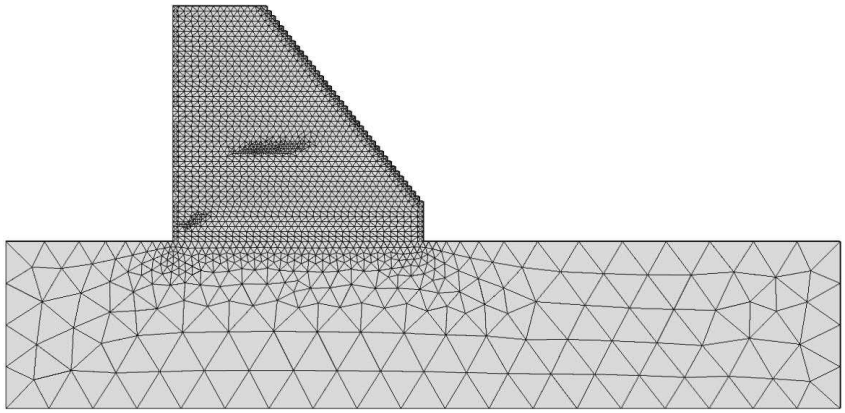

Figure 3.17: Finite element mesh

3.3.1 Modelling the construction method

As previously mentioned, an RCC dam is constructed by successive layers. The fact that this concrete has a lower cement content when compared with conventional concrete, will lead to a lower hydration heat while casting. Still, in the case of an RCC dam, an adequate thickness need to be adopted for the casting layers. Due to its low conductivity, the rapid layered construction of such a massive structure will generate an almost adiabatic behaviour in the dam core. In fact, between the cast of two consecutive layers, there is no time for the completion of the hydration reaction. Hence, one layer will continue to generate heat and to deform when the upper layer is posed. Therefore, between the two layers thermal gradients will occur and the volumetric changes will be restrained which can lead to tensile stresses and, eventually, cracking. It is then essential to model the layered construction of RCC dams in order to predict its behaviour. The heat transfer between two consecutive casted lifts is illustrated in Figure 3.18.

Modelling the construction procedure of RCC dams is one of the most delicate steps of the present numerical model. As already specified in chapter 1, this kind of dams are constructed by superposing layers such as in an embankment dam. Details on the construction scheme, such as the height of each layer, the number of layers constructed per day and the time delays between

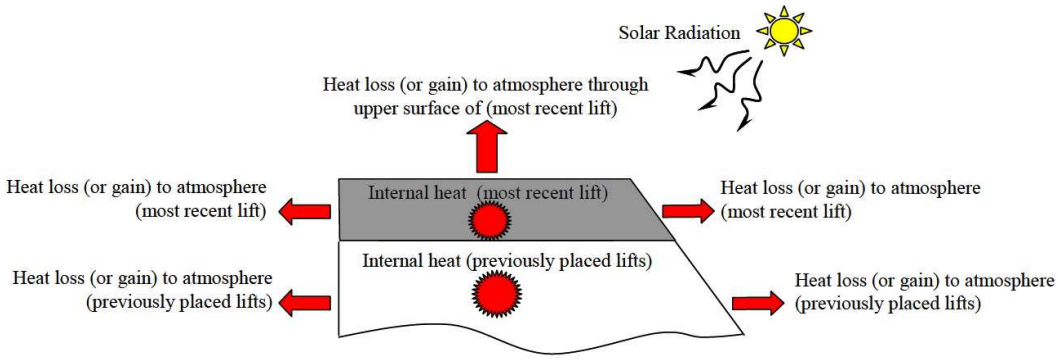

Figure 3.18: Heat transfer during dam construction (Nisar et al., 2008)

consecutive casted layers are of extreme importance on this kind of structures, and therefore essential to achieve a good representation of the RCC dam's thermo-mechanical behaviour during construction. The compaction of each RCC layer after casting is not modelled in the present work. It is therefore assumed that the considered layer's thickness and mechanical properties are representative of the material state after compaction. However, it is known that the compaction loads change the skeletal structure of the RCC. Nevertheless, the compaction effect plays a positive role on the RCC behaviour by reducing creep and shrinkage (Shaw, 2010). This behaviour is due to the aggregates' rearrangement during compaction which, by creating inter-aggregate particle contact, contributes to the stiffening of the material.

The layered construction is often modelled in the available literature by means of the "birth and death of elements" technique (Jaafar et al., 2007). This technique consists of activating mesh elements corresponding to each casted layer according to a given construction schedule. The activation of each layer would consist of enabling temperature and hydration degree evolutions as well as gravity forces according to the adopted construction scheme. The advantage of this technique relies on the fact that the model geometry and mesh are the same all along the simulation. However, to account for heat exchange with the environment on each layer's top surface is of difficult achievement.

The birth and death of elements technique was introduced in the numerical software ANSYS. In this code, this technique is achieved by the elements deactivation and reactivation. The elements "death", or deactivation, is done by multiplying stiffness, conductivity or other analogous quantity by a reduction factor, which is set to $1.0 \cdot 10^{-6}$ by default. On the other hand, their "birth", or reactivation, is done by setting their properties into given values. It needs to be pointed out that, for an element to be born, it needs to be "killed" before, or deactivated, and then "reborn", or reactivated. This procedure is already implemented in the numerical code

GEFDyn (Aubry et al., 1986) and Code_Aster developed by EDF (*Eléctricité de France*). In COMSOL Multiphysics® (version 4.2), the numerical software used in this work, this technique is not implemented in an explicit way. Therefore, a solution was needed to achieve the layered simulation of the RCC dam construction. Four approaches were studied in the framework of the present thesis: by giving a high conductivity coefficient to the deactivated layers; by using a tool available in the adopted software on which a moving boundary is accounted for to simulate the layered construction; by replacing the moving boundary for a thin layer intending to simulate the heat convection flux on the top boundary; by adopting a multi-model concept. The first three approaches are presented in the appendix A of this thesis. The last approach is the adopted one and is described hereafter.

The adopted technique to model the layered construction and account for the heat exchange on all of the dam surfaces, is based on a multi-model method concept. The multi-model method consists of solving a sequence of models, to which a 0.6m thick RCC layer is added at a time. The initial conditions and model history variables for the already constructed layers of each sub-model are the solution of the previous solved one. Therefore, the multi-model is made of N sub-models, N being the number of casted layers. This method, not only allows to account for the heat flux exchange with the environment on all of the dam surfaces, but also to account for different casting conditions for each layer, such as different ambient temperature evolutions, casting temperatures and construction time delays. To each sub-model the self-weight if the casted layer is accounted by activating the gravity forces.

In order to implement and validate the multi-model procedure, the construction of a 5 layered column was simulated (Figure 3.19). As the first layer (foundation) is already "activated" since the beginning, then this multi-model is composed of 4 sub-models. At this first stage, since the objective is just to validate the procedure, the sub-models are created manually. On further modeling and for greater structures, a coupling between COMSOL Multiphysics® and Matlab® is done, creating a routine to automatize this procedure.

Table 3.6: Material properties

Material	Foundation	RCC
Density ρ[kg/m^3]	2710	2400
Specific heat c[J/(kg·K)]	921	921
Heat conduction coefficient k[W/(m·K)]	1.5	2.33
Heat transfer coefficient h[W/(m^2·K)]	10	10

A first calculation is performed, considering a constant ambient temperature of $T_{ext} = 30°C$. The adopted construction speed is of 1 layer per 12h and the casting temperature of 20°C. The time-step is of 0.01h and the material properties are given in Table 3.6. In this first approach, heat generation in the material is not accounted for. The results are plotted in Figure 3.20. It can be concluded from Figure 3.20a that the layered construction is well simulated, the temperature at the upper layer being equal to its 20°C casting temperature at the moment of construction ($t = 36h$), which is enhanced in Figure 3.20c for each layer on nodes 7 to 11, placed at the middle of each layer. Concerning the thermal boundary conditions, only the top surface of each casted layer is non-insulated. Since only the thermal behaviour is simulated here, the mechanical boundary conditions do not apply.

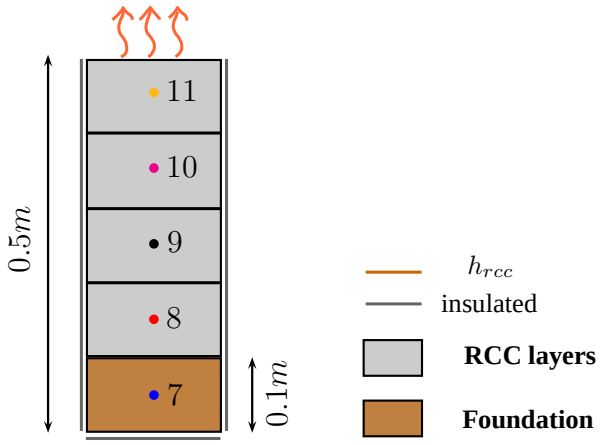

Figure 3.19: Scheme for 5 layered column

In order to verify the performance of the implemented procedure, the hydration heat generation of concrete is added to this model by means of an adiabatic temperature evolution $T_{ad}(t)$, such as in equation 3.13. The adopted parameters are described in Table 3.7.

$$T_{ad}(t) = T_{max} \cdot (1 - \exp(-\alpha \cdot t)) \tag{3.13}$$

$$\dot{Q} = \rho \cdot c \cdot T_{max} \cdot \alpha \cdot \exp(-\alpha \cdot t) \tag{3.14}$$

The results are plotted in Figure 3.21. In comparison with the other three studied approaches (presented in appendix A), the multi-model approach leads to temperature evolutions on which the thermal effect of each casted layer on the previous ones is clearly simulated, as it is proved by the temperature decrease on each curve of Figure 3.21 at the instant of each layer casting.

With the multi-model approach it is then possible to account for different casting tempera-

Table 3.7: Parameters for adiabatic heat generation model

Material	RCC
Density ρ[kg/m^3]	2400
Specific heat c[J/(kg·K)]	921
T_{max}[°C]	12
α[1/h]	$[0.01 - 0.04]$

tures for different layers as well as different ambient temperatures and casting schedules.

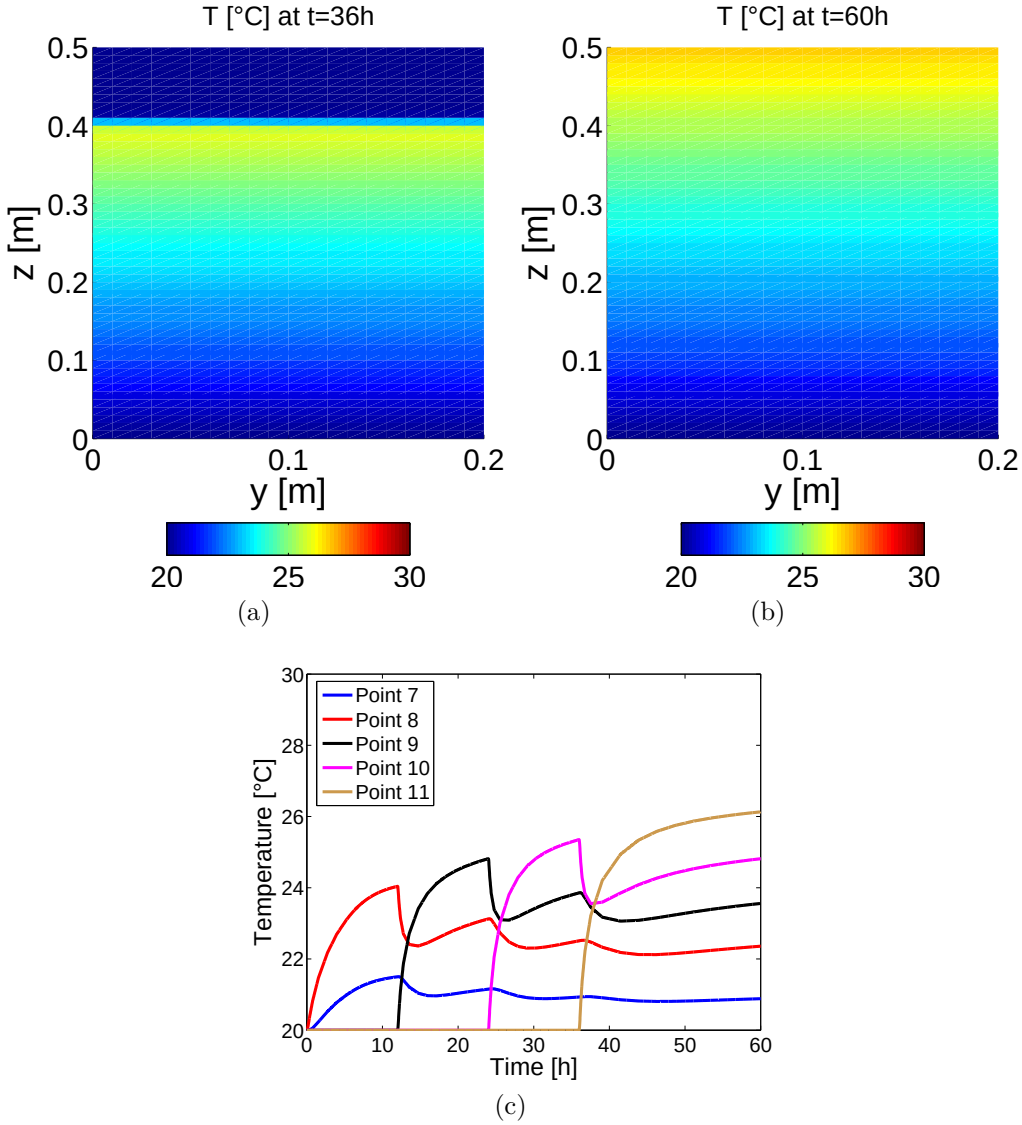

Figure 3.20: Multi-model results, $T_{ext} = 30$°C, without accounting for hydration heat generation ($\dot{Q}$): a) Temperature surface at $t = 36$h; b) Temperature surface at $t = 60$h; c) Temperature evolution in the discretized points.

3.3.2 Boundary conditions

While simulating the layered construction, to account for the heat exchange that occurs on the surface is of extreme importance. However, this aspect is often object of simplifications in some works found in the available literature. For example, in Jaafar et al. (2007), the top surface of each casted layer is considered to be insulated and no heat exchange with the environment is considered. Another approach is adopted in Cervera and García-Soriano (2002) by giving a fixed temperature at the top layer boundary.

Thermal gradients are responsible for thermal stresses to which each layer is subjected. The top surface of each layer consists of a big area that will be exposed to ambient temperature and solar radiation. Those top surfaces consist of horizontal joints, a major concern of RCC dams. The horizontal joints' quality needs to be controlled and measurements are undertaken while constructing in order to improve their quality (please refer to section 2.4 for more details). Therefore, simulating the heat flux exchange with the environment on all of the dam faces is important.

Concerning the thermal boundary conditions, the bottom and lateral faces of the foundation are insulated, while all the dam faces interact with the surrounding environment by a heat flux exchange, described by equation 3.15, where h[W/(m^2·K)] is the heat transfer/convection coefficient, T_{ext}[°C] is the ambient temperature and $\underline{n}$ is the normal vector to the surface.

$$\frac{\partial T}{\partial \underline{n}} = \begin{cases} \frac{h}{k} \cdot (T_{ext} - T) \\ 0 \text{ if insulated surface} \end{cases} \tag{3.15}$$

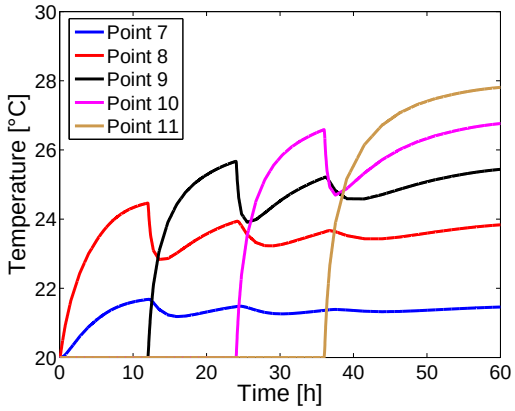

Figure 3.21: Multi-model with adiabatic hydration heat generation

The heat transfer phenomena is accounted for by a heat transfer coefficient h[W/(m^2·K)], which is here divided into a convection h_c and a radiation part h_r, such as in equation 3.16. The convection coefficient h_c accounts for the wind speed v_w[m/s] in equation 3.17, where k_f[W/(m·°C)], ρ_f[kg/m^3] and μ_f[kg/(m·s)] are the air thermal conductivity, its specific weight and its absolute viscosity respectively, L[m] being the horizontal surface length on the wind flow direction.

$$h = h_c + h_r \tag{3.16}$$

$$h_c = 0.055 \cdot \frac{k_f}{L} \cdot \left(\frac{L \cdot v_w \cdot \rho_f}{\mu_f} \right)^{0.75} \tag{3.17}$$

The ambient temperature evolution is accounted for by means of a sinusoidal function, which can be given by equation 3.18, where T_{max} and T_{min} are the maximum and minimum ambient temperatures, f[d^{-1}] is the daily frequency and $\phi[rad]$ is the phase. In a parametric study discussed in chapter 5, other sinusoidal temperature evolutions are also adopted in this work, given by equations 3.19, 3.20 and 3.21, where T_m[°C] and $T_{d,m}$[°C] are the mean annual and daily temperatures, ΔT_y[°C] and ΔT_d[°C] are the annual and daily temperature amplitudes, ϕ_y[rad] and ϕ_d[rad] are the annual and daily phases, P[d] is the period and $T_d(t)$[°C] is the daily temperature variation given by equation 3.21.

$$T_{ext} = \frac{T_{max} + T_{min}}{2} + \frac{\Delta T}{2} \cdot \sin(2\pi f t + \phi) \tag{3.18}$$

$$T_{ext}(t) = T_m + \Delta T_y \cdot \sin\left(2\pi \cdot f_y \cdot t + \phi_y\right) + \Delta T_d \cdot sin\left(2\pi \cdot f_d \cdot t + \phi_d\right) \tag{3.19}$$

$$T_{ext}(t) = T_m - \Delta T_y \cdot \cos \frac{2\pi \cdot (t - \phi_y)}{P} - \frac{T_d(t)}{2} \cdot \cos\left(2\pi \cdot (t - \phi_d)\right) \tag{3.20}$$

$$T_d(t) = T_{d,m} - \Delta T_d \cdot \cos \frac{2\pi \cdot (t - \phi_{d,2})}{P} \tag{3.21}$$

The three different adopted equations for the ambient temperature are plotted in Figure 3.22. All of the computed three curves traduce ambient temperature that begins in summer. For equation 3.18 it may be observed that the mean annual temperature stays constant at 20°C, while for the other two equations it varies sinusoidally. On all of the three approaches the ambient temperature varies daily according to the sinus function.

Concerning the mechanical boundary conditions, the foundation is blocked on both horizontal and vertical directions at its bottom and horizontally on its lateral boundaries, such as represented in Figure 3.23. All of the dam faces are considered mechanically free.

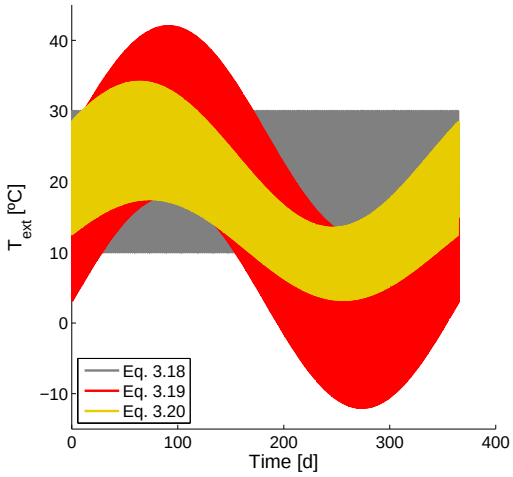

Figure 3.22: Ambient temperature evolution using different equations

However, it is known that in reality the dam lateral faces should be considered as mechanically blocked in order to account for formwork. Even if this is not current practice in numerical studies about RCC dams, a parametric study about this point is dealt with in chapter 5 by changing both thermal and mechanical boundary conditions of the dam's lateral faces.

3.3.3 Casting temperature

The casting temperature is dependent on several factors, which can be related to environmental conditions, transportation of the material, time delay between the mixing of all the components and effective casting, temperature of the aggregates used in the mix (e.g. if they were stocked during winter or summer), among others. All of these factors may be very variable during the dam construction, which is why uncertainty related to the casting temperature is dealt with in chapter 5. Most of the approaches to account for the casting temperature found in literature

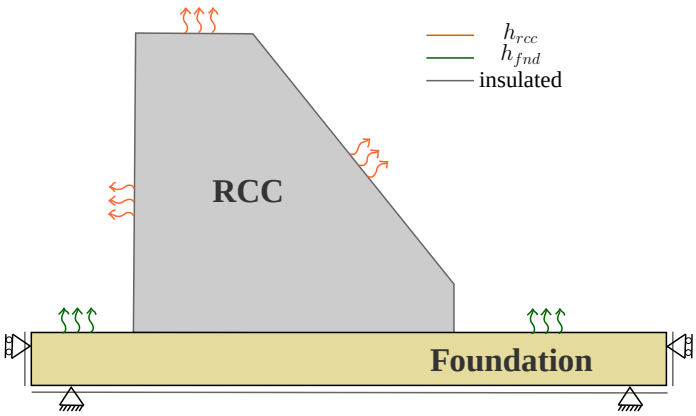

Figure 3.23: Dam thermal and mechanical boundary conditions

account for the added temperature due to aggregate, mixing and transportation, by adding it to the ambient temperature at the moment of each layer casting (e.g. Jaafar et al., 2007; Cervera et al., 2000a). In the present work, the casting temperature is given by equation 3.22, where $T_{ext}(t = t_0)$ is the ambient temperature at the instant of casting and ΔT_0 is the added temperature. Values of 1.1°C (Jaafar et al., 2007) and 5°C (Cervera et al., 2000a) were found in literature for ΔT_0.

$$T_0 = T_{ext}(t = t_0) + \Delta T_0 \tag{3.22}$$

In the present thesis, different values were adopted, either by simply considering that the casting temperature is equal to the mean annual ambient temperature (adopted in chapter 4), or by applying equation 3.22 (in chapters 5 and 6). A brief parametric study over ΔT_0 is performed in chapter 5. Moreover, uncertainties on ΔT_0 are also considered, by giving this parameter a random character on the probabilistic approach used in chapter 6.

3.3.4 Zero-stress reference temperature

The zero-stress reference temperature is a parameter that enters in the computation of thermal strains ε_T, given by equation 3.23, where $\alpha_T[1/°C]$ is the coefficient of thermal dilation, $T[°C]$ is the temperature and $T_{ref,\alpha_T}[°C]$ the zero-stress reference temperature. As its name indicates, T_{ref,α_T} is the temperature at which the material is free from thermal stresses.

$$\varepsilon_T = \alpha_T \cdot (T - T_{ref,\alpha_T}) \tag{3.23}$$

Because in this work a concept of ageing degree is adopted to account for the mechanical properties' evolution as functions of both the hydration degree and temperature, there shall be no thermal stresses before the hydration threshold ξ_{set}. Therefore, the coefficient of thermal dilation shall only be activated when $\xi \geq \xi_{set}$ (or $\kappa > 0$), and the condition described in equation 3.24 is introduced in the model by applying a step function centered at ξ_{set}, such as in equation 3.25.

$$\alpha_T = 0.6 \cdot 10^{-5}, \text{ for } \xi \geq \xi_{set} \tag{3.24}$$

$$\text{step1}(\xi) = \begin{cases} 0 \text{ for } \xi < \xi_{set} \\ 1.0 \text{ for } \xi \geq \xi_{set} \end{cases} \tag{3.25}$$

Accounting for the zero-stress reference temperature is not an easy task in a non-linear model where there is a dependence on both the hydration degree and temperature. As discussed in the previous subsection, the boundary conditions play an important role on the spatial temperature evolution inside the RCC structure. This means that, on a given casted layer, the hydration threshold ξ_{set} will not be reached at the same time for all discretized mesh nodes. This can be solved by adding a partial derivative equation to each casted layer (such as it is already done for the hydration degree) to account for the zero-stress reference temperature such as in equation 3.26. This is achieved by applying a step function centered at ξ_{set} such as in equation 3.27.

$$\frac{\partial T_{ref,\alpha_T}}{\partial t} = \text{step2}(\xi) \cdot \frac{\partial T}{\partial t} \tag{3.26}$$

$$\text{step2}(\xi) = \begin{cases} 1.0 \text{ for } \xi < \xi_{set} \\ 0 \text{ for } \xi \geq \xi_{set} \end{cases} \tag{3.27}$$

With this condition, the zero-stress reference temperature can be correctly evaluated on each node, being equal to the temperature evolution until ξ_{set} is attained, and constant afterwards (conf. Figure 3.24a, where $\xi_{set} = 0.3$).

In Figure 3.24a are plotted the zero-stress reference temperature evolution as functions of the hydration degree, on two points inside the dam ("Pt lu" for a point near both the foundation and the upstream face of the dam, "Pt i" for a point inside the core of the dam, whose behaviour is adiabatic). Figure 3.24b represents the contours of T_{ref,α_T} on which are clearly represented the different values obtained inside each casted layer and on its boundaries, as well as for different layers. For this computation, the construction occurs during winter and a casting speed of $0.6m$ per day with 3-day stops at the end of each 5-day period is considered.

However, adding a partial derivative equation to each casted layer has numerical costs, increasing the calculation time. As enhanced before, the objective of the present thesis is to perform probabilistic studies, and it was therefore decided that the added time cost inherent to this procedure should be avoided and another hypothesis should be taken into account for the zero-stress reference temperature. That hypothesis consists then in accounting T_{ref,α_T} as being equal to the casting temperature (which, itself, depends on the ambient temperature) added by 5°C. This, however, shall be seen as a rough approximation, based on the adiabatic temperature evolution of "Pt i" in Figure 3.24a, taking ΔT that occurs when ξ_{set} is achieved.

$$T_{ref,\alpha_T} = T_0 + 5°C \tag{3.28}$$

The zero-stress reference temperature contours of this approach are plotted in Figure 3.25. As it can be observed by comparison with Figure 3.24b the differences are evident, with lower T_{ref,α_T} for the second approach, constant at each casted layer. This will lead to some differences on the obtained stress results for both approaches, namely on the dam faces, such as displayed in Figure 3.26. It shall be enhanced here that, because stresses' redistribution due to cracking

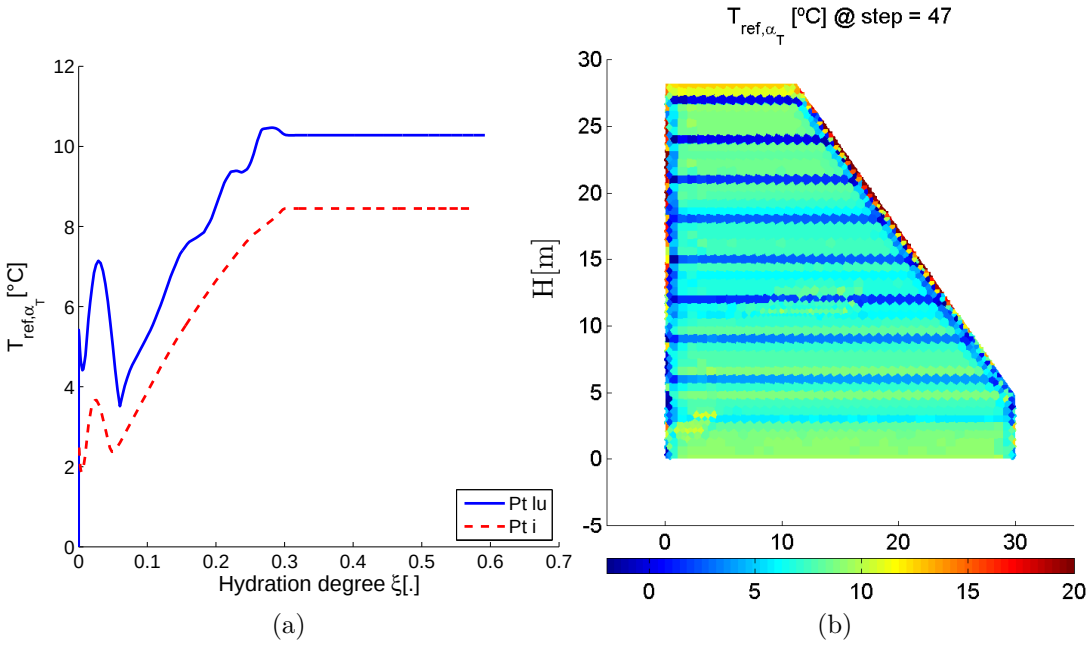

Figure 3.24: Zero-stress reference temperature as function of ξ: a) T_{ref,α_T} evolution; b) T_{ref,α_T} contours.

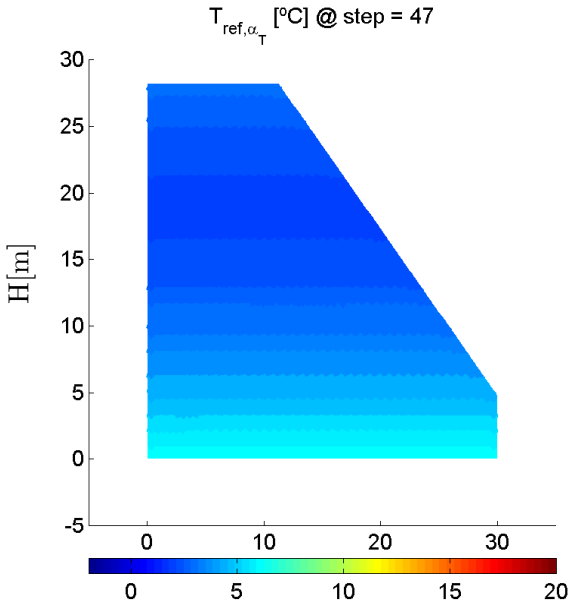

Figure 3.25: Zero-stress reference temperature contours for $T_{ref,\alpha_T} = T_0 + 5°C$

is not modelled in the present work, high localized values for the first principal stresses may appear in the dam faces. In a real case, such high stresses (on the order of 20 to 30MPa) will most likely do not occur.

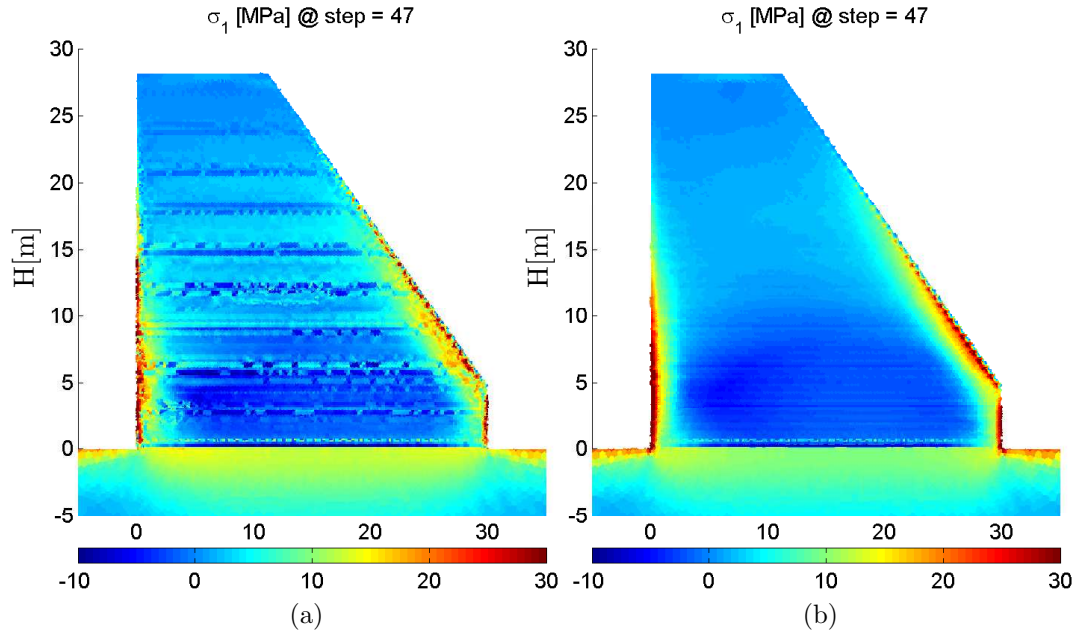

Figure 3.26: First principal stresses contours: a) σ_1 for $T_{ref,\alpha_T}(\xi)$; b) σ_1 for $T_{ref,\alpha_T} = T_0 + 5°C$.

However, the differences obtained for the cracking index, which is the "target" of this thesis work, are not that important, as it can be concluded by Figures 3.27.

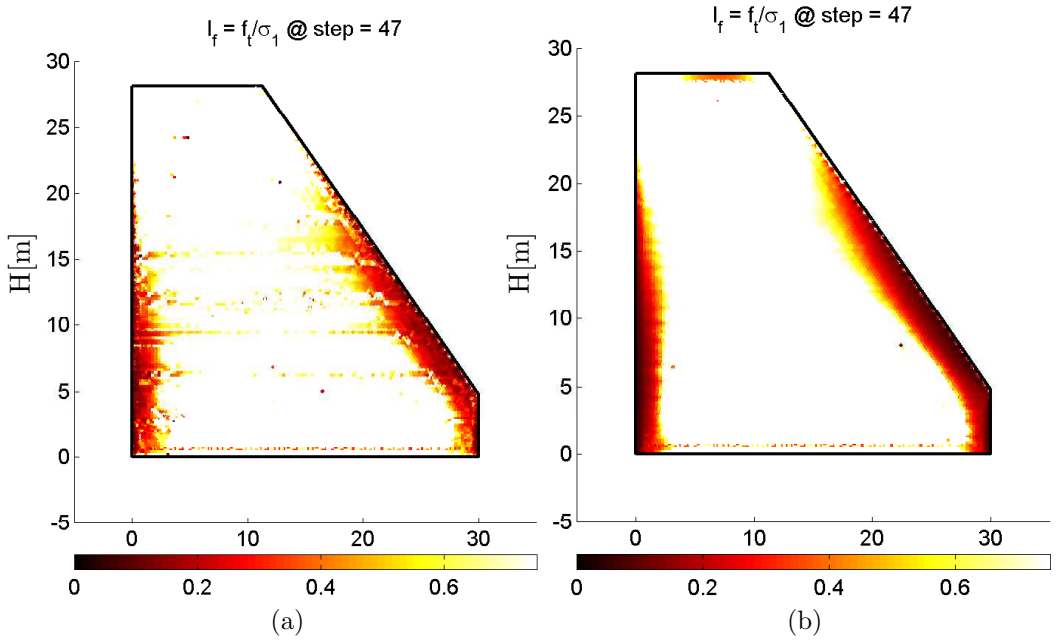

Figure 3.27: Cracking index contours: a) $I_f = f_t/\sigma_1$ for $T_{ref,\alpha_T}(\xi)$; b) $I_f = f_t/\sigma_1$ for $T_{ref,\alpha_T} = T_0 + 5°C$.

The obtained results are considered to be sufficient to justify the choice of $T_{ref,\alpha_T} = T_0 + 5°C$. However, the concept of zero-stress reference temperature shall always be kept in mind, which is a detail often ignored in these kind of studies.

3.3.5 Cracking index and density concepts

As previously referred in section 2.4, a concept of cracking index and density are adopted in this thesis in order to evaluate the cracking potential of each RCC casted layer.

The cracking index, given by equation 3.29, is here defined as being the ratio between the tensile strength f_t[MPa] and the first principal stress σ_1[MPa]. Therefore, for values of the cracking index greater than 1.0, the material is not cracked.

$$I_f = \frac{f_t(t)}{\sigma_1(t)} \tag{3.29}$$

The U.S. Army Corps of Engineers (USACE, 1995) establishes some limits for cracking of RCC. Based on the stress/strain behaviour of RCC (Figure 3.28), the following limits are given:

- for $\sigma \leq 0.6 f_t$, no cracking occurs;
- for $0.6 f_t < \sigma \leq 1.25 f_t$, microcracking occurs;
- for $1.25 f_t < \sigma \leq 1.33 f_t$, macrocracking occurs.

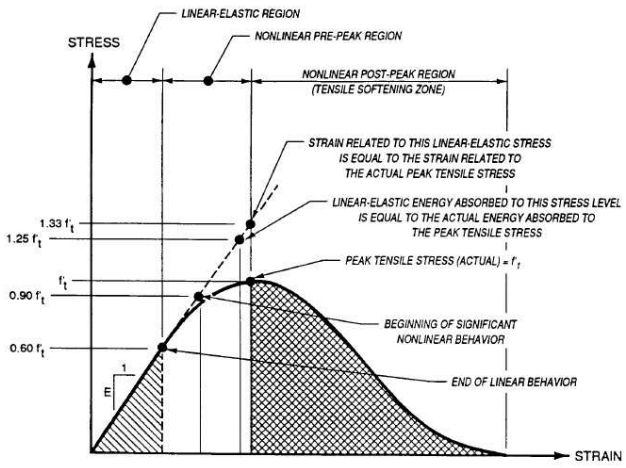

Figure 3.28: Tensile stress/strain diagram for RCC (USACE, 1995)

The limits established by the USACE will be used in this thesis as the criteria for certain allowable damage extents. For the cracking index I_f used in this thesis, these limits will lead to the following:

- for $I_f > 1.67$, no cracking occurs; $I_f = 1.67$: slight damage level;
- for $0.8 < I_f \leq 1.67$, microcracking occurs; $I_f = 0.8$: moderate damage level;
- for $0.75 < I_f \leq 0.8$, macrocracking occurs; $I_f = 0.75$: ultimate damage level.

Note that I_f may actually be seen as equivalent to the "safety factor" γ defined in Emborg (1998) as equal to 1.4 for CVC. For RCC that value is of 1.67 (for microcracking).

Then, based on the cracking index concept, a cracking density concept is introduced and applied in the present thesis. The cracking density is given by equation 3.30 and intends to give a measure of the cracking extent at the level of each casted layer/lift.

$$\rho_f = \frac{N_{0 \leq I_f < I_{f,lim}}}{N_T} \tag{3.30}$$

In figure 3.29 is schematically described the adopted procedure to compute the cracking density in the present work. After the model has been run and the results obtained, at the end of each layer's construction, a "secondary mesh" is defined over the RCC layers. This secondary mesh has nothing to do with the finite element mesh used to solve the thermo-chemo-mechanical problem, and it is composed by points discretized regularly over the domain by increments of 0.1m on both horizontal and vertical directions. The cracking index I_f is therefore calculated at each point of that secondary mesh.

Then the cracking density is evaluated by the ratio between the number of points of the secondary mesh on which cracking occurs (i.e. $0 \leq I_f < I_{f,lim}$, $I_{f,lim}$ being a pre-established limit according to the above cited limits of USACE) over the total number of points discretized per constructed lift. Afterwards, the cracking density evolution during construction is evaluated per layer and two situations may occur in the present work: either the computation is deterministic and therefore the obtained result consist on only one ρ_f curve, or the study accounts for random variables and uncertainty propagation within the model, which will lead to the obtention of a group of ρ_f curves, equal to the number of computations performed. In this last situation, the probability of exceeding a certain cracking density limit $\rho_{f,lim}$ may be assessed at a given time/age. The main objective of the present thesis is therefore achieved, by obtaining a cumulative distribution function (CDF) which traduces the probability of exceeding a certain cracking density limit for a given layer and under the considered random conditions/uncertainties.

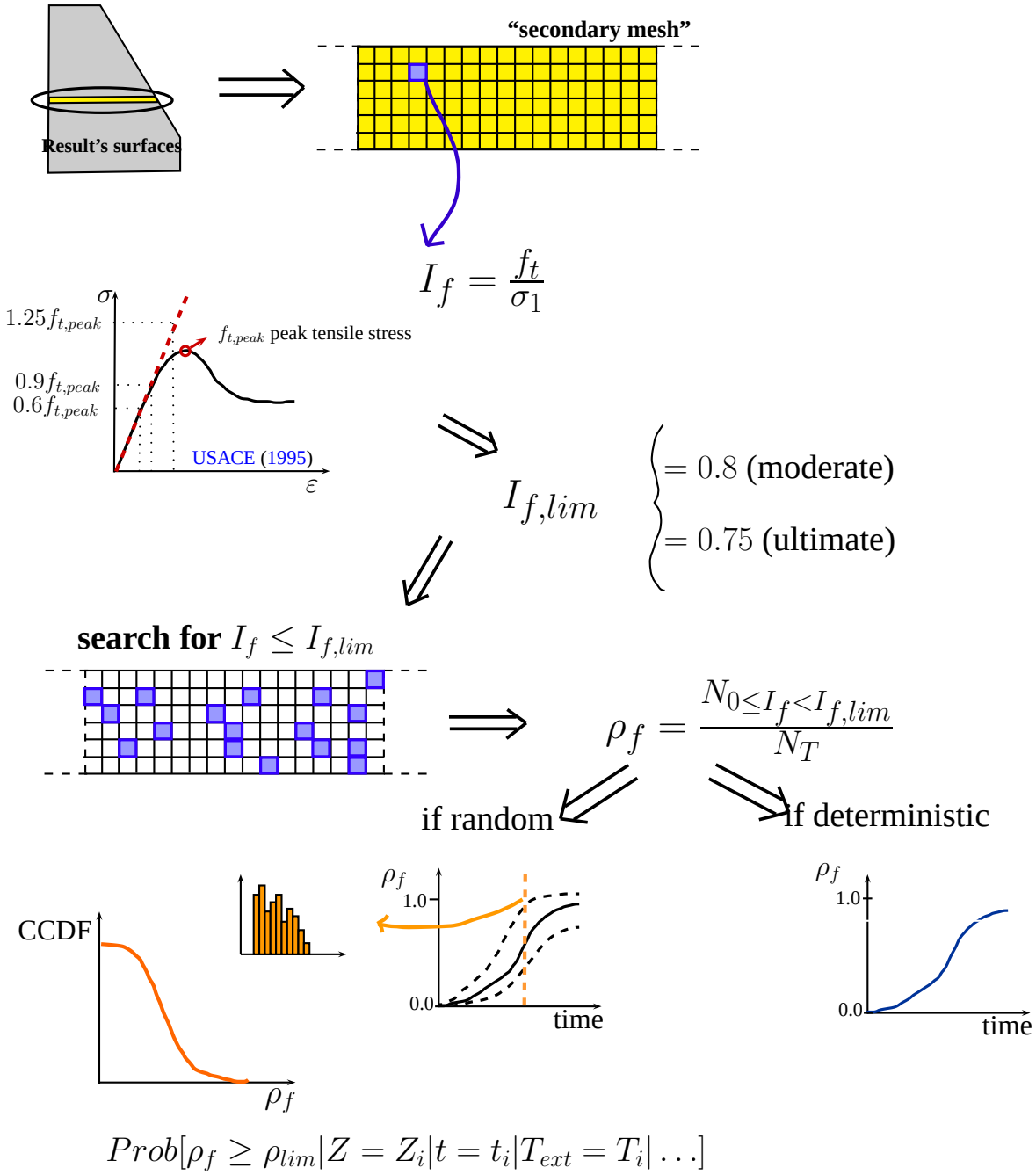

Figure 3.29: Cracking index and density conceptual scheme

3.4 Summary

This chapter provides the numerical framework and basis to justify the adopted numerical model. Firstly, the coupling between the hydration degree ξ and ageing degree κ is discussed and a test is performed over a beam model.

Then, some elementary tests are presented and performed over different RCC mixtures (for the adiabatic and isothermal tests) and a OPC mixture (for the cyclic test). These tests intend

to validate and verify the model performance by comparing the results with measured data from literature, when available.

Also, details about the dam case study are given, namely in what concerns the cross section geometry. Moreover, a multi-model procedure is adopted to achieve the modelling of the layered construction. In this procedure, the multi-model is composed of N sub-models, where N is the number of casted layers. Then, each model is run one after the other, the solution of the $N-1$ sub-model being the initial conditions of the N sub-model. For the case study of this thesis, the RCC dam is 28.2m height and each layer is 0.3m thick. However, according to the adopted construction schedules, it was decided to model two layers on each sub-model, meaning that the multi-model is composed of $28.2/0.6 = 47$ sub-models.

Then, details on the boundary conditions, casting temperature and zero-stress reference temperature are presented and discussed. This last point is not generally discussed in the available literature and is here object of several hypothesis. The consequences of those hypothesis on the output of the model are also briefly discussed within this chapter.

Finally, this chapter gives the definition of the two concepts used in this thesis to assess the cracking extent within each casted layer: the cracking index I_f and the cracking density ρ_f. These two key-concepts will be the basis of chapters 4 and 6 to assess, firstly in a deterministic manner and then by using a probabilistic approach, the cracking potential of each casted layer. In chapter 6, the probability of exceeding a certain pre-defined cracking density limit $\rho_{f,lim}$ is assessed, which is the main objective of the present work.

Chapter 4

Deterministic thermo-chemo-mechanical modelling of an RCC dam

In this chapter, a fully thermo-chemo-mechanical analysis is performed over an RCC gravity dam during construction. With the aim of evaluating the cracking that may occur on each casted RCC layer/lift, cracking index and density concepts are introduced and assessed, using a deterministic approach. Those concepts will be further evaluated in a probabilistic framework in chapter 6, by applying the probabilistic methodology described in chapter 5. Details on the procedure to compute the cracking index and density were previously described in chapter 3.

The deterministic assessment of the thermo-chemo-mechanical behaviour is performed by considering different case scenarios related to the ambient temperature (whether the construction begins during the hot or cold season), the casting temperature (which depends, in practice, on the applied cooling techniques and on the ambient temperature) and the construction scheme, which can be very variable along the dam construction (due, for example, to delays on delivering the materials). Other two aspects are also dealt with within this chapter: the cold joints' treatment and the account for formwork on lateral boundaries of the dam. At the end, the objective is to assess the changes on the cracking density evaluated on certain layers, due to those different case scenarios.

This chapter may be seen as an introductory work preceding the main contribution of this thesis which is the probabilistic approach. Here, the adopted concepts that will be further used to assess the cracking probability are firstly applied in a deterministic manner, giving essential

details to further understand their probabilistic application in chapter 6.

4.1 Application

The roller compacted concrete (RCC) is a low cement content ($\approx 200\text{kg/m}^3$) type of concrete which can be casted and compacted by successive layers/lifts. These two characteristics are inter-related since the layered construction is only possible because the low cement content leads to less heat production and consequently lower temperature gradients within the structure. Those temperature gradients shall, however, be controlled in order to avoid cracking (e.g. by changing/adapting the construction schedule). The RCC is then more cost-attractive than the conventional vibrated concrete (CVC), allowing a faster construction (i.e. successive layered placement of the material) at lower costs (less cement content).

Even if the RCC mixture has less cement than a conventional one, it remains a concrete and, as in such a material, the mechanical properties (e.g. compressive and tensile strengths, and the Young's modulus) will evolve during the formation of the hydration products that will give consistency to the material. Those products are the result of the exothermic and thermally-activated chemical hydration reaction that occurs between cement and water. Therefore, a thermo-chemo-mechanical model is needed in order to express the behaviour of the RCC. Such models have been developed and applied by several authors, such as Cervera et al. (1999a) (strong coupling) and Lackner and Mang (2004) (weak coupling).

The thermo-chemo-mechanical model applied in this work is based on the model developed and presented by Cervera et al. (1999a,b), on which the heat of hydration $\dot{Q}[\text{J/m}^3]$ is accounted for by means of equation 4.1, where $l_\xi[\text{J/m}^3]$ is the heat generated per cubic meter of RCC and $\xi[.]$ is the hydration degree. In this work, an Arrhenius-type function is adopted to describe the hydration degree rate $\dot{\xi}$, given by equation 4.2, where $\tilde{A}(\xi)[s^{-1}]$ is the chemical affinity function, the activation energy is given by $E_a[\text{kJ/mol}]$ and $R[\text{kJ/(K}\cdot\text{ mol)}]$ is the universal gas constant. The chemical affinity $\tilde{A}(\xi)$ is given by equation 4.3 by Cervera et al. (1999a), where k_ξ, η_{ξ_0}, A_{ξ_0} and $\overline{\eta}$ are material properties derived from the reactive porous media theory presented by Coussy (1996).

$$\dot{Q} = l_\xi \cdot \dot{\xi} \tag{4.1}$$

$$\dot{\xi} = \tilde{A}(\xi) \cdot \exp\left(-\frac{E_a}{R \cdot T}\right) \tag{4.2}$$

$$\tilde{A}(\xi) = \frac{k_\xi}{\eta_{\xi_0}} \left(\frac{A_{\xi_0}}{k_\xi \cdot \xi_\infty} + \xi\right) \cdot (\xi_\infty - \xi) \cdot \exp\left(-\overline{\eta} \cdot \frac{\xi}{\xi_\infty}\right) \tag{4.3}$$

The mechanical properties' evolution are dependent on the ageing degree $\kappa[.]$ given by equation 4.4, being dependent on both the temperature (via λ_T) and hydration degree (via λ_{f_c}). The hydration threshold given by ξ_{set} defines the beginning of the material's stiffening, above which the mechanical properties begin to evolve. The compressive and tensile strength, as well as the Young's modulus' evolution are therefore given by equations 4.7, 4.8 and 4.9.

$$\dot{\kappa} = \lambda_T(T) \cdot \lambda_{f_c}(\xi) \cdot \dot{\xi} \geq 0 \tag{4.4}$$

$$\lambda_T(T) = \left(\frac{T_T - T}{T_T - T_{ref}}\right)^{n_T} \tag{4.5}$$

$$\lambda_{f_c}(\xi) = A_f \cdot \xi + B_f \quad , \quad \text{for} \xi \geq \xi_{set} \tag{4.6}$$

$$f_c(\kappa) = \kappa \cdot f_{c,\infty} \tag{4.7}$$

$$f_t(\kappa) = \kappa^{2/3} \cdot f_{t,\infty} \tag{4.8}$$

$$E(\kappa) = \kappa^{1/2} \cdot E_\infty \tag{4.9}$$

The dam model used in this chapter was previously described in chapter 3 and consists of an RCC gravity dam body of 28.2m high, 30m wide at its base level and with a downstream slope of 0.8 (Figure 5.1). The foundation is also represented in this model in order to account for its thermo-chemo-mechanical effect on the first layers of the RCC dam.

Concerning the thermal boundary conditions, the bottom and lateral faces of the foundation are insulated, while all the dam faces interact with the surrounding environment by heat flux exchange (equation 4.10, where $h[\mathrm{W/(m^2 \cdot ^\circ C)}]$ is the heat transfer coefficient, $T_{ext}[^\circ\mathrm{C}]$ is the ambient temperature and $\underline{n}$ is a normal vector of the surface). The dam construction simulation is performed by using a "multi-model" concept which consists of solving a sequence of models. To each of those models a 0.6m thick layer is added, the initial conditions of each one being

the solution of the previous solved one. For more details about the dam model please refer to chapter 3.

$$\frac{\partial T}{\partial \underline{n}} = \begin{cases} \frac{h}{k} \cdot (T_{ext} - T) \\ 0 \text{ if insulated surface} \end{cases} \tag{4.10}$$

In Figure 4.1, the two discretized points correspond to the locations that were chosen to assess the dam response in more detail. "Point i" is located at the center of the dam body, while "point lu" is near to both the foundation and the upstream face of the dam. Points "lu" and "i" were chosen with the only intention of analyzing a point that should be more mechanically and thermally loaded (point "lu", located both near the foundation and the upstream face of the dam), and another point whose response is expected to be adiabatic and therefore less influenced by the external ambient temperature evolution (point "i", located in the dam core).

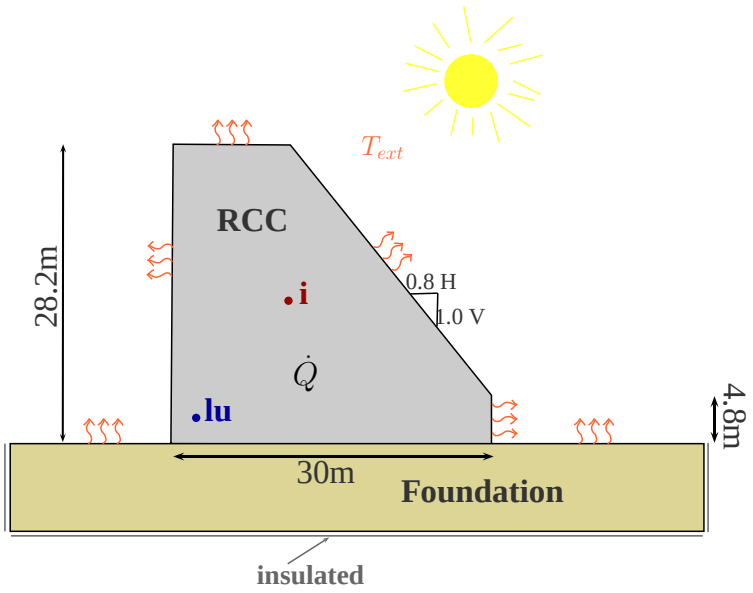

Figure 4.1: Dam model scheme

Regarding the environmental conditions, two evolutions are used in this study to represent the annual and daily sinusoidal ambient temperature variation. The first one, given by equation 4.11 is here denominated "S1" and "W1" whether the dam construction begins in summer or winter, respectively. Equation 4.12 gives the second one, which is denominated "S2" and "W2", following the same logic. The four adopted external thermal loads are represented in Figure 4.2.

In equations 4.11 and 4.12, T_m[°C] and $T_{d,m}$[°C] are the mean annual and daily temperature, ΔT_y[°C] and ΔT_d[°C] are the annual and daily temperature amplitudes, ϕ_y[rad] and ϕ_d[rad] are

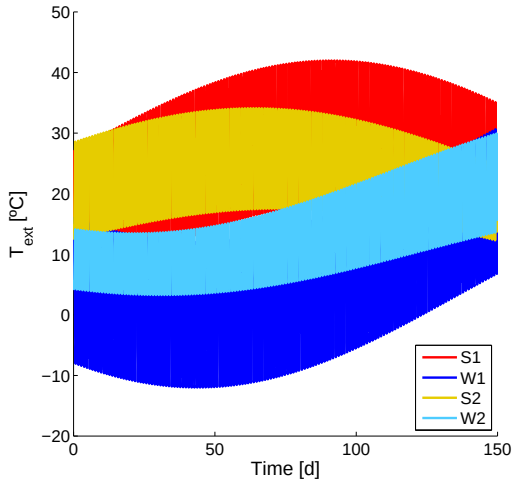

Figure 4.2: Ambient temperature S1, W1, S2, W2

the annual and daily phases, P[d] is the period and $T_d(t)$[°C] is the daily temperature variation given by equation 4.13. The adopted parameters are described in Table 4.1.

$$T_{ext}(t) = T_m + \Delta T_y \cdot \sin\left(2\pi \cdot f_y \cdot t + \phi_y\right) + \Delta T_d \cdot \sin\left(2\pi \cdot f_d \cdot t + \phi_d\right) \tag{4.11}$$

$$T_{ext}(t) = T_m - \Delta T_y \cdot \cos\frac{2\pi \cdot (t - \phi_y)}{P} - \frac{T_d(t)}{2} \cdot \cos\left(2\pi \cdot (t - \phi_d)\right) \tag{4.12}$$

$$T_d(t) = T_{d,m} - \Delta T_d \cdot \cos\frac{2\pi \cdot (t - \phi_{d,2})}{P} \tag{4.13}$$

Table 4.1: Parameters for ambient temperature evolution

	T_m[°C]	$T_{d,m}$[°C]	ΔT_y[°C]	ΔT_d[°C]	f_y[year^{-1}]
W1-S1	15	-	15	12	1
W2-S2	17.1	13.4	8.7	3.5	-
	$f_d[d^{-1}]$	ϕ_y[rad]	ϕ_d[rad]	$\phi_{d,2}$[rad]	$P[d]$
W1-S1	1	0	0.5	-	-
W2-S2	-	25.3[d]	0.125	1.4	365

Before entering into the study under different case scenarios, the following points should be stressed out:

- the properties coefficient of thermal expansion (α_T), compression (f_c) and tensile (f_t) strengths, Young's modulus (E), only begin to evolve when the hydration degree has reached a percolation threshold ξ_{set};

- for the adopted model, the hydration reaction has not yet been finished at the end of the

analysis, which means that the final resistances have not yet been reached at the end of the dam's construction;

- the model does not account for the material self-healing at early ages, and therefore all of the points on which the stress has reached the resistance developed so far, are considered to be cracked;
- the present model does not account for damage either, which means that even when cracking occurs, that does not interfere with the Young's modulus and stress state evolution. Therefore, stresses' redistribution is not modelled;
- the dam faces are mechanically free, meaning that formwork restrains are not accounted for. This point will be the object of a parametric study later in this chapter (section 4.3.2).

4.2 Study under different case scenarios

The different case scenarios adopted in this work are mainly related to aspects concerning the construction site of the dam. Due to some (uncontrolled) aspects related to the dam construction site, such as, for example, delays on the material supply or non-favorable meteorological conditions, the dam construction is often delayed and subjected to stops that were not foreseen. This accentuates the uncertainty related to some practical aspects of a dam construction site. The idea of this study is to observe the behaviour of the model response while, for example, the construction begins during summer or winter, or the construction speed is accelerated or reduced, in a deterministic manner.

The considered case scenarios are schematically represented in Figure 4.3 and concern the ambient temperature (Figure 4.3b), the casting temperature (Figure 4.3c) and the construction schedule (Figure 4.3d). Figure 4.3a represents the reference case, on which construction begins during winter "W1" (Figure 4.2), the casting temperature is equal to the ambient temperature at the instant of each layer posing, and the construction schedule corresponds to constructing 0.6m per day continuously ("cc0" in Figure 4.4).

All of the four adopted ambient temperature evolutions are represented in Figure 4.2. In Figure 4.4 are depicted all of the four construction schedules applied in the present chapter. Please note that in Figure 4.4, "construction step" corresponds to each casted layer of 0.6m height and that "time" is the time that has passed since the beginning of the dam construction.

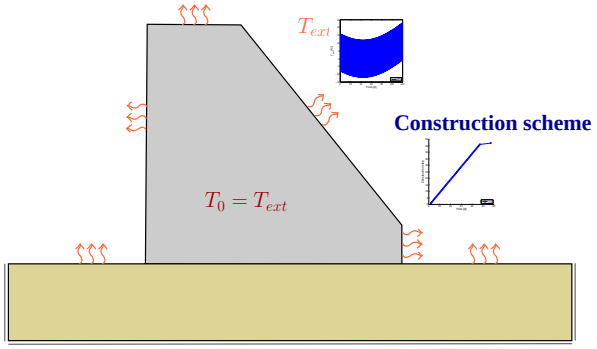

(a) Reference/default case

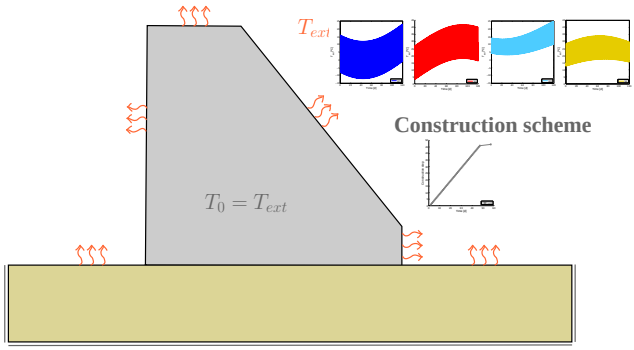

(b) Ambient temperature T_{ext}

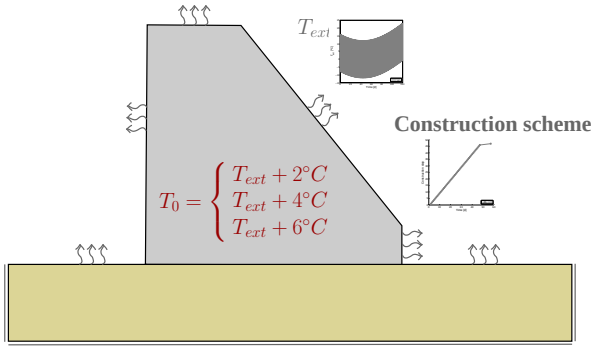

(c) Casting temperature T_0

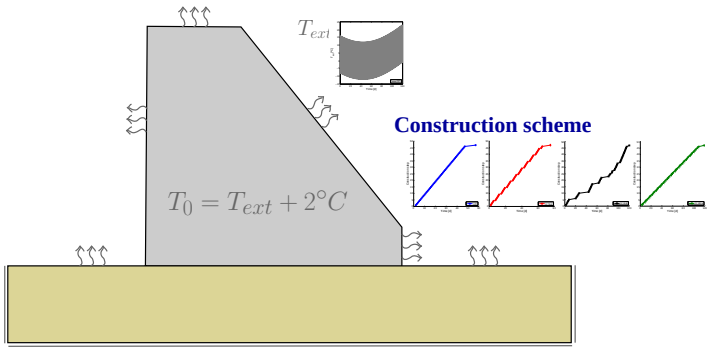

(d) Construction schedule

Figure 4.3: Different adopted case scenarios

To each construction step corresponds the final time of each layer construction simulation and the casting instant of the next layer. For example, for construction step/layer #6, and con-

struction scheme “cc real”, its construction occurred approximately 8 days after the beginning of the dam’s construction and any layer was further casted until 20 days.

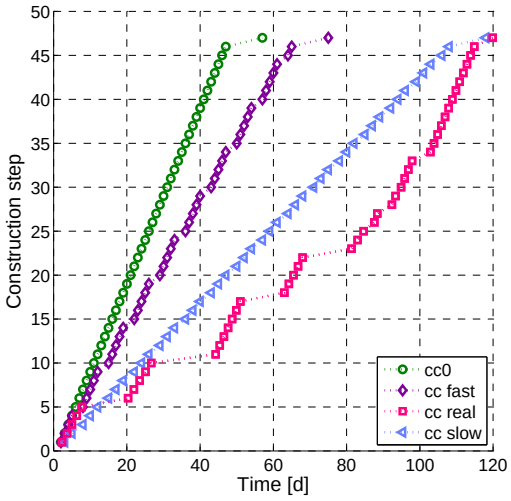

Figure 4.4: Construction schedules adopted for different case scenarios

The hydration and mechanical model parameters (Table 5.2) correspond to a typical RCC and are based on both the work of Leitão et al. (2007) (hydration model) and of Cervera et al. (2000b) (mechanical model). The respective chemical affinity and the compressive strength evolution obtained for isothermal tests at 5, 20 and 40°C are displayed in Figure 5.2.

Table 4.2: Model parameters

Hydration	$\frac{E_a}{R}$[K]	$\frac{k_\xi}{\eta_{\xi_0}}[s^{-1}]$	$\frac{A_{\xi_0}}{k_\xi}$	$\overline{\eta}$	ξ_∞	–
model	5000	2500	0.005	8.1	0.779	–
Viscoelastic	$E^1 : E^2$	τ_2[h]	ν	E_∞[GPa]	$f_{c,\infty}$[MPa]	$f_{t,\infty}$[MPa]
model	3:1	1	0.2	25	40	4
Mechanical	A_f	B_f	n_T	ξ_{set}	–	–
coupling	3.0	0.1	0.12	0.3	–	–
General	$\rho[\frac{kg}{m^3}]$	$c[\frac{J}{kg \cdot K}]$	$q_c[\frac{kJ}{kg}]$	$k[\frac{W}{m \cdot °C}]$	$h[\frac{W}{m^2 \cdot °C}]$	$\alpha_T[\frac{1}{°C}]$
parameters	2400	921	284	2.3	27	$0.6 \cdot 10^{-5}$

While each case scenario is studied, all of the other model parameters remain defined as the “default case scenario” ones given in Table 4.3. An exception is made for the case scenario about the construction schedule, where the casting temperature is taken equal to $T_0 = T_{ext} + 2°C$.

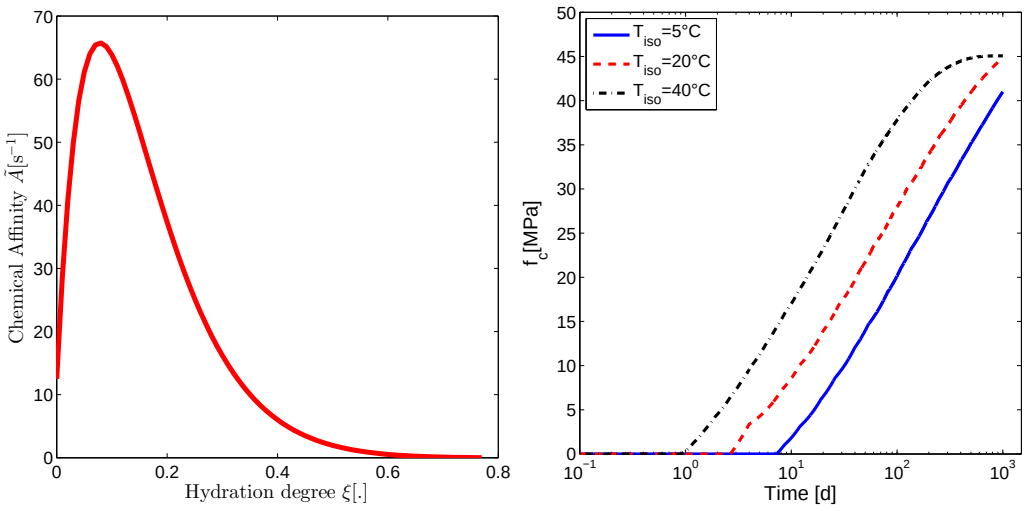

(a) (b)

Figure 4.5: a) Chemical affinity; b) Compressive strength evolution during isothermal tests, using parameters of Table 5.2

4.2.1 Default case scenario

First of all, the presented methodology is applied to the default case scenario. The results on both points "lu" and "i" are plotted in Figure 4.6. Before entering into the results' analysis, it shall be pointed out here that, in this chapter, all of the analyzed results are functions of the time of construction (or construction step for cracking density results), and not functions of the material age. This is due to the fact that, while comparing results of case scenarios using different construction schemes, it is of easier interpretation if the analysis is made as function of the "real" time.

In Figure 4.6a is plotted the temperature evolution on both points "lu" and "i". It may be noticed that the casting temperature is not the same on both points. This is because the casting temperature T_0 is equal to the ambient temperature at the instant of casting. Since the ambient temperature evolves sinusoidally over the day and the year, the casting temperature of each casted layer is different from one another.

In Figure 4.6b are plotted the thermal deformations on both analyzed points. Notice that the thermal deformation only begins to evolve when the hydration degree ξ has passed the

Table 4.3: Default case scenario

	T_{ext}	T_0	Const. scheme
"Default"	W1	$T_{ext}(t = t_0)$	cc0

threshold value of $\xi_{set} = 0.3$ (for more details please refer to chapter 3). The positive rates of the thermal deformation indicate that the material is expanding, meaning that point "i" is expanding during all of the construction, and that point "lu" is expanding until approximately 15 days after the beginning of the construction (approximately 10 days of age) and begins retracting afterwards (when the temperature begins to decrease, such as depicted in Figure 4.6a).

In Figures 4.6c and 4.6d are plotted the evolutions of the hydration and ageing degrees, respectively, that correspond to the given chemical affinity function. It may be noticed that the final hydration degree, $\xi_\infty = 0.779$ has not yet been reached at the end of the construction. This means that the hydration reaction has not finished yet and that the mechanical properties have not yet attained their final values.

In Figures 4.6e and 4.6f are plotted the first and second principal stresses' evolutions, as well as the compressive and tensile strengths' evolutions. The results are compared with the resistances' evolution, so that when the stress is greater than the developed resistance, the material is considered to be cracked (or crushed, under compression). Therefore, applying the cracking index concept, when the first principal stress is greater than the developed tensile strength, the cracking index $I_f = f_t/\sigma_1$ is lower than 1.0 and the material is considered to be cracked. In the present work, it is decided to fix an ultimate limit state for the cracking index at $I_f = 0.75$, above which only microcracking may occur. For more details about the cracking index please report to chapter 3. Please notice that tension is positive and compression is negative in the present work. It shall also be stressed once more that the present model does not account for damage, which means that even when crack occurs, that does not interfere with the Young's modulus and stress state. The computation will move forward since the model is formulated within the non-linear viscoelasticity domain.

Basically, point "lu" is under compression until approximately 35 days after the beginning of the construction, where tension stresses appear. The stress rate is greater than the resistance rate after a certain point, however point "lu" does not cracks (Figure 4.6e) because tensile strength is always greater than the tensile stress, for the period under analysis in this case. Point "i", on the other hand, is under tension since its construction but does not crack during the period under analysis. This means that the adopted ageing degree evolution is sufficient to guarantee that the material does not cracks at early ages. At some point in time those early age stresses will begin to decrease (around 35 days for point "i" in Figure 4.6e). Under compression (Figure 4.6f) it is observed that both points do not crush, since the compressive strength f_c is

greater than the second principal stress σ_2.

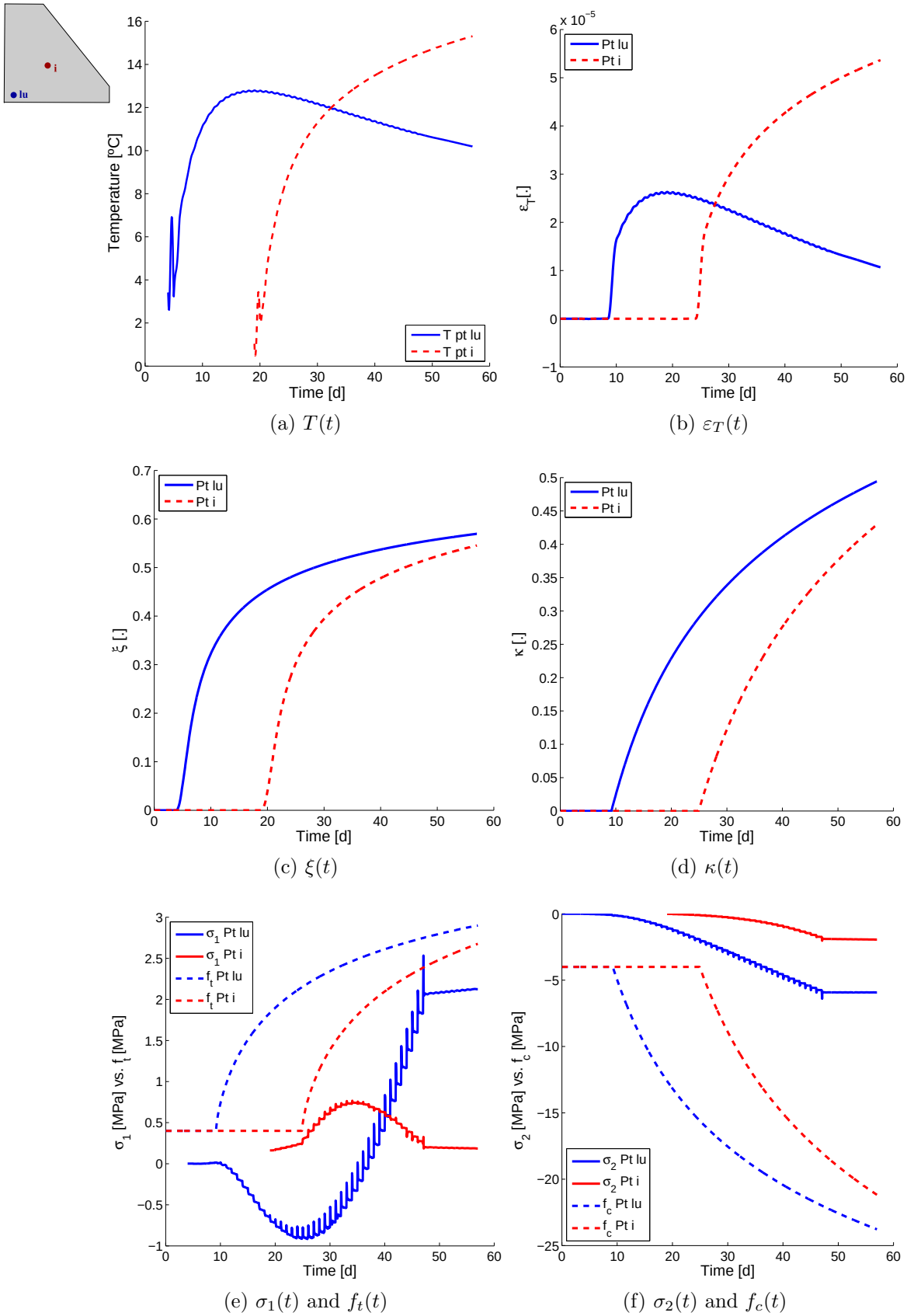

(a) $T(t)$ (b) $\varepsilon_T(t)$

(c) $\xi(t)$ (d) $\kappa(t)$

(e) $\sigma_1(t)$ and $f_t(t)$ (f) $\sigma_2(t)$ and $f_c(t)$

Figure 4.6: Results for the default case scenario

Even if both of the analyzed points do not crack, the same may not occur for other points located on the same layer but near its surface, which are subjected to greater temperature gradients leading to greater thermal deformations. Those points may crack at early ages and later in time the stress rate eventually changes (just like in point "i" after approximately 35 days). This early age cracking could eventually "heal" during that period. Nowadays, there are models that allow the account for that early age healing which is due to the ongoing chemical hydration and formation of hydrates that will fill the micro fissuration that occurs in concrete at those early ages (Lackner and Mang, 2004). However, self-healing is not considered in the present model and therefore, for the purpose of the present work, the material is considered to be cracked from the moment that the stress overlaps/exceeds the resistance developed so far.

This fact is important to understand the cracking density evolution. As it was previously explained in chapter 3, the cracking density is evaluated within each layer. The cracking density's main objective is to assess the cracking extent on each casted layer and may vary from 0 (no cracking), to 1 (the layer is completely cracked). Its assessment comes purely from the post-treatment of the cracking indexes results obtained through the thermo-chemo-mechanical model. Basically, a secondary mesh is defined over each casted layer, and then the number of points on which the cracking index has attained a certain limit ($I_f = 0.75$ for the ultimate limit) is divided by the total number of points, giving a measure of the cracking extent: the cracking density. For more details please refer to chapter 3.

In Figure 4.7a is plotted the cracking index contour at the end of construction.

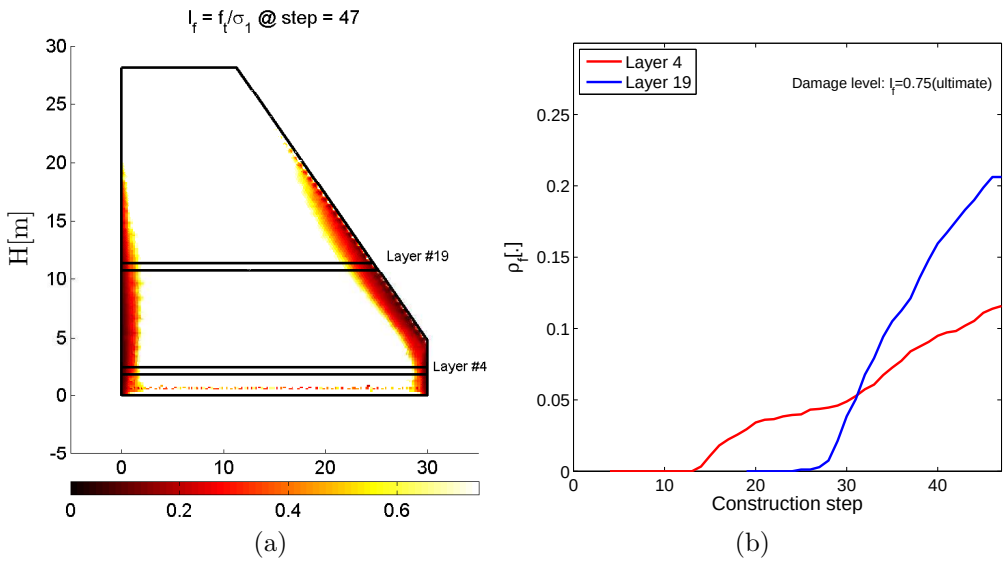

Figure 4.7: Cracking at the end of the construction, reference case: a) Cracking index; b) Cracking density.

It is considered here the ultimate damage level ($I_f = f_t/\sigma_1 = 0.75$), which means that all of the points that present $I_f \geq 0.75$ are considered to be "safe" (i.e. not cracked). In Figure 4.7b are plotted the cracking densities evolutions on layers #4 and #19 (layers where points "lu" and "i" are located, respectively, and that are represented within black lines in Figure 4.7a).

It can be concluded from Figure 4.7b that layers #4 and #19 will be cracked at approximately 10 and 20% of their area, respectively, at the end of the dam construction, for the default case scenario.

It shall be stressed here that the cracking density's evaluation does not account for the cracking index value attained at each point. Meaning that for $\rho_f > 0$, all of the points that present I_f lower than the adopted damage limit (e.g. $I_f < 0.75$ for ultimate damage limit) are considered to be cracked. The "crack level" (that goes from $I_f = 0$ to $I_f = 0.75$) is not accounted for.

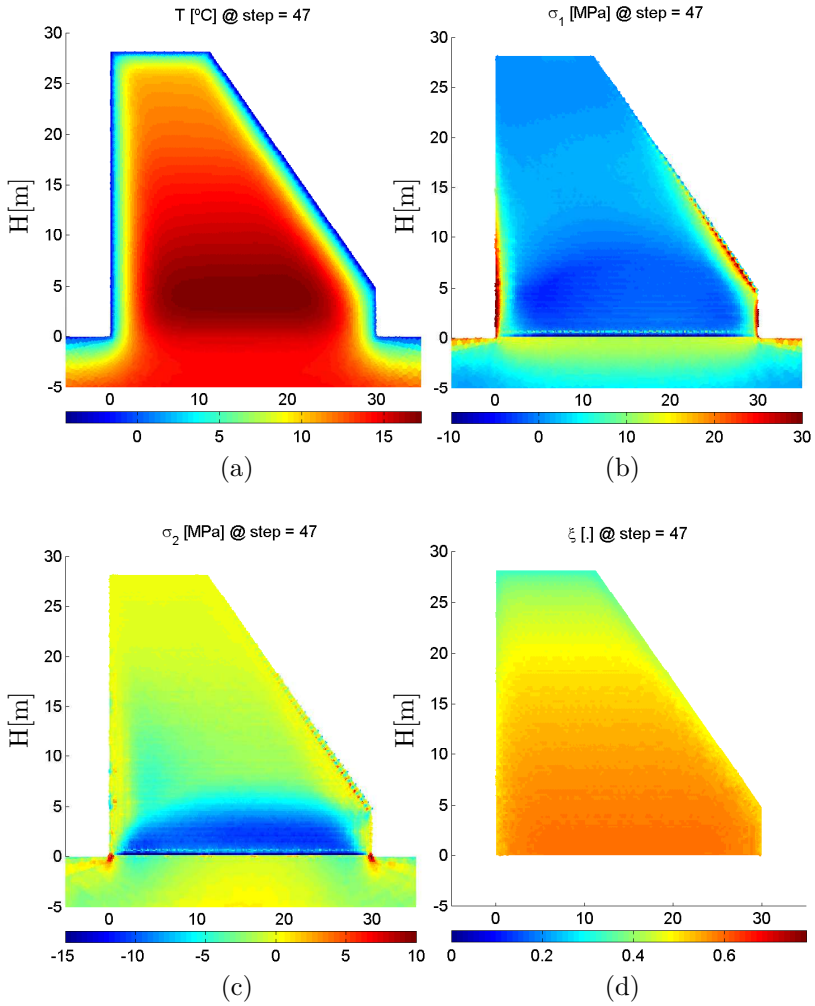

Figure 4.8: Results' contours at the end of the construction: a) Temperature; b) First principal stress; c) Second principal stress; d) Hydration degree.

In Figure 4.8 are plotted the contours of temperature, first and second principal stresses, and the hydration degree at the end of construction, for the reference case. For the considered ambient temperature evolution, at some point, temperature goes down to negative values close to the dam surface, which is why there may be negative temperatures on the dam faces. In the center of the dam, the temperature may grow up to 20°C during the construction period, and further if the analysis went longer in time (this is because, as it is clear in Figure 4.6c, $\xi < \xi_\infty$ and the hydration reaction is not finished yet). From Figures 4.8b and 4.8c it may be concluded that lower (and older) layers are mostly under compression, the dam surfaces being subjected to higher tensile stresses. This explains why the cracking indices (Figure 4.7a) are located near the dam up and downstream faces. On the upper (younger) layers, the hydration degree is lower and, consequently, the mechanical resistances will also be smaller. But since the stress state is lower than the resistance developed so far, cracking does not occur (Figure 4.7a).

4.2.2 Ambient temperature case scenarios

This first study consists of considering four different ambient temperature evolutions (Figure 4.2): two different daily and annual amplitudes are chosen (defined as pairs S1-W1 and S2-W2); the construction begins for each one of those pairs, either during summer (S1 and S2) or winter (W1 and W2). Details about the four adopted daily and annual sinusoidal evolutions of the ambient temperature may be found at the beginning of this chapter (section 4.1).

In Figure 4.9 are plotted the temperature contours inside the dam, at the end of construction, concerning the four applied ambient temperatures. The impact of lower ambient temperatures during winter is evident (Figures 4.9a and 4.9c). It can be noticed that there is a significant difference between results obtained for W1 and W2, even if both concern winter season. Actually, W2 is a much "softer" winter than W1, with temperatures that do not go under 0 (Figure 4.2). Also, the daily ΔT_d and annual ΔT_y is smaller for W2 than for W1 (and also for S2 than for S1) leading to lower temperature gradients.

For a construction that begins during the hot season (S1 and S2), the final temperatures are not as different as for the cold season, with a slight difference on the upper layers, that present greater temperature values for S1 than for S2.

The smoother daily ambient temperature oscillations (ΔT_d in equation 4.12) that are characteristic of W2 and S2 lead to a greater temperature evolution inside each casted layer, while

the higher daily temperature oscillations of W1 and S1 represent a bigger obstacle to the temperature evolution inside each layer (also verified in Figure 4.10a). Therefore, the thermal deformations and stresses will be lower for pair W1-S1 than for W2-S2, however always greater for a construction during the hot season.

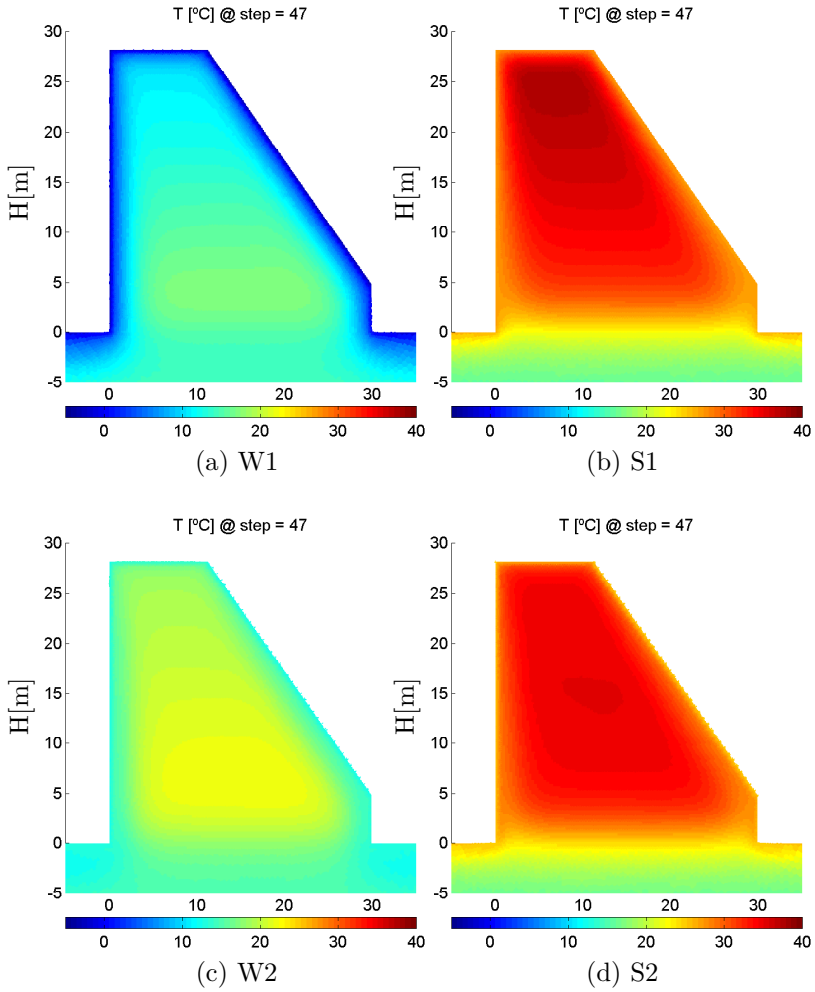

Figure 4.9: Temperature contours at the end of construction

In Figure 4.10a are plotted the temperature evolutions on both points "lu" and "i" for the four different ambient temperatures adopted. Note that is plotted ΔT, meaning that the plotted temperature is normalized over the casting temperature T_0 (which is different for each case). The different external thermal loads lead to different stress states inside the dam. In general, constructing during winter leads to lower stress states, which can be verified in Figure 4.11, namely near the dam faces. It shall be enhanced here that, because stresses' redistribution due to cracking is not modelled in the present work, high localized values for the first principal stresses may appear in the dam faces. In a real case, such high stresses (on the order of 20 to 30MPa) will most likely do not occur.

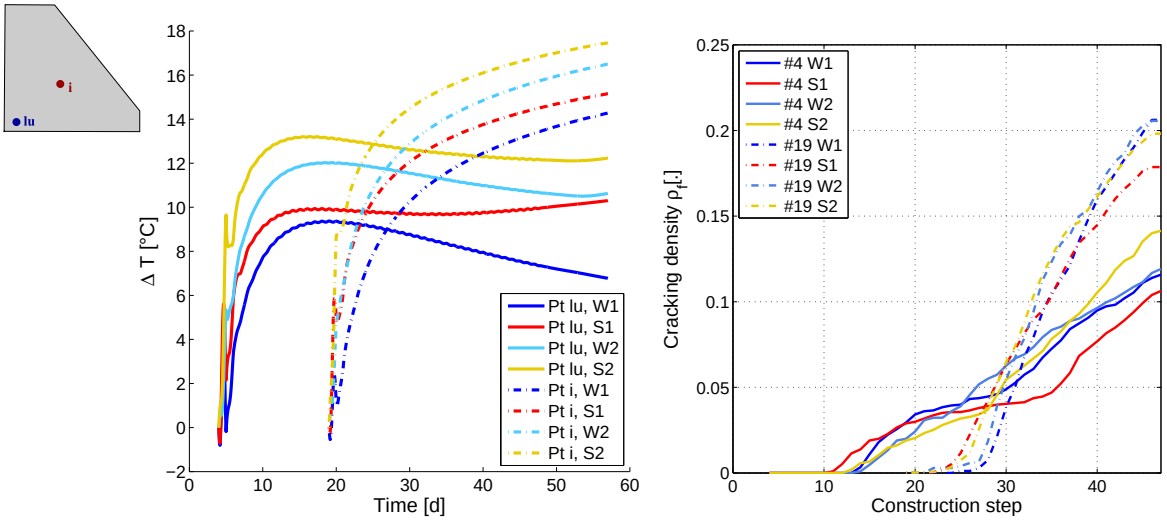

(a) (b)

Figure 4.10: T_{ext} influence: a) Temperature $\Delta T = T - T_0$; b) Cracking density.

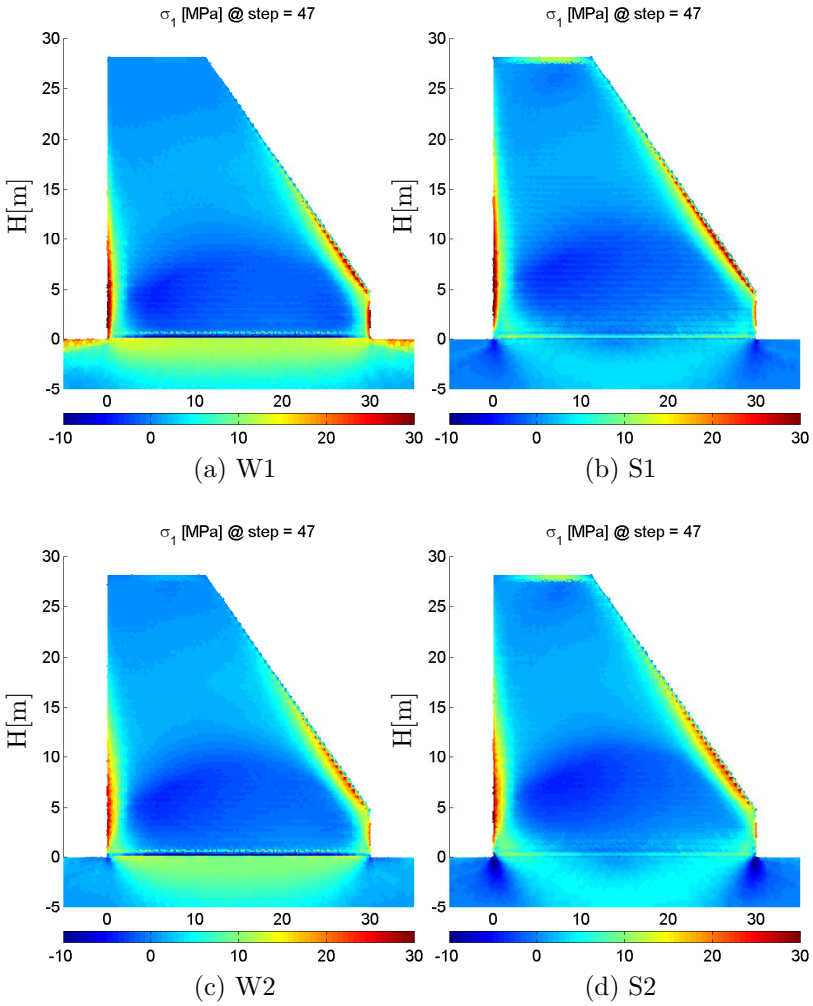

(a) W1 (b) S1

(c) W2 (d) S2

Figure 4.11: First principal stress contours at the end of construction

Regarding the cracking density evolution depicted in Figure 4.10b, it is concluded that on layer #4, the final value is greater for S2, attaining values of 0.14. However, for layer #19, the cracking density is greater for a construction during winter, attaining values of 0.21 for both W1 and W2. It shall be noticed that, on both analyzed layers, the cracking density at early ages, right after each layer has been casted, is bigger for a construction during the hot season. Actually, since the hydration reaction will evolve more rapidly during the hot season, the ξ_{set} threshold will be attained earlier, meaning that both thermal stresses and mechanical resistances will evolve earlier than during winter. This is evidenced in Figure 4.10b, where the cracking density ρ_f begins to evolve earlier during summer on both layers. These results enhance the fact that during the hot season attention shall be paid to the temperature gradients that occur in each layer during construction and eventually apply cooling techniques. While during winter the cracking density attained on both layers is very similar, there is a difference of 0.03 between S1 and S2 on layer #4 and of 0.02 on layer #19, which evidences the effect of the ambient temperature evolution.

According to the previous results, it can be concluded that: the thermo-chemo-mechanical behaviour of the dam during construction not only depends on whether the construction has begun during winter or summer, but also on the adopted sinusoidal daily and yearly evolution for the ambient temperature. It was shown that different daily temperature oscillations of the ambient temperature may lead to significant differences on cracking extent on each casted layer, measured by means of the cracking density concept.

4.2.3 Casting temperature case scenarios

For the case scenarios about the casting temperature, four situations are considered: $T_0 = T_{ext}(t = t_0)$, t_0 being the instant of casting; $T_0 = T_{ext}(t = t_0) + 2°\text{C}$; $T_0 = T_{ext}(t = t_0) + 4°\text{C}$ and $T_0 = T_{ext}(t = t_0) + 6°\text{C}$. Even if the differences on temperature evolution on both analyzed points are evident (Figure 4.12a), the adopted variations on the casting temperature do not lead to significant differences on the obtained cracking density on both layers #4 and #19 (Figure 4.12b), exception made for $T_0 = T_{ext}(t = t_0)$.

There is an increase of approximately 0.05 on the cracking density of layer #19 while increasing the casting temperature from $T_0 = T_{ext}(t = t_0)$ to $T_0 = T_{ext}(t = t_0) + 2°\text{C}$. Then, increasing the casting temperature leads to a slight increase of the cracking density. From now on, it was decided to adopt a casting temperature $T_0 = T_{ext}(t = t_0) + 2°\text{C}$, the 2°C being

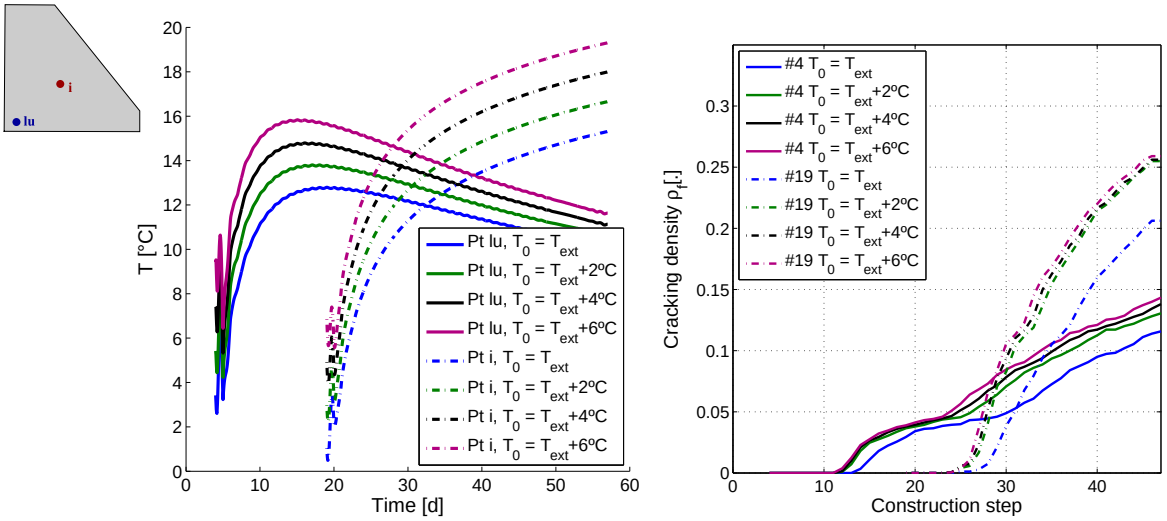

(a) (b)

Figure 4.12: T_0 influence: a) Temperature; b) Cracking density.

interpreted here as a sort of heating during the material mixing and transportation.

4.2.4 Construction schedule case scenarios

Four different scenarios for the construction schedule are adopted:

- the first one, "cc 0", applied on the reference case, consists of constructing 2 layers of 0.3m per day ($v = 0.6$m/day), without stops;
- the second one, "cc fast", uses the same rate of 0.6m per day but stops during 3 days at the end of each 5-day period;
- the third one, "cc real", inspired from a real case, uses the same rate of the two previous ones but the stops are not regular during all of the construction;
- the fourth one, "cc slow", adopts a construction rate of one layer per day (or one layer per periods of 2 days $v = 0.6$m/2day) and stops during 10 days at the end of each 5 day period.

In all of the four cases, the ambient temperature corresponds to W1 of Figure 4.2. The casting temperature is equal to $T_0 = T_{ext} + 2°$C.

In Figure 4.13a are plotted the temperature evolutions on both points "lu" and "i" for the four applied construction schemes. As expected, point "lu" is more affected by the ambient temperature than point "i".

Here, even if the ambient temperature evolution is the same, changes in the construction scheme lead to differences on the time of exposure of each layer. This is evident on point "lu", which presents almost the same temperature evolution at the beginning for "cc0", "cc fast" and "cc real", which adopt the same construction rate for lower layers. However, for "cc slow", each 0.6m thick layer is exposed during 48h, meaning that the area closer to the surface is more influenced by the ambient temperature evolution, which is characterized by low temperatures, consisting of an obstacle to temperature evolution inside the material. This explains why temperature on point "lu" does not increases right after the layer posing for "cc slow" as it happens for the other construction schedules. Moreover, around 80 days, temperature on point "lu" begins to increase (for "cc slow" and "cc real"). This can be explained by the increasing mean ambient temperature around that time of the year for W1 (Figure 4.2).

On point "i", at the center of the dam body, the differences in temperature are not as significative as on point "lu". Still, because of the longer stops, for the slower construction schemes "cc real" and "cc slow", lower temperatures are attained at the same age, when compared with "cc 0" and "cc fast".

The influence of the construction schedule on the obtained cracking density on each analyzed layer is plotted in Figure 4.13d. Basically, the difference obtained for cracking density on both layers for "cc0", "cc fast" and "cc slow" is not very significant, when compared with ρ_f for "cc real". The great difference arises when the "cc real" case is adopted, attaining values that are 4 times greater for layer #4 and 2.6 times greater for layer #19 than for the other construction schedules. The reason why there are such "jumps" on the cracking density for "cc real" is due to the time delay that occurs when the construction is stopped. During that time, the layer surface is exposed to the weather conditions (winter in this case). As a consequence, the temperature gradients that occur are greater than if the construction had continued such as for "cc0", "cc fast" or "cc slow". Therefore, thermal tensile stresses are produced and by overlapping the tensile strength attained so far, cracking occurs.

In order to further understand what happens, layer #19 will be analyzed in more detail for both "cc slow" and "cc real". It shall be noticed here that both of these construction schedules end at the same time of the year, meaning that the construction of the dam takes place during the same period, however with different stops and time delays between them.

In Figure 4.14 are plotted the cracking density evolution during construction for layer #19 as well as the construction scheme, "cc slow" in Figure 4.14a and "cc real" in Figure 4.14b. For

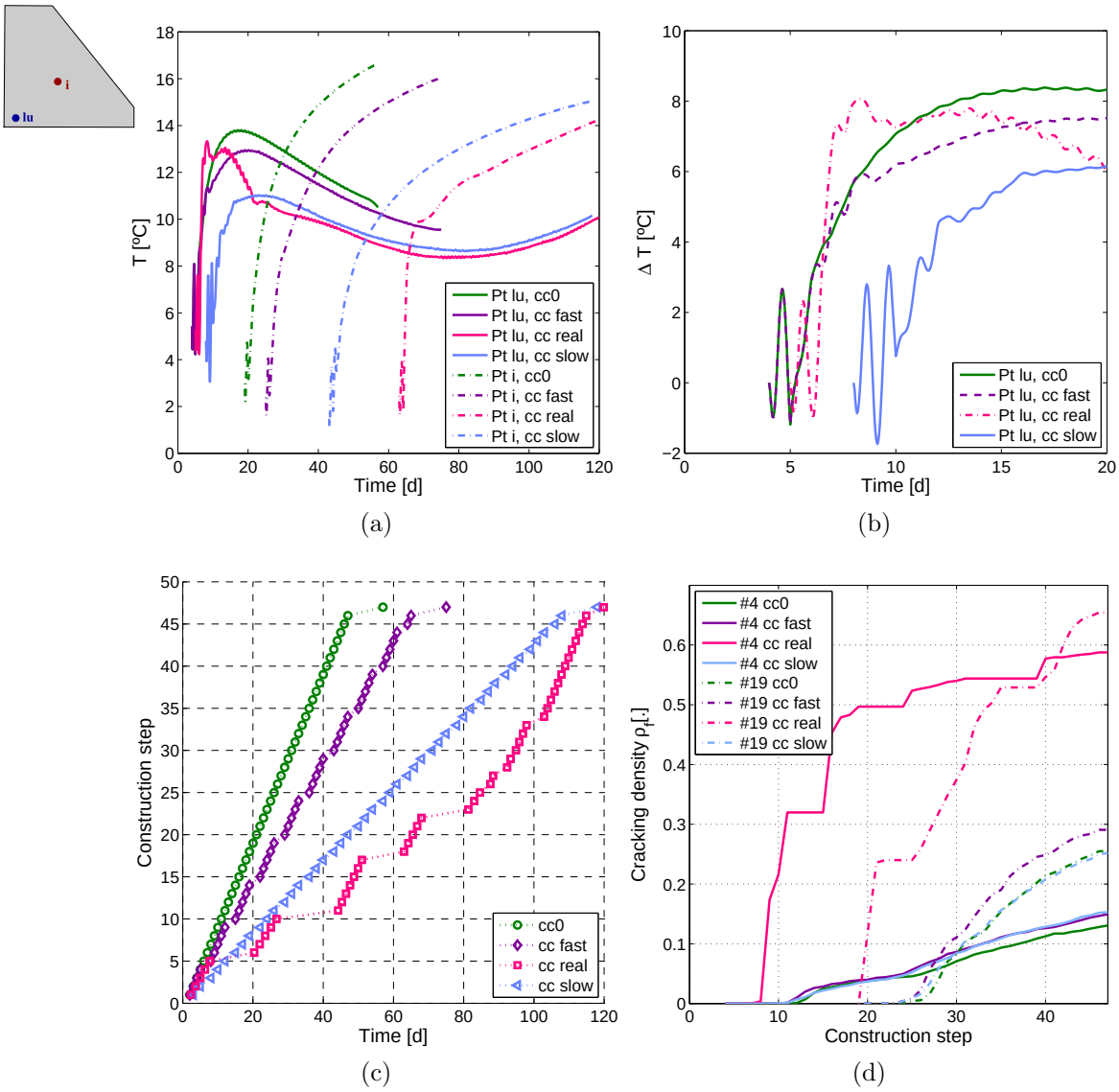

Figure 4.13: Influence of the construction schedule: a) Temperature; b) ΔT, detail on "point lu"; c) Construction schedules; d) Cracking density.

both of these cases, the only difference is that the time of exposure of casted layers is much more variable for "cc real" than for "cc slow". This is the first reason why cracking densities obtained for the same layer are more than the double for "cc real" at the end of the construction.

Actually, if we analyse the first principal stress and the cracking index contours on layer #19 for "cc slow" and "cc real" such as in Figure 4.15 at construction step 36, it may be noticed that for "cc real" the results are less smoother. It can also be noticed that for "cc real" the lateral cracked zones go more deeply into the layer. Also, the bottom part of layer #19 presents cracking indices of 0.5 to 0.6 (please recall that for ρ_f, these areas are considered to be cracked, independently of their cracking index value). This happens because the time of exposure of the precedent layer #18 is too big, meaning that there is a contrast on the thermo-chemo-

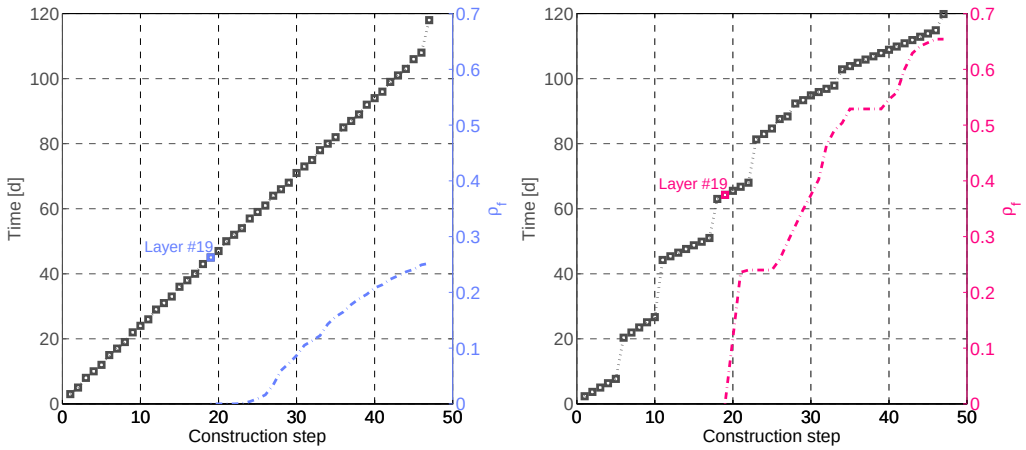

Figure 4.14: Cracking density on layer #19 for two of the applied construction schemes: a) "cc slow"; b) "cc real".

mechanical properties at the interface of these two layers, leading to greater tensile stresses and consequently cracking indices. Please recall that each construction step on Figure 4.14 is plotted as a function of its final time of construction, and not of its casting instant. Layer's #18 top surface may be a cold joint and should therefore be treated. This will be further discussed in the following paragraphs.

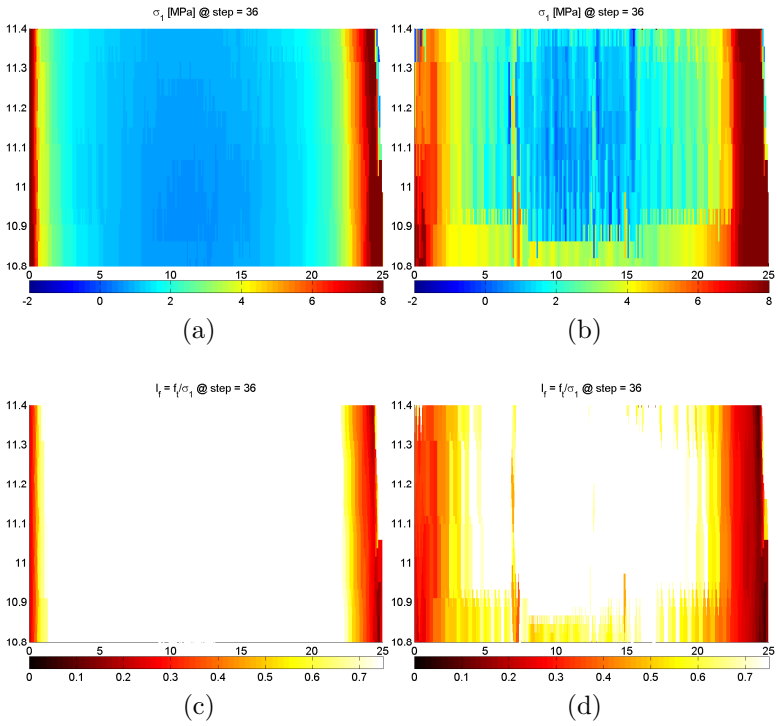

Figure 4.15: Results contours on layer #19 at construction step 36: a) σ_1 contour for "cc slow"; b) σ_1 contour for "cc real"; c) I_f contour for "cc slow"; d) I_f contour for "cc real".

The joint maturity index (JMI) (BaCaRa, 1996; ACI Committee 207, 1999; Bettencourt Ribeiro et al., 2001) may be applied here in order to support the results obtained with this parametric study. As previously explained in section 2.4, the JMI is a measure of the lift joint quality, usually given by $JMI = AST \cdot TE$, where AST is the average surface temperature and TE the time of exposure. For greater times of exposure, JMI will increase. In the present work, the average surface temperature AST is taken as being equal to the casting temperature. This approach is valid only because we are leading here with the same material and therefore, the heat generated will be the same for all of the cases. Still, this approach enables the account for the influence of the casting temperature and, consequently, of the ambient temperature (reminder: $T_0 = T_{ext} + 2°\text{C}$).

In Figure 4.16 is plotted the JMI evolution during construction, each point corresponding to the JMI of each casted layer/construction step. As it may be concluded by comparing JMI of "cc slow" with JMI of "cc real", not only the values of the latter are greater, exception made after construction step 30, but also the JMI changes abruptly from one layer to the next one. The negative values indicate that RCC is being casted at temperatures below zero, which is not at all convenient, but is here the consequence of the casting temperature hypothesis $T_0 = T_{ext}(t = t_0) + 2°C$, while T_{ext} corresponds to W1 and negative ambient temperatures occur. Those negative casting temperature, associated with a big time of exposure, lead to tensile stresses and consequent cracking, which can explain the evolution of the cracking density presented in Figure 4.13d.

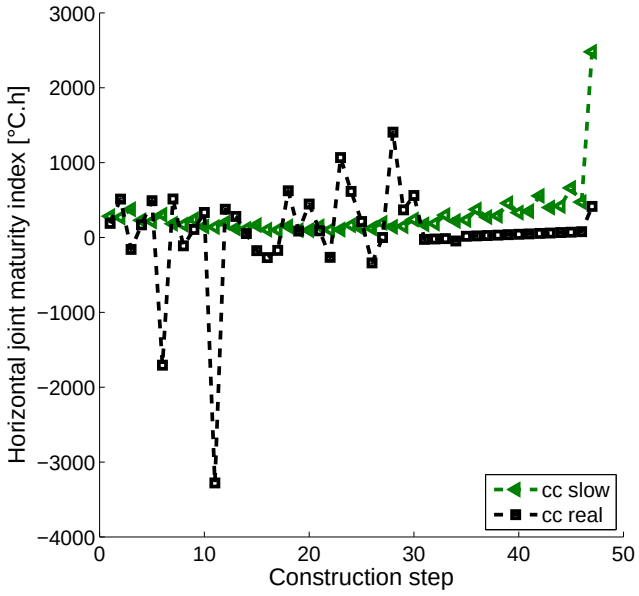

Figure 4.16: Joint maturity index (JMI) evaluated for "cc slow" and "cc real" for each casted layer

Two solutions could be adopted in this case in order to minimize cracking: first of all, cold joints should be treated, measures should be undertaken in order to avoid its contamination and to assure that the best conditions possible are guaranteed when the subsequent layer is casted (either by simply protecting them from the adverse weather conditions, or by removing the surface of the layer before constructing the next one, adding a bedding mortar to guarantee a good joint quality); second of all, negative casting temperatures should be avoided and therefore, either the layer is casted during a time of the day when temperatures are above zero, or the construction schedule shall be delayed until better weather conditions occur (i.e. spring season).

Still, these conclusions shall be seen within the framework of the performed numerical model. There are some hypothesis taken in the present work that, even if they were made based on the available literature, may be object of uncertainties, being too much conservative, or even not realistic at all. For example, the adopted convection coefficient is the same all along the dam construction for all of the dam lateral faces, which may not be realistic if cold joints treatment takes place or if formwork is applied on the dam faces. This means that maybe a different convection coefficient should be adopted for layers that have been exposed over a certain time period (or for layers that overlap a certain JMI level). Another aspect concerns the casting temperature, here adopted as being equal to the ambient temperature at the time of the layer posing, added by (only) 2°C, which may not be sufficiently realistic, allied to a certain construction scheme and ambient temperature, to describe the real casting temperature.

It is concluded with this study that the time delay that occurs between successive layers casting may lead to a decrease of the lift joints quality (characterized by greater JMI values), and an increase, often abrupt, of the cracking density. In the analyzed construction scheme "cc real", periods of intense construction are intercalated with stop delays/times of exposure that can reach 18 days. This leads to stress contours that are less smother than the ones obtained for a more "regular" construction scheme, contributing to the increase of the cracking index and, consequently, of the cracking density. It shall therefore be enhanced here, once more, that the cracking density does not accounts for the level of cracking. This means that if the cracking index is lower than the acceptable damage level (here equal to 0.75), the cracking density concept will consider it to be cracked for good, not weighting the actual damage level.

The analysis of the joint maturity index JMI for the case study lead to the conclusion that the following parameters shall be object of more attention in the numerical model: the convection coefficient and the casting temperature. These parameters shall be adapted to each case study,

accounting for the ambient temperature evolution, the time instant of construction and the construction scheme/time of exposure of each layer. The JMI gives relevant information, being a very useful tool to support/limit some parameters' choice.

4.3 Discussion on other aspects

This section intends to proceed with the discussion initiated within the study performed over the construction schedule (section 4.2.4). Two aspects will be dealt with within this section: the heat convection coefficient (or the account for cold joints treatment) and the account for formwork (thermal and mechanical) restrains. These two aspects are not much dealt with within the available literature. Generally, a constant convection coefficient is adopted, even if it is well known that it changes during the construction period, mostly due to weather conditions and specially due to radiation. Also, formwork is not usually taken into account in the numerical analysis of RCC dams.

In the following subsections, two studies concerning the convection coefficient and formwork simulation are performed.

4.3.1 Cold joints treatment

For the present study, the adopted construction scheme is "cc real" (Figure 4.4) and the ambient temperature is "W1" (Figure 4.2), maintaining the casting temperature equal to $T_0 = T_{ext}(t = t_0) + 2°C$.

It has been discussed previously in this chapter (section 4.2.4) that cold joints treatment should be accounted for in the numerical simulation of an RCC dam construction. Here, a parametric study about the heat convection coefficient is performed in order to understand how it affects the cracking density evolution of a certain layer. It is believed that the adopted cold joints treatment should be accounted for on the choice of the convection coefficient in order to better model the heat flux exchange at the top of each casted layer.

In this study, it was decided to keep the initial value for the convection coefficient for most of the layers, only adopting a different value on those who are subjected to greater times of exposure, of which surfaces will be considered as "cold joints", and that will therefore be more likely to be object of cold joints treatment. The identification of those layers needing cold joints treatment is supported by the analysis of the ageing degree attained after the time of exposure

and the joint maturity index (JMI).

As it was previously exposed, cold joints treatment may consist of a variety of procedures: cleaning of the surface; protecting it from radiation by adding water; removal of a superficial layer in order to remove the segregated material and expose aggregates (increasing the surface's rugosity and improving the subsequent layer adherence); and finally adding a high paste bedding mix before casting the next layer (Hansen and Reinhardt, 1991; ACI Committee 207, 1999; Schrader, 2008). The application of one or all of these procedures depends on decisions made by the project team and may vary within a same dam project.

The choice of the layers on which a different heat convection coefficient will be adopted is based on whether or not each layer has passed the percolation threshold ξ_{set} (above which the material has begun to stiffen) or not. This is equivalent of searching for ageing degree values $\kappa > 0$ at the surface of each casted layer, such as plotted in Figure 4.17a. Based on the ageing degree values of Figure 4.17a, it may be concluded that only layers #6, #11, #18, #23 and #47 (red round points) have passed the hydration degree threshold ξ_{set} (for which $\kappa > 0$). Then, the joint maturity index (JMI) may be evaluated for each layer and a certain limit could be defined, supported by the hydration and ageing degree attained at each layer surface, for the case under study. In Figure 4.17b are plotted the JMI for each casted layer, corresponding the red squared points to layers #6, #11, #18, #23 and #47.

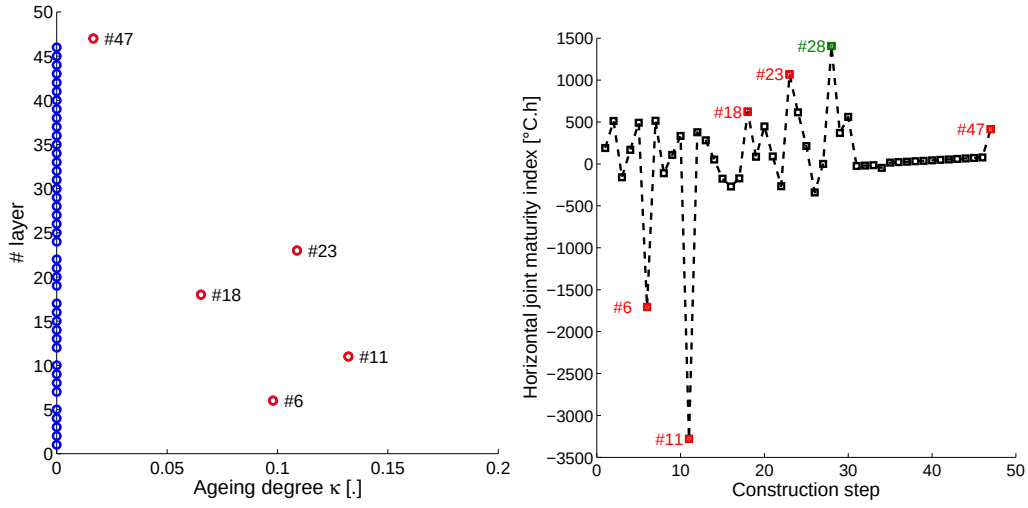

(a) (b)

Figure 4.17: Ageing degree and joint maturity index: a) Ageing degree for each layer after time of exposure; b) Joint maturity index.

As it may be observed, there are some layers characterized by high JMI levels, but on which

the hydration degree threshold ξ_{set} has not yet been reached. For example, layer/construction step #28 (green squared point in Figure 4.17b) presents a JMI$\approx$ 1500[°C·h] but $\kappa = 0$ after a time of exposure of approximately 4 days ("cc real" in Figure 4.4). This high JMI value may be related to the time of the day on which casting occurs and to the subsequent ambient temperature to which the material is subjected. If, for example, a layer is casted at the time of the day on which temperatures are the greatest, that layer will be characterized by a high JMI (if the AST temperature is the casting temperature, as it was adopted in the present work). However, that does not means that the time of exposure was sufficient to the hydration degree attaining ξ_{set} and therefore the ageing degree κ has not begun to evolve yet. This leads to the conclusion that, for the present case, relying only on the JMI values is not sufficient to decide whether or not cold joints treatment should take place.

However, attention shall still be paid to the hydration degree value at the surface of each casted layer. In Figure 4.18 are plotted the hydration degree contours at the end of the time of exposure for three distinct layers: #14 ($\kappa = 0$), #18 ($\kappa > 0$ and high JMI) and #28 ($\kappa = 0$ and high JMI). Each layer is limited in Figure 4.18 by horizontal black lines. These three layers may represent the three types of horizontal joints, defined in BaCaRa (1996): hot joint, in Figure 4.18a, on which RCC is still in a moist condition and as not yet begun to stiffen ($\xi < \xi_{set}$ and $\kappa = 0$); cold joint, in Figure 4.18b, on which the percolation threshold $\xi_{set} = 0.3$ has already been reached and RCC has stiffened; and warm joint, in Figure 4.18c, which is an intermediate state between hot and cold, usually very difficult to define. In this particular case, the surface of layer #28 being a warm joint, it could be decided that the hydration degree is sufficiently high to justify the need of joint treatment, even if $\kappa = 0$.

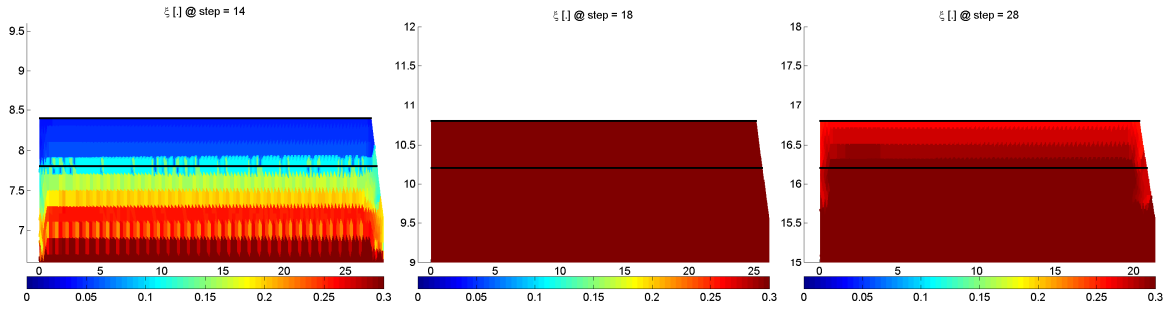

(a) Layer #14 (b) Layer #18 (c) Layer #28

Figure 4.18: Hydration degree contours after different times of exposure ($\xi_{set} = 0.3$)

Concluding, for the case under study, the decision of performing joint treatment or not should be supported not only by the joint maturity index (JMI), but also by the ageing and

hydration degrees occurring at the surface of each casted layer, after the time of exposure to which each one is subjected.

In the present work, it was firstly decided to reduce the heat convection coefficient of certain layers in order to account for an eventual protection from radiation. Therefore, in a first approach, only the radiation part h_r was ruled out from equation 4.14, and the adopted convection coefficient is of 22[W/(m^2·K)]. Then, it was decided to adopt a smaller value of almost the half of the initial one (13[W/(m^2·K)]). Several adopted values for the convection coefficient were found in the available literature and are placed within the range adopted in this study (i.e., $h = 19.3$[W/(m^2·K)] in Luna and Wu (2000), $h = 15$[W/(m^2·K)] in Malkawi et al. (2003), $h = 14$[W/(m^2·K)] in Calmon et al. (2003)). Finally, a more "dramatic" case is adopted, by insulating the layer surface, not accounting for heat exchanges with the environment, or by fixing the top layer temperature. This last hypothesis has been adopted in some works found in literature, such as in Jaafar et al. (2007) (insulated boundary) or in Cervera and García-Soriano (2002) (fixing the boundary temperature).

$$h = h_c + h_r \tag{4.14}$$

$$h_c = 0.055 \cdot \frac{k_f}{L} \cdot \left(\frac{L \cdot v_w \cdot \rho_f}{\mu_f} \right)^{0.75} \tag{4.15}$$

$$h_r = 5W/(m^2 \cdot K) \tag{4.16}$$

Given the discussion above, the parametric study about the heat convection coefficient adopted for the surface of casted layers is performed by adopting a different convection coefficient on layers #6, #11, #18, #23 and #47. For the sake of simplicity, these layers are going to be called "top layers" from now on.

In Figure 4.19 are plotted the cracking density evolutions on layers #4 and #19 using a constant convection coefficient of 27[W/(m^2·K)] against convection coefficients of 22 and 13[W/(m^2·K)] adopted on top layers (named h_{top} in Figure 4.19). It is concluded that on both layers #4 and #19, lower cracking densities are obtained when reducing the convection coefficient on top layers. On layer #4, even if the cracking densities exceed 0.1 of difference at some point, at the end of the construction that difference is not significant. On the other hand, for layer #19, reducing the convection coefficient of top layers lead to a significant reduction on the cracking density of approximately 0.15 at the end of the construction. On both analyzed layers, the difference observed between 22 and 13[W/(m^2·K)] is not significative.

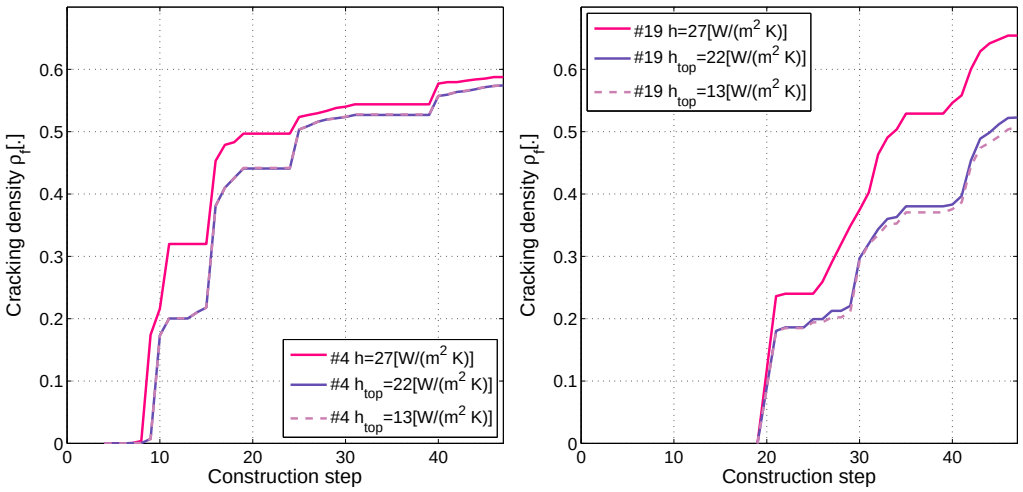

(a) Layer #4 (b) Layer #19

Figure 4.19: Cracking density on layers #4 and #19 for different heat convection coefficients on top layers

In Figure 4.20 are plotted the results of cracking density on both layers #4 and #19, comparing the reference case $h = 27[\mathrm{W/(m^2{\cdot}K)}]$ with the case on which the top layers are considered insulated. Again, for layer #4 the difference is not significative at the end of the construction. For layer #19, even if right after casting the cracking density is greater while insulating top layers (from construction step 20 to 30), at the end of construction the difference between the results exceeds 0.15.

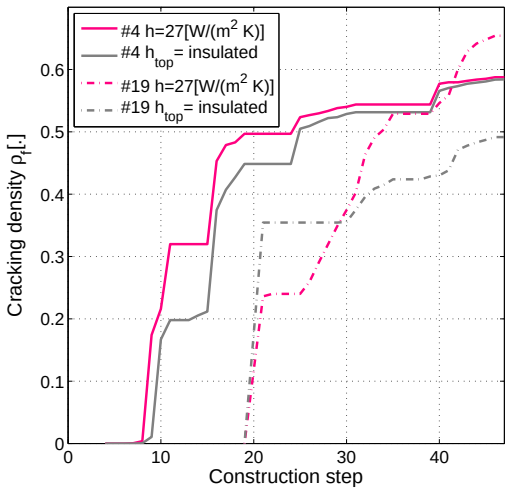

Figure 4.20: Cracking density on layers #4 and #19 adopting insulated top layer

Finally, in Figure 4.21 is considered the case in which a fixed constant temperature is given to the surface of the top layers. In the present study, that fixed temperature is equal to $T_{top} = T_{ext}(t = t_0) + 2°\mathrm{C}$, which is actually equal to the casting temperature. As it was

previously concluded on Figures 4.19 and 4.20, for layer #4 the difference obtained for the cracking density at the end of construction is not significant. For layer #19, however, this is the case on which a lower cracking density was observed, with a difference that attains slightly more than 0.25 at the end of construction.

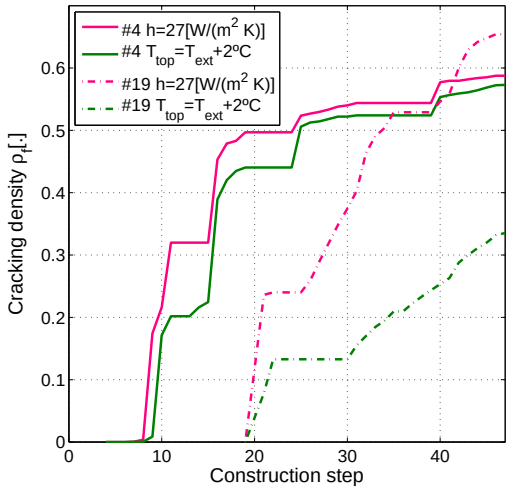

Figure 4.21: Cracking density on layers #4 and #19 adopting fixed temperature on top layer

4.3.2 Formwork simulation on lateral boundaries

In this subsection are discussed the results of a last parametric study, which consists of the lateral formwork simulation during the dam construction. Generally, in cases found in the available literature, formwork effects are not accounted for in the numerical simulation of RCC dam performances. However, formwork affects both thermally and mechanically the material behaviour and taking it into account may lead to a different stress state.

In a first approach, for this parametric study, the heat convection coefficient of each layer's lateral faces is changed in order to account for the insulation imposed by formwork. Then, lateral faces are blocked mechanically by imposing nil horizontal deformations. In a final computation, both effects are taken into account simultaneously.

In the present parametric study, the adopted construction scheme is "cc fast" (Figure 4.4) and the external ambient temperature is W1 (Figure 4.2).

In Figure 4.22 are plotted the cracking density's evolution for both layers #4 and #19 for all of the considered lateral convection coefficients. The results of Figure 4.22 lead to the conclusion that reducing the lateral heat convection coefficient will decrease the cracking density on both analyzed layers, layer #19 being much more affected than layer #4. On layer #19 there is a reduction of approximately 0.05 at the end of the construction. It shall however

be noticed that for all of the "new" tested lateral convection coefficients ($h_{lateral}$ = 19, 10 and 7[W/(m^2·K)], the cracking densities' evolutions are really close to one another, but still lower for lower heat convection coefficients. The phenomena that happens here was discussed in the previous section 4.2.4 while changing the heat convection coefficient applied on the top surface of certain layers. Basically, reducing the heat convection coefficient will limit heat exchanges with the environment, leading to lower thermal gradients and consequently lower thermal stresses. This is traduced by a lower cracking density, which will decrease with the decrease of the heat convection coefficient until a certain point because it will only have an influence on a limited region near the dam faces. One may note that the convection coefficient of each layer's top surface is maintained at its "default" value of 27[W/(m^2·K)].

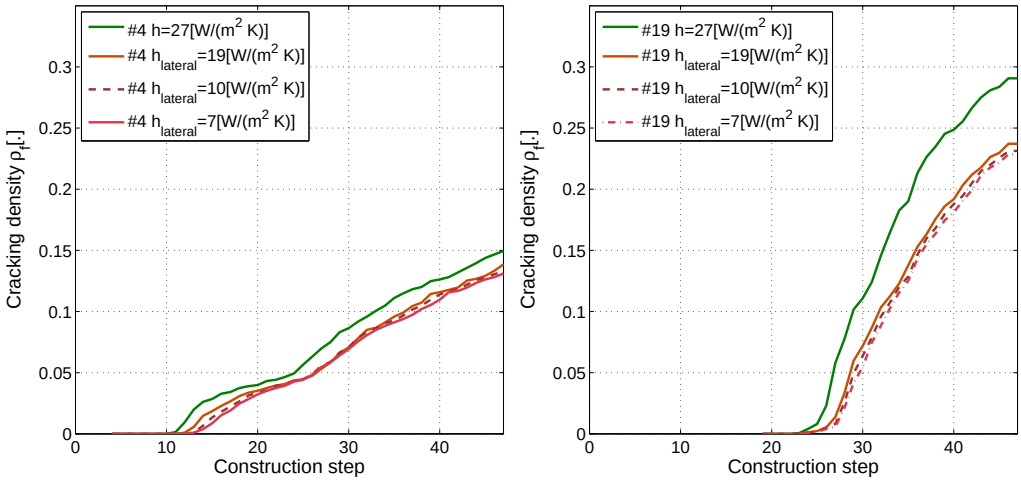

(a) (b)

Figure 4.22: Cracking density evolution on layers #4 and #19, influence of the lateral heat convection coefficient: a) Layer #4; b) Layer #19.

In Figure 4.23 are plotted the results of the cracking density evolution on layers #4 and #19 taking into account the mechanical lateral restrain on each casted layer. In the present study it was supposed that formwork is not removed during all of the dam construction. Therefore, each casted layer is maintained mechanically blocked on the horizontal direction. This will lead to an increase of the compression stresses, as it can be concluded by comparing Figures 4.24a with 4.24b, and Figures 4.25a with 4.25b.

The cracking density's evolution obtained in Figure 4.23a does not change much for layer #4 because this layer is already sufficiently close to the foundation and therefore already restrained by it. However, for layer #19 there is a reduction of approximately 0.18 on the final cracking density. The decrease on the tensile stress state leads here to a reduction on the cracking index,

and, consequently, on the cracking density. The same comparison is made while accounting for a lateral heat convection coefficient of 10[W/(m^2·K)] in Figure 4.23b. Comparing Figures 4.26a and 4.26b is clearly visible the reduction of the cracked areas while accounting for the lateral formwork thermal and mechanical restrain.

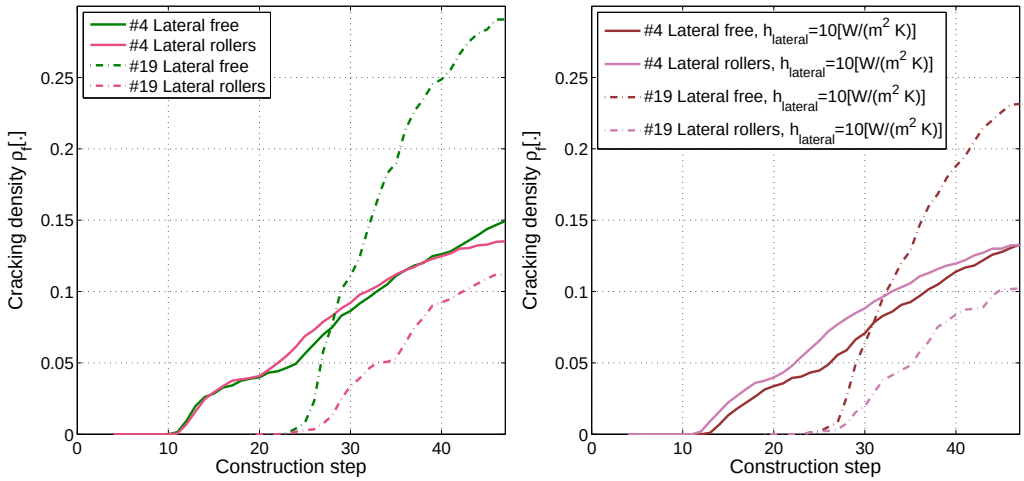

(a) (b)

Figure 4.23: Cracking density evolution on layers #4 and #19, influence of mechanically blocking lateral surfaces: a) Lateral rollers, $h_{\text{lateral}} = 27$; b) Lateral rollers, $h_{\text{lateral}} = 10$.

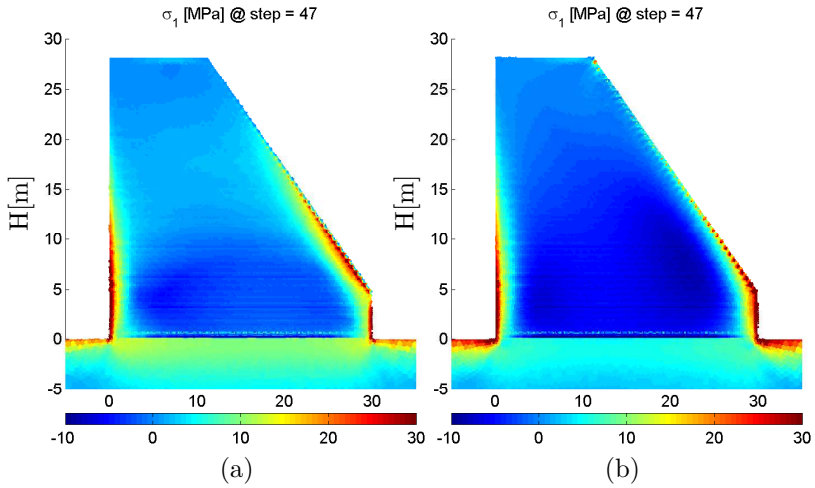

(a) (b)

Figure 4.24: First principal stress contours at the end of construction: a) Lateral free; b) Lateral horizontally blocked.

4.4 Conclusions

In this chapter, the fully thermo-chemo-mechanical model was applied to the RCC gravity dam construction. The potential of cracking during early ages was evaluated by means of two

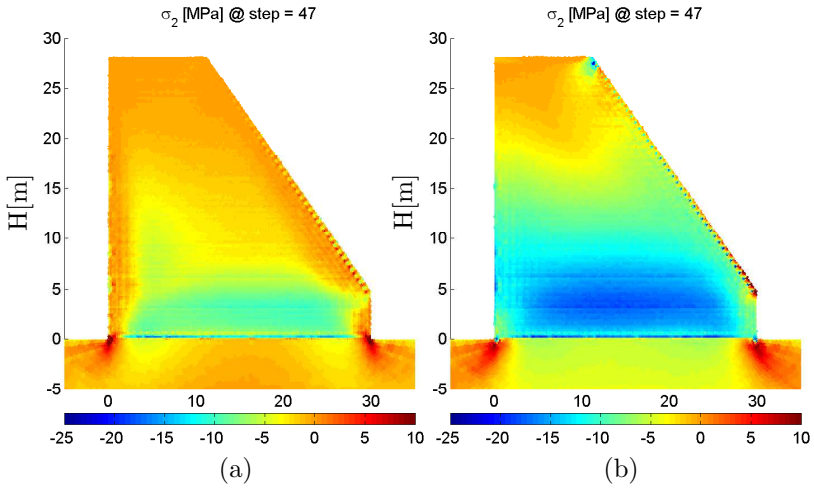

Figure 4.25: Second principal stress contours at the end of construction: a) Lateral free; b) Lateral horizontally blocked.

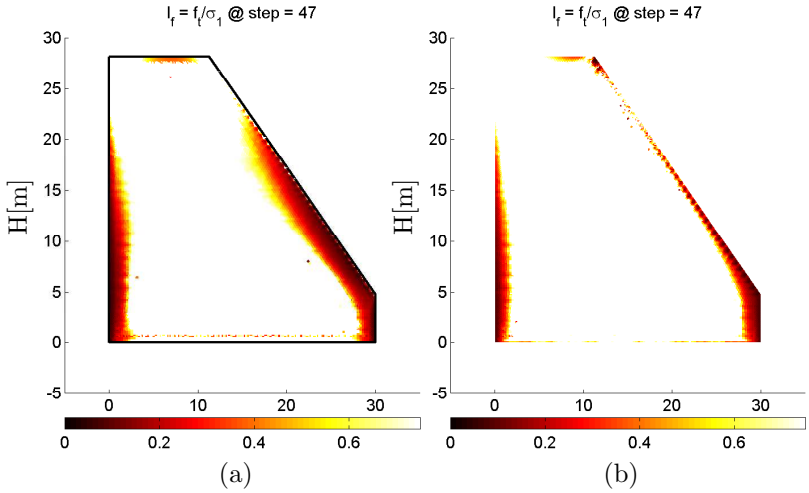

Figure 4.26: Cracking index contours at the end of construction: a) Lateral free; b) Lateral rollers, $h_{\text{lateral}} = 10$.

concepts: cracking index $I_f = f_t/\sigma_1$ and cracking density ρ_f.

With the objective of analyzing the model response in terms of cracking density results, several case scenarios are adopted in this chapter. In those case scenarios the idea was to vary some aspects related to the construction site which are often object of unpredicted changes. Those aspects are the ambient temperature evolution (whether the construction begins during summer or winter), the casting temperature (which depends, in practice, on the adopted cooling techniques) and the construction schedule (which can be object of several unpredicted delays during the dam construction). Two other aspects are dealt with within this chapter: the account for cold joints treatment in the numerical modelling by changing the top layer boundary condition, and the account for thermal and mechanical restrains imposed by formwork on the

dam lateral boundaries.

For the ambient temperature case scenarios related to the ambient temperature, four cases were adopted, two for a construction that begins in winter and the other two for a construction that begins in summer. The four cases are described by two different sinusoidal functions, on which distinct temperature amplitudes are adopted, simulating rougher and softer winters and summers. It was concluded that the model behaviour not only depends on whether the construction has begun during the cold or hot season, but also on the adopted sinusoidal daily and yearly ambient temperature evolution. It was shown, as expected, that different cracking densities are obtained for different ambient temperature amplitudes.

Concerning the casting temperature $T_0 = T_{ext}(t = t_0) + \Delta T_0$, it was concluded that the adopted changes on the added temperature ΔT_0 do not significantly affect the cracking density results.

For the different studied construction schemes, it was concluded that increasing the duration of stops between the casting of two layers will increase the cracking extent within each layer. An analysis was made by applying the joint maturity index (JMI) concept, which allows to evaluate the quality of the joint (top surface of each casted layer) by multiplying the surface temperature with the time of exposure. The layers on which the construction has stopped for longer periods of time are subjected to greater times of exposure and will be classified by higher JMI. The JMI reveals to be a useful tool in these kind of analyses.

The application of the JMI concept was further studied within a parametric study related to the convection coefficient of the top boundary of casted layers. This parametric study intended to account for a possible cold joints' treatment in the numerical modelling of the dam construction. The cold joints are those layers that have been exposed for a sufficient period of time during which the material has begun to stiffen and is no longer under a moist condition, being an obstacle to the good adherence of the subsequent layer. It was concluded that relying only on the JMI value is not sufficient to evaluate cold joints. Therefore, it was proposed to identify the layers that should be considered as cold joints by evaluating at the same time the ageing degree κ attained at the end of the time of exposure, as well as the JMI. It was finally concluded that accounting for cold joints' treatment, either by reducing the convection coefficient, insulating the top boundary of those layers considered to be cold joints or by fixing the temperature of the top boundary, lead in all cases to a reduction of the cracking density of the analyzed layers.

Finally, a last study was performed about the simulation of the thermal and mechanical

restrains imposed by formwork on lateral boundaries. It was concluded that accounting for formwork either by reducing the lateral convection coefficient or imposing nil horizontal deformations, or both at the same time, lead to a reduction of the cracking density.

Now, after analyzing the model behaviour in a deterministic manner, a question rises within the framework of this thesis: what will be the probability of exceeding a cracking density limit within a layer if uncertainties on some model parameters related to the material and ambient conditions are accounted for? This will be the object of chapter 6, on which this study is performed within a probabilistic framework. But before passing directly to that question, the proposed probabilistic approach is firstly presented in chapter 5 over the thermo-chemical behaviour of the dam.

Chapter 5

Methodology for probabilistic analysis of the thermo-chemical behaviour of an RCC gravity dam construction

The main objective of this chapter is to describe and present a methodology to account for uncertainties related to the behaviour of RCC dams during their construction using numerical modelling. In this sense, a probabilistic approach is proposed to propagate uncertainties on some RCC's physical properties. A thermo-chemo-mechanical model is used to describe the RCC behaviour, such as in the previous chapter 4. However, only the thermo-chemical behaviour is analyzed here.

Hence, a novel application of probabilistic tools is introduced and applied to improve the comprehension of heat transfer phenomena during an RCC dam construction. However, as the temperature and hydration degree control the mechanical characteristics of the material (via the ageing degree), some interesting conclusions related to the mechanical strength are made.

This approach will be extended to the full thermo-chemo-mechanical case in the next chapter 6. Therefore, the conclusions achieved at the end of this chapter may be seen as preliminary conclusions of the present thesis, in the sense that any probability of "failure" is evaluated yet.

A global sensitivity analysis is performed in order to evaluate the influence of some parameters in the thermal behaviour of the dam during construction. Heterogeneity on those parameters is further taken into account by means of bi-dimensional random fields. A variance reduction of the model output is observed while using random fields to propagate uncertainties.

The results presented in this chapter are included in a published paper in *Engineering*

Structures (Gaspar et al., 2014).

In the following, in order to lighten the reading of this chapter, a brief theoretical description of the adopted probabilistic tools is firstly exposed. More details about the adopted tools and techniques may be found with more detail in the appendix B. Then, the application of the proposed methodology is explained by describing the case study, the model parameters and random variables. A brief reminder of the most important aspects of the adopted thermo-chemo-mechanical model is exposed. Finally, the results are presented and discussed.

5.1 Application

The dam model consists of the same RCC gravity dam used in chapter 4 and described in chapter 3 (Figure 5.1). The foundation is also represented in this model in order to account for its thermal effect on the first layers of the RCC dam. As recalled before, in chapter 6 the mechanical behaviour of both RCC and the foundation will be accounted for. Concerning the thermal boundary conditions, the bottom and lateral faces of the foundation are insulated, while all the dam faces interact with the surrounding environment by a heat flux exchange. The dam construction simulation is performed by using a "multi-model" concept which consists of solving a sequence of models. To each of those models a 0.6m thick layer is added, the initial conditions of each one being the solution of the previous solved one.

A schematic representation of the dam model is shown in Figure 5.1. The two discretized points in this scheme correspond to the locations that were chosen to assess the dam response in more detail. On "point i" at the center of the dam body, the behaviour is expected to be adiabatic, while the "point d" near the downstream face of the dam is expected to be strongly influenced by the surrounding environment.

Regarding the environmental conditions, or "external thermal load", it is characterized by a daily sinusoidal variation of the ambient temperature. This one will oscillate between $T_{max} = 30°C$ and $T_{min} = 10°C$ according to equation 5.1, where $\Delta T[°C] = (T_{max}\text{-}T_{min})$, $f[d^{-1}]$ is the daily frequency and ϕ[rad] is the phase.

Concerning the numerical model, the mesh is composed of 3300 triangular elements, the time-step is of 0.5[h] and the construction rate 0.6m/24h. Please note that for the thermo-chemical modelling the foundation size is smaller than for the full thermo-chemo-mechanical modelling, and therefore the mesh is composed of less elements (please refer to chapter 3 for more details).

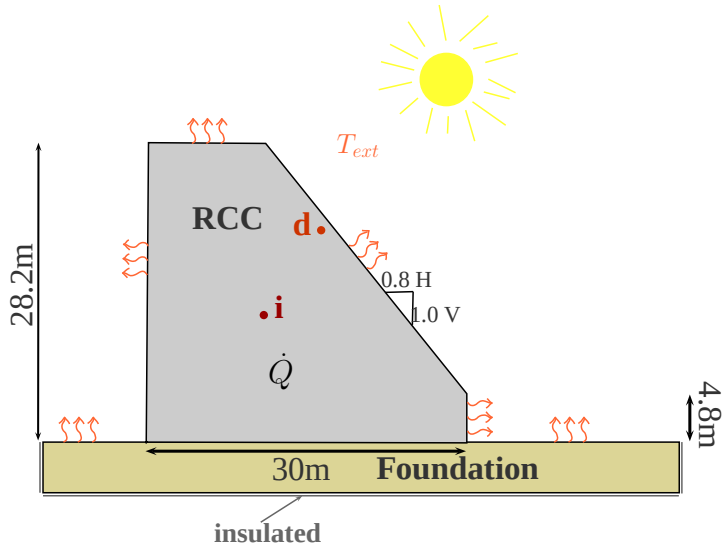

Figure 5.1: Dam model scheme

$$T_{ext} = \frac{T_{max} + T_{min}}{2} + \frac{\Delta T}{2} \cdot \sin(2\pi f t + \phi) \tag{5.1}$$

Wind effects can be taken into account via the convection coefficient h[W/(m^{2}K)], described by equation 5.2 (Leitão et al., 2007). The convection phenomenon is here divided into a convection h_c (equation 5.3) and a radiation part h_r. The parameters of equation 5.3 k_f[W/(m·°C)], ρ_f[kg/m^3] and μ_f[kg/(m·s)] are the air thermal conductivity, its specific weight and its absolute viscosity respectively, L[m] being the surface length on the wind flow direction and v_w[km/h] the wind speed.

$$h = h_c + h_r \tag{5.2}$$

$$h_c = 0.055 \cdot \frac{k_f}{L} \cdot \left(\frac{L \cdot v_w \cdot \rho_f}{\mu_f} \right)^{0.75} \tag{5.3}$$

In Table 5.1 are described the parameters used for equation 5.2.

Table 5.1: Parameters for equation 5.2

L[m]	k_f[W/(m°C)]	ρ_f[kg/m^3]
0.6	0.026	1.2
μ_f[kg/(m·s)]	h_r[W/(m^2 °C)]	
1.8e-5	5	

The numerical model used in this work is intended to represent the construction phase of an RCC gravity dam such as previously applied in chapter 4 in a deterministic manner.

As previously stated, the work presented in this chapter focuses on the thermo-chemical coupling. However, the mechanical characteristics, such as the compressive strength, may be computed since they depend on the hydration reaction evolution. It should be kept in mind that, however, the mechanical behaviour is not implicitly taken into account at this stage.

In order to allow an independent reading of the present chapter, a brief description of the adopted full thermo-chemo-mechanical model is made. Further details may be found in chapters 2 and 4.

The thermal behaviour of RCC (as well as for CVC) may be described by the following heat transfer equation:

$$\rho \cdot c \cdot \dot{T} = \underline{\nabla} \left(\underline{\underline{k}} \, \underline{\nabla} T \right) + \dot{Q} \tag{5.4}$$

$$\underline{\nabla} = \left(\frac{\partial}{\partial x}, \frac{\partial}{\partial y} \right) \tag{5.5}$$

where ρ[kg/m^3] is the material density, c[J/(kg·K)] the specific heat, T[°C] the temperature and $\underline{\underline{k}}$ [W/(m·°C)] the thermal conductivity, which in this case is considered as being isotropic. The heat generated due to the hydration reaction $\dot{Q}$ [W/m^3] is given by:

$$\dot{Q} = l_\xi \cdot \dot{\xi} \tag{5.6}$$

where l_ξ[J/m^3] is the heat generated per cubic meter of RCC and ξ[.] is the hydration degree which expresses the evolution of the hydration reaction. The hydration degree ξ may vary, theoretically, between 0 and 1. However it is known in practice that the final hydration degree is only achieved under ideal conditions, the latter being generally represented by a $\xi_\infty < 1.0$ (Cervera et al., 2000a).

The boundary conditions involve the heat flux at surfaces (equation 5.7), where h[W/(m^2·°C)] is the heat transfer coefficient, T_{ext}[°C] is the ambient temperature and $\underline{n}$ is a normal vector of the surface.

$$\frac{\partial T}{\partial \underline{n}} = \begin{cases} \frac{h}{k} \cdot (T_{ext} - T) \\ 0 \text{ if insulated surface} \end{cases} \tag{5.7}$$

The hydration degree evolution $\dot{\xi}$[s^{-1}] may be expressed by the following Arrhenius-type function:

$$\dot{\xi} = \tilde{A}(\xi) \cdot \exp\left(-\frac{E_a}{R \cdot T} \right) \tag{5.8}$$

where $\tilde{A}(\xi)[s^{-1}]$ is the chemical affinity function, the activation energy is given by E_a[kJ/mol] and R[kJ/(K· mol)] is the universal gas constant. The E_a/R ratio ranges between 3000 and 8000K (Cervera et al., 1999a). It shall be kept in mind that each RCC mixture is unique and that several parameters shall be carefully evaluated for each mixture. For example, the amount of pozzolan incorporated within an RCC mixture will, in high proportions, influence the activation energy in which case laboratory testing should be reinforced. In the present work it was decided to proceed with the currently adopted values.

The chemical affinity function is provided by equation 5.9 (Cervera et al., 1999a), where k_ξ, η_{ξ_0}, A_{ξ_0} and $\overline{\eta}$ are material properties derived from the reactive porous media theory presented by Coussy (1996). For more details about this hydration law, the reader is refered to Cervera et al. (1999a).

$$\tilde{A}(\xi) = \frac{k_\xi}{\eta_{\xi_0}} \left(\frac{A_{\xi_0}}{k_\xi \cdot \xi_\infty} + \xi \right) \cdot (\xi_\infty - \xi) \cdot \exp\left(-\overline{\eta} \cdot \frac{\xi}{\xi_\infty} \right) \tag{5.9}$$

The mechanical characteristics of the RCC, as it has already been underlined before, will also depend on the hydration reaction evolution. In this work an *ageing degree* κ[.] concept is used, based on the one proposed by Cervera et al. (1999a). The ageing degree evolution $\dot{\kappa}$ is described as in equation 5.10 and will depend on both temperature and hydration degree's evolutions. In equation 5.11, T_T is the maximum temperature for concrete hardening, T_{ref} is the reference temperature used for determining the final compressive strength (generally = 20°C) and n_T is a material property. In equation 5.12, A_f and B_f are material constants, while ξ_{set} is the hydration degree that defines the end of the setting phase and the beginning of the material's solidification (Byfors, 1980; Cervera et al., 1999a).

$$\dot{\kappa} = \lambda_T(T) \cdot \lambda_{f_c}(\xi) \cdot \dot{\xi} \geq 0 \tag{5.10}$$

$$\lambda_T(T) = \left(\frac{T_T - T}{T_T - T_{ref}} \right)^{n_T} \tag{5.11}$$

$$\lambda_{f_c}(\xi) = A_f \cdot \xi + B_f \,, \text{ for } \xi \geq \xi_{set} \tag{5.12}$$

Then, the mechanical properties, such as the compressive strength f_c, may be described as function of the ageing degree (equation 5.13, where $f_{c,\infty}$[MPa] is the final compressive strength).

$$f_c(\kappa) = \kappa \cdot f_{c,\infty} \tag{5.13}$$

5.2 Probabilistic tools

The main objective of the probabilistic model used in this chapter is to assess the variability of the model output by accounting uncertainties inherent to some input parameters. Uncertainties are propagated through the model by means of an Monte Carlo (MC)-type method (in this case, the RBD-FAST is used).

In a first approach, sensitivity analyses are performed in order to assess the influence of input uncertainties on the output of the model. Generally, sensitivity analyses are carried out via the Sobol indices (Sobol, 1993) (e.g. in the work of Venkovic et al. (2013) on a probabilistic microporomechanics model for cement paste at early-age). However, the Sobol indices technique is numerically expensive and not affordable in the present work. Therefore, the RBD-FAST (Tarantola et al., 2006; Mara, 2009), a less expensive method, is here preferred over the Sobol indices. For more details about sensitivity analysis methods please refer to the appendix B. In a second approach, the variables' spatial randomness is considered via bi-dimensional random fields theory.

5.2.1 Sensitivity test

The Random Balance Design FAST (RBD-FAST) (Tarantola et al., 2006) is a sensitivity test derived from the Fourier Amplitude Sensitivity Test (FAST) (Saltelli et al., 1999). The FAST method is based on the variance decomposition, used here to compute the first-order sensitivity indices S_i. In this work, the RBD-FAST is chosen over the FAST method because of the increased number of needed simulations of the latter, for the number of random variables that are dealt with in this chapter (minimum of 570 against 250 simulations (Saltelli et al., 1999)). On the other hand, RBD-FAST has the disadvantage of leading to a lower accuracy for low values of the sensitivity indices. A brief description of FAST and RBD-FAST is made here.

In FAST, each independent random variable (r.v.) is generated from a periodic search function (equation 5.14), on which each r.v. is assigned a characteristic integer frequency w_i (Xu and Gertner, 2008). Those frequencies shall be chosen in such a way that they avoid interferences between the outputs on those frequencies and their higher order harmonics $\{w_i, 2w_i, \ldots, Mw_{max}\}$ (Tarantola, 2006). In equation 5.14, x_i is one realization of the r.v. and F_i^{-1} is the inverse

cumulative distribution function over x_i.

$$x_i = F_i^{-1}\left(\frac{1}{2} + \frac{1}{\pi}\arcsin(\sin(w_i s))\right),\ -\pi \leq s \leq \pi \tag{5.14}$$

Therefore, the model output will be a periodic function and a Fourier analysis can then be performed over it, the Fourier coefficients A_j and B_j being determined (equations 5.16 and 5.17, where f is the model output) and used to compute the total (V) and partial (V_i) variances of the model output. The first order sensitivity indices are finally obtained by equation 5.19.

$$V \approx 2\sum_{j=1}^{+\infty}\left(A_j^2 + B_j^2\right) \tag{5.15}$$

$$A_j = \frac{1}{2\pi}\int_{-\pi}^{\pi} f(x(s)) \cdot \cos(js)ds \tag{5.16}$$

$$B_j = \frac{1}{2\pi}\int_{-\pi}^{\pi} f(x(s)) \cdot \sin(js)ds \tag{5.17}$$

$$V_i = 2\sum_{p=1}^{+\infty}\left(A_{pw_i}^2 + B_{pwi}^2\right) \tag{5.18}$$

$$S_i = \frac{V_i}{V} \tag{5.19}$$

The number of simulations N needed in FAST may be found by means of equation 5.20, let $M = 4$ and $w_{max} = 35$ in this work.

$$N = (2 \cdot M \cdot w_{max} + 1) \cdot 2 \tag{5.20}$$

The advantage of RBD-FAST is that each r.v. may be sampled from a periodic search function considering a single frequency w_i for all r.v., which will lead to a reduction on the number of simulations N. This is possible thanks to a randomization procedure used in RBD-FAST (Mara, 2009). The randomization procedure consists of randomly permuting the set of samples for each r.v., run the model using those permuted sets of r.v., and finally reorder the model output according to the input permutation for each r.v.. Then, for each reordered set of output the single frequency w_i is restored and the sensitivity indices may be evaluated using the same procedure as in FAST.

Moreover, this randomization procedure also assures the obtention of unbiased r.v., enabling RBD-FAST to be applied as a screening method such as Monte Carlo-type sampling methods.

The fact that sampling is made from a periodic search function allows the covering of the entire probabilistic search space. Therefore, the RBD-FAST is not only applied in this thesis to perform sensitivity analysis, but also to propagate uncertainties within the model, given the advantages and characteristics referred here.

For further details about FAST and RBD-FAST the reader is referred to Tarantola (2006), Xu and Gertner (2008), Mara (2009) and to the appendix B of this thesis.

5.2.2 Random fields

The usefulness of random field theory relies on the possibility to represent the spatial variability of a given parameter (or set of parameters) over a model. On a random field, the random variables are sampled over space, given autocorrelation functions, on which are specified the correlation lengths assigned to each random variable on each field direction (θ_x and θ_y in a 2D random field).

Random field theory has been applied in several research domains, such as in structural engineering (e.g. Liu et al., 2001)) and in geotechnical engineering (e.g. Vanmarcke (1977) and more recently Griffiths and Fenton (2004), Popescu et al. (2005), Lopez-Caballero and Modaressi-Farahmand-Razavi (2010), Caro et al. (2011), among others).

A random field is called stationary or homogeneous if the joint probability functions are independent of the absolute location and if the covariance only depends on the relative location between each couple of points discretized over the domain.

There exist several methods available to discretize a random field, such as the midpoint method (used in this thesis), the spatial average method and series expansion-based methods (e.g. Karhunen-Loève or Newman). In the midpoint method, the model is sub-divided into several cells, each one being assigned a random value of the parameter of interest, constant within that cell. The autocorrelation function defines the correlation between the values of adjacent cells of the model. Here, the field is bidimensional (2D) and two autocorrelation functions are given, one in each direction, characterized by two different correlation lengths: θ_x and θ_y. Because of the lack of field data about the parameters' spatial variation, the squared exponential autocorrelation function, given by equation 5.21, was assumed to be well adapted to this study.

$$\hat{\rho}_{G_i,G_j} = \exp\left[-\pi\left[\left(\frac{d_x}{\theta_x}\right)^2 + \left(\frac{d_y}{\theta_y}\right)^2\right]\right] \tag{5.21}$$

In equation 5.21, $\hat{\rho}$ is the correlation coefficient between points G_i and G_j, d_x and d_y being the horizontal and vertical distances between those two points.

In this work, the stationary Gaussian random fields have been generated via Monte Carlo sampling method. The generation method used in this work is based on the covariance matrix decomposition technique (Lopez-Caballero and Modaressi-Farahmand-Razavi, 2010; Davis, 1987), used in the work of Caro et al. (2011) and proposed by El-Kadi and Williams (2000).

This technique is here briefly described. Based on principal components analysis, the correlated random field P is obtained by equation 5.22, where B is the matrix of the eigenvectors of the correlation matrix R (obtained via equation 5.21 for each pair of points), Λ is the diagonal matrix of the square root of the eigenvalues of R and C is the matrix of the Gaussian uncorrelated random variables. The variables of the random field P are Gaussian $N[0,1]$ and correlated following the R matrix.

$$[P] = [B] * [\Lambda] * [C] \tag{5.22}$$

Afterwards, the Gaussian correlated field P is transformed into a non-Gaussian random field by using the *inverse CDF* (cumulative distribution function) method:

$$f_B(x) = F_B^{-1}\left[F_G[f_P(x)]\right] \tag{5.23}$$

where F_B and F_G are the CDFs of the non-Gaussian and Gaussian random field respectively. For further details about this method please refer to Lopez-Caballero and Modaressi-Farahmand-Razavi (2010) and to the appendix B of this thesis.

5.3 Model parameters and random variables

The adopted hydration and mechanical model parameters (Table 5.2) correspond to a typical RCC and are based on the work of Leitão et al. (2007). The respective chemical affinity and the compressive strength evolution for an isothermal test at 20°C are displayed in Figure 5.2.

The mechanical coupling model parameters (i.e. A_f, B_f, ξ_{set} and n_T) were obtained by using an optimization procedure in order to minimize the difference between the measured and computed values (Figure 5.2b). The measured values were taken from Leitão et al. (2007). Details on the optimization procedure may be found in previous works (Pimentel-Torres-Gaspar, 2010; Lopez-Caballero et al., 2011).

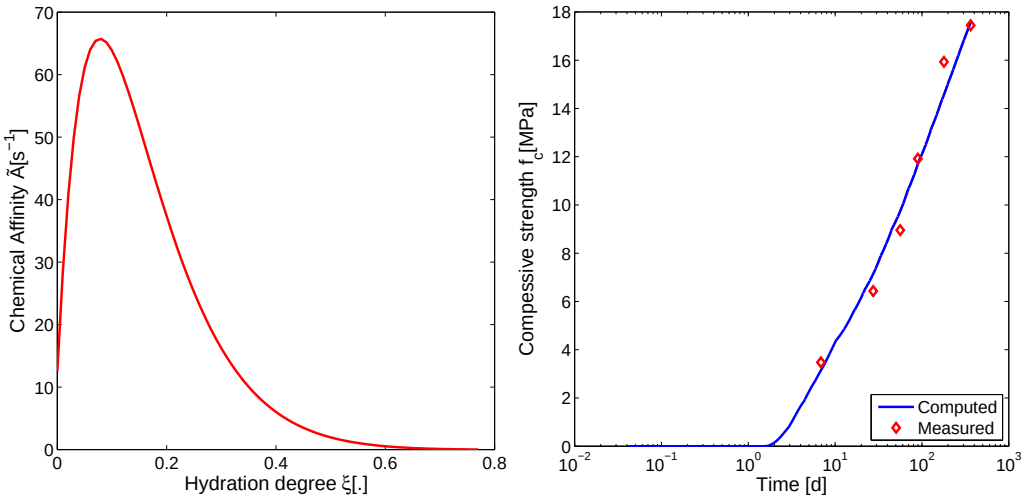

(a) (b)

Figure 5.2: a) Chemical affinity ; b) Compressive strength evolution during isothermal test.

As recalled before, the RBD-FAST technique is used in this work to perform a sensitivity analysis with the objective of studying the influence of each chosen parameter on the thermal behaviour of the dam.

During a dam construction, one may say that the material composition will not be exactly the same all along the construction phase. The material heterogeneity may be due to the material's components themselves or due to human errors on the mixing of those components, which will affect some material properties, such as enhanced by Schrader (2008). Also, the meteorological conditions will vary and influence the material thermo-chemo-mechanical behaviour. Therefore, in a first approach, the following material characteristics were considered as being random variables: the water-to-cement ratio ($w/c[.]$), the cement content ($c[\mathrm{kg/m^3}]$), the thermal conductivity ($k[\mathrm{W/(m{\cdot}K)}]$) and the wind speed ($v_{wind}[\mathrm{km/h}]$).

While the thermal conductivity is a parameter that influences directly the thermal equa-

Table 5.2: Model parameters

Hydration	$\frac{E_a}{R}[\mathrm{K}]$	$\frac{k_\xi}{\eta_{\xi_0}}[\mathrm{s}^{-1}]$	$\frac{A_{\xi_0}}{k_\xi}$	$\overline{\eta}$	ξ_∞
model	5000	2500	0.005	8.1	0.779
Mechanical	A_f	B_f	n_T	ξ_{set}	–
coupling	4.2	-1.05	0.12	0.25	–
General	$\rho[\frac{kg}{m^3}]$	$c[\frac{J}{kg{\cdot}K}]$	$q_c[\frac{kJ}{kg}]$	–	–
parameters	2400	921	500	–	–

tion, the same does not happen to the water-to-cement ratio, cement content and wind speed. However, there are other parameters which depend on these, such as the final hydration degree $\xi_\infty[.]$ (equation 5.24 by Pantazopoulo and Mills (1995)), the hydration heat generated by cubic meter of material $l_\xi[\mathrm{kJ/m^3}]$ (equation 5.25, where $q_c[\mathrm{kJ/kg}]$ is the hydration heat generated by kg of cement, here assumed 500 kJ/kg) and the convection coefficient $h_c[\mathrm{W/(m^2{\cdot}K)}]$ (equation 5.3).

$$\xi_\infty = \frac{1.031 \cdot w/c}{0.194 + w/c} \tag{5.24}$$

$$l_\xi = c \cdot q_c \tag{5.25}$$

Concerning the hydration model, the only random variable that will input some variability on the chemical affinity curve is the final hydration degree ξ_∞, while all the other parameters described in Table 5.2 remain constant. The resulting variability about the chemical affinity curve is plotted in Figure 5.3.

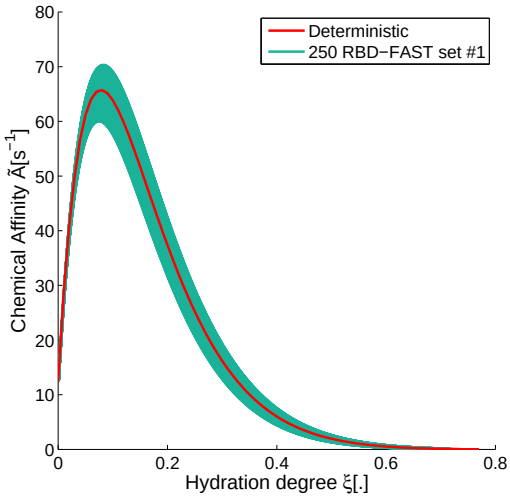

Figure 5.3: Chemical affinity curve variability, 250 RBD-FAST set#1

In a first approach, and because of the lack of statistical information, all four random variables w/c, c, k and v_{wind} are supposed to be independent and uniformly distributed. Four sets of 250 RBD-FAST computations were performed, each one using different combination of r.v., such as described in Table 5.3.

The statistics of the input random variables for the RBD-FAST set #1 are plotted on Figure 5.4. It may be noticed the relationships between w/c and ξ_∞, and c and l_ξ that were previously described by equations 5.24 and 5.25.

Table 5.3: Random variables for RBD-FAST

	w/c[.]	c[kg/m^3]	k[W/(m°C)]	v_{wind}[km/h]
#0	0.6	220	2.96	17
#1	$\mu = 0.6$ $CV = 0.1$	$\mu = 220$ $CV = 0.15$	$\mu = 2.96$ $CV = 0.25$	cte. $h = 27$ W/(m^2 °C) –
#2	$\mu = 0.6$ $CV = 0.1$	$\mu = 220$ $CV = 0.15$	$\mu = 2.96$ $CV = 0.25$	cte. $h = 10$ W/(m^2 °C) –
#3	$\mu = 0.6$ $CV = 0.1$	$\mu = 220$ $CV = 0.15$	$\mu = 2.96$ $CV = 0.25$	$\mu = 17$ ($\mu_h = 27$) $CV = 0.2$
#4	$\mu = 0.6$ $CV = 0.1$	$\mu = 220$ $CV = 0.15$	cte. $k = 2.96$ –	$\mu = 17$ ($\mu_h = 27$) $CV = 0.2$

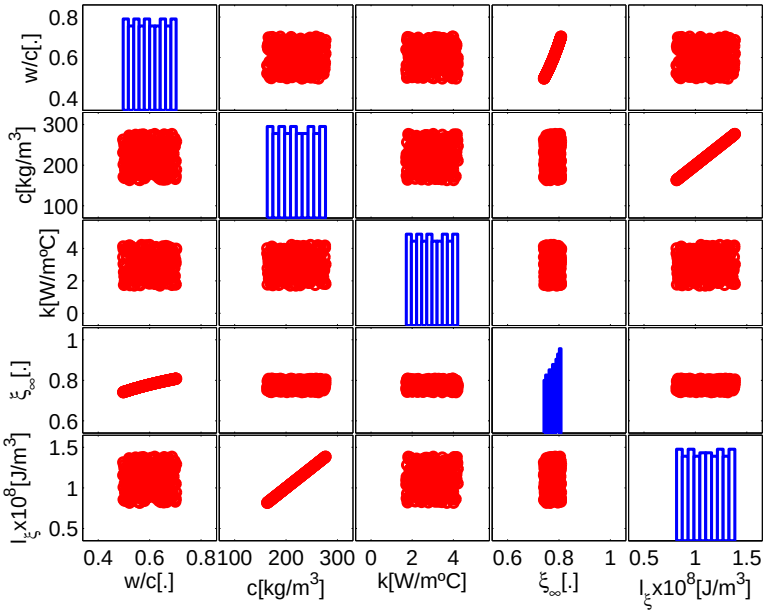

Figure 5.4: Statistics of the input random variables of the 250 RBD-FAST set#1

In order to assess the effect of the RCC properties' heterogeneity on the model response, two sets of random fields calculations were performed. The random variables' characteristics are described in Table 5.4. The correlation lengths used for each set of random fields are not based on any field measure. Within the framework of this study it was decided to consider two sets of random fields adopting correlation lengths that will lead to significantly different random fields. The choice of θ_y is simply based on the height of each RCC layer, being for set #5 equal to half the height of each layer (this means that the correlation between two consecutive layers will be negligible), and for set #6 equal to the height of two layers (which can be seen as equivalent to the construction rate of 0.6m per day used in this work).

In Figures 5.5a and 5.5b are plotted one sample of the random field realizations for sets #5

and #6 respectively.

Table 5.4: Random variables for random fields

	w/c[.]	c[kg/m^3]	k[W/(m°C)]	h[W/(m^2 °C)]
#5	$\mu = 0.6$	$\mu = 220$	$\mu = 2.96$	cte. $h = 27$
	$CV = 0.1$	$CV = 0.15$	$CV = 0.25$	–
	$\theta_x = 0.5m$	$\theta_x = 0.5m$	$\theta_x = 0.5m$	–
	$\theta_y = 0.15m$	$\theta_y = 0.15m$	$\theta_y = 0.15m$	–
#6	$\mu = 0.6$	$\mu = 220$	$\mu = 2.96$	cte. $h = 27$
	$CV = 0.1$	$CV = 0.15$	$CV = 0.25$	–
	$\theta_x = 5m$	$\theta_x = 5m$	$\theta_x = 5m$	–
	$\theta_y = 0.6m$	$\theta_y = 0.6m$	$\theta_y = 0.6m$	–

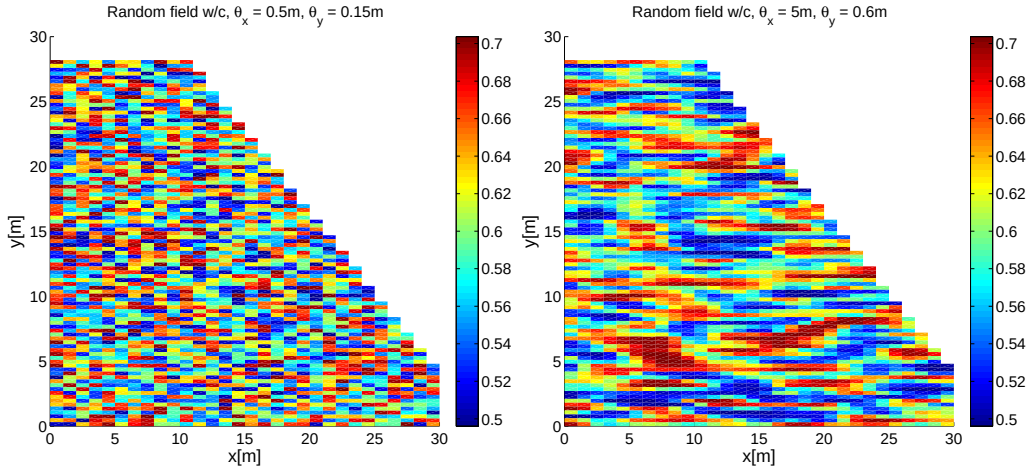

(a) (b)

Figure 5.5: One realization of the random fields: a)set #5; b)set #6.

5.4 Results and discussion - RBD-FAST

First of all, a deterministic calculation, that will serve as reference result, is performed using the mean values for each parameter described in Table 5.3. The temperature, hydration degree and compressive strength evolutions will be analyzed on the two points within the dam body, introduced in section 5.1.

It shall be reminded that the RBD-FAST technique is here applied both to propagate uncertainties within the model (MC-type technique) and to analyse the outputs by performing a sensitivity analysis.

5.4.1 Reference results

For the RBD-FAST computation sets, only some relevant results will be presented here. For the computation set #1, the temperature, hydration degree and compressive strength evolutions on "point i" are plotted in Figure 5.6 so that the reader can have an idea of the shape of those results and comparison with the reference (deterministic) one (i.e. computation set #0). As expected, the temperature evolution on "point i" (i.e. at the center of the dam body) is characteristic of an adiabatic behaviour. If the analysis would have continued during the exploitation years of the dam, that temperature would eventually decrease in time. It may be concluded by analyzing Figure 5.6b that the hydration degree at the end of the dam construction has not yet reached its final value $\xi_\infty = 0.78$. Therefore, the compressive strength (Figure 5.6c) has not reached the final value either. Still regarding compressive strength evolution, it should be noticed the effect of ξ_{set} on defining the end of the setting phase and beginning of RCC's solidification. Finally, the deterministic result is in good agreement with the mean curves of the RBD-FAST computations, which was expected since the mean values of the parameters are the same for the two cases.

Figure 5.7 displays the temperature evolution on "point d" (Figure 5.7a) as well as the convergence of the mean, standard deviation (Figure 5.7b) and coefficient of variation (Figure 5.7c) estimators at the end of the dam construction (for an age of 18 days on "point d"). Regarding the temperature evolution on "point d" (near the downstream face of the dam) the influence of the external thermal load is obvious, leading to serious temperature oscillations during the first days after placing. The statistical convergence of the results plotted in Figures 5.7b and 5.7c is assumed to be sufficient for the application considered in this work. In these figures are also represented by dashed lines the confidence intervals at 5% and 95% obtained via the t-student and χ^2 statistical model at 5% of confidence for the mean and standard deviation respectively.

Still concerning the RBD-FAST set #1, are also plotted, in Figure 5.8, the temperature contours at several construction stages. It shall be enhanced here that the results of Figure 5.8 concern only one computation and may therefore be seen as deterministic ones.

5.4.2 Sensitivity analysis

The global sensitivity analysis performed over the results of the RBD-FAST computation sets leads to the obtention of the first-order sensitivity indices (S_i). Here, for the sake of brevity,

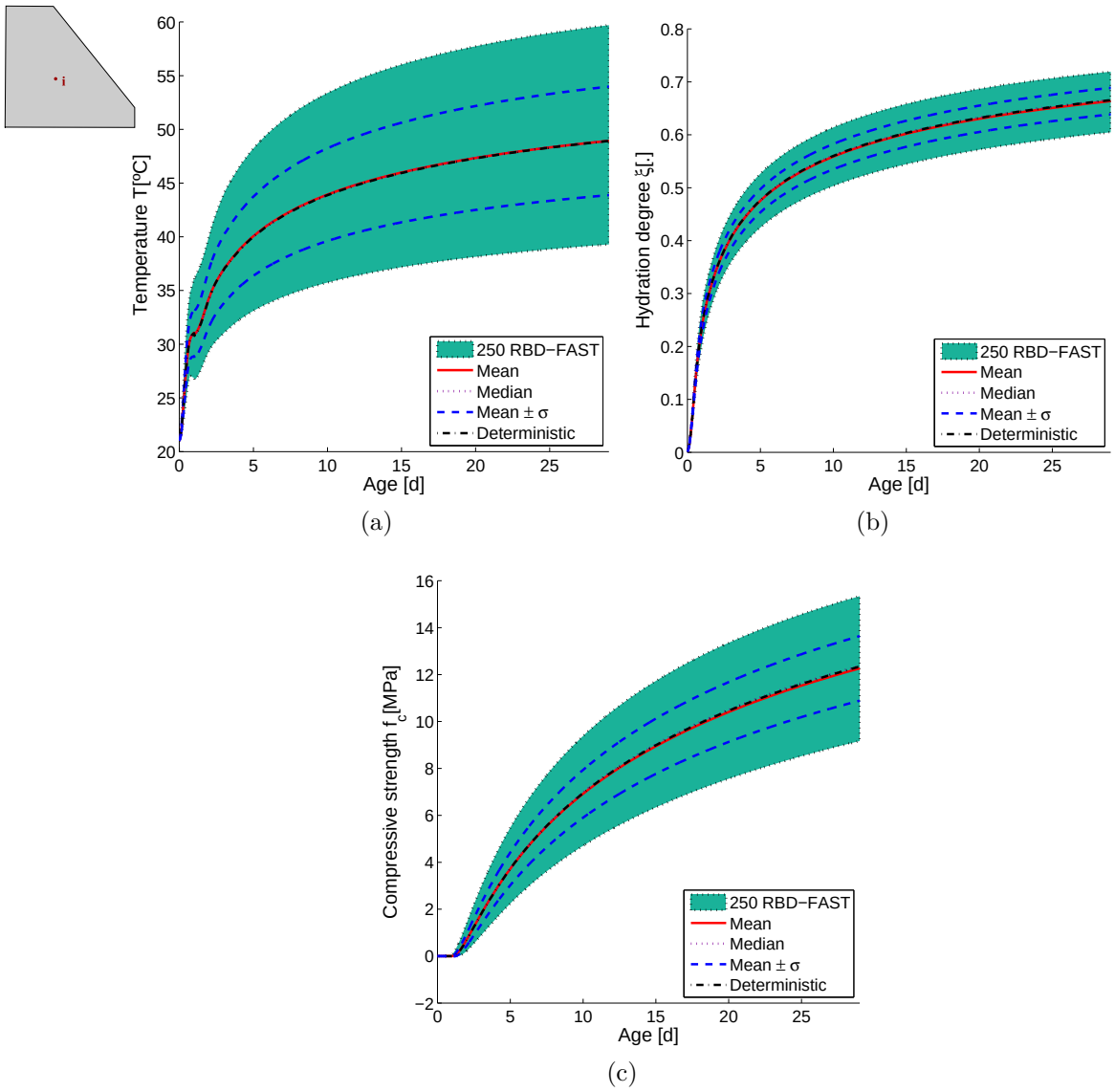

Figure 5.6: Deterministic set **#0** vs. RBD-FAST set #1, "point i": a) Temperature; b) Hydration degree; c) Compressive strength.

only some relevant results will be presented.

The sensitivity indices traduce the contribution of each random parameter on the response of the model (in this case, on the temperature, hydration degree and ageing degree evolutions). As stated before, for this study the analysis was performed over the results obtained at two different points within the dam: one in the center of the dam body ("point i") and another near the downstream face of the dam ("point d"). In Figure 5.9 are plotted the S_i obtained for RBD-FAST computation set #1 concerning both points i and d for temperature T (Figures 5.9a and 5.9c) and hydration degree ξ (Figures 5.9b and 5.9d) as functions of the age. It was observed that the S_i values obtained for the ageing degree κ evolution are very similar to the ones obtained for the hydration degree ξ. Therefore, for the sake of brevity, S_i for κ results will

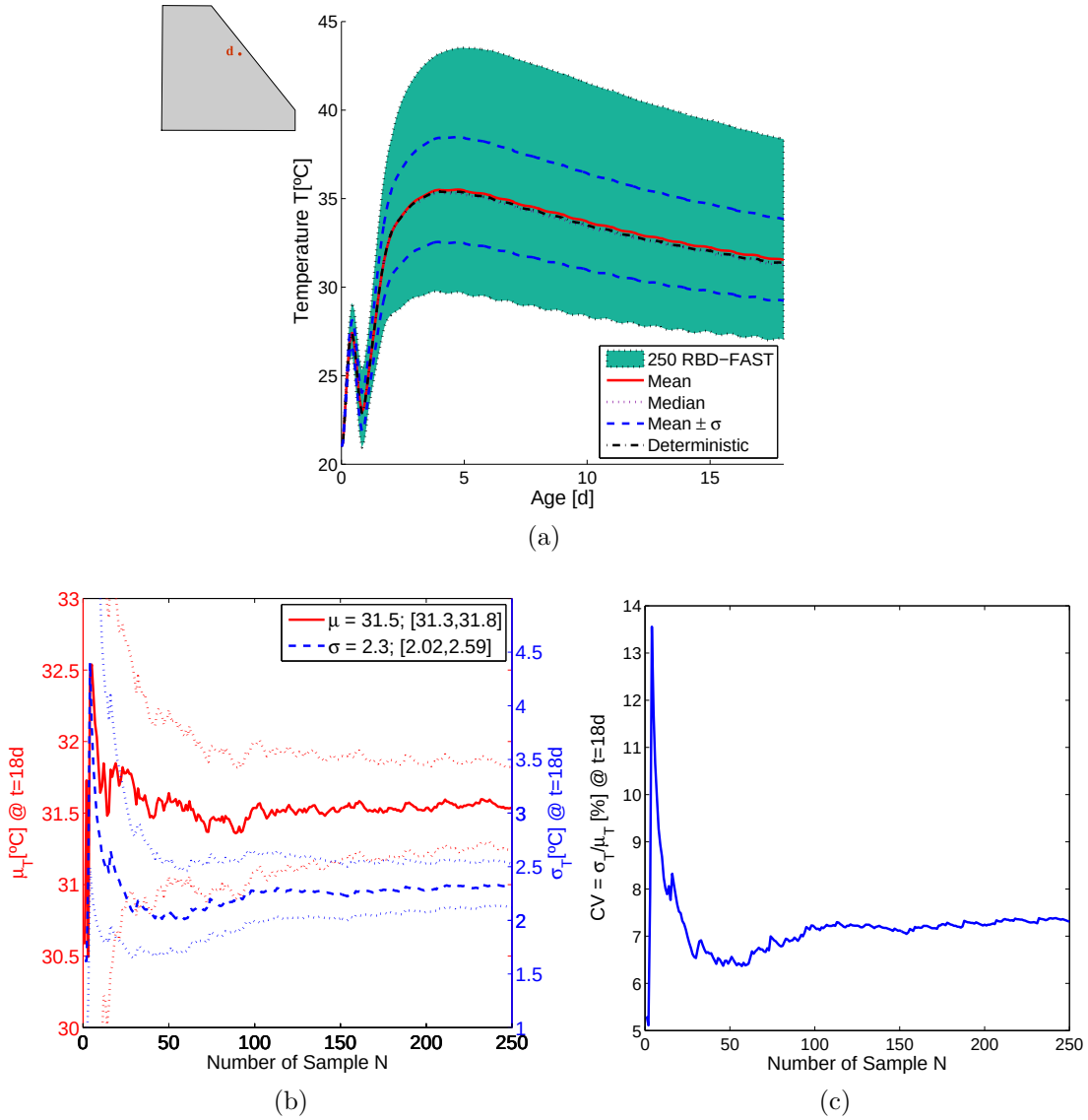

Figure 5.7: RBD-FAST set #1, "point d": a) Temperature; b) Convergence of the temperature $\hat{\mu}$ and $\hat{\sigma}$ estimators; c) Convergence of the temperature CV estimator.

not be presented here. Also, from here on, emphasis will be given to the results concerning the point located near the downstream face of the dam ("point d").

From the sensitivity analysis performed over the RBD-FAST computation set #1 several conclusions may already be made. First of all, it may be concluded that the considered r.v. affect the results in different ways. Also, according to the emplacement of the analyzed point, the sensitivity analysis can lead to very different results. For example, by comparing Figures 5.9a and 5.9c, can be noticed the great different responses of S_i for the thermal conductivity. In the point near the downstream face of the dam ("point d", Figure 5.9c) the thermal conductivity presents an increasing influence on the temperature results, with a S_i that grows up to $\approx$ 0.3, while in the point at the center of the dam body ("point i", Figure 5.9a) its influence is

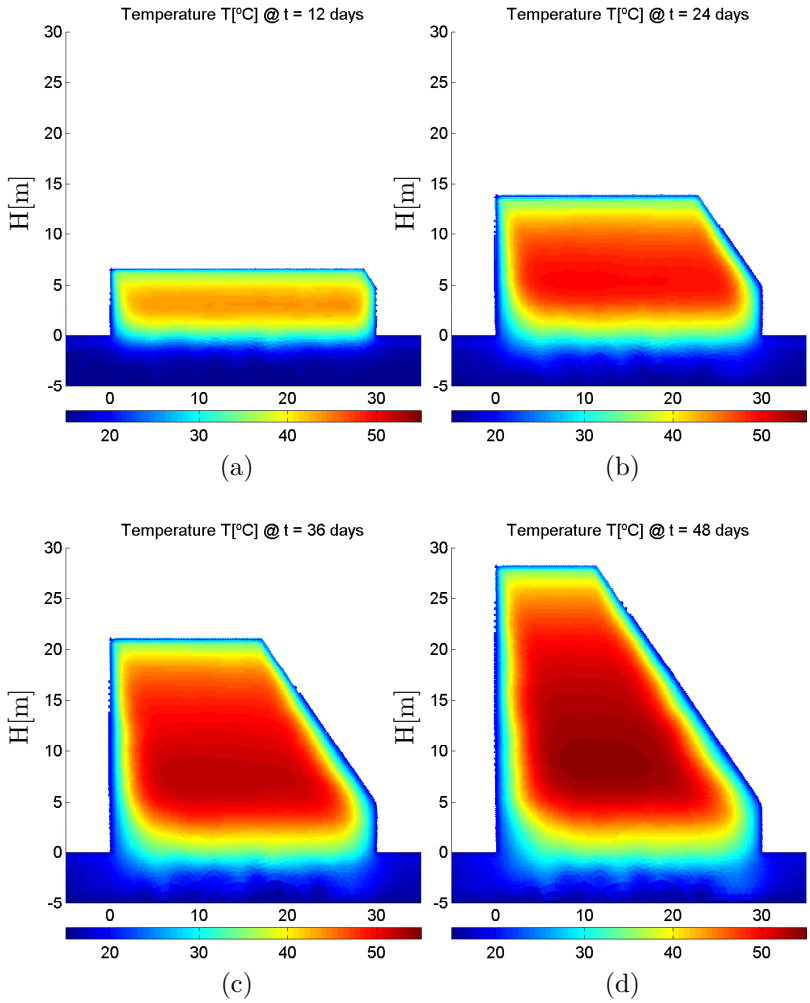

Figure 5.8: Temperature contours, RBD-FAST set #1: a) $t = 12$ days; b) $t = 24$ days; c) $t = 36$ days; d) $t = 48$ days

barely noticed. Another important conclusion is that the cement content will dominate the temperature responses both in the center and near the downstream face of the dam, even if for the latter its influence will decrease in time due to the increasing influence of the thermal conductivity. Regarding the water-to-cement ratio, it presents insignificant S_i for temperature results. However, in what concerns hydration degree results, it is the water-to-cement ratio that dominates the response (Figures 5.9b and 5.9d). This means that the uncertainty induced in the chemical affinity curve (Figure 5.3) via ξ_∞ (which depends on w/c) does not significantly affects temperature within the dam body but it affects the hydration degree and therefore the mechanical properties, presenting a sensitivity index that varies between 0.6 and 0.7 during the dam construction.

The sensitivity index can also be evaluated within the entire dam model at each construction step, giving S_i contours as the ones plotted in Figure 5.10. It shall be noticed that these results

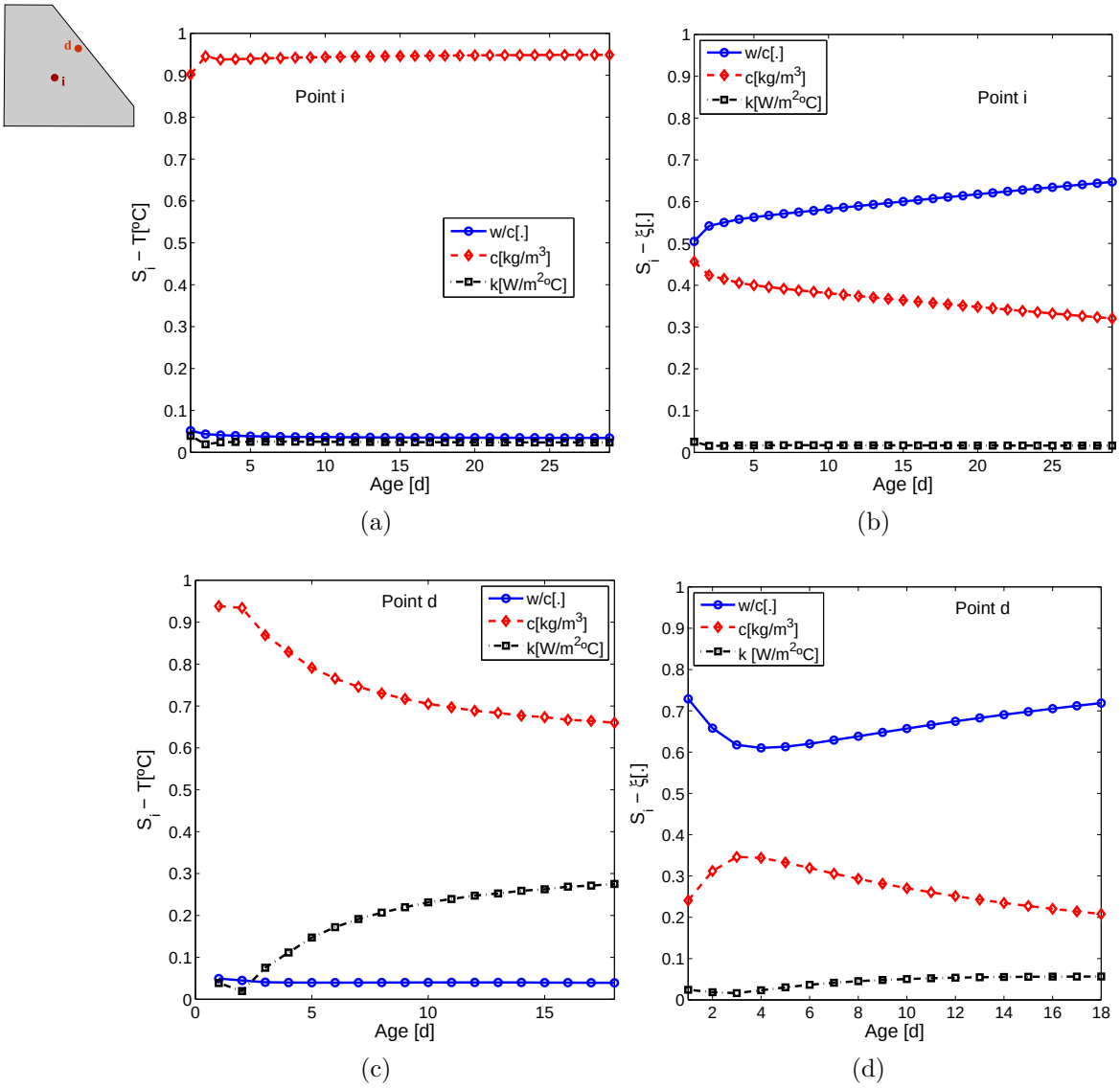

Figure 5.9: RBD-FAST set #1: a) S_i over temperature at "point i"; b) S_i over the hydration degree at "point i"; c) S_i over temperature at "point d"; d) S_i over the hydration degree at "point d".

concern the sensitivity index at a given time of construction. Even if these kind of analysis is more numerically expensive than the one of Figure 5.9, it gives a spatially distribution of S_i, allowing the identification of the most sensible zones. For example, the S_i spatial variations within the model concerning the cement content and the thermal conductivity, that had already been analyzed from the results of Figure 5.9, may now be confirmed: in Figure 5.10a the cement content is clearly more influent in the center of the model; in Figure 5.10b the thermal conductivity is clearly more influent near the boundaries of the model and presents $S_i \approx 0$ in the center of the model.

In Figures 5.11 and 5.12 are displayed the sensitivity indices obtained for the four sets of RBD-FAST computations, on the point near the downstream face of the dam. A general

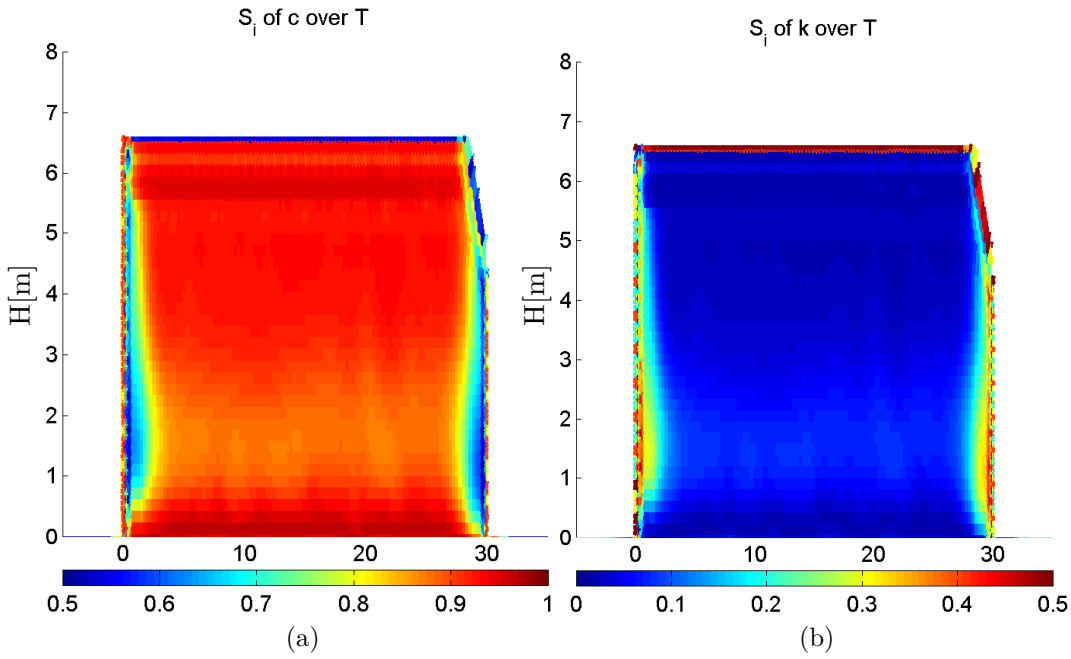

Figure 5.10: RBD-FAST set #1, surfaces of S_i: a) S_i of c over temperature; b) S_i of k over temperature.

conclusion that may be drawn from these results is that the contribution of each studied variable does not change much from one computation set to another. However, it is interesting to observe the differences on the thermal conductivity's S_i evolution in computations #1, #2 and #3. Between sets #1 and #2 the only difference on the computations relies on the h_c (deterministic) value (Table 5.3). While using the lowest value for h_c, the thermal conductivity affects the temperature results, slightly but yet differently: first of all, at the very beginning of the computation (that is, right after the placing of the RCC layer), it may be observed that the S_i is of ≈ 0.12, greater than the S_i for water-to-cement ratio; second of all, the evolution rate of S_i is slower than the one observed in set #1, reaching a final value of almost the half of the one reached for set #1.

According to these conclusions it seemed important to perform an RBD-FAST sensitivity test by giving the h_c parameter a random character, which is the case of sets #3 and #4. As stated in section 5.3, the convection coefficient h_c is given a random character via the wind speed v_{wind}. It may be observed in Figures 5.11c and 5.11d that the influence of the wind speed on temperature is insignificant, exception made for the instant right after placing where $S_i \approx 0.12$.

This behaviour indicates that probably there exists a relationship between the thermal conductivity and the convection coefficient (and/or the wind speed), specially right after placing

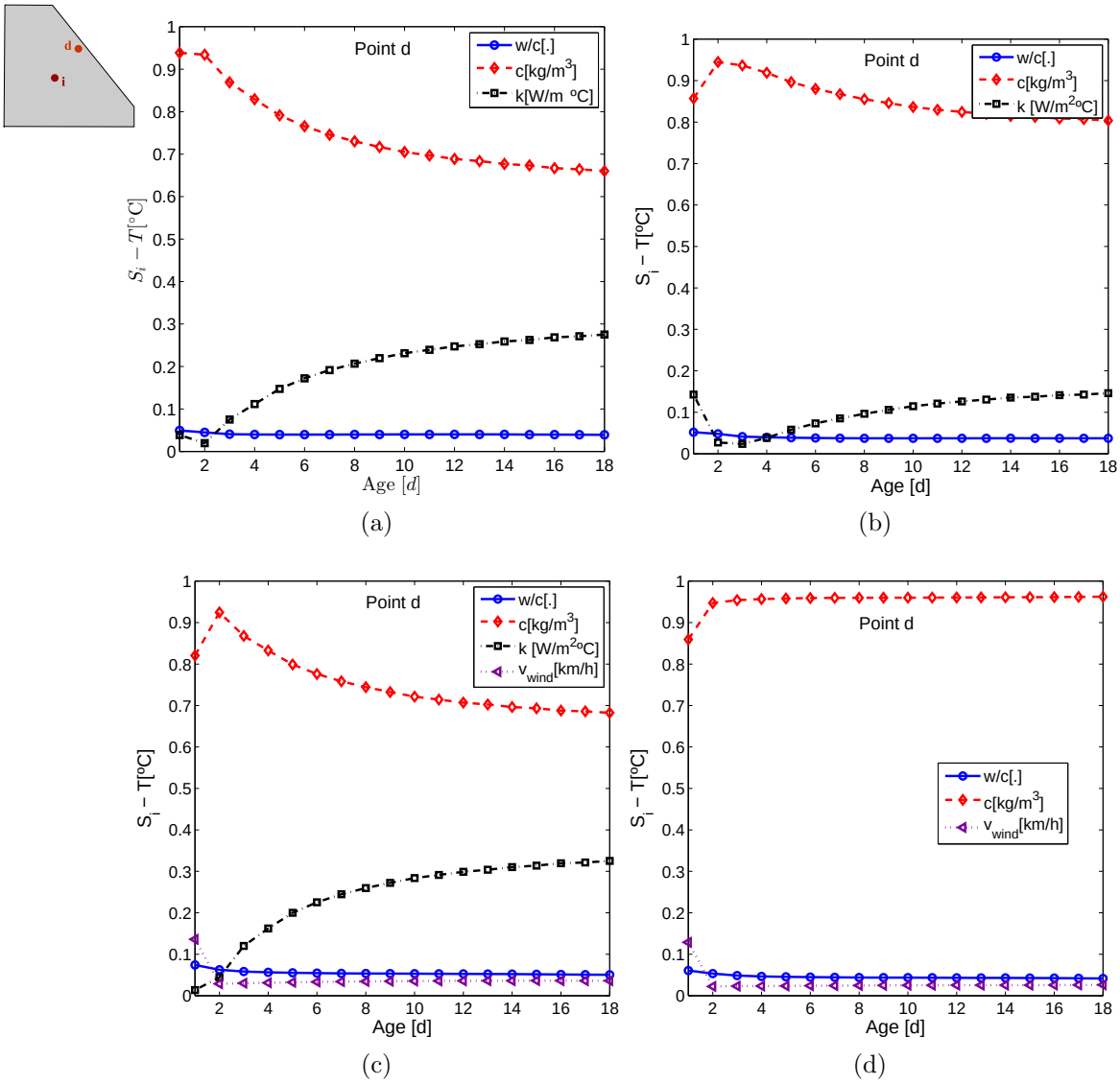

Figure 5.11: S_i over **temperature**, "point d": a) RBD-FAST set #1; b) RBD-FAST set #2; c) RBD-FAST set #3; d) RBD-FAST set #4.

and near the dam surfaces. The same behaviour may be observed for the hydration degree in Figure 5.12.

5.5 Results and discussion - 2D random fields

In the RBD-FAST computations described previously, the random variables are homogeneous within the dam model. This means that for each computation, only one set of (constant) parameters was used, which is equivalent to a random field with correlation lengths $\theta_x = +\infty$ and $\theta_y = +\infty$. In practice, this ideal situation never occurs. For example, while placing RCC there may be changes in the mixture or even in the compaction schedule all along the dam construction, which may lead to heterogeneity in some properties. This heterogeneity (or

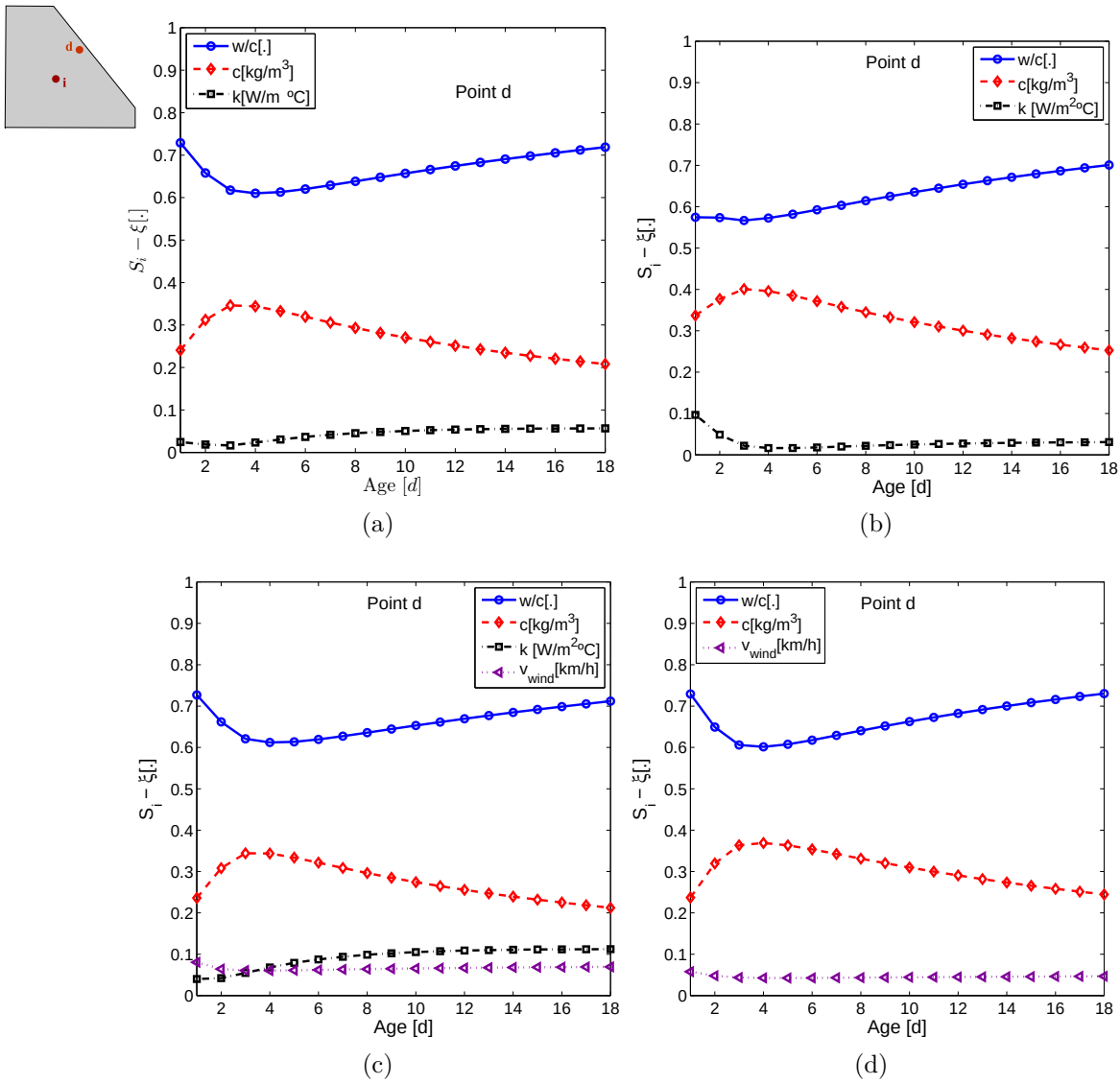

Figure 5.12: S_i over the **hydration degree**, "point d": a) RBD-FAST set #1; b) RBD-FAST set #2; c) RBD-FAST set #3; d) RBD-FAST set #4.

spatial variability) may be numerically expressed by considering those properties not only as random variables, but also as bi-dimensional random fields.

In this way, 2D random fields for the cement content, water-to-cement ratio and thermal conductivity were generated via the method described in section 5.2. It shall be enhanced here that the correlation lengths θ_x and θ_y are not based on any field measures and may be said to be too extreme, specially for set #6. Still, in future works, this methodology could be applied to a real case, depending on the availability of field data that would allow an accurate evaluation of the actual properties' spatial variation.

The input spatial variability on some model parameters will certainly lead to heterogeneity on the model output. This may be confirmed by the final surfaces of temperature, hydration

degree and compressive strength plotted in Figures 5.13 and 5.14. Please notice that these plots result from one sample of the random fields computation for set #5.

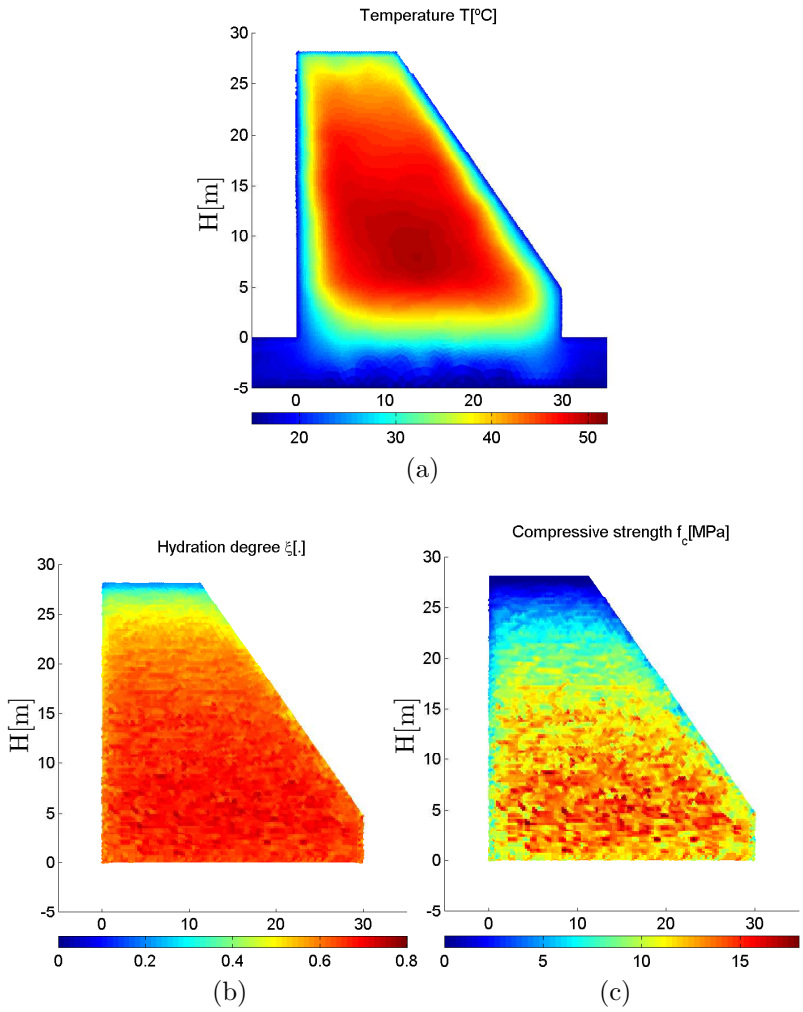

Figure 5.13: One result sample of the random fields computation set #5: a) Temperature; b) Hydration degree; c) Compressive strength.

Finally, in Figure 5.15a are compared the temperature evolution on "point d" for RBD-FAST computation set #1 and 2D random fields computations sets #5 and #6. It is interesting to observe the variance reduction on the results of the random fields computation when compared to the RBD-FAST computations. This behaviour is observed not only on temperature results but also on hydration and ageing degrees, on both points "i" and "d" (Figures 5.15b and 5.15c). In Figure 5.15a may also be observed the difference between sets #5 and #6. Random fields for set #6 are characterized by greater correlation lengths than set #5 (Table 5.4), which leads to a bigger range of output temperatures (greater variance).

Even if these results concern extreme cases (specially set #5), they illustrate well the importance of an accurate evaluation of the random variables/fields' statistical characteristics as

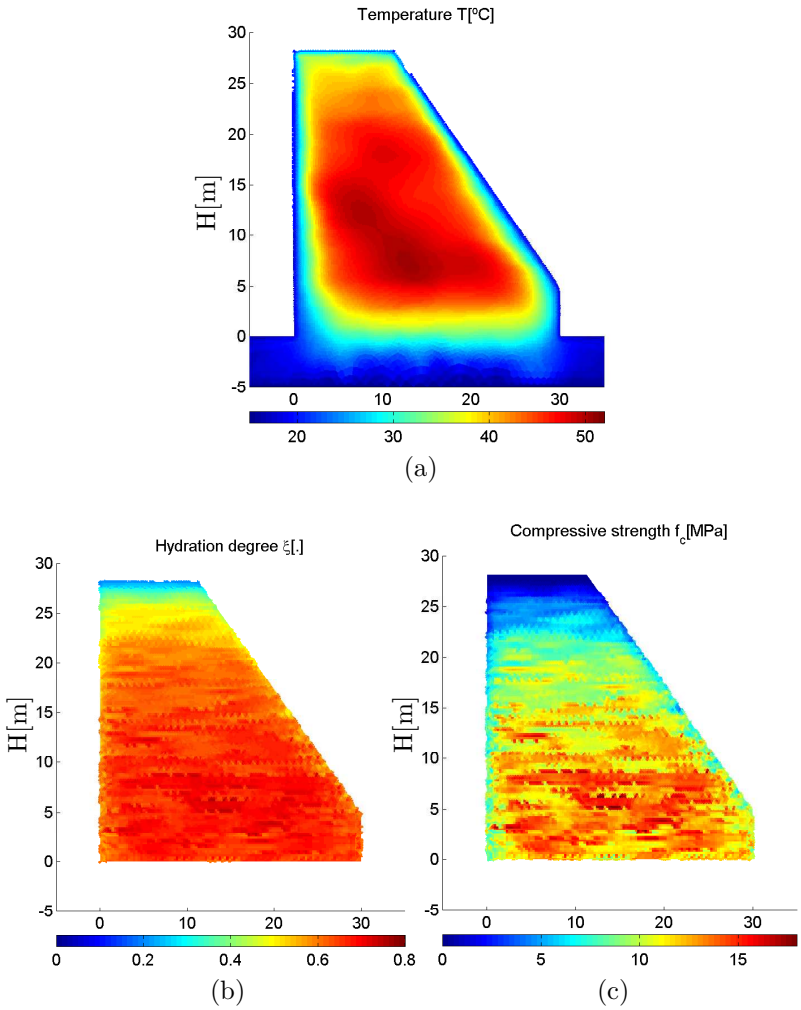

Figure 5.14: One result sample of the random fields computation set #6: a) Temperature; b) Hydration degree; c) Compressive strength.

well as their impact on the variance reduction of the model output.

5.6 Conclusions

A probabilistic numerical model was used to investigate the effect of some RCC properties' variability on the thermo-chemical behaviour of a dam. As far as the author is aware, this is the first application of uncertainty and sensitivity analysis, using RBD-FAST method and random fields to input material heterogeneity, in the analysis of an RCC dam behaviour during its construction phase.

The global sensitivity analysis, performed via RBD-FAST sensitivity test, revealed to be a very useful tool, giving precious information about the influence of each random variable on the model output. It also allowed to understand the different hierarchies existing for the studied uncertainties as function of the thermal loading and boundary conditions of the problem, that is,

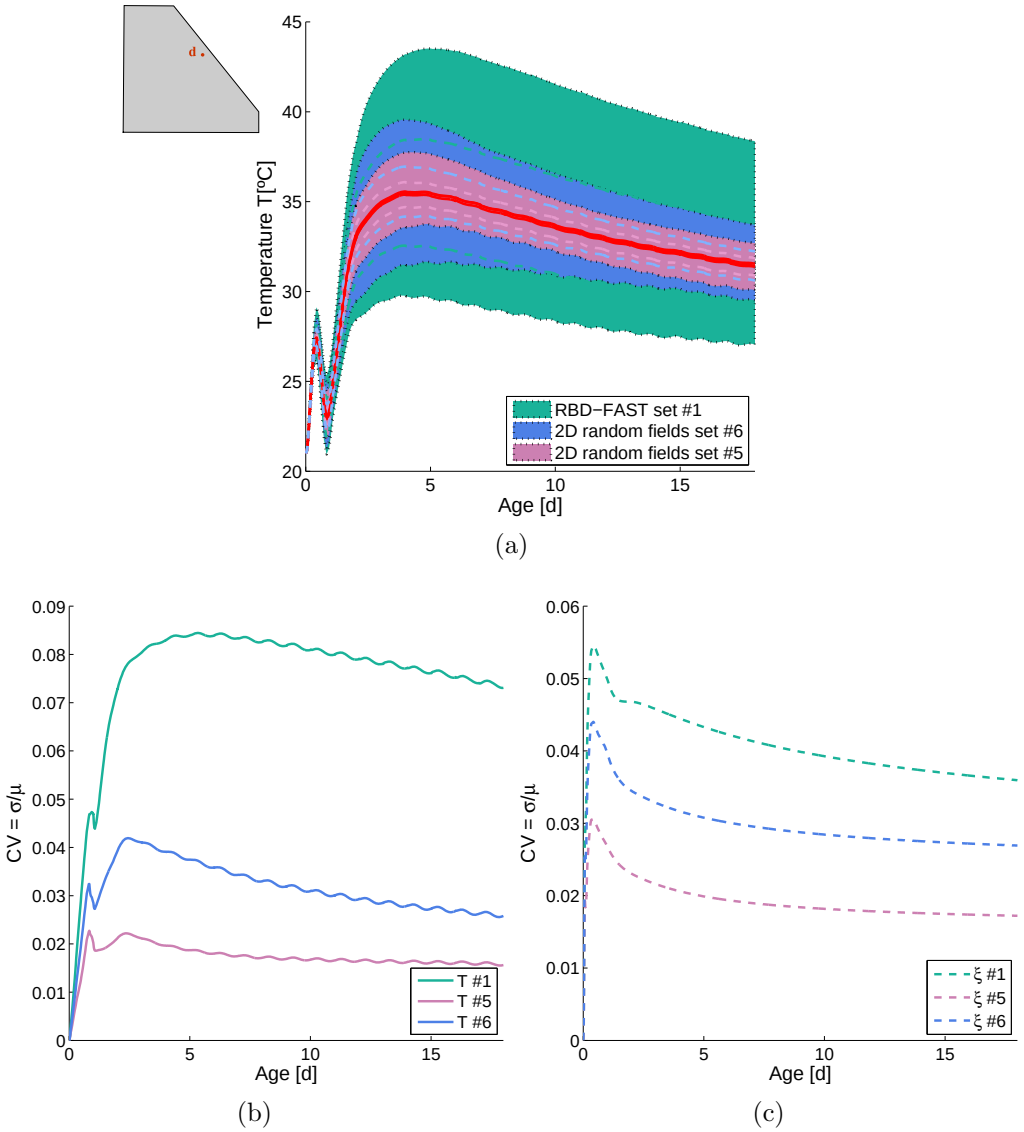

Figure 5.15: Results of computations #1, #5 and #6: a) Temperature; b) CV(t) "Point d" for temperature; c) CV(t) "Point d" for hydration degree.

different sensitivity indices are obtained whether the analyzed point is place on the center of the dam (adiabatic conditions) or near the downstream face of the dam (non-adiabatic conditions).

Within the four studied random variables, the convection coefficient presented negligible sensitivity indices, and was therefore given a deterministic value for the 2D random fields computations. However, a relation seems to exist between the thermal conductivity and the convection coefficient, which reveals to be an important fact to pay attention to in such a study.

The 2D random fields computations allowed the input of some spatial heterogeneity in the model, leading to a variance reduction on the model output.

Some hypotheses were adopted for this study, which will need to be revisited in further studies, such as: the random variables are independent and uniformly distributed; the construction scheme used for the simulation of the dam construction corresponds to a non-stop construction

with a rate of 0.6m/day, which is not realistic; the correlation lengths used to define the 2D random fields are not based on field measures.

It is important to stress out the following: each case study is unique and therefore the adopted parameters and random variables' statistical distributions in this chapter may be seen and interpreted as an example within the proposed methodology. Within each case study, parameters shall carefully be evaluated and decisions about their variation, either statistically (mean and CV values) or spatially (correlation lengths for the random fields), may rely not only on engineering expertise but also on available laboratory and field data. Of course, if such a study is to be performed during the design phase of a dam project, decisions about those statistical distributions will mostly be supported by the experts' experience and most likely be much conservative. However, a continuous monitoring during the dam's construction shall also greatly contribute to the learning process about how to account for uncertainties in such a project.

Chapter 6

Probabilistic thermo-chemo-mechanical analysis of an RCC gravity dam construction

In this chapter is achieved the main goal of the present thesis: to assess a probability of "failure" in an RCC dam during construction. The concept "failure", object of numerous meanings, is here considered as representing RCC cracking within each casted layer, ruled simply by the moment when the developed stresses are greater than the tensile strength attained so far.

The probabilistic model adopted here was previously presented in chapter 5, on which the proposed methodology was tested over the thermo-chemical model of the dam. Therefore, a Monte Carlo (MC) type method is used here both to propagate uncertainties through the model and to perform a sensitivity analysis over its output.

The probability of "failure" is here assessed using different approaches. First, an application using the reliability index β is made. Also, the FOSM method, a level II reliability method, is applied and the results compared with the ones obtained using a level III method (i.e. MC type simulations, in this case, the RBD-FAST method). Moreover, the cracking density is evaluated on some chosen layers and the probability of exceeding a given cracking density limit is assessed. Finally, a sensitivity analysis is carried out by means of the RBD-FAST test, over the temperature, hydration and ageing degrees, and stresses' results. Moreover, a naive Bayesian approach is applied as a kind of sensitivity analysis over the results of cracking density.

Such as in chapter 4, the full thermo-chemo-mechanical model is considered, allowing the computation of the stress level during the dam construction. The adopted procedure to evaluate

cracking index and density was previously applied in a deterministic context in chapter 4. Since this chapter concerns the application of that methodology to the thermo-chemo-mechanical model, uncertainties related to the mechanical behaviour are added those which were concluded to me more influent in chapter 5. Furthermore, the sensitivity analysis' results are compared with the ones presented in chapter 5. Finally, it shall be enhanced here that, as it was previously discussed in chapter 4, the adopted model is not able to account for the material self-healing at early ages, and therefore, once stress is greater than strength, it is considered to be cracked. Because the model does not accounts for damage either, cracking does not interfere with the evolution of mechanical properties such as the Young's modulus, since the model traduces a non-linear viscoelastic behaviour.

6.1 Application

The dam model used in the present chapter is the same as the one adopted in previous chapters 4 and 5. For the sake of brevity, only some general information is presented here. The model consists of an RCC gravity dam body of 28.2m high, 30m wide at its base level and with a downstream slope of 0.8, such as schematically represented in Figure 6.1.

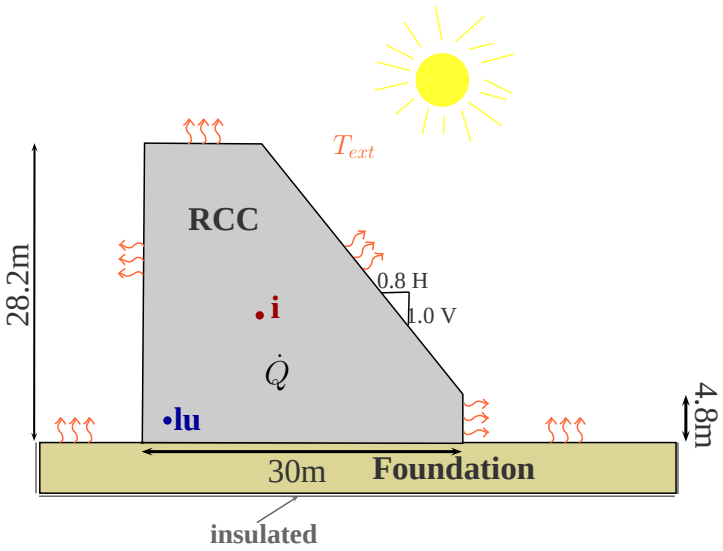

Figure 6.1: Dam model scheme

The construction schedule is performed by using a "multi-model" concept which consists of solving a sequence of models. To each of those models a 0.6m thick layer is added, the initial conditions of each one being the solution of the previous solved one. More details about the "multi-model" concept may be found in chapter 3. The adopted construction schedule for the

present chapter consists on casting one 0.6m thick layer per day and stopping for a 3-day period at the end of each set of 5 layers. This construction schedule corresponds to "cc fast" used in chapter 4, and is here depicter in Figure 6.2a.

The thermo-chemo-mechanical model used in this work accounts for the heat of hydration within the dam, given by $\dot{Q}[\mathrm{J/m^3}]$ (equation 6.1, where $l_\xi[\mathrm{J/m^3}]$ is the heat generated per cubic meter of RCC and $\xi[.]$ is the hydration degree). The evolution of the mechanical properties is dependent on both temperature and hydration degree by means of the ageing degree $\kappa[.]$ (equation 6.2). The hydration threshold given by ξ_{set} defines the beginning of the material's stiffening, above which the mechanical properties begin to evolve. Equations 6.5, 6.6 and 6.7 give the mechanical properties' evolution.

$$\dot{Q} = l_\xi \cdot \dot{\xi} \tag{6.1}$$

$$\dot{\kappa} = \lambda_T(T) \cdot \lambda_{f_c}(\xi) \cdot \dot{\xi} \geq 0 \tag{6.2}$$

$$\lambda_T(T) = \left(\frac{T_T - T}{T_T - T_{ref}} \right)^{n_T} \tag{6.3}$$

$$\lambda_{f_c}(\xi) = A_f \cdot \xi + B_f \quad \text{, for} \quad \xi \geq \xi_{set} \tag{6.4}$$

$$f_c(\kappa) = \kappa \cdot f_{c,\infty} \tag{6.5}$$

$$f_t(\kappa) = \kappa^{2/3} \cdot f_{t,\infty} \tag{6.6}$$

$$E(\kappa) = \kappa^{1/2} \cdot E_\infty \tag{6.7}$$

All of the dam faces, as well as the top foundation boundaries, interact with the environment through heat flux exchange, given by equation 6.8, where $h[\mathrm{W/(m^2 \cdot °C)}]$ is the heat transfer coefficient, $T_{ext}[°\mathrm{C}]$ is the ambient temperature, $k[\mathrm{W/(m \cdot °C)}]$ is the thermal conductivity and $\underline{n}$ is the normal vector to the surface. In the present chapter, two cases are considered for the ambient temperature evolution: winter and summer, depicted in Figure 6.2b. Equation 6.9 traduces the evolution of the ambient temperature. The adopted parameters are the same as those used in chapter 4 for cases "W1" and "S1", here described in Table 6.1.

$$\frac{\partial T}{\partial \underline{n}} = \begin{cases} \frac{h}{k} \cdot (T_{ext} - T) \\ 0 \text{ if insulated surface} \end{cases} \tag{6.8}$$

$$T_{ext}(t) = T_m + \Delta T_y \cdot \sin\left(2\pi \cdot f_y \cdot t + \phi_y\right) + \Delta T_d \cdot sin\left(2\pi \cdot f_d \cdot t + \phi_d\right) \tag{6.9}$$

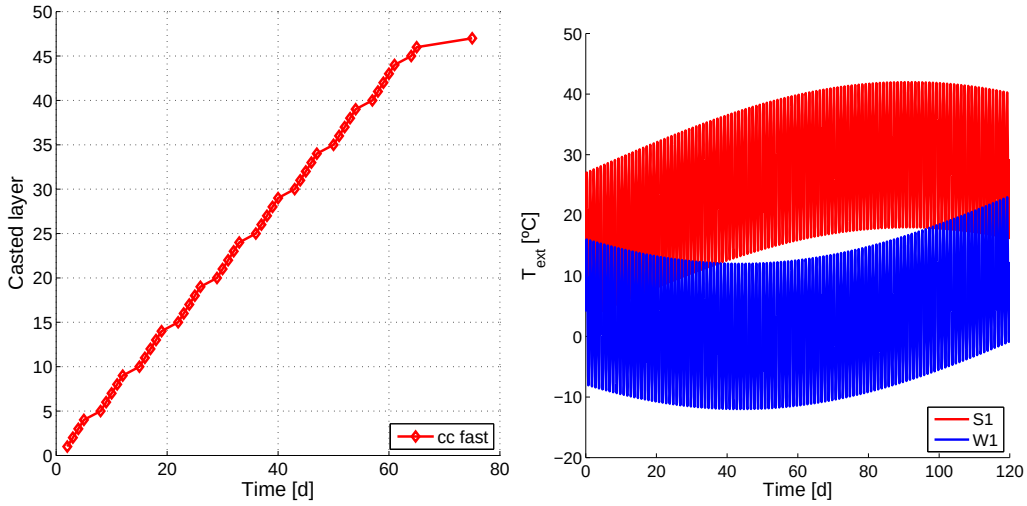

(a) (b)

Figure 6.2: a) Construction scheme; b) Ambient temperature.

Table 6.1: Parameters for ambient temperature evolution

	T_m[°C]	ΔT_y[°C]	ΔT_d[°C]	f_y[year^{-1}]	f_d[d^{-1}]	ϕ_y[rad]	ϕ_d[rad]
W1-S1	15	15	12	1	1	0	0.5

Such as in chapter 4, the results analyzed here concern the model response on both points "lu" and "i" (Figure 6.1), as well as layers on which those points are located. Moreover, other critical layers are also analyzed. These points intend to represent the model response in a point which is more mechanically and thermally loaded ("point lu" located at 2.1m from both the foundation and dam face) and a point where the thermal behaviour is expected to be adiabatic ("point i").

6.2 Model parameters and random variables

As recalled before, the hydration and mechanical model parameters adopted in this chapter are the same as in chapter 4, here described in Table 6.2. This set of model parameters corresponds to a typical RCC and are inspired from the work of Leitão et al. (2007) (hydration model) and the work of Cervera et al. (2000b) (mechanical model).

In order to account for some uncertainties related to the material behaviour, a random character is given to some model parameters. The choice of the thermal model parameters that have a random character (w/c, c and k) is here supported by the conclusions of chapter 5. Then, the hydration threshold ξ_{set} and the final compressive strength $f_{c,\infty}$ have also a random

character in order to account for uncertainty directly related to the mechanical model. Finally, a parameter that is related not only to the thermal model, but also to the environmental conditions that occur at the dam construction site, the casting temperature $T_0 = T_{ext} + \Delta T_0$, is also accounted for as a random variable (through uncertainties related to ΔT_0, which is the added temperature due to RCC mixing and transportation).

Therefore, in this work, uncertainties related to the following 6 parameters are accounted for by means of random variables, described in Table 6.3: water-to-cement ratio $w/c[.]$, cement content $c[\mathrm{kg/m^3}]$, hydration threshold $\xi_{set}[.]$, thermal conductivity $k[\mathrm{W/(m{\cdot}°C)}]$, added casting temperature $\Delta T_0[°\mathrm{C}]$ and final compressive strength $f_{c,\infty}[\mathrm{MPa}]$.

The statistics of all of the six independent and uniformly distributed random variables are plotted in Figure 6.3. Such as in chapter 5, not all of these random variables will directly influence the model parameters. The model parameters which are affected by the randomness injected on those variables are the final hydration degree $\xi_\infty[.]$ (equation 6.10), the hydration heat per unit volume $l_\xi[\mathrm{J/m^3}]$ (equation 6.11, where $q_c = 283.6\ \mathrm{kJ/m^3}$), the final tensile strength $f_{t,\infty}[\mathrm{MPa}]$ (equation 6.12, where $A_+ = 0.342$) and the final Young's modulus $E_\infty[\mathrm{GPa}]$ (equation 6.13, where $A_e = 3.95$). The correspondent histograms of the input distributions for these parameters are plotted in Figure 6.4.

$$\xi_\infty = \frac{1.031 \cdot w/c}{0.194 + w/c} \tag{6.10}$$

$$l_\xi = c \cdot q_c \tag{6.11}$$

$$f_{t,\infty} = A_+ \cdot f_{c,\infty}^{2/3} \tag{6.12}$$

$$E_\infty = A_e \cdot f_{c,\infty}^{1/2} \tag{6.13}$$

Table 6.2: Model parameters

Hydration model	$\frac{E_a}{R}[\mathrm{K}]$ 5000	$\frac{k_\xi}{\eta_{\xi_0}}[\mathrm{s^{-1}}]$ 2500	$\frac{A_{\xi_0}}{k_\xi}$ 0.005	$\overline{\eta}$ 8.1	ξ_∞ 0.779	– –
Viscoelastic model	$E^1 : E^2$ 3:1	$\tau_2[\mathrm{h}]$ 1	ν 0.2	$E_\infty[\mathrm{GPa}]$ 25	$f_{c,\infty}[\mathrm{MPa}]$ 40	$f_{t,\infty}[\mathrm{MPa}]$ 4
Mechanical coupling	A_f 3.0	B_f 0.1	n_T 0.12	ξ_{set} 0.3	– –	– –
General parameters	$\rho[\frac{kg}{m^3}]$ 2400	$c[\frac{J}{kg \cdot K}]$ 921	$q_c[\frac{kJ}{kg}]$ 284	$k[\frac{W}{m \cdot °C}]$ 2.3	$h[\frac{W}{m^2 \cdot °C}]$ 27	$\alpha_T[\frac{1}{°C}]$ $0.6 \cdot 10^{-5}$

Table 6.3: Random variables

	w/c[.]	c[kg/m^3]	ξ_{set}[.]	k[W/(m·°C)]	ΔT_0[°C]	$f_{c,\infty}$[MPa]
μ	0.6	220	0.3	2.3	2	40
CV	0.1	0.15	0.2	0.25	0.5	0.25

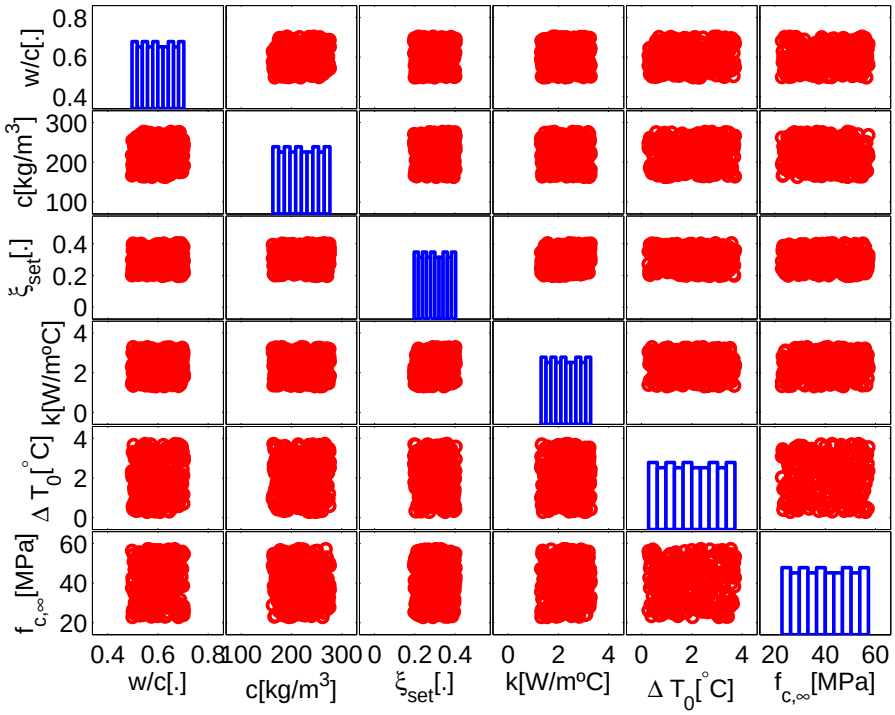

Figure 6.3: Statistics of the input random variables

All of the random variables are considered to be uniformly distributed. This choice relies on the fact that, even if the existent database for RCC dams is large, each dam project and RCC mixture is unique. To rely on an ensemble of data from different dam projects in order to define probability distributions of the desired parameters could be done but seemed risky in the present framework, and it was therefore decided to perform the study by adopting uniform distributions for all of the random parameters. This does not invalidates, however, the applicability of the presented methodology by adopting normal or lognormal distributions to account for uncertainties related to model parameters. Still, the adopted mean and coefficient of variation values were carefully chosen relying on available data from literature (ACI Committee 207, 1999; Conrad, 2006; Leitão et al., 2007). For example, the choice of the final compressive strength's $f_{c,\infty}$ mean and coefficient of variation is justified by the data from literature which relates this parameter to the amount of cement (in this case, cement and fly ash, C+F). This relationship was reported by Conrad (2006) and may be found in chapter 2 of this thesis, in

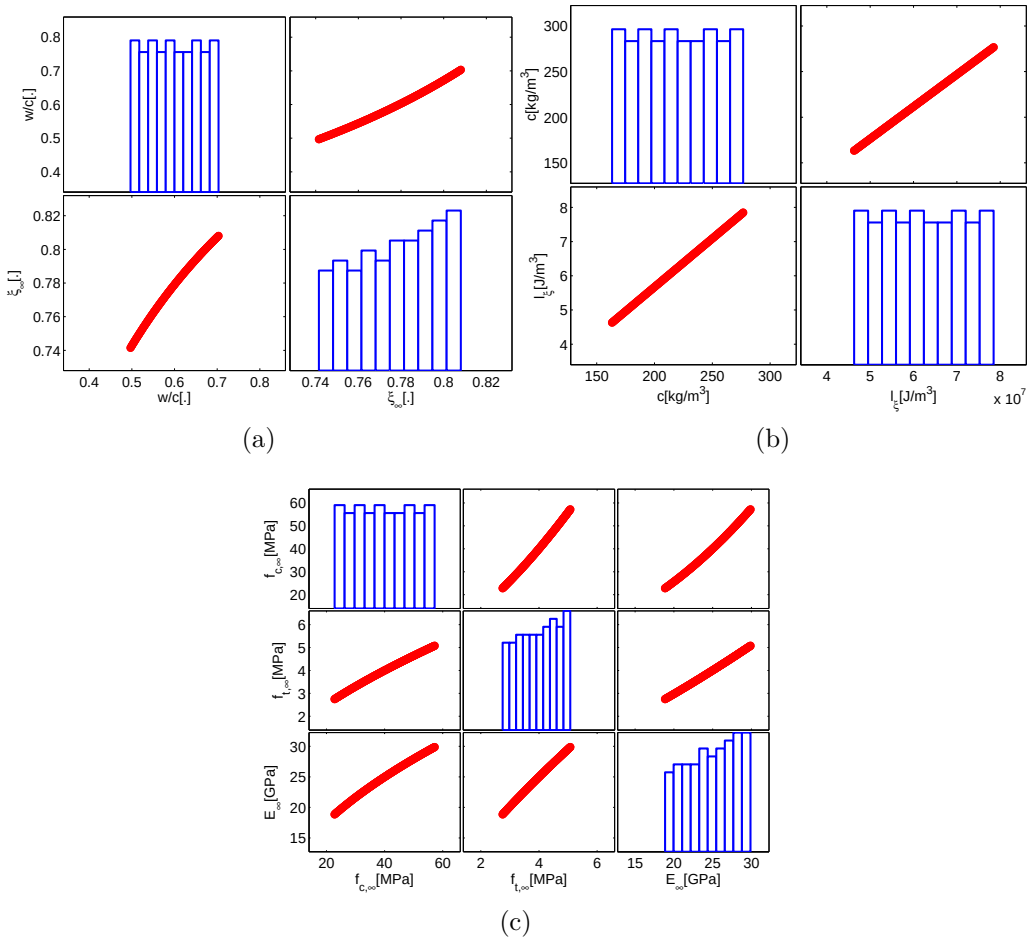

Figure 6.4: Statistics of model parameters affected by random variables: a) Water-to-cement ratio and final hydration degree; b) Cement content and heat of hydration; c) Final compressive and tensile strengths and Young's modulus.

Figure 2.18. In this Figure 2.18, the compressive strength at 365 days of age, for $c + f \simeq 220\text{kg/m}^3$ is of approximately 40MPa, if the USACE curve is considered. Then, in the case of Mujib dam also reported by Conrad (2006), the Young's modulus at 365 days of age (Figure 2.19) presents a coefficient of variation $CV = 0.26$. Based on these records, a mean value of 40MPa and a CV of 0.25 was adopted for $f_{c,\infty}$, which, given equation 6.13 will lead to a similar CV for E_∞.

6.3 Evaluation of the probability of cracking

At the image of the work presented in chapter 4, which concerns deterministic evaluations of the cracking density in a given layer, the same analysis is performed in this chapter in a probabilistic manner, leading to the obtention of a complementary cumulative distribution function (CCDF) which traduces the probability of exceeding the cracking density in each layer at a given age.

The adopted procedure to compute the cracking density is fully addressed in chapter 3.

In the present study, two sets of 250 computations are performed. For each set, the random variables are the same, the ambient temperature evolution differing. As previously exposed, two different scenarios are considered for T_{ext}, as described in Figure 6.2b: one for a construction during winter/cold season, and another for a construction during summer/hot season.

In the following, firstly the output of the model (temperature, hydration and ageing degrees and first principal stresses) are evaluated in the two analyzed points "lu" and "i". Then, the probability of cracking (i.e. $P[(f_t - \sigma_1) \leq 0]$) is assessed on those two points by means of the commonly used reliability index (β of Cornell (1967)). Also, the FOSM method is applied and the results compared. Afterwards, the cracking density is evaluated on some chosen layers. Then, probability curves are assessed on those layers and at different ages of the material.

6.3.1 Temperature, hydration and ageing degrees, and first principal stress results

In Figure 6.5 is plotted the obtained temperature evolution on "point lu" corresponding to the 250 computations, as well as the mean, median and standard deviation for both case scenarios, winter and summer. It is also depicted the result of a deterministic computation performed with the mean values of all of the considered random variables. The ambient temperature influence on the output of the model is well evidenced in Figure 6.5 both by the casting temperature (around 6°C for winter and 20°C for summer) and by the temperature evolution itself: the temperature output is decreasing during winter after the temperature peak due to hydration and continuously increasing during summer until the end of construction due to an increasing mean ambient temperature (conf. Figure 6.2b).

The statistical convergence of the results was evaluated and assumed to be sufficient for the purpose of the present study. In Figure 6.6 are plotted the convergence of the mean, standard deviation and CV estimators for temperature evaluated on "point lu" at the end of dam's construction simulation, for the winter case scenario. In Figure 6.6 are also plotted, by dashed lines, the confidence intervals obtained via the t-student and χ^2 statistical models at 5% of confidence for the mean and standard deviation estimators, respectively.

These results concern the temperature obtained on a point located near the foundation and upstream face of the dam ("point lu"). As it was previously observed in chapter 5, for the point located near the dam faces (here "point lu", in chapter 5 "point d"), the temperature evolution

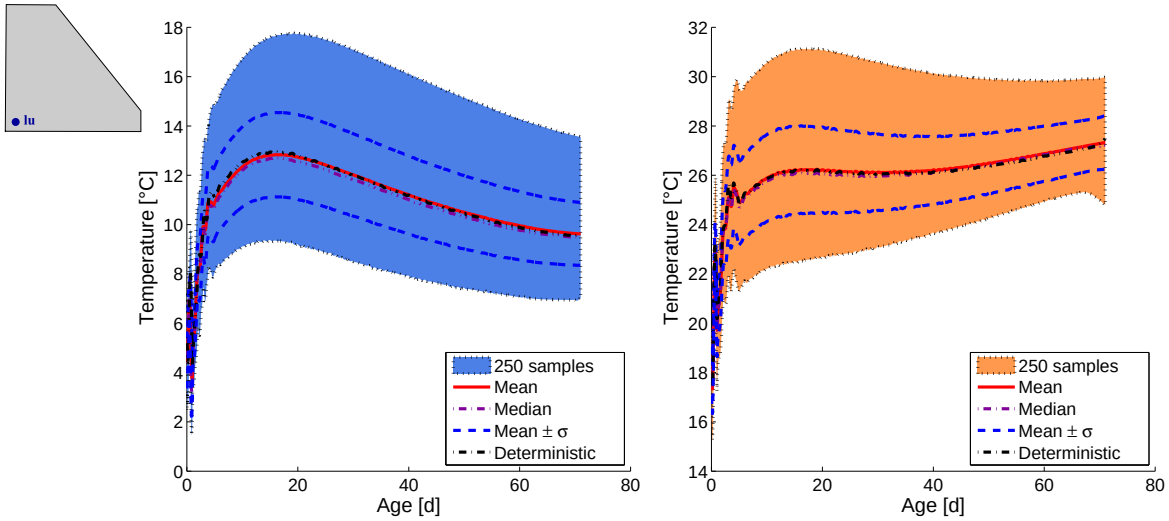

Figure 6.5: Temperature evolution on "point lu": a) Construction during winter; b) Construction during summer.

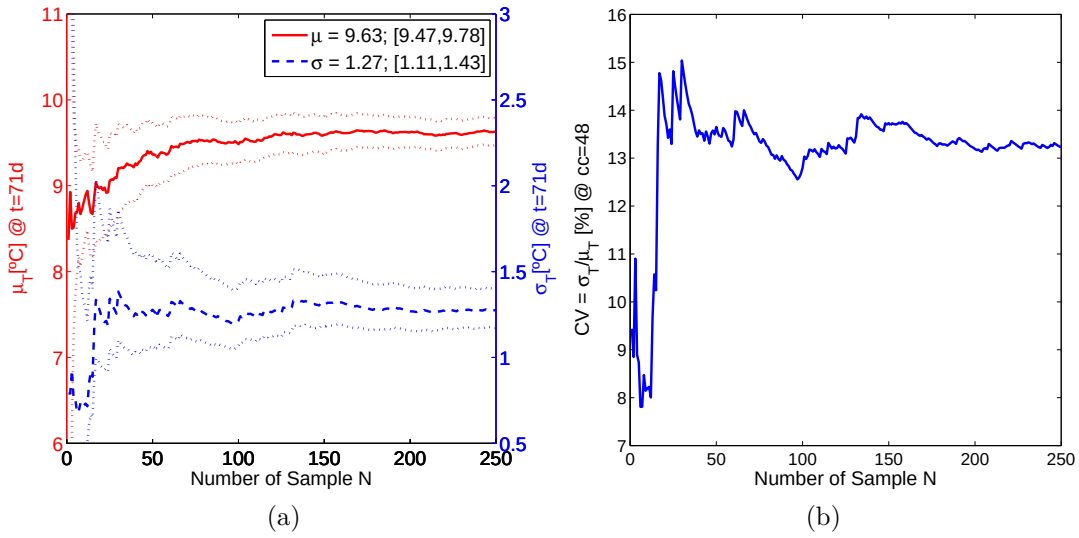

Figure 6.6: Convergence of temperature results on "point lu" at the end of construction: a) Mean and standard deviation estimators; b) CV estimator.

right after casting (in the first days of age) is very much influenced by the daily oscillations characteristic of the ambient temperature. Analyzing Figure 6.7 it may be seen that the same happens for the point at the interior of the dam ("point i"), right after casting. This is because, for the adopted construction scheme, there is a 3-day pause in construction after casting layer #20. "Point i", located in layer #19 is therefore at 0.9m from the surface of layer #20 and suffers from the ambient temperature oscillations (please recall that "point lu" is located at 2.1m from the dam surface). However, after the stopping period of 3 days, the temperature at "point i" continues to increase either during winter and summer, representing the expected

adiabatic behaviour in the dam core.

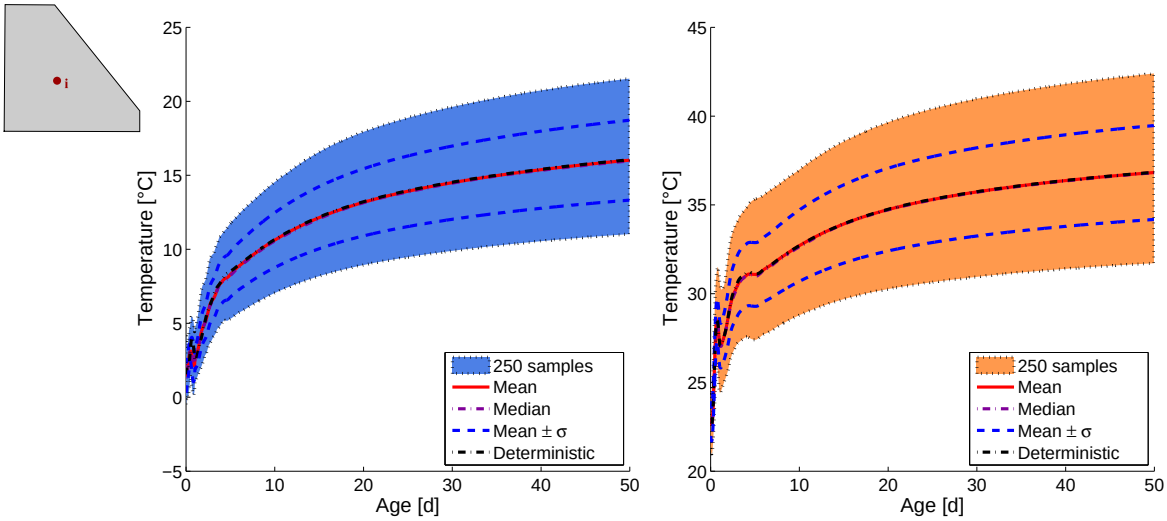

Figure 6.7: Temperature evolution on "point i": a) Construction during winter; b) Construction during summer.

The hydration and ageing degree evolutions are very similar on both points "lu" and "i" for the two case scenarios. Therefore, for the sake of brevity, in Figure 6.8 are only plotted the results in "point lu". The randomness introduced in ξ_{set} is well evidenced in Figure 6.8b by a wide range of ages for $\kappa = 0$ that covers the beginning of the ageing degree evolution for all of the 250 computations.

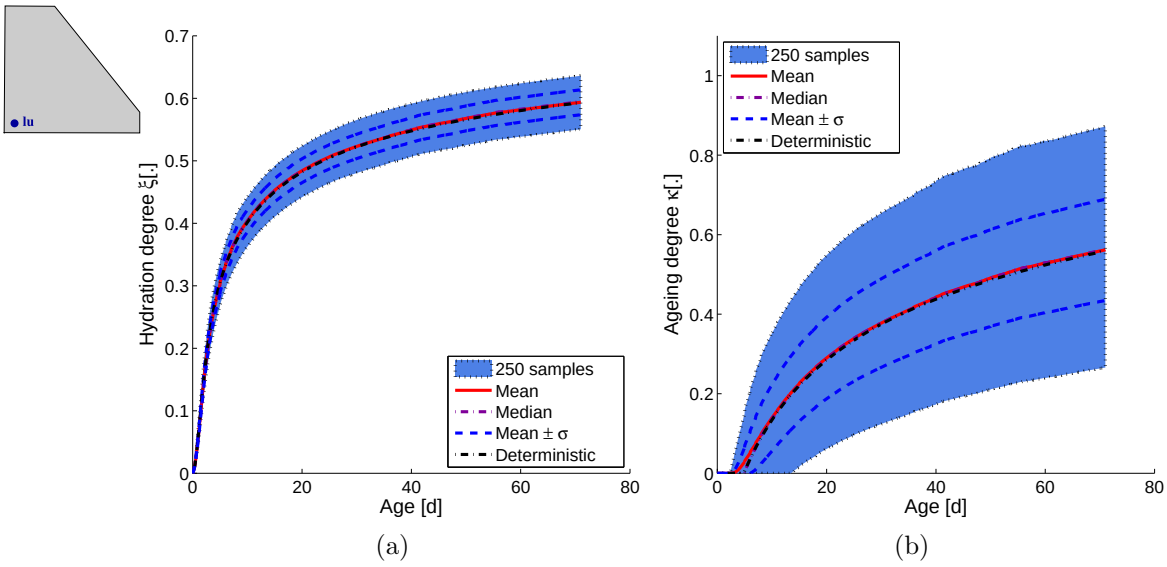

Figure 6.8: Hydration and ageing degrees evolution on "point lu": a) Construction during winter; b) Construction during summer.

In Figures 6.9 and 6.10 are plotted the first principal stresses and tensile strengths evolutions

obtained on points "lu" and "i", respectively.

For both case scenarios winter and summer, "point lu" is mostly under compression until approximately 30 days of age, when the inflection changes, stresses begin to increase and tensile stresses arise. When the tensile stress is greater than the tensile strength (grey area), then cracking occurs. However, there may be some computations on which the set of random values is such that it leads to stresses that will never overlap the developed strength during the construction period. It shall be enhanced here that in the present model the stresses' redistribution that occurs once cracking takes place is not accounted for in the present approach, which is why high tensile stress values are obtained when compared with the reality. If a comparison is done between the mean results of Figure 6.9a and the results of the default case of Figure 4.6e (in chapter 4), the differences are due to the construction scheme, which was continuous in the deterministic default case of chapter 4 and is, on the other hand, discontinuous in the present chapter, by accounting for stops of 3 days after each 5-day construction period.

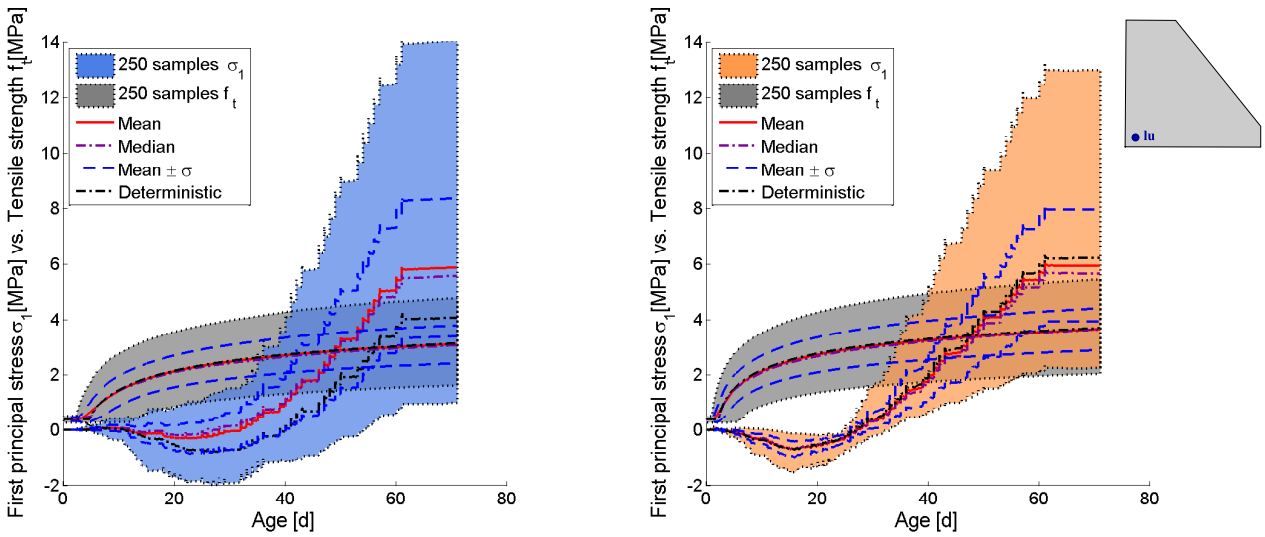

(a) (b)

Figure 6.9: First principal stress and tensile strength evolution on "point lu": a) Construction during winter; b) Construction during summer.

On "point i", in Figure 6.10, it is concluded that during summer greater compressive stresses occur during the construction period. By comparing the developed stresses and strengths, it may be concluded that "point i" is more prone to cracking at early ages right after casting, specially for a construction during summer. However, the stress mean response never overlaps the strength mean response, for both case scenarios winter and summer.

It shall be reminded here that on the present model, once failure has occurred (i.e. once $\sigma_1 \geq f_t$), the material is considered to be cracked for the rest of the analysis. This means that,

even if later in time the stress state has changed from tension to compression, if during tension the tensile strength was not sufficient to sustain it, then cracking occurs. This is well evidenced in Figure 6.10, where tensile stresses occur at early ages and may be greater than the tensile strength, passing later to the compression side.

6.3.2 Reliability index and FOSM

Now, the analysis of the obtained results could proceed in a more "traditional" manner by calculating the Cornell's reliability index β. Even if this approach is not adopted in the present work to achieve its main goal, an example is performed here in order to support its comprehension. The reliability index, previously presented in chapter 1, may be obtained here such as in equation 6.14, where μ_{f_t} and μ_{σ_1} are the mean values of the tensile strength ("capacity") and first principal stress ("demand"), respectively, σ_{f_t} and σ_{σ_1} being their standard deviations. This method assumes that both f_t and σ_1 may be represented by normal distributions and only uses the mean and standard deviation information resulting from the 250 computations to compute the probability of failure, which is obtained by the CDF of the standard normal distribution, Φ, such as in equation 6.15.

$$\beta = \frac{\mu_{f_t} - \mu_{\sigma_1}}{\sqrt{\sigma_{f_t}^2 + \sigma_{\sigma_1}^2}} \tag{6.14}$$

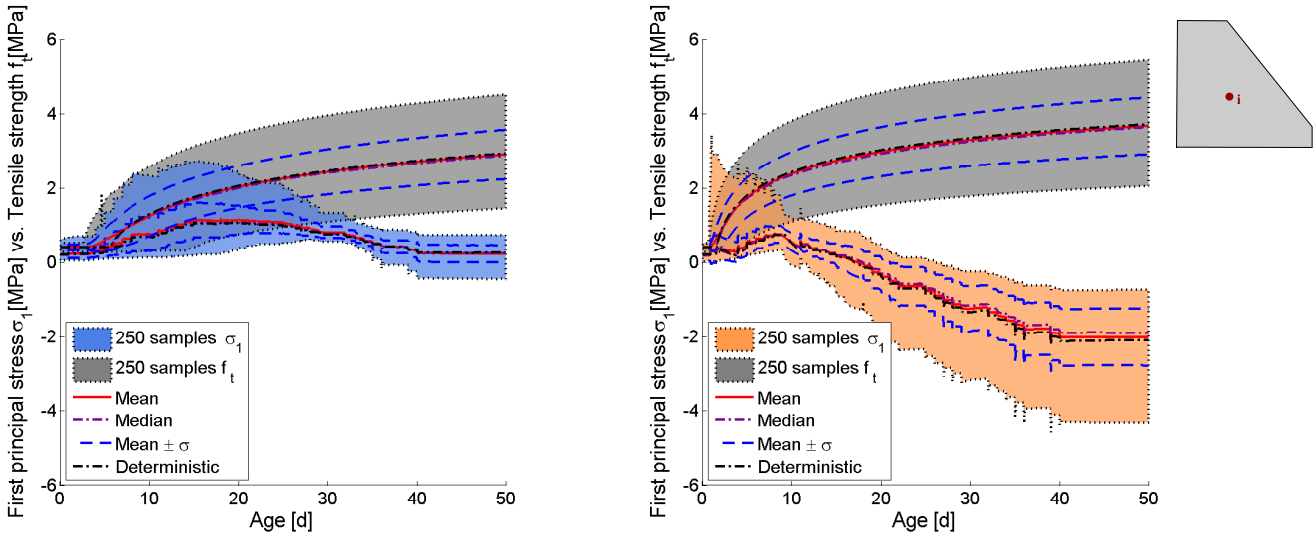

Figure 6.10: First principal stress and tensile strength evolution on "point i": a) Construction during winter; b) Construction during summer.

$$p_f = \Phi(-\beta) \tag{6.15}$$

In Figure 6.11 are plotted the evolutions of the reliability index β as well as the probability of failure $p_f = P[(f_t - \sigma_1) \leq 0]$ on "point lu" for both case scenarios. It may be concluded that for a construction during summer, the probability of failure between ages of 40 and 60 days is slightly higher, and that for both case scenarios the obtained reliability indexes and probabilities of failure are similar after the age of 60 days.

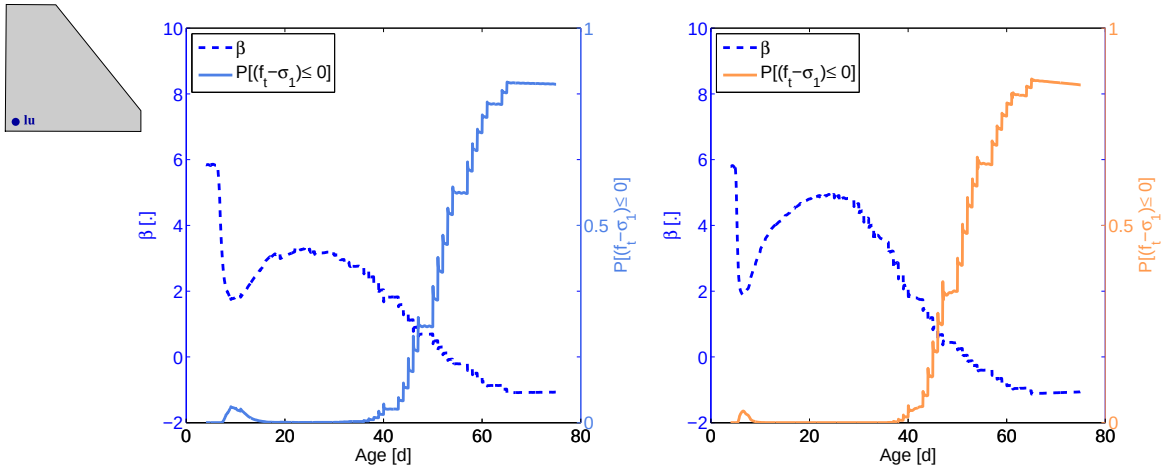

Figure 6.11: Reliability index β and probability of failure $P[(f_t - \sigma_1) \leq 0]$ on "point lu": a) Construction during winter; b) Construction during summer.

Now, a comparison of the obtained probability of failure by using all of the data resulting from the 250 computations, with an analysis using the FOSM method (*First Order Second Moment*, a level II reliability method). The results are plotted in Figure 6.12 for the summer case scenario.

For the 250 MC-type computations, the probability of failure estimator $\hat{p}_f$ and its coefficient of variation $CV[\hat{p}_f]$ are here computed by means of equations 6.16 to 6.20, where $g(X)$ is the so-called performance function, previously defined in chapter 1. For FOSM results (from $2 \cdot n + 1 = 13$ computations, n being the number of uncertain parameters), the probability of failure is obtained through the reliability index β (equation 6.14). It is concluded that the probabilities of failure obtained with the two approaches diverge for lower probabilities (at lower ages) and converge to the same values for greater probabilities.

$$p_f = \int_{g(X)\leq 0} f(X) \cdot dX \tag{6.16}$$

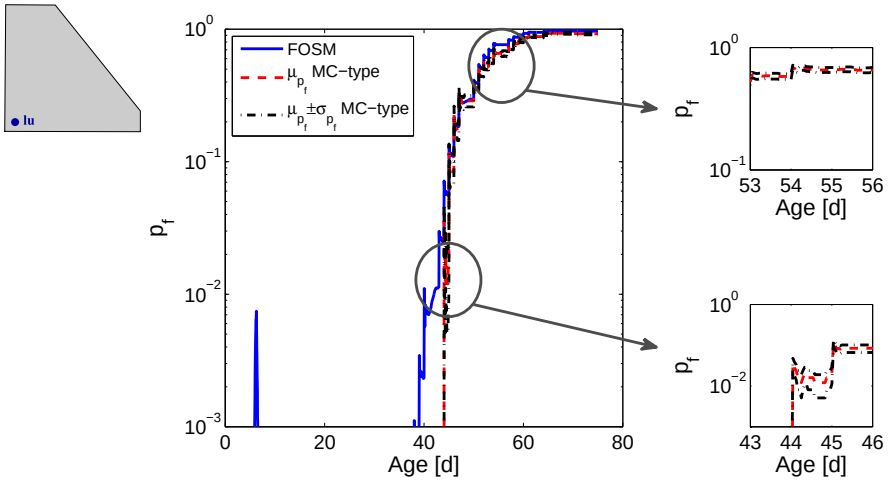

Figure 6.12: Probability of failure, FOSM vs. MC-type computations, evaluated in "point lu", summer case scenario

$$I_g = \begin{cases} 1 & g(X) \leq 0 \\ 0 & g(X) > 0 \end{cases} \tag{6.17}$$

$$p_f = \int_X I_g(X) \cdot f(X) \cdot dX \tag{6.18}$$

$$\hat{p}_f = \frac{1}{N} \sum_{i=1}^{N} I_g(X_i) \tag{6.19}$$

$$CV[\hat{p}_f] = \sqrt{\frac{1 - \hat{p}_f}{(N-1)\hat{p}_f}} \tag{6.20}$$

It is enhanced here that the probabilities of failure obtained for the MC-type computations are an estimate that will converge for an exact value by increasing the number of computations (here of 250). It may also be observed that the CV obtained for the 250 computations decreases for greater values of $\hat{p}_f$, which is expected, meaning that the uncertainty on the results is bigger for lower probabilities. Moreover, the fact that the results diverge for lower probabilities when comparing the FOSM and the MC-type computations enhances the importance of fully probabilistic methods on the reliability analysis of this kind of problems.

The probabilities of failure obtained here concern the response of the model in a single point within the dam body. Since the main goal of this work is to assess the cracking density within each casted layer, in the following the cracking density is evaluated in two different layers and furthermore the probability of failure within those layers is assessed.

6.3.3 Cracking density results

The cracking density may firstly be evaluated on all of the layers at the same time, i.e. for a given instant of construction, such as depicted in Figure 6.13 on which ρ_f is plotted as a function of the casted layer number at the end of the dam construction. The differences between winter and summer are evident. First of all, it may be observed that the cracking densities of the first 12 layers are similar for both case scenarios, with a slightly wider range of values for summer and a bigger peak value on the first layer. Apart from the first 12 layers, the differences on the obtained ranges of cracking densities are obvious, evidencing the construction scheme influence and its interaction with the ambient temperature.

During winter, some computations have reached a complete cracking ($\rho_f = 1.0$) on several subsequent layers. However, it is also observed that the mean result does not exceeds $\rho_f = 0.4$, which means that those curves attaining $\rho_f = 1.0$ consist on extreme cases. Moreover, the fact that the mean and deterministic curves do not coincide traduces the complex behaviour of the present analysis and, since the deterministic computation consists on using the mean values of the random variables, this may be an indicator that there may be an interaction between the adopted random variables, which should be further explored in future developments. This aspect will be further discussed for the sensitivity analysis in section 6.4.1.

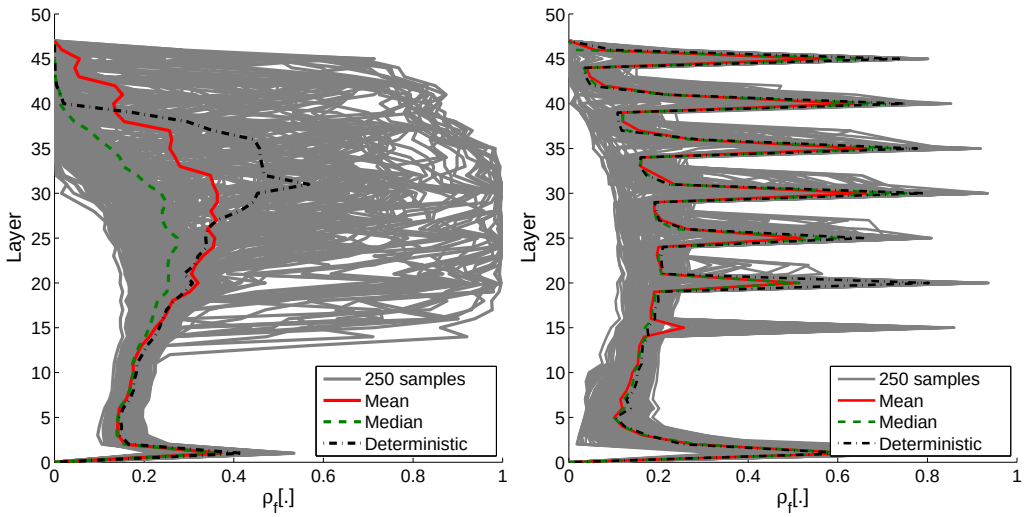

Figure 6.13: Cracking density in all layers at the end of construction: a) Construction during winter; b) Construction during summer.

Now, the following layers are chosen here in order to assess the cracking density evolution during construction in more detail: layers #4, #9 and #19. Layers #4 and #19 are those on

which points "lu" and "i" are located, respectively.

As depicted in Figures 6.14 and 6.15, a wider range of cracking density values is found for layers #4 and #9 at the end of construction, while constructing during summer. On both layers and for both scenarios, the maximum cracking density is around 0.2, the mean curve being characterized by lower values for the summer case scenario.

This analysis may be accompanied by Figure 6.13, from which these conclusions can also be drawn if the intention is to assess the cracking density at the time instant of the end of construction. It shall be enhanced here that those layers on which peak values of ρ_f are found in Figure 6.13b (layers #15, #20, #25, #30, #35, #40 and #45) are actually layers on which construction has stopped for a 3-day period (Figure 6.2a). As previously discussed in chapter 4, those are critical layers on which cold joints' treatment should take place, and may therefore be object of attention. This point will be further addressed in this chapter. Therefore, with Figure 6.13 it may also be concluded, if the peak values obtained for the summer case scenario are ignored, by comparing the mean (red) curves, that during winter greater cracking density values are obtained.

On the other hand, on layer #19, a wider range of values for cracking density is obtained for a construction during winter (Figure 6.16). In this layer, even if the mean curve stays below $\rho_f = 0.3$, some extreme cases occur, attaining the maximum $\rho_f = 1.0$. However, and if the peak values during summer are ignored, by comparing the mean curves (red ones) of Figures 6.13a and 6.13b it may be concluded that during winter, greater cracking density values are obtained.

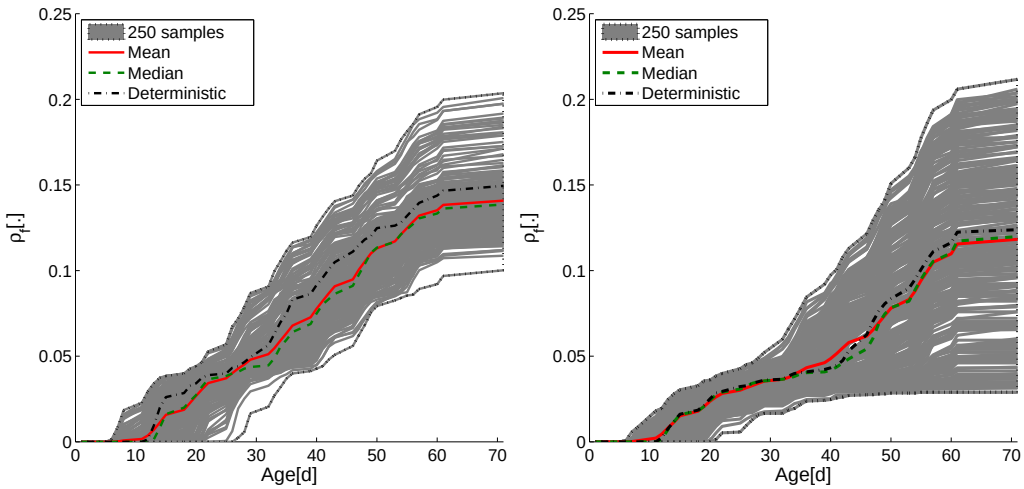

(a) (b)

Figure 6.14: Cracking density evolution in layer #4: a) Construction during winter; b) Construction during summer.

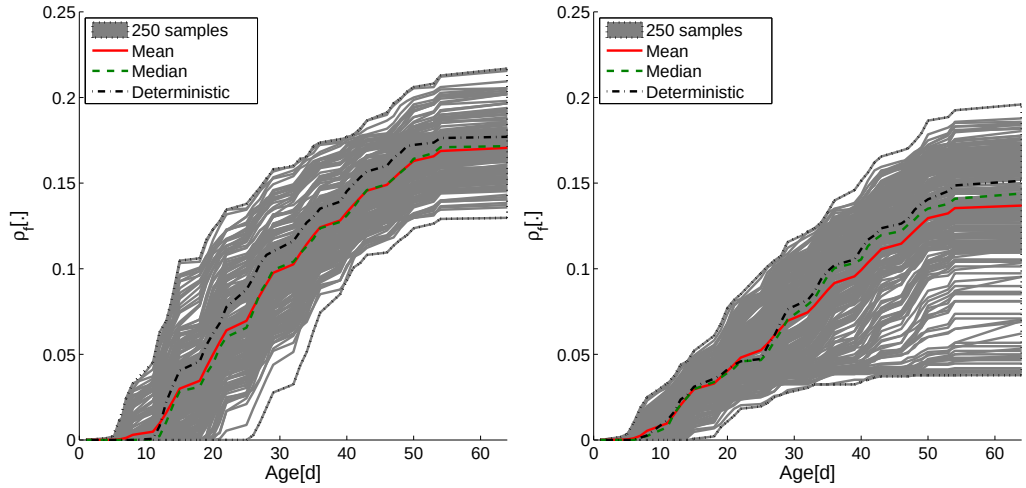

Figure 6.15: Cracking density evolution in layer #9: a) Construction during winter; b) Construction during summer.

For layer #19 (Figure 6.16a) it is well evidenced what was previously discussed in Figure 6.13: there are several sets of random variables that lead to complete cracking of the layer ($\rho_f = 1.0$) right after casting, which happens during winter (Figure 6.16a), and not during summer (Figure 6.16b), under the same construction schedule. This enhances the fact that it is not sufficient to rely on the mean and standard deviation results in this case, since the risk of neglecting extreme cases is higher. Moreover, those extreme cases may correspond to random variables' combinations which are less realistic. This can be further understood by applying a naive Bayesian approach, which is further presented in section 6.4.4.

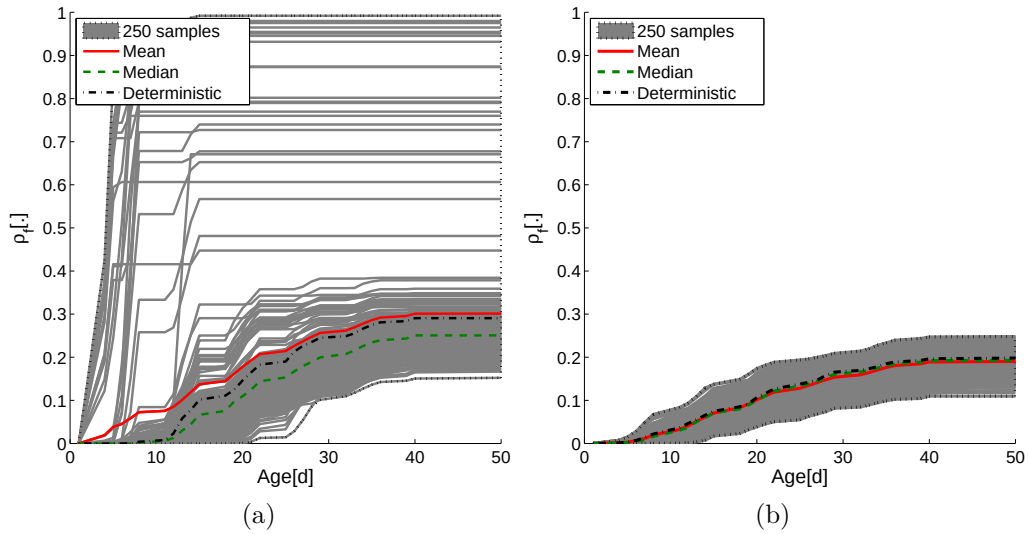

Figure 6.16: Cracking density evolution in layer #19: a) Construction during winter; b) Construction during summer.

6.3.4 Probability function for cracking density

In order to assess the probability of exceeding a certain cracking density within each layer, the complementary cumulative distribution function (CCDF) may be evaluated over the results of ρ_f, at each construction step (i.e. for a given material age). Here, an example is firstly performed over layer #9. In Figure 6.17 are plotted the cracking density results for the two considered scenarios, winter (Figure 6.17a) and summer (Figure 6.17b), as well as the probability distribution functions (pdf), evaluated at three different moments of construction: ages 15, 29 and 43 days, which correspond, in the construction schedule, to the instants of casting of layers #19, #29 and #39 respectively (Figure 6.2a). By comparing the pdf obtained at 43 days of age, the bigger output variability obtained for a construction during summer is clear, such as previously discussed in Figure 6.13 and verified in Figure 6.15b.

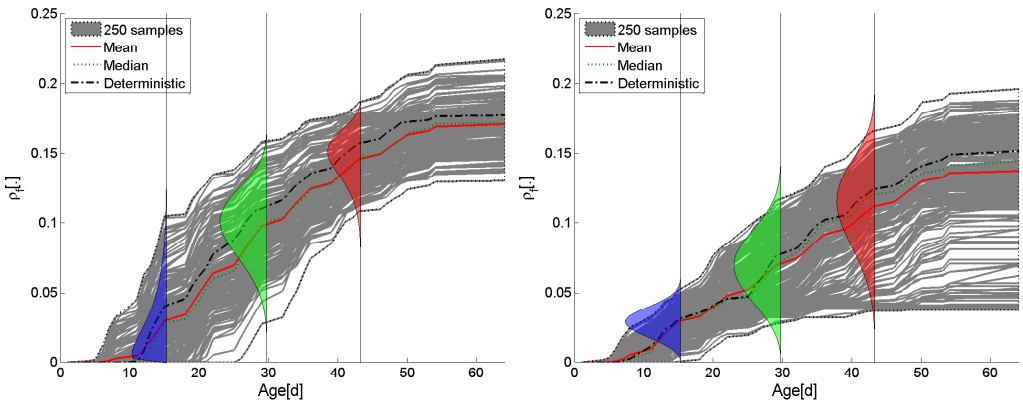

(a) (b)

Figure 6.17: Cracking density evolution in layer #9 and pdf at 15, 29 and 43 days of age: Construction during winter; b) Construction during summer.

It was found that the data adjusts well with the Weibull probability distribution function, given by equation 6.21, where α and m are the scale and shape factors, respectively. The Weibull CDF, given by equation 6.22, traduces the probability of the cracking density being lower than a certain limit $\rho_{f,lim}$. In this work, the aim is to assess the probability of exceeding $\rho_{f,lim}$ and therefore the complementary CDF (equation 6.23), here denominated CCDF, is evaluated instead (Helton et al., 2006).

$$f(\rho_f) = \frac{m}{\alpha}\left(\frac{\rho_f}{\alpha}\right)^{m-1} \exp\left[-\left(\frac{\rho_f}{\alpha}\right)^{m}\right] \tag{6.21}$$

$$P[\rho_f \leq \rho_{f,lim}] = 1 - \exp\left[-\left(\frac{\rho_f}{\alpha}\right)^{m}\right] \tag{6.22}$$

$$P[\rho_f \geq \rho_{f,lim}] = \exp\left[-\left(\frac{\rho_f}{\alpha}\right)^m\right] \tag{6.23}$$

In Figure 6.18 are plotted the obtained CCDF distributions corresponding to the pdf plotted in Figure 6.17 at 15, 29 and 43 days of age. The round points correspond to the data obtained from the 250 computations, being the continuous line the approximation obtained while applying the Weibull CCDF. A similar form of CCDF was found in the work of the Japan Concrete Institute (JCI, 2012) concerning cracking in concrete at early ages. The CCDF curve that resulted from JCI's work is based on numerical and experimental data performed over different concrete structures such as multi-layered members and columns on which cracking has occurred or not. In JCI (2012) it is concluded that the probability curve obtained is not independent of the type of structure under analysis and that much more data would be needed in order to increase the reliability of the obtained result, namely concerning structures without cracking.

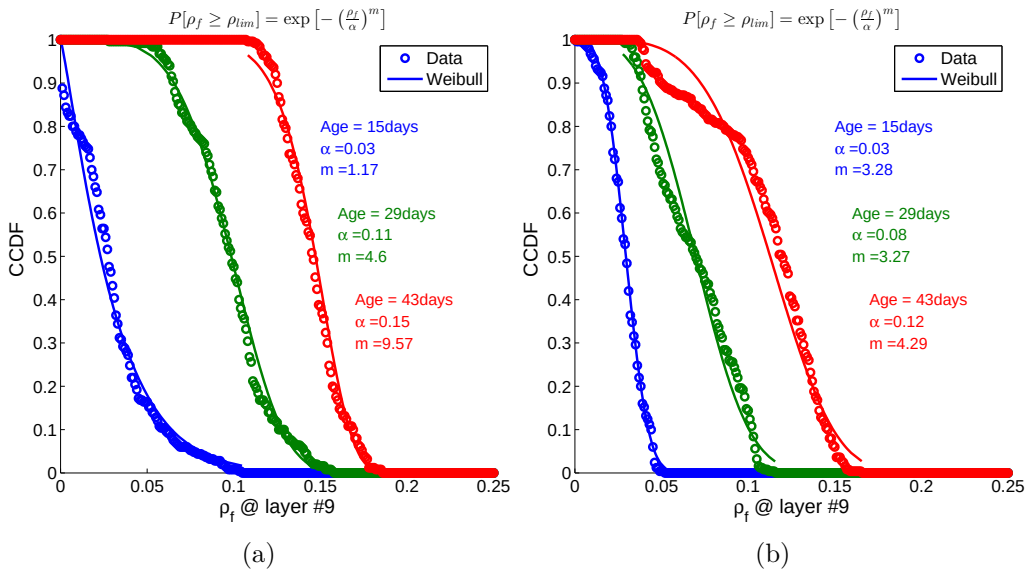

Figure 6.18: CCDF curves, $P[\rho_f \geq \rho_{f,lim}]$ in layer #9 at 15, 29 and 43 days of age: a) Construction during winter; b) Construction during summer.

From the results of Figure 6.18, it is concluded that the CCDF form will evolve with the layer's age, presenting changes on both scale and shape factors, α and m which are increasing with age. By comparing winter and summer results it is observed that, at the same age, α is very similar, while m presents bigger differences, namely at ages of 15 and 43 days: m more than doubles for 15 days of age during summer when comparing with winter; on the other hand, at 43 days of age, the opposite occurs and m is more than the double during winter than during summer. It may also be concluded that for the same level of cracking density limit $\rho_{f,lim}$, the probability $P[\rho_f \geq \rho_{f,lim}]$ is greater while constructing during winter, exception made

for the lower cracking densities at 15 days of age, on which $P[\rho_f \geq \rho_{f,lim}]$ is greater for the summer case scenario. Actually, it is the only case on which the shape factor m of the Weibull function is bigger for summer than for winter. This indicates that this particular layer would be more prone to develop cracking at early ages if the construction takes place during summer. However, this is only observed for very low values of the cracking density, since for higher values, the probability of exceeding them will be higher during winter than during summer (i.e. for $\rho_{f,lim} = 0.05$, $P[\rho_f \geq \rho_{f,lim}] = 0.15$ during winter and of $P[\rho_f \geq \rho_{f,lim}] = 0.0$ during summer, for layer #9 at 15 days of age). Therefore, these conclusions can not be generalized for all layers.

Now, this analysis may be performed over different layers, at the same material age, such as in Figure 6.19. It may be observed that, even if the age is the same on all of the three layers, the CCDFs present different shape and scale factors. This evidences the fact that this analysis not only accounts for the influence of the material age on the probability of exceeding a certain cracking density limit, but also for the position of the layer, its boundary conditions, ambient temperature and construction schedule scenarios. Once more, this enhances the fact that no conclusions about $P[\rho_f \geq \rho_{f,lim}]$ can be generalized from one layer to another.

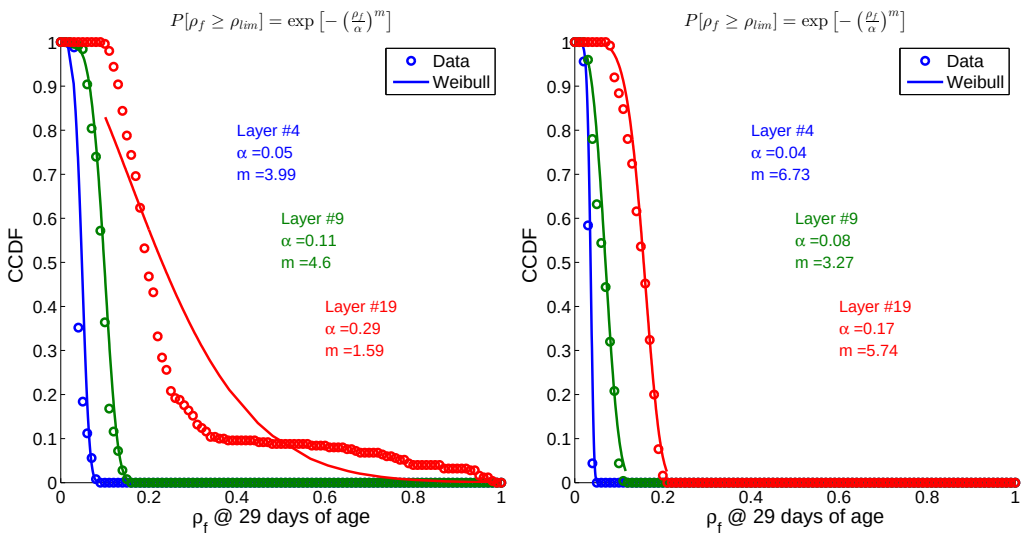

Figure 6.19: CCDF curves, $P[\rho_f \geq \rho_{f,lim}]$ in layers #4, #9 and #19 at 29 days of age: a) Construction during winter; b) Construction during summer.

It is interesting to analyze here those layers on which construction has stopped for a 3-day period and whose surfaces are considered to be cold joints. Let's consider layers #5, #10, #15 and #20, on which construction has stopped for a period of 3 days after their casting (Figure

6.2a). The CCDFs curves are evaluated at the end of the dam's construction and the results are plotted in Figure 6.20. What can be concluded here is that the Weibull distribution appears to fit well layers #5 and #10, which are located lower in the dam body. Not much difference is obtained for these two layers for both case scenarios. On the other hand, for layers #15 and #20, which are located higher in the dam body, the Weibull distribution seems not to fit as well to the computed 250 data. It is also observed that during summer, $P[\rho_f \geq \rho_{f,lim}]$ is higher for the summer case scenario. This has actually been reported before in Figure 6.13b, where it was clear that those layers on which construction has stopped show higher mean values for cracking density. These results enhances the conclusion that special attention shall be paid to layers on which the construction has stopped for several days and whose surfaces are considered to be cold joints, which had already been discussed in the deterministic approach presented in chapter 4. The results presented here lead also to the conclusion that even if this is a useful method, it concerns one layer at a time and a singular CCDF curve will not traduce the behaviour of the entire dam. This can be further enhanced by analyzing the obtained probabilities on all the entire dam body, such as demonstrated hereafter.

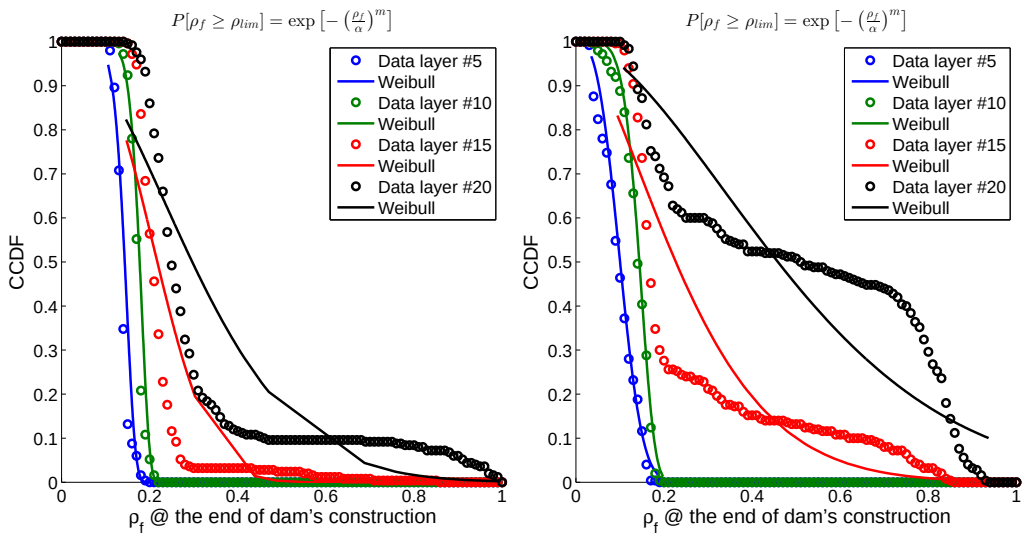

Figure 6.20: CCDF curves, $P[\rho_f \geq \rho_{f,lim}]$ in layers #5, #10, #15 and #20 at the end of dam's construction: a) Construction during winter; b) Construction during summer.

An example is performed by fixing $\rho_{f,lim} = 0.2$. In Figure 6.21 $P[\rho_f \geq \rho_{f,lim}]$ is plotted, assessed on each casted layer at the end of the dam's construction, for both case scenarios winter (Figure 6.21a) and summer (Figure 6.21b). The layers whose surfaces are considered to be cold joints (#5, #10, #15, #20, #25, #30, #35, #40 and #45) are indicated between black

bold lines. The higher probabilities obtained for the layers on which construction has stopped for 3 days are evident for a construction during summer, while during winter the probabilities surfaces evolve more smoother with the height of the dam. It is also concluded that, apart from the first two casted layers, there is a zone between heights of 2 and 7m on which the probabilities are very low for both case scenarios. As it was previously observed in Figure 6.13, the cracking densities obtained for the first 12 layers stay generally below the value of $\rho_f = 0.2$, which is why in this analysis $P[\rho_f \geq 0.2]$ is that low. Moreover, the reason why on those first 12 layers the output variability is lower is due to the compressive stresses which are acting on that lower part of the dam (such as demonstrated in chapter 4 with the deterministic results).

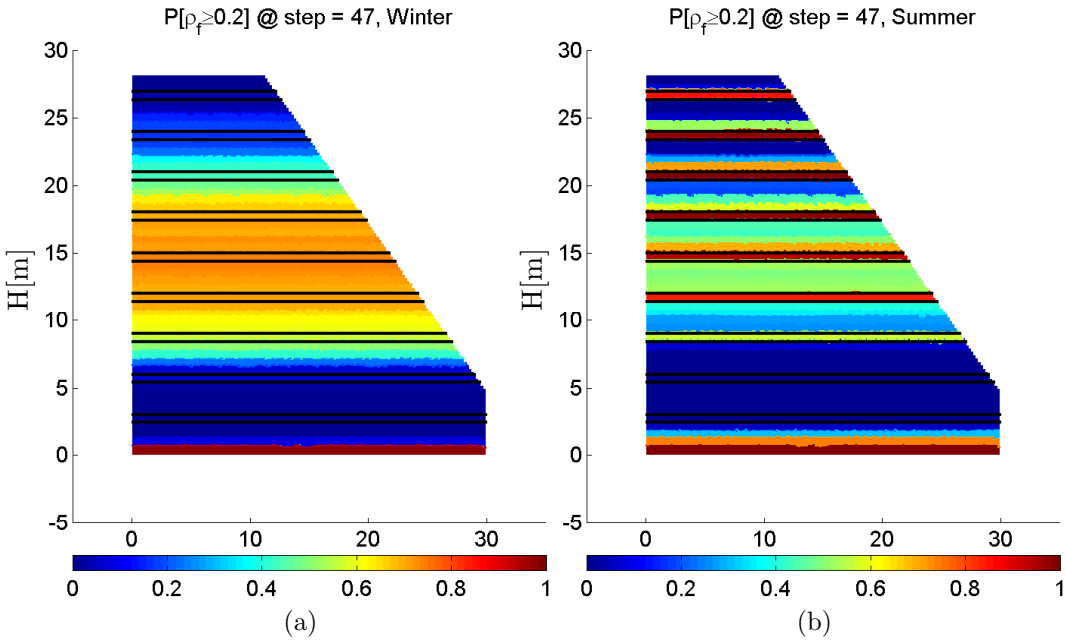

Figure 6.21: Probability surfaces at the end of the dam's construction a) Construction during winter; b) Construction during summer.

6.4 Sensitivity analysis

In this section is performed a global sensitivity analysis by means of the RBD-FAST test over the fully thermo-chemo-mechanical model. The same analysis was previously performed over the thermo-chemical model, and the results are exposed and discussed in chapter 5.

In this chapter is also introduced a naive Bayesian approach in order to overcome the impossibility of applying the sensitivity test RBD-FAST to the cracking density results.

6.4.1 RBD-FAST method

The RBD-FAST is a sensitivity test based on the Fourier Amplitude Sensitivity Test (FAST), and that uses the variance decomposition method in order to assess the first-order sensitivity indexes given by equation 6.24, where Y is the model output, X_i is a generic input variable, $V(E[Y|X_i])$ is the variance over the mean of the output given X_i, and $V(Y)$ is the variance of the model output. More details about the RBD-FAST are given in chapter 5 and in the appendix B.1 of this thesis.

$$S_i = \frac{V_i}{V} = \frac{V(E[Y|X_i])}{V(Y)} \tag{6.24}$$

The first-order sensitivity indexes are analyzed on both chosen points "lu" and "i" and intend to give information about the influence of each random variable on the output of the model, namely on temperature, hydration and ageing degrees, first principal stress and cracking index.

6.4.2 Temperature, hydration and ageing degrees, and first principal stress

The first-order sensitivity indexes plotted in Figure 6.22 traduce the influence of each random variable on the temperature output on "point lu". It is clear that the uncertain parameter that most influences the temperature output is the cement content c[kg/m^3], for both case scenarios, winter and summer. However, a clear difference is observed between the two scenarios: the S_i for thermal conductivity k[W/(m°C)] increases with age for a construction during winter, attaining $S_i = 0.4$ at the end of the analysis; the increasing of S_i for the thermal conductivity k[W/(m°C)] is accompanied by a decrease of S_i for the cement content c[kg/m^3]; on the other hand, during summer it presents values that do not exceed 0.15 at 20 days of age and that are almost zero at the end of construction.

From the results of the sensitivity analysis previously performed over the thermo-chemical model (chapter 5), the behaviour traduced in Figure 6.22a was expected. It was concluded on chapter 5 that, on a point near the dam face, the thermal conductivity plays an important role on the temperature evolution. However, the results obtained for a construction during summer for the thermo-chemo-mechanical model (Figure 6.22), on which the thermal conductivity appears to have little influence, prove that the complexity of the problem shall not be reduced to one only case scenario concerning the ambient temperature evolution. Moreover, the remain

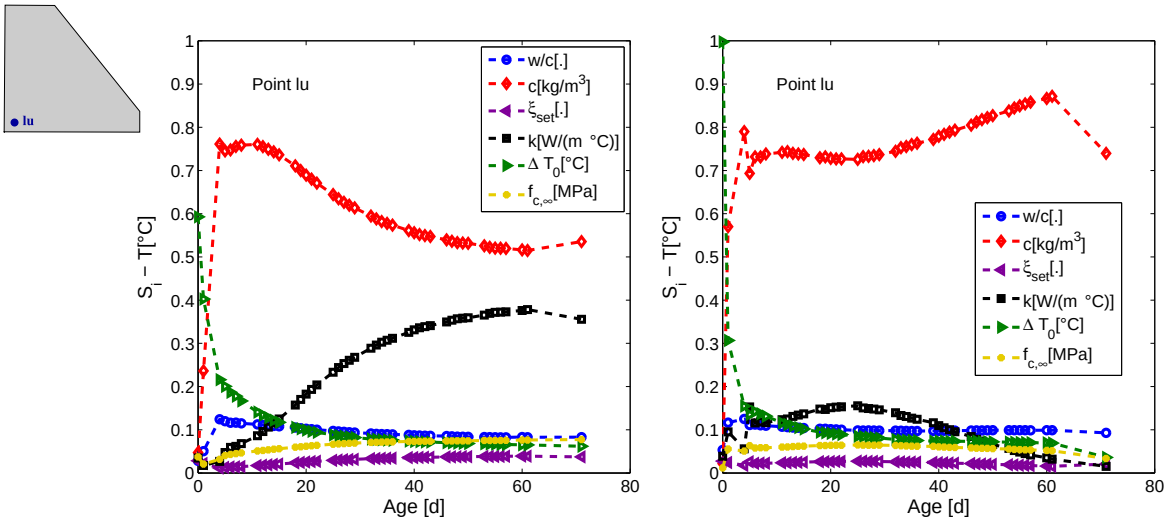

Figure 6.22: S_i over temperature at "point lu": a) Construction during winter; b) Construction during summer.

uncertainties considered through parameters w/c, ξ_{set} and $f_{c,\infty}$ present sensitivity indexes that do not exceed 0.1. An exception is made for ΔT_0, which greatly influences the temperature right after the construction (by means of the casting temperature $T_0 = T_{ext}(t = t_0) + \Delta T_0$), on the first days after casting, presenting values of 0.6 and 0.95 for winter and summer, respectively.

In Figure 6.23 are plotted the sensitivity indexes over temperature at "point i". As previously concluded in chapter 5 and verified in Figure 6.23, the cement content is the most important considered uncertainty. The results obtained for winter and summer are similar.

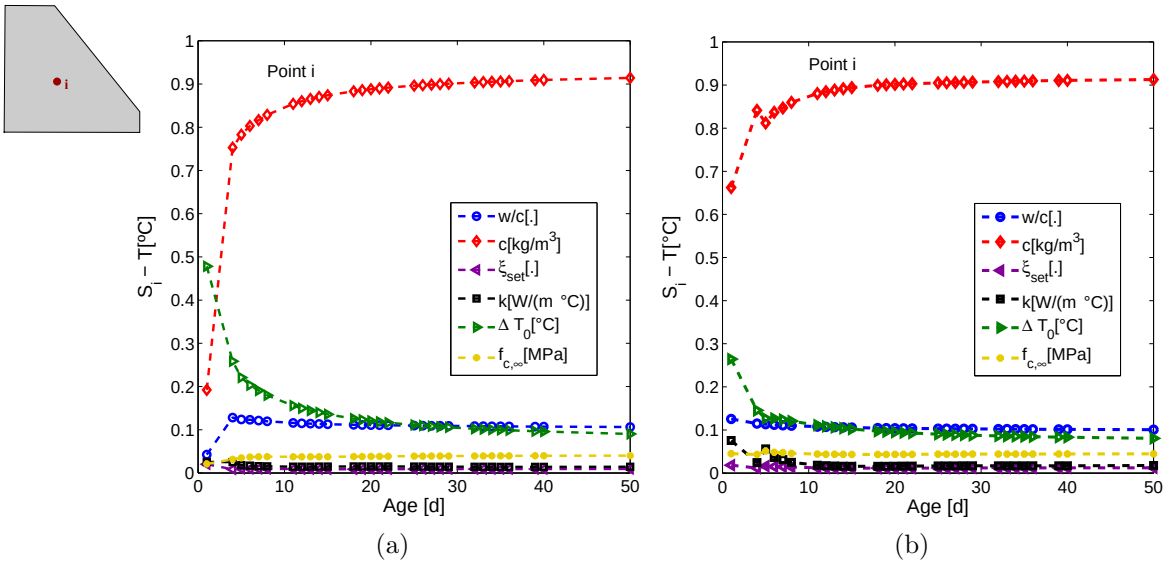

Figure 6.23: S_i over temperature at "point i": a) Construction during winter; b) Construction during summer.

The sensitivity indexes may also be evaluated within the entire dam model at each con-

struction step, which leads to S_i surfaces such as the ones depicted in Figures 6.24, 6.25 and 6.26. Such as previously discussed in chapter 5, even if they require a greater numerical effort, these kind of results allows the identification of the most sensible zones by giving a spatial distribution of the sensitivity index.

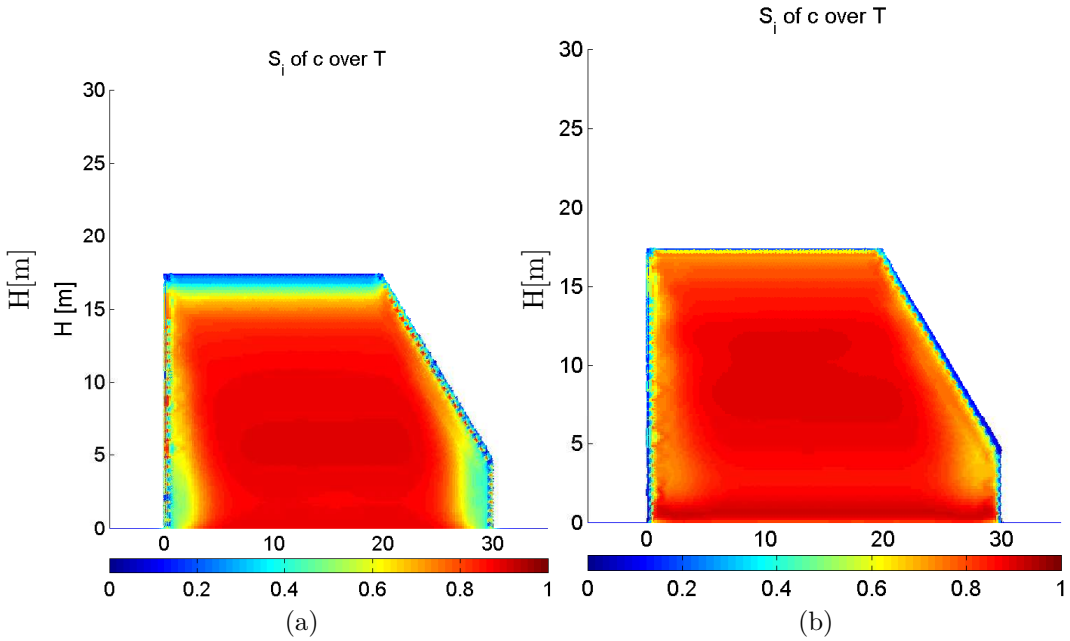

Figure 6.24: S_i surfaces of c over temperature: a) Construction during winter; b) Construction during summer.

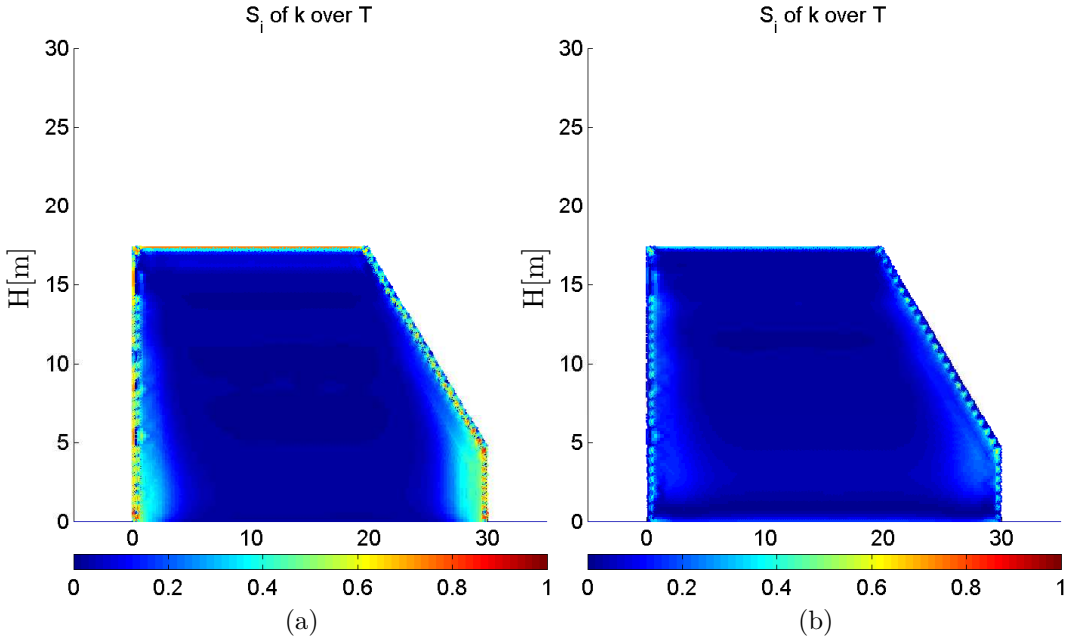

Figure 6.25: S_i surfaces of k over temperature: a) Construction during winter; b) Construction during summer.

For example, Figure 6.24 supports the conclusions achieved with Figures 6.22 and 6.23 by enhancing lower S_i for cement content over the temperature output found close to the foundation and near the dam faces (where "point lu" is located) for the winter case scenario, and also on the top (younger) layers, on which higher S_i are found during summer ($S_i = 0.65$ right after casting in Figure 6.23). This last remark is also supported by the S_i surfaces of Figure 6.26, on which higher S_i values for ΔT_0 over temperature are obtained on the upper (younger) layers for the winter case scenario, in agreement with the first S_i value depicted in Figure 6.23a. The conclusions made over Figure 6.22 about the thermal conductivity influence may also be supported by the S_i surfaces plotted in Figure 6.25, on which higher values are obtained near the dam faces for the winter case scenario.

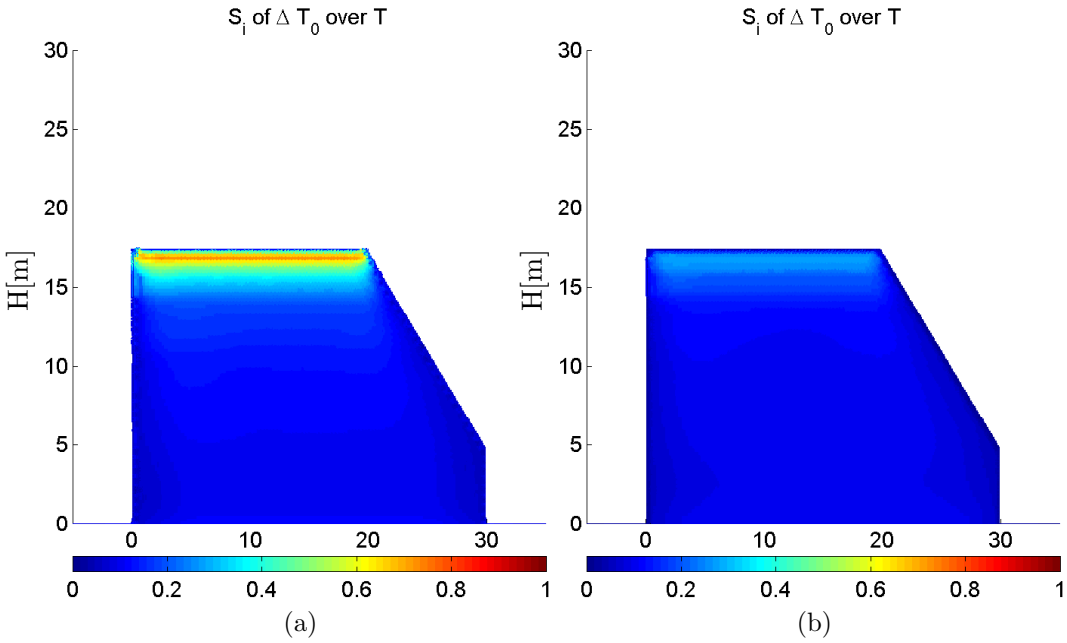

Figure 6.26: S_i surfaces of ΔT_0 over temperature: a) Construction during winter; b) Construction during summer.

Passing now to the hydration and ageing degree results (Figure 6.27), the obtained sensitivity indexes on "point lu" are similar for both case scenarios. Also, on "point i" the sensitivity indexes found for the ageing degree evolution are very similar. Therefore, in Figure 6.27 it was decided only to plot the winter case scenario. For the hydration degree (Figure 6.27a), the results are similar to the ones obtained for the thermo-chemical model (chapter 5), with the water-to-cement ratio being the most influencing parameter. Still, right after construction, ΔT_0 presents a non-negligible S_i of around 0.45.

For the ageing degree, the most influencing considered uncertainty is, undoubtedly, the

hydration threshold ξ_{set} which dictates the beginning of the ageing degree evolution and, consequently, of the mechanical properties. This study reveals that the uncertainty related to the ξ_{set} parameter shall not be ignored since it plays an important role on the model output. This uncertainty was not previously considered on the sensitivity analysis performed over the thermo-chemical model in chapter 5 since the objective was not centered on the mechanical behaviour, and therefore the sensitivity indexes presented in chapter 5 for the ageing degree were very similar to the ones found for the hydration degree.

The sensitivity indexes found for the hydration degree on "point i" suffer some differences between the two case scenarios. Such as depicted in Figure 6.28, the overall evolution of the sensitivity indexes resembles between both scenarios but the final values for w/c and c present an overall difference of 0.1.

Concerning the sensitivity indexes obtained over the first principal stress results, there are significant differences between the two case scenarios on both analyzed points. For "point lu" the evolution of the sensitivity indexes presents several oscillations and peak values until the age of 30 days. While during winter, those peaks values concern ξ_{set} and the cement content, during summer they also concern the thermal conductivity and present more oscillations. Also it is noticed that for a construction during winter, around 10 and 30 days of age, all of the sensitivity indexes are lower than 0.2. This behaviour could be due to two causes: whether this indicates that there mat be are second-order effects that the present analysis is not able to account for; or this is due to the nil first principal stresses that occur during this period, such

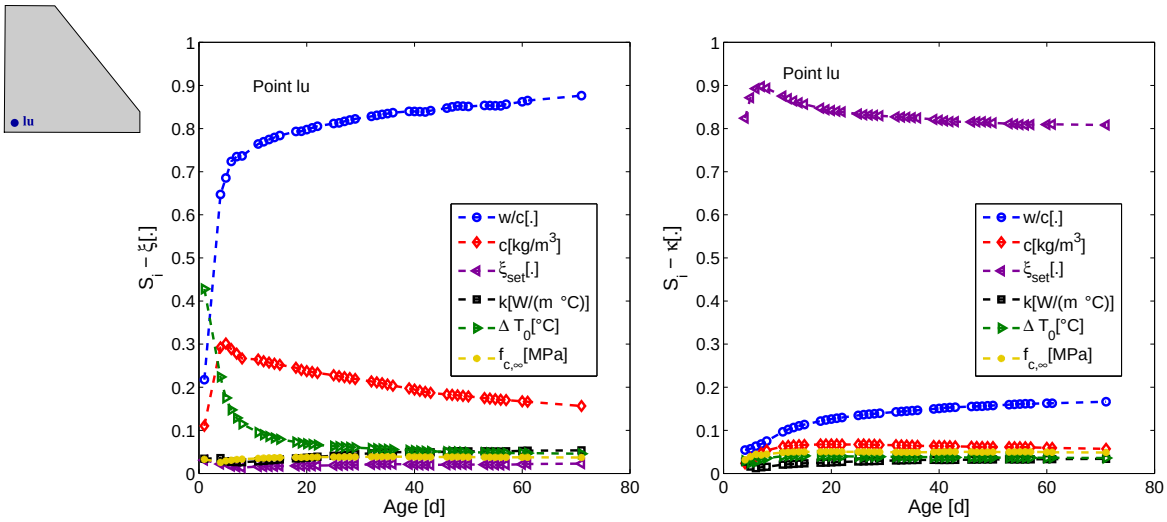

Figure 6.27: S_i over hydration and ageing degrees at "point lu" for construction during winter: a) Hydration degree; b) Ageing degree.

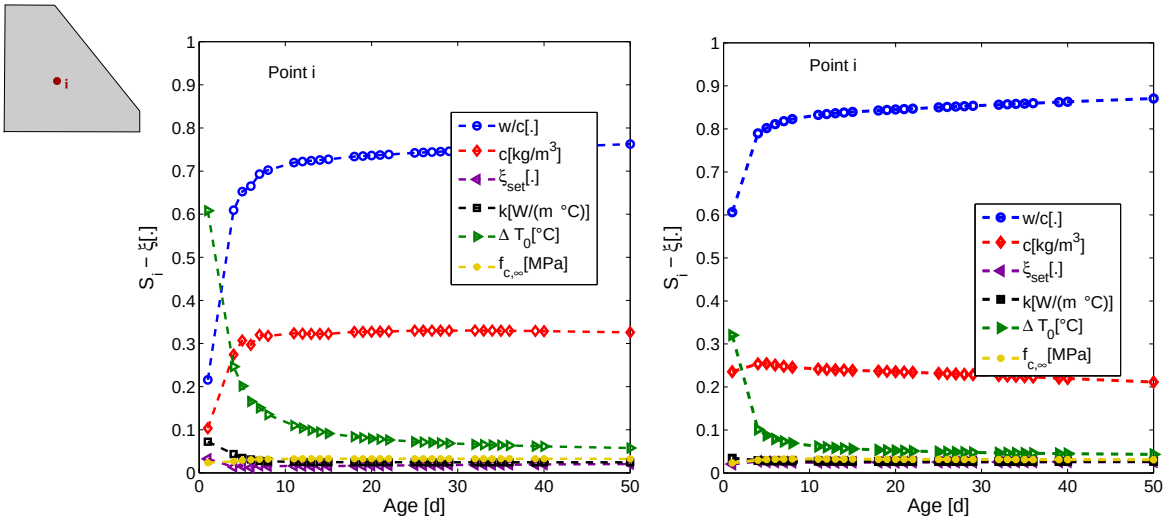

Figure 6.28: S_i over hydration degree at "point i": a) Construction during winter; b) Construction during summer.

as previously depicted in Figure 6.9a. In Figure 6.9a it can also be observed that the instant of 30 days of age corresponds to the age on which the mean values of σ_1 passed from compression to tension. Even if the results do not lead to clear conclusions until 30 days of age for both case scenarios, it may still be concluded that at the end of construction it is the cement content which will rule the first principal stress evolution, presenting S_i of 0.45 in winter and 0.65 in summer.

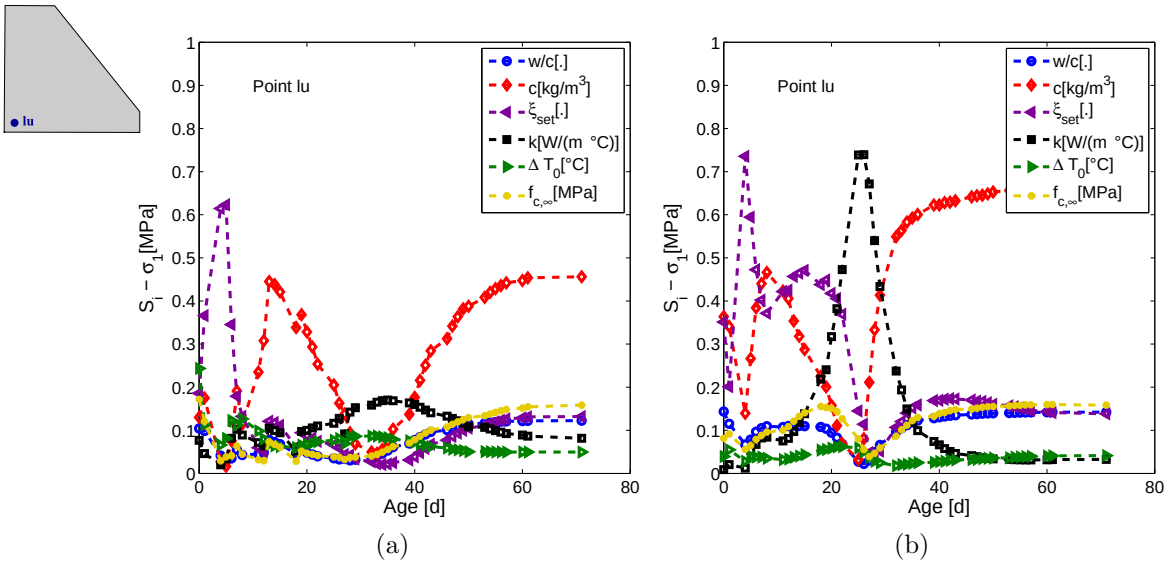

Figure 6.29: S_i over the first principal stress at "point lu": a) Construction during winter; b) Construction during summer.

In Figure 6.30 are plotted the sensitivity indexes over the first principal stress on "point i". From these results it is clear that the two considered uncertainties that have most impact on

the first principal stresses are related to the hydration threshold ξ_{set} and the cement content. Higher S_i values were found for ξ_{set} between ages of 10 and 20 days during winter and between 10 and 30 days during summer, approximately. It is also noticed that around 30 and 10 days of age for winter and summer case scenarios, respectively, the final compressive strength presents a peak value. Going back to Figure 6.10, it may be concluded that these values correspond to ages during which the range of obtained stresses is narrower and tends towards compression. At the end of construction, at 50 days of age, it may be concluded that the most influencing uncertainty is related to the cement content, presenting S_i values of 0.55 during winter and 0.5 during summer. The hydration threshold ξ_{set} attains S_i values of 0.2 during winter and 0.3 during summer.

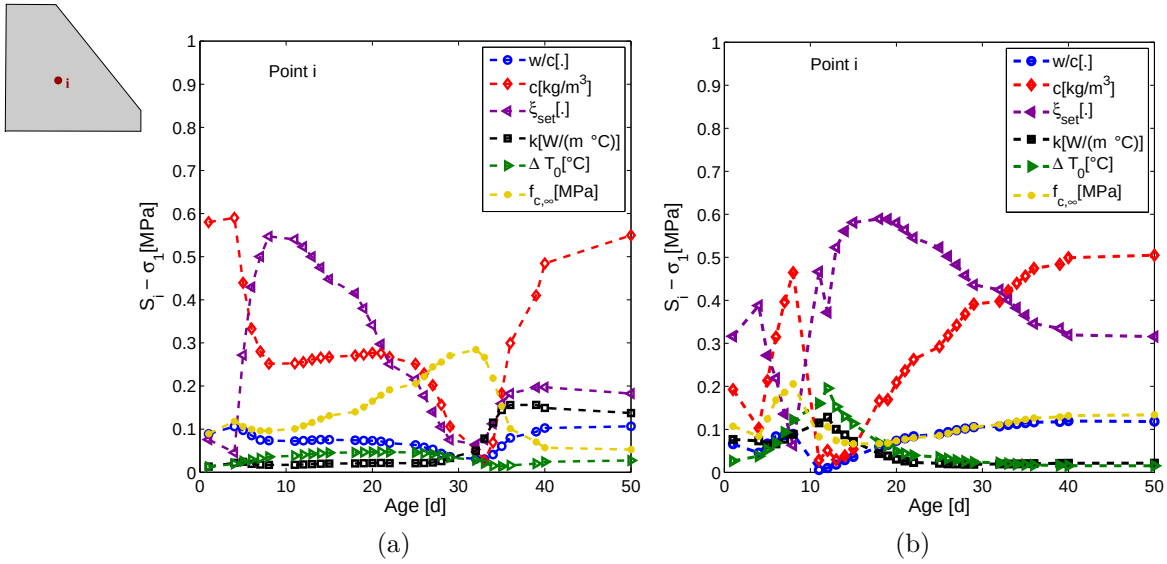

Figure 6.30: S_i over the first principal stress at "point i": a) Construction during winter; b) Construction during summer

The results discussed here about the sensitivity analysis performed over the first principal stresses output appear to lead to the conclusion that it is the thermal behaviour which is most influencing the stress state at the end of construction, by giving higher sensitivity indexes to the cement content which directly influences the heat generated per cubic meter of RCC l_ξ[J/m^3]. The cement content was previously concluded to highly influence the temperature evolution. Moreover, this sensitivity analysis also shows that at earlier ages the hydration threshold ξ_{set}, which rules the beginning of the evolution of the mechanical properties, presents non-negligible sensitivity indexes. This is a parameter of difficult estimation in practice and therefore object of uncertainties, which are here proven that shall not be neglected.

6.4.3 Cracking index

A sensitivity analysis may also be performed over the cracking index $I_f = f_t/\sigma_1$ via the RBD-FAST test. Here are plotted some of the results of S_i surfaces obtained over the cracking index output of the model. Once more, it is clear that the behaviour changes significantly with the case scenarios winter and summer.

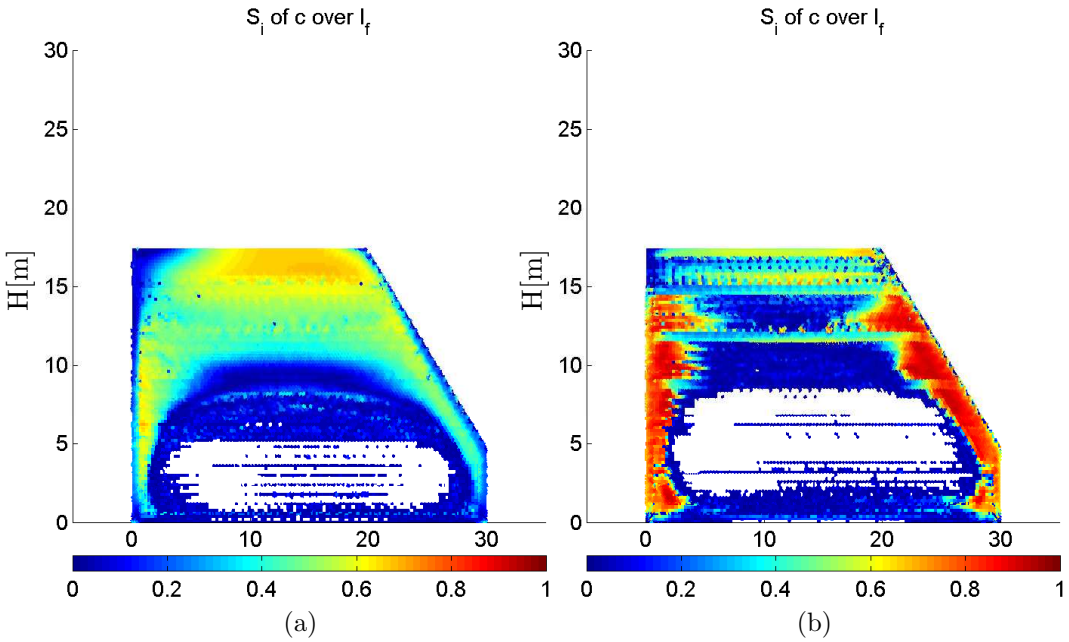

Figure 6.31: S_i surfaces of c over the cracking index: a) Construction during winter; b) Construction during summer.

It is here once more depicted the importance of the cement content c[kg/m^3] on the model output. In Figure 6.31 are evidenced the different sensitivity index contours obtained for both cases scenarios, as well as their spatial variation inside the dam body. It is particularly enhanced the higher sensitivity indexes on the dam faces as well as on the upper (and younger) layers.

The sensitivity index contours for the hydration threshold ξ_{set} and the thermal conductivity k[W/(m°C)] show the difference on the results obtained for the two case scenarios. It appears that for a construction during summer, ξ_{set} has more influence on the cracking index in the upper (and younger) layers, while the same behaviour is not verified during winter. For the thermal conductivity, the sensitivity indexes are obtained on the same areas within the dam, presenting higher values for a construction during summer.

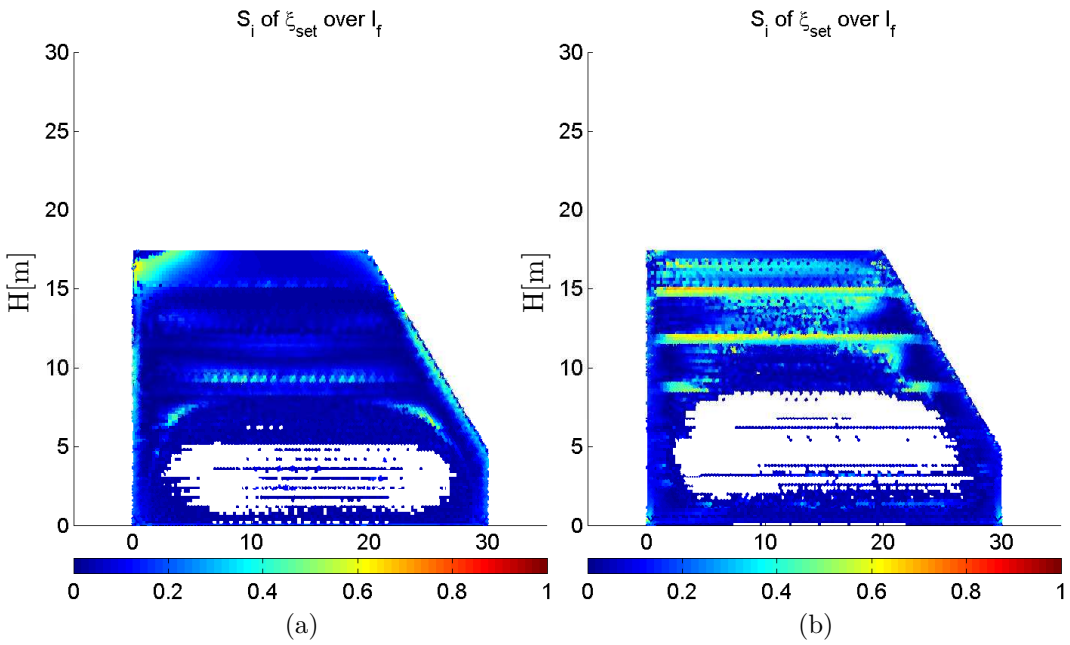

Figure 6.32: S_i surfaces of ξ_{set} over the cracking index: a) Construction during winter; b) Construction during summer.

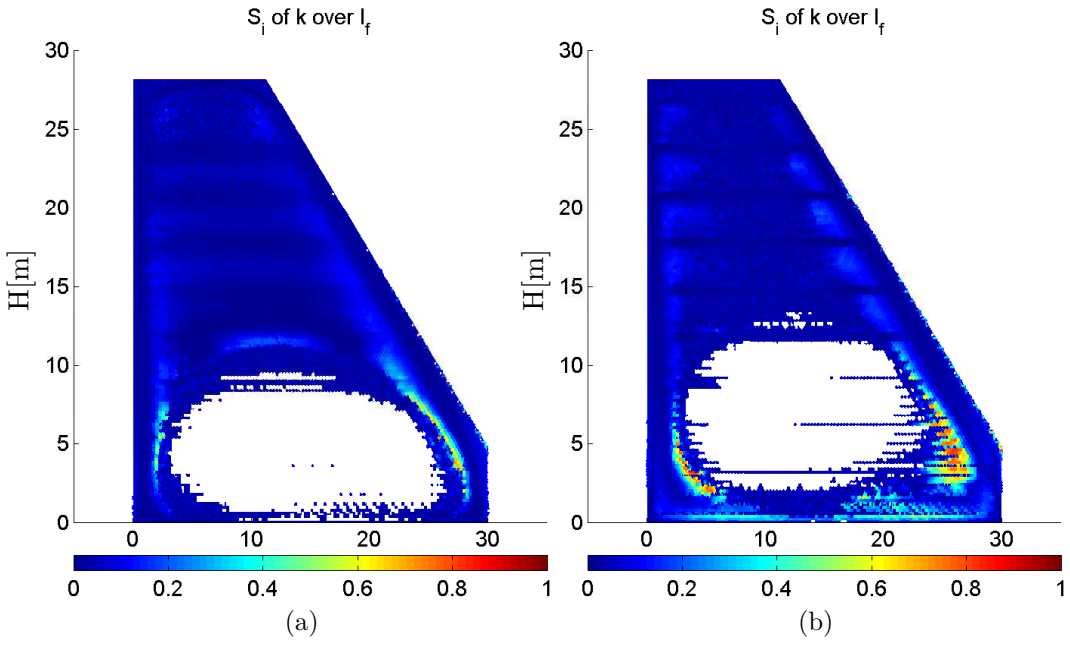

Figure 6.33: S_i surfaces of k over the cracking index: a) Construction during winter; b) Construction during summer.

6.4.4 Naive Bayesian approach

Performing a sensitivity analysis via the RBD-FAST test over the cracking density results makes no sense in the present work. This is because the cracking density assessment results from a post-treatment of the model output on which a hypothesis is made: the evolution of the

cracking index evaluated on each point of a secondary mesh is considered to be monotonically increasing during all of the analysis (more details may be found in chapter 3). This means that if the tensile stress is greater than the tensile strength developed so far at each time instant, cracking occurs and is irreversible. Therefore, even if the stress state changes to compression and the value of cracking index turns to "safe" values, this is not accounted for in the cracking density concept.

In order to overcome this limitation, it is proposed here to perform a sensitivity analysis based on the naive Bayesian approach, described hereafter. This approach is generally applied in order to compute conditional probabilities by means of the Bayes' rule and/or to perform the so-called Bayesian updating. In the present work, however, none of these applications is done, the target consisting on simply performing a kind of sensitivity analysis by evaluating the random variables' combinations which will lead to extreme values of cracking density.

In the naive Bayesian framework applied here, the obtained cracking density curves could be seen as a database resulting from a training data set on which variability of some input parameters is accounted for. Examples of this approach may be found in literature on the seismic field, such as in Lancieri and Zollo (2008), among others. In this sense, the probability of exceeding a certain cracking density limit, on a given layer, could be estimated for a specific combination of input variables such as the cement content and final compressive strength. At the same time, the results could be updated given new input variables' combinations. However, and as already stated, in the framework of this thesis, these features are not exploited.

Suppose that A is a variable that depends on some other variables $\underline{B} = \{B_1, \ldots, B_p\}$. The so-called Bayes' rule (Bayes and Price, 1763) may be described by equation 6.25, where $P(A|B_1, \ldots, B_p)$ is the conditional probability of A given $\underline{B}$ and is commonly called *posterior*, $P(B_1, \ldots, B_p|A)$ is the conditional probability of $\underline{B}$ given A, commonly called *likelihood*, $P(A)$, the *prior*, is the probability of occurrence of A, and $P(B_1, \ldots, B_p)$ is the probability of occurrence of $\underline{B}$, that is, the *evidence*.

$$P(A|B_1, \ldots, B_p) = \frac{P(B_1, \ldots, B_p|A) \cdot P(A)}{P(B_1, \ldots, B_p)} \tag{6.25}$$

In the present context, the *prior* would be the output of the model, that is, all of the 250 cracking density curves evaluated for a given layer. The *evidence*, on the other hand, would be the input of the model, in this case the statistical distributions of the input random variables. As it was previously presented in section 6.3.4 of this chapter, the objective is to assess the

probability of exceeding a predefined limit value for the cracking density $\rho_{f,lim}$. Given this, the *posterior* $P(A|B_1,\ldots,B_p)$ would be the cracking density curves on which, for a chosen instant of time or age, the cracking density exceeds the adopted limit. Therefore, the *likelihood* would be the input random variables' combinations that lead to those extreme cases of cracking density.

In order to better illustrate this naive Bayesian approach, the cracking density limit and the random variables' combinations are identified on layers #4 and #19. Figure 6.34 represents the analysis over layer #4 for a construction during winter, while Figure 6.35 concerns the same analysis for a construction during summer. For layer #4, a cracking density limit $\rho_{f,lim}$ at the end of construction of 0.18 was established.

A correspondence between equation 6.25 and the results plotted in Figures 6.34 and 6.35 may be done. To improve the results' reading, equation 6.25 is written using different colors. Therefore, the *posterior* $P(A|B_1,\ldots,B_p)$ are the red curves of Figure 6.34a, the *likelihood* $P(B_1,\ldots,B_p|A)$ are the plain blue distributions of random variables of Figure 6.34b, the *prior* $P(A)$ are the 250 grey cracking density curves of Figure 6.34a and finally, the *evidence* $P(B_1,\ldots,B_p)$ are the input random variables' green distributions of Figure 6.34b.

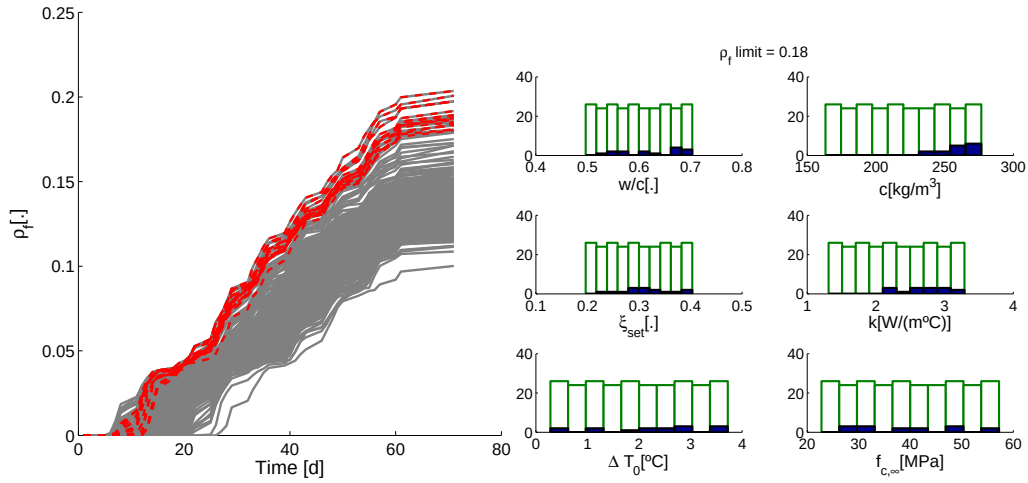

(a) $\rho_{f,lim} = 0.18$ (b) r.v. set for $\rho_{f,lim} = 0.18$

Figure 6.34: Naive Bayesian approach to evaluate sets of r.v. that lead to $\rho_f > \rho_{f,lim}$ on layer #4 for a construction during winter.

Now, given this analysis, some conclusions can be drawn. From the results plotted in Figures 6.34 and 6.35 it is clear that higher values of the cement content c[kg/m^3] are leading to the higher cracking densities in layer #4. Moreover, it may also be concluded that for a construction during winter, higher values of the thermal conductivity k[W/(m°C)] are also leading to greater cracking densities (Figure 6.34b). All of the other input random variables

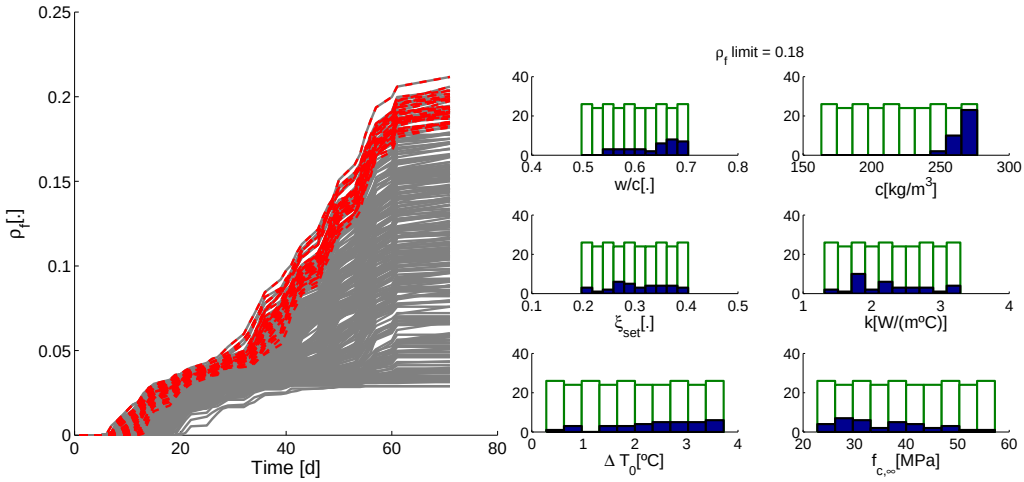

(a) $\rho_{f,lim} = 0.18$ (b) r.v. set for $\rho_{f,lim} = 0.18$

Figure 6.35: Naive Bayesian approach to evaluate sets of r.v. that lead to $\rho_f > \rho_{f,lim}$ on layer #4 for a construction during summer.

that lead to $\rho_f \geq \rho_{f,lim}$ are covering the entire range of values of the input distribution.

These results corroborate the conclusions drawn from the sensitivity analysis, indicating that higher cement contents lead to a higher cracking density. The higher cement content actually means higher hydration heat generated per cubic meter of RCC, meaning that the cracking density distribution is being highly influenced by the thermal behaviour of the dam. Moreover, it is also concluded that for a construction during winter, it higher values of the thermal conductivity also influence those higher cracking densities. These conclusions may therefore be confirmed and supported by the global sensitivity analysis performed over the temperature output of the model via the RBD-FAST test. Once more, it is proven here that the thermal behaviour of the dam is highly contributing to the cracking extent inside each casted layer.

Now, the same naive Bayesian approach can be applied to a previously identified critical layer: layer #19 for a construction during winter (Figure 6.16a). This time, the considered cracking density limits are of 0.4 and 0.8. It is observed in Figure 6.36 that, once more, higher cement contents lead to higher cracking density. However, for layer #19, not much can be said about the thermal conductivity k[W/(m°C)], since its distribution covers all of the values' input range.

The application presented here and the conclusions drawn from it could be useful in practice if the aim is to limit the cracking density. For example, in the particular case dealt with within this thesis, it could be concluded that if the cracking density is to be limited at 0.4 in layer

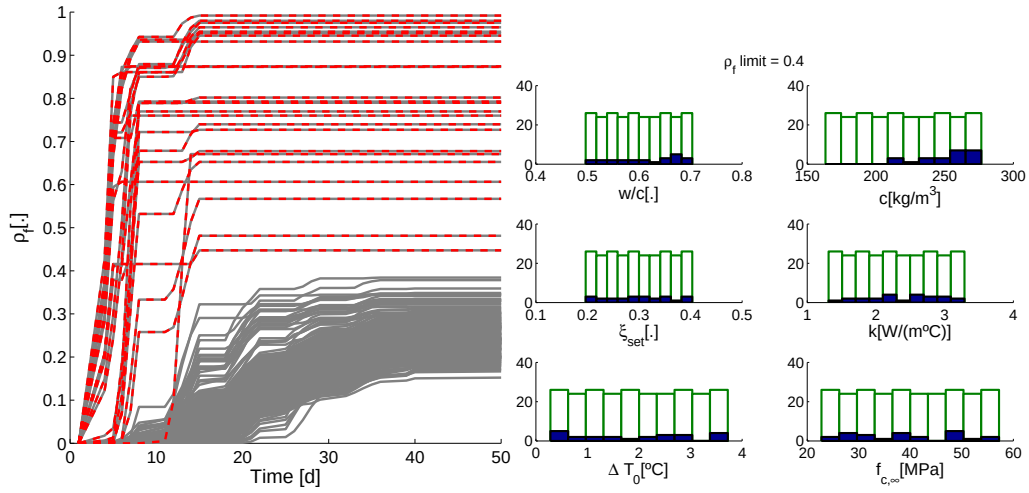

(a) $\rho_{f,lim} = 0.4$ (b) r.v. set for $\rho_{f,lim} = 0.4$

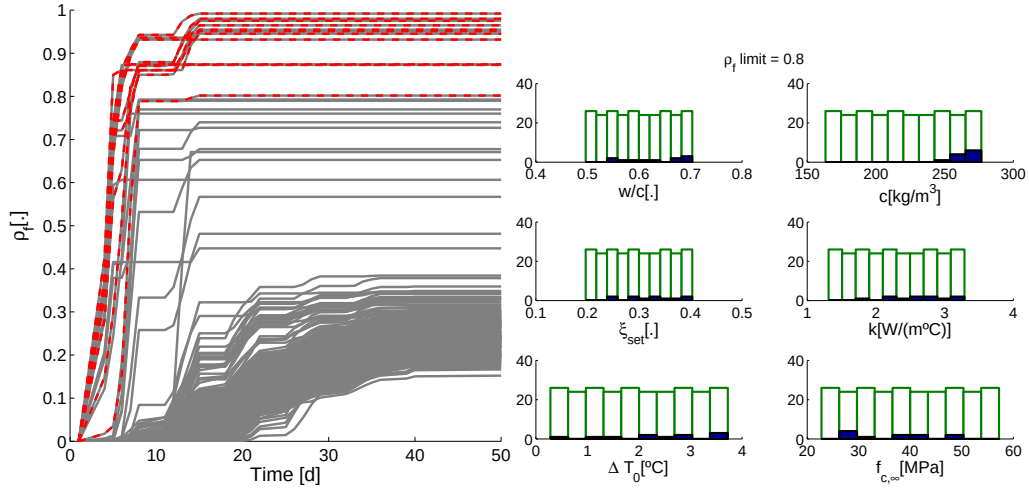

(c) $\rho_{f,lim} = 0.8$ (d) r.v. set for $\rho_{f,lim} = 0.8$

Figure 6.36: Naive Bayesian approach to evaluate sets of r.v. that lead to $\rho_f > \rho_{f,lim}$ on layer #19 for a construction during winter

#19 for a construction during winter, then cement contents higher than 220kg/m^3 should be avoided, as depicted in Figures 6.36a and 6.36b.

It is believed that the naive Bayesian approach applied here is of very much interest in this kind of analysis by giving useful information about how the input random variables will affect the cracking density output, allowing in this sense a kind of sensitivity analysis. As previously stated, a great advantage of this kind of procedure is that it can be completed with more information coming from other computations, even if they use different distributions for the input random variables. Moreover, the conclusions drawn from this analysis are supported by the global sensitivity analysis previously performed in section 6.4.1.

6.5 Conclusions

In this chapter, the thermo-chemo-mechanical modelling of an RCC dam construction was assessed within a probabilistic context. Uncertainties related to some model parameters and material properties were accounted for in the framework of a sensitivity test performed through RBD-FAST analysis. Those uncertainties are related to parameters that concern both the thermal and mechanical behaviour: water-to-cement ratio w/c, cement content c[kg/m^3], hydration threshold ξ_{set} that dictates the beginning of mechanical properties' evolution, thermal conductivity k[W/(m°C)], the added casting temperature ΔT_0[°C] and final compressive strength f_c[MPa]. These uncertainties will interfere with other parameters such as the final hydration degree ξ_∞ (via w/c), the heat generated per cubic meter of RCC l_ξ[J/m^3] (via the cement content), the final tensile strength $f_{t,\infty}$[MPa] and Young's modulus E_∞[GPa] (via $f_{c,\infty}$).

An example by using the reliability index, commonly used in practice, to compute the probability of failure was performed. This analysis was carried out over the output of the model in a single point, which is either located near the foundation and upstream face of the dam (point "lu"), either in the core of the dam (point "i"). It was concluded that the probability of failure increases with age and is higher during summer between ages of 40 and 60 days, being similar afterwards. However, β only uses the mean and standard deviation information of the output and higher-order reliability methods should be applied. Moreover, the FOSM method, a level II reliability method, is performed and the reliability index obtained. The probability of failure assessed via the FOSM method and an MC-type method (a level III reliability method, in this case, RBD-FAST sampling) are compared and it is concluded that those results diverge for lower probabilities, enhancing the importance of reliability analysis of higher levels to estimate lower probabilities.

Two case scenarios were applied concerning the ambient temperature: winter and summer. For the MC-type method results, wider ranges of the cracking density ρ_f were observed for a construction during summer, characterized by lower mean values of ρ_f when compared with the winter case scenario. However, in some layers (i.e., layer #19), extreme values of ρ_f are observed for the winter case scenario.

The probability of failure related to the cracking density on each casted layer was further assessed. The complementary cumulative distribution function (CCDF), which gives the probability of exceeding a given cracking density limit $\rho_{f,lim}$ ($P[\rho_f \geq \rho_{f,lim}]$), is obtained on three analyzed layers at different ages. It is concluded that the obtained CCDFs adjust well to

the Weibull distribution function, which was reported by the Japanese Concrete Institute in a study about early-age cracking of concrete structures (JCI, 2012). For the present study and the considered uncertainties, it is concluded that $P[\rho_f \geq \rho_{f,lim}]$ depends on the position of each layer, on the age of the correspondent material and on the ambient temperature case scenario. Therefore, $P[\rho_f \geq \rho_{f,lim}]$ shall not be described by one single curve representative of the entire dam since it changes significantly from one layer to another.

Moreover, by analyzing those layers on which construction has stopped for longer periods, the most critical layers are characterized by higher probabilities of failure. Decisions on changing the mixture of those layers, adjusting the construction schedule or performing cold joints treatment could be supported with this analysis. In the present case, lower probabilities $P[\rho_f \geq \rho_{f,lim}]$ are found for the summer case scenario, exception on the layers considered to be cold joints. Then, it it appears that the adopted construction scheme is better adapted to the summer case scenario, provided that cold joints' treatment takes place in order to reduce the higher $P[\rho_f \geq \rho_{f,lim}]$ found in those layers.

The results of the RBD-FAST analysis not only allow the evaluation of the variability on the model output, but also to perform a global sensitivity analysis which gives useful information about the influence of each random variable on the output of the model. The same analysis was previously performed over the thermo-chemical part of the model only (in chapter 5). The results found within this chapter are compared and revealed to be in agreement with the results of chapter 5. Such as in 5, it was concluded that the cement content, which affects the amount of heat generated per cubic meter of material ($l_\xi[\mathrm{J/m^3}]$), is the most influencing parameter on the temperature evolution.

However, two exceptions were found with the sensitivity analysis in this chapter. First of all, the sensitivity index obtained for thermal conductivity over temperature results for both case scenarios is different, attaining values of 0.4 during winter and remaining insignificant during summer, which enhances the importance of the ambient temperature evolution on the model behaviour. This behaviour is observed due to the higher temperature gradients that occur for the winter case scenario between the dam faces and the environment. Second of all, concerning the ageing degree it is observed that the random variable that most influences is the hydration threshold ξ_{set}, which was not accounted for in chapter 5, and proves here to have high importance on the model behaviour, in particular in the mechanical properties' evolution (which are dependent on the ageing degree).

Concerning the sensitivity analysis over the mechanical behaviour, namely the first principal

stress results, it is concluded that the oscillations obtained for the sensitivity indexes may be due to: interaction between the random variables that can not be captured and assessed by the present approach; or to nil stresses that occur on the analyzed points until a certain age. The obtained results appear to lead to the conclusion that it is the thermal behaviour which is most influencing the stress state at the end of construction, by giving higher sensitivity indexes to the cement content which directly influences the heat generated per cubic meter of RCC $l_{\xi}[\mathrm{J/m^3}]$. It shall however be enhanced that at earlier ages the hydration threshold ξ_{set}, which rules the beginning of the evolution of the mechanical properties, presents non-negligible sensitivity indexes. It is concluded with the obtained results that ξ_{set} presents significant sensitivity indexes concerning the stress state, namely at very early ages. However, it is also observed that those S_i evolve with age, being higher at early ages on points located near the dam faces, and later in time on points located in the core of the dam. Since the hydration threshold is a parameter of difficult estimation in practice (values that ranges from 0.1 to 0.6 in the available literature De Schutter and Taerwe, 1996) and therefore object of uncertainties, these results enhance, once more, its importance and prove that it shall not be neglected.

Moreover, a naive Bayesian approach was applied in order to illustrate how to easier assess the set of random variables that lead to extreme values of the cracking density in a given layer and perform a sort of sensitivity analysis. It was concluded that higher cement contents lead to a higher cracking density and also that, for a construction during winter, higher values of thermal conductivity also influence those extreme cracking densities.

Concluding, it is interesting to mention that in the naive Bayesian approach presented in section 6.4.4, the conclusions drawn before with the RBD-FAST sensitivity test were also found in this approach by analyzing the random variables combinations that lead to extreme values of the cracking density in a given layer. It is therefore here believed that this naive Bayesian approach is a useful tool which supports the sensitivity analysis. Moreover, a database of input random variables could be enlarged from this first one by feeding it with other input distributions and consequent cracking densities outputs of the model, provided that the same RCC dam case scenario is applied.

Chapter 7

Conclusions and recommendations for future research

After the description of this thesis' framework in chapters 1 2, 3, the conclusions drawn from this work are presented and discussed partially at the end of the applied chapters 4, 5 and 6. As frequently as possible, references between chapters and comparisons about their conclusions were made. In this last chapter, the main conclusions are reviewed in order to give the general framework of the thesis' contribution and future applications.

7.1 Main conclusions

The main conclusions of the present thesis are here gathered and organized within the following structure: deterministic approach and probabilistic approach over the thermo-chemical behaviour and over the thermo-chemo-mechanical behaviour.

Deterministic approach:

- It was concluded that the model behaviour not only depends on whether the construction has begun during winter or summer, but also on the daily and yearly ambient temperature evolution.
- The changes adopted for the construction scheme show that increasing the duration of stops between the casting of two layers will increase the cracking extent within each layer.
- The account for cold joints' treatment by changing the convection coefficient of the top surface of each layer, as well as thermal and mechanical restrains imposed by formwork

are two aspects which are not commonly accounted for in this kind of analysis. They were here demonstrated as leading to non-negligible reduction of the cracking density extent.

Probabilistic approach, thermo-chemical behaviour:

- The convection coefficient revealed not to be very influent in the model output by presenting low sensitivity indexes S_i and was therefore considered as deterministic in the further applications.

- By applying the random fields theory, the spatial variability of some parameters was accounted for (i.e., water-to-cement ratio, cement content and thermal conductivity), which lead to a reduction of the output variance when compared with the results using random variables only.

Probabilistic approach, thermo-chemo-mechanical behaviour:

- By applying FOSM (a level II reliability method) and an MC-type method (a level III reliability method) it is observed that for lower probabilities the results diverge when comparing the two methods. For the MC-type method, the uncertainty on the results is bigger for lower probabilities, which actually correspond to ages of the material around 40 days. This analysis enhances the importance of the input uncertainties related to the model parameters that traduce the material behaviour during hardening, when the aim is to estimate lower probabilities.

- The Weibull distribution is concluded to be well adapted to the CCDFs for the cracking density ρ_f. Attention shall however be paid to layers which are considered to be cold joints (layers on which construction has stopped for 3 days, in the present case study).

- The CCDFs allow the estimation of the probability of exceeding a certain pre-defined cracking density limit. It is concluded that those probabilities increase with the material's age and one single curve is not representative of the entire dam because it changes according to the layers' position.

- It is concluded that, for the case dealt with in this thesis, and given the considered uncertainties, lower probabilities of exceeding $\rho_{f,lim}$ are found for the summer case scenario, excepting when analyzing cold joints. Therefore, the adopted construction scheme is better adapted for a construction during summer, provided that cold joints' treatment takes place.

- The thermal conductivity is characterized by higher values of S_i on those cases on which higher thermal gradients occur between the dam faces and the environment.

- The percolation threshold ξ_{set} reveals to have high influence on the ageing degree and consequently on the mechanical properties' evolution. Also, it presents significant S_i for the stress state evolution, namely at very early ages, right after casting for points located closer to the dam faces, and later in time for points located in the core of the dam.

- The casting temperature reveals to be influent at very early ages on the temperature evolution, presenting very low S_i later in time. It can then be concluded that this parameter could be considered as deterministic in future applications. This conclusion was also verified with the deterministic study performed in chapter 4.

- By applying the naive Bayesian approach to cold joints' layers, decisions on limiting the cement content or the water-to-cement ratio on those critical layers could be supported.

By placing this work in the bigger framework of dam risk analysis, it is believed that the proposed methodology could be seen as a contribution to help engineers understand how uncertainties will affect the dam behaviour during construction and rely on it in the future to improve and support the design phase of the dam project.

7.2 Recommendations for future research

Some recommendations for future research are suggested here. An idea for future work would be to account for spatial variability within the full thermo-chemo-mechanical analysis, such as it was done for the thermo-chemical analysis in chapter 5. Also, a 3D modelling could be performed in order to study the transverse joints' location that would minimize the cracking damage extent.

Concerning the non-linear viscoelastic behaviour model, some improvements could also take place by including plastic deformations and the early-age crack healing due to the ongoing hydration process. Furthermore, accounting for the crack opening and growth could also be foreseen.

Moreover, some hypothesis were made within this work that should be object of further studies and improvements. One example are the random variables, which were always considered as being independent and described by uniform distributions. This hypothesis was taken

under the basis that the available information on RCC dams properties is too vast and may vary considerably from one project to another. It is enhanced several times along the text that the random variables' definition much be object of a very careful assessment, adapted to each dam project and rely on experimental and *in situ* data as frequently as possible, which is why it was decided in this thesis to describe them as uniform independent random variables. This does not mean, although, that the presented methodology must be confined to this kind of distributions, and other distributions could and should be applied in further studies. For example, it is known that the mechanical properties are generally characterized by lognormal distributions, which could be included in the present methodology. Also, other model parameters which are related to the cementitious matrix and aggregates could be further explored by accounting more explicitly for other additives and other type of aggregates.

Another hypothesis concern the adopted correlation lengths used to describe the random fields in chapter 5, which were not based in any field measure. This point should be further explored by trying to assess with as much accuracy as possible correlations lengths on field.

Still about the probabilistic model, it is concluded that the Weibull distribution does not adjusts as well for on some critical layers. Those results, as well as the convergence of the probabilities of failure, should be improved by increasing the number of MC-type computations.

About the naive Bayesian approach presented at the end of chapter 6, it could be further explored in order to feed the model with more data and assess the probability of failure. This approach could also be further applied in order to estimate probabilities of failure, which is not addressed in the present thesis.

Finally, other Level III reliability methods could be applied in this thesis' framework. An example could be by performing importance sampling (IS). The IS would center the search space around lower probabilities of failure. A quick application of IS was actually made at the end of this thesis' work but did not reveal to lead to improvements of the reliability analysis. It was believed that this was due the fact that all of the random variables' distributions are uniform. A future application would be to use IS and other random variables' distributions.

Appendix A

Studied approaches to model the dam layered construction

In this appendix are presented three approaches that were studied to model the layered construction of the dam. The adopted approach used in this thesis is described in chapter 3.

A.1 High conductivity coefficient

In this first approach, the non-activated/unconstructed layers are modeled and given material properties that are not the ones of the RCC material (Figure A.1).

Because the heat flow is applied on the upper boundary of the column, the idea of this approach is to assure that all this heat flow arrives at the upper activated layer. Therefore, the non-activated layers properties are chosen in order to allow the heat to be directly transmitted to the activated layers. This means that the "pre-constructed" material is a very conductive one. Hence, the thermal conductivity coefficient k[W/(m·°C)] is very high. For the specific heat c[J/(kg·°C)] and density ρ[kg/m^3], the adopted values correspond to air at 20°C. In order to simulate the layered construction, each of the materials properties follows a construction curve. This curve is based on the construction schedule of the column: the first layer (foundation) is already activated since the beginning of the computation; the second layer is activated at 24h; each one of the upper layers is activated 12h after the activation of the precedent layer. The model parameters are described in Table A.1.

Firstly, the heat flow applied on the surface needs to be accurately transmitted to the non-activated layers. Therefore, a first computation was performed, considering both a 5 and 10 layered column. The models are described in Figure A.1 by a simplified scheme. In the 5 layered

column, all of the layers are "activated" (i.e. their properties are the RCC properties). In the 10 layered column, the first 5 layers are "activated" and the 5 upper ones are "non-activated". On both columns, the heat flow is applied on the upper boundary. The initial temperature of all layers is of 20°C and the ambient temperature is of 30°C. The lower boundary is maintained at 20°C during all the simulation.

As it can be concluded by analyzing Figure A.2, the temperature evaluated on the same points for the two simulations is slightly lower for the 10 layered column case. Still, those differences do not exceed 0.5°C, which is considered here not to be too significative. This means that the assumption of giving the non-activated columns a very high conductivity coefficient is valid.

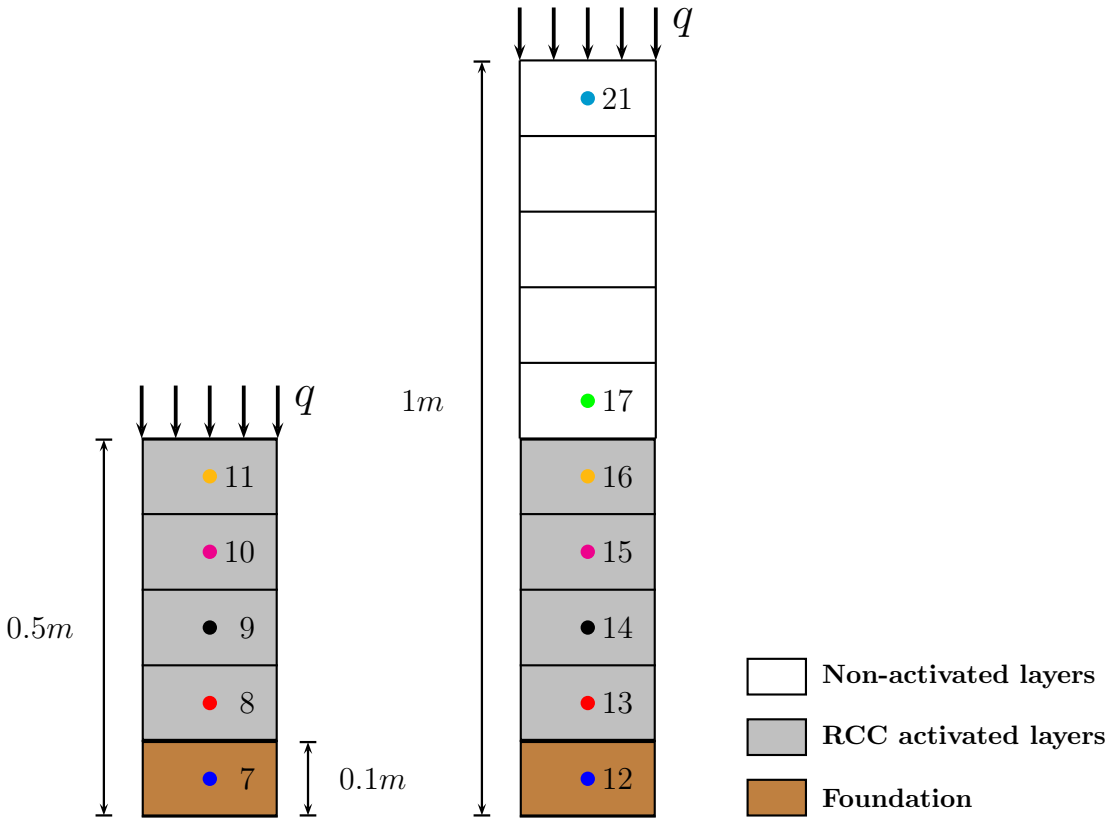

Figure A.1: Model scheme for 5 and 10 layered column

Table A.1: Material properties

Material	Foundation	Non-activated layers	RCC
Density ρ[kg/m^3]	2710	1.2	2400
Specific heat c[J/(kg·°C)]	921	1000	921
Heat conduction coefficient k[W/(m·°C)]	1.5	3000	2.33
Heat transfer coefficient h[W/(m^2·°C)]	10	1000	10

After validating this hypothesis, a computation was performed this time considering the layered construction. The numerical time step for this computation was of 360s (0.1h).

In Figure A.3a are plotted the densities evolutions of each layer during the computation. As it was mentioned earlier, the foundation layer is already activated since the beginning of the computation. That is why the blue line in Figure A.3a is constant at 2710kg/m^3.

Analyzing Figure A.3b the instants of activation of each layer can easily be distinguished. It

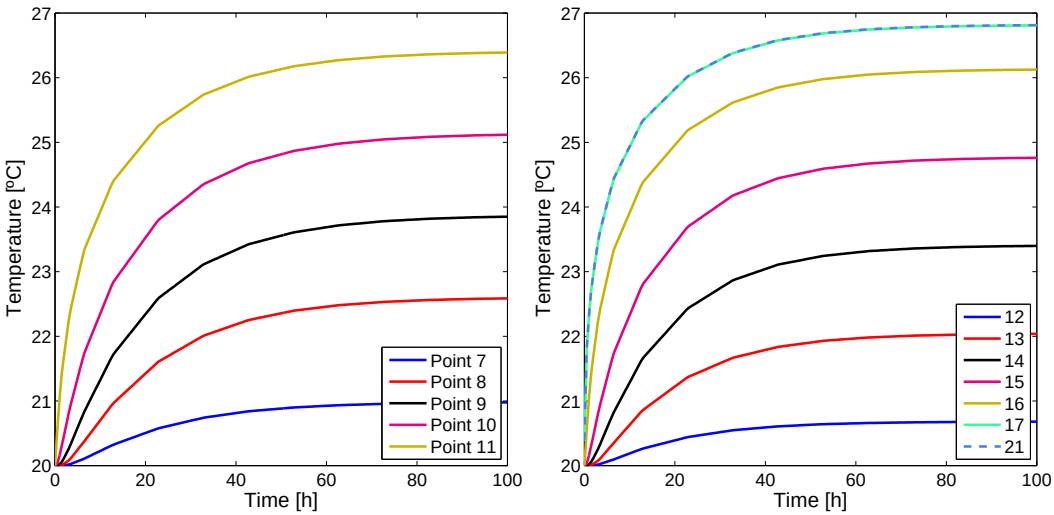

(a) (b)

Figure A.2: Heat flow on surface, two approaches for the birth and death of elements technique: a) 5 layered column; b) 10 layered column.

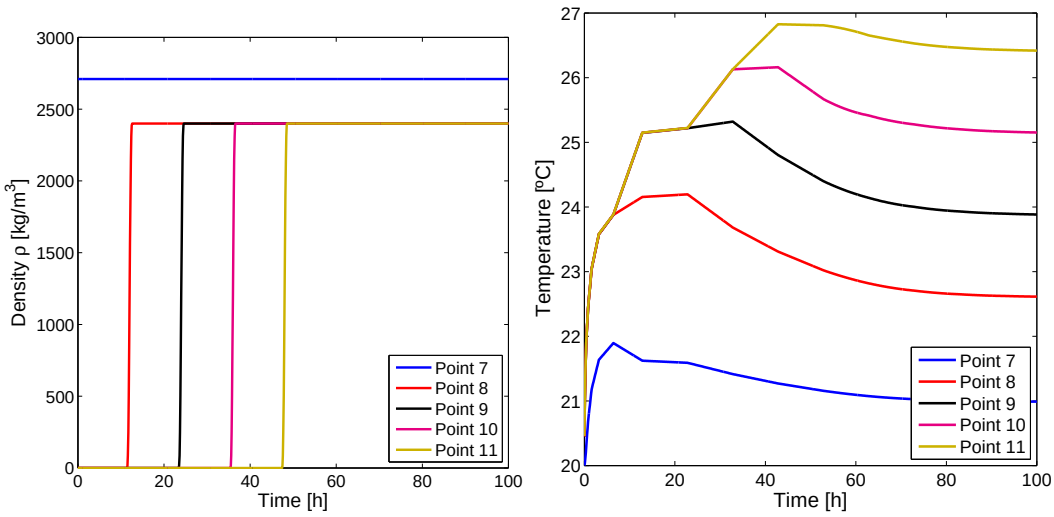

(a) (b)

Figure A.3: Layers' construction simulation and temperature evolution in time, first approach: a) Layered construction simulation; b) Temperature evolution in time.

is also evidenced in this figure that each layer, after being activated, heats up until the following layer is activated. This was expected because the exterior temperature (30°C) is greater than the temperatures developed so far inside each layer. However, this procedure is not able to impose the casting temperature of each layer at their respective activation times. Another point to be remarked here is that each layer begins to cool down right after the activation of the following layer. This point is not correct because it would be expected that each layer continues to heat due to the higher temperatures verified on the upper layers.

A.2 Moving mesh

In this subsection is described the second approach that was studied in order to simulate the birth and death of elements technique.

"Moving mesh" is a functionality of COMSOL Multiphysics® that allows the simulation of a moving boundary according to a given construction curve.

As in the first approach, the foundation layer is already activated since the beginning of the computation. The time step is of 60s and the total time of the simulation is of 100h.

The foundation and RCC properties are described in Table A.1. However, the material properties of the "non-activated" layers are not the same as the ones described in Table A.1. Because in this approach is the upper boundary that moves, the properties' values of each layer before being constructed/activated will be almost zero.

Figure A.4a shows the evolution of the material density in time according to the construction schedule. This validates the layered construction. Compared to the first approach, the same result is obtained.

Analyzing Figure A.4b one may easily detect the instant of construction of each layer, here represented by the round points. This instant of construction corresponds, in this second approach, to the instant when the upper boundary is moved to this new constructed layer. As is can be seen, the temperature of each layer at its correspondent construction instant is approaching the casting temperature of $20°C$. However, namely for the last layer, we haven't already attained the desired casting temperature at each construction instant.

In order to improve the model response, a simulation was performed this time using a time-step of 2 seconds and a total time of 48 hours. The result is plotted in Figure A.5a. In this figure, the round points correspond to the instants of construction of each layer. As it can be concluded, and as it was expected, by diminishing the time-step, the results are improved and

the temperature of each layer at its correspondent instant of construction/activation decreases when compared with the previous simulation, with exception of the upper layer, whom's temperature is higher for a lower time step. It needs to be taken into account that a time-step of 2 seconds leads to a numerical cost increase.

With the objective of studying the error that occurs between the desired casting temperature

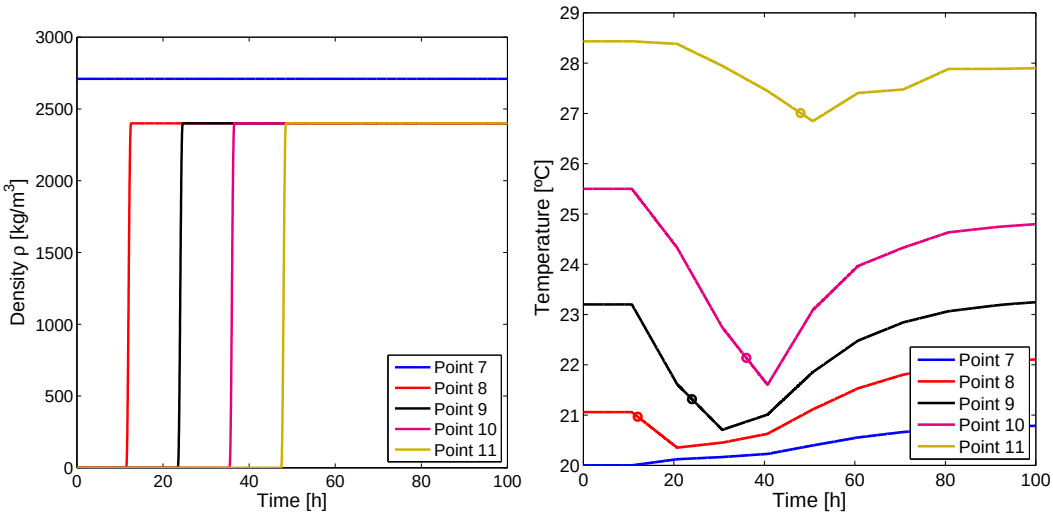

(a) (b)

Figure A.4: Layers' construction simulation and temperature evolution in time, second approach: a) Layered construction simulation; b) Temperature evolution in time.

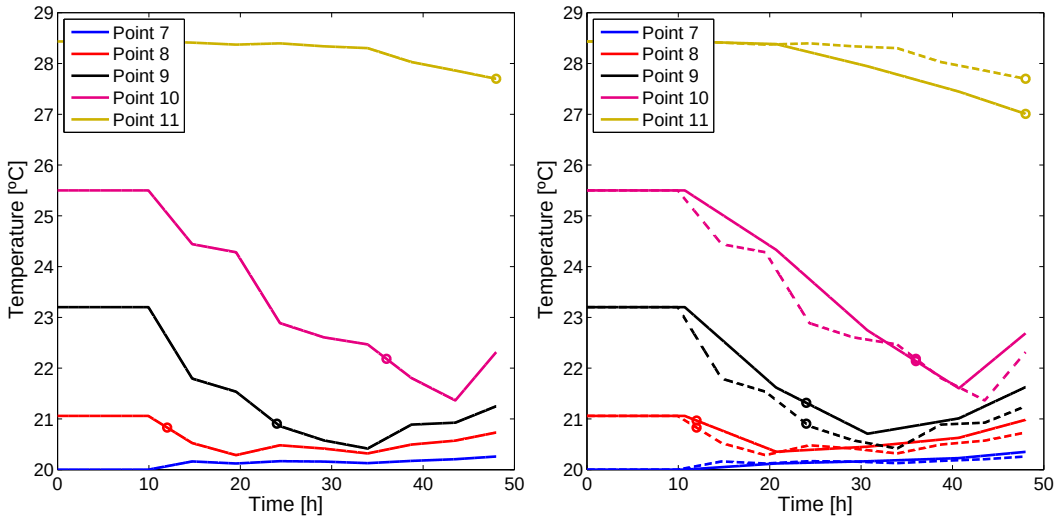

(a) (b)

Figure A.5: Temperature evolution in time, second approach, different time steps: a) Temperature evolution in time for a time-step of 2 seconds; b) Continuous line: $\Delta t = 60s$; Dashed line: $\Delta t = 2s$.

for each layer and the numerical obtained at each construction instant, it was decided to perform a calculation, this time imposing an ambient temperature of $21°C$. Then, the "error" obtained for the two cases ($T_{ext} = 30°C$ and $T_{ext} = 21°C$), for each posed layer, is calculated by means of equation A.1, where T_i^c is the computed temperature at each studied point, $T_{init,i}^{th}$ is the desired/theorectical casting temperature at the same point and T_{ext} is the ambient temperature. The results are plotted in Figure A.6. These calculations were performed considering a time step of $\Delta t = 0.5h$.

$$Err = \frac{\left|T_i^c - T_{init}^{th}\right|}{\left|T_{ext} - T_{init,i}^{th}\right|} \tag{A.1}$$

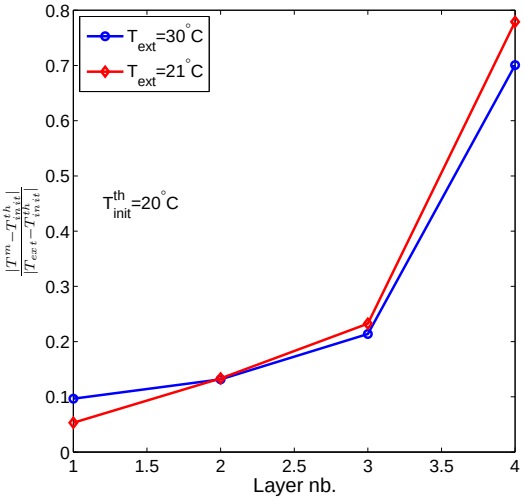

Figure A.6: Error for two different ambient temperatures

Considering the results presented in Figure A.6 it seems that the error is independent of the ambient temperature. It was also concluded that, as excepted, the maximum error occurs at the top layer. Therefore, it was decided to re-mesh the upper layer, which is now composed of 2092 triangular elements, instead of 536. A computation was performed, with a total simulation time of $50h$ and a time-step of $60s$. The result is plotted in Figure A.7a. As it can be seen analyzing Figure A.7b, the model's response improvement is not significant.

A.3 Thin layer in a column

Is here described the third studied approach to simulate the layered construction of the dam, consisting on introducing a thin layer to replace the moving boundary of the second approach. Then, this thin layer will be moved upwards in order to simulate the convection boundary while

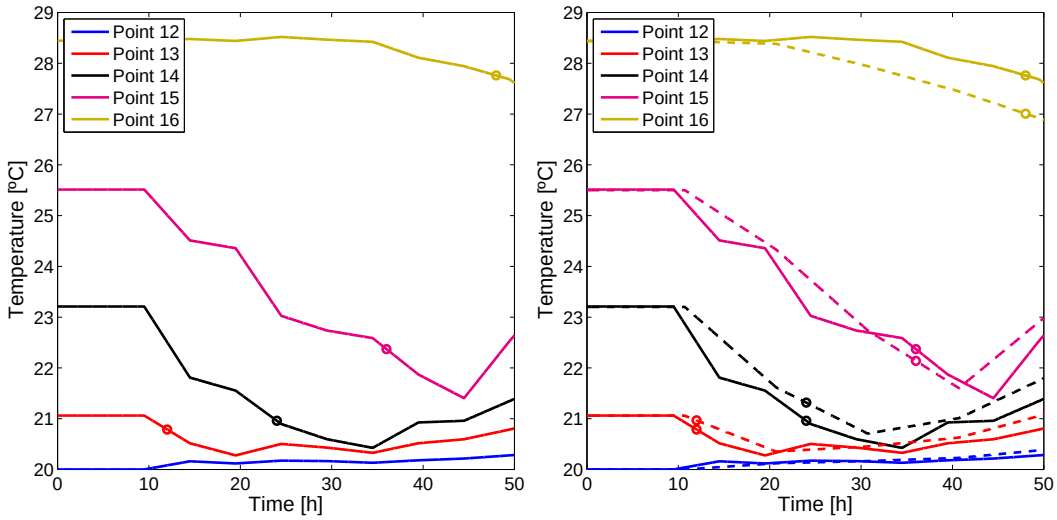

Figure A.7: Temperature evolution in time, with and without finer upper layer: a) Temperature evolution in time for a time-step of 60 seconds and a finer upper layer; b) Continuous line: finer upper layer; Dashed line: "normal" upper layer

constructing. Within this thin layer there will be a heat source, which is intended to simulate the heat convection flux on the top boundary, described by equation A.2, where e[m] is the layer thickness, here taken as 0.01m. The material properties of the thin layer are described in Table A.2. Following the same reasoning as for other tests, it was decided to validate the "thin layer methodology" with a simple model of a column.

$$\dot{Q} = h \cdot (T_{ext} - T) \cdot \frac{1}{e} \tag{A.2}$$

Table A.2: Material properties for the thin layer

Material	Thin layer
Density ρ[kg/m^3]	1.2
Specific heat c[J/(kg·°C)]	1000
Heat conduction coefficient k[W/(m·°C)]	3000
Heat convection coefficient h[W/(m^2°C)]	10

A first computation was made, not considering the layered construction simulation. A thin layer was applied at the upper surface of the column.

The results are compared with the ones obtained with a simple heat flow condition as presented in section A.1, Figure A.2a. The time step was of 1800s and the total time of the

simulation was of 100h. Analyzing Figure A.8a, one may conclude that the results are identical.

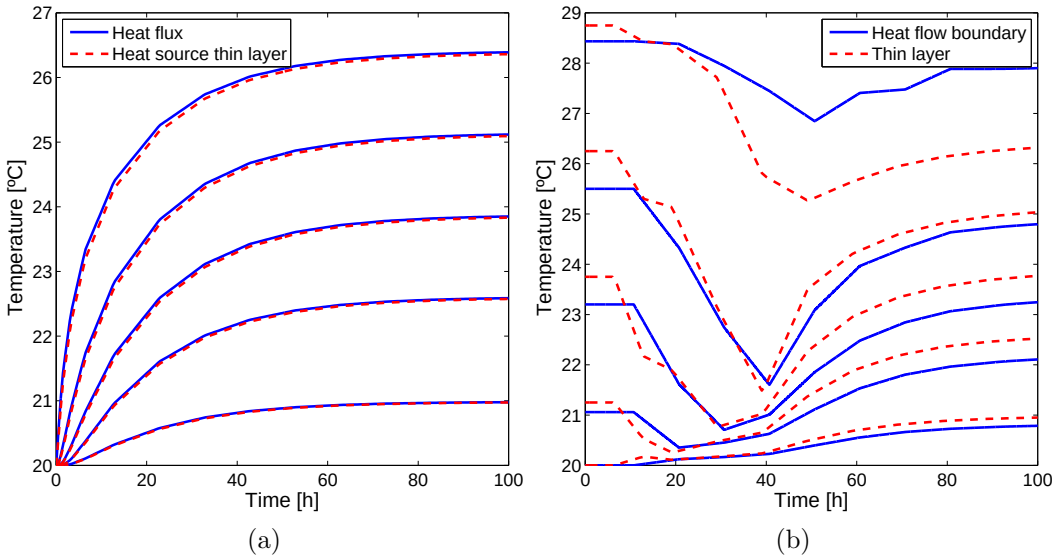

(a) (b)

Figure A.8: Temperature evolution in time for the thin layer model: a) Temperature distribution comparison between thin layer and heat flow; b) Temperature distribution comparison between thin layer and heat flow with construction simulation.

Then, the layered construction was added to this model. This approach consists on applying a prescribed deformation to a thin layer using the "Moving Mesh" functionality of COMSOL Multiphysics®.

A first simulation was done with a time-step of 1800s and a total time of simulation of 100h. The results of temperature evolution in time for each layer are plotted in Figure A.8b, with both the thin layer and the simple heat flow condition on surface. When compared with the results obtained using the heat flow boundary condition, one can conclude that their evolution is similar but, when using the thin layer approach, the temperature at the instant of construction is lower, which is favorable.

However, the casting temperature of each layer, which is supposed to be of 20°C is not achieved with this approach either.

Appendix B

Probabilistic tools to propagate uncertainties

In this appendix are given some details on the theory behind sensitivity analysis, with emphasis given to the sensitivity test applied in the present thesis: the RBD-FAST, *Random Balanced Design Fourier Amplitude Sensitivity Test*. Also some details about the Random Field Theory are discussed.

B.1 Sensitivity analysis methods

The main objective of a sensitivity analysis is to provide information about how randomness in the input variables of a model will affect its output variability.

In the present thesis, the effect of uncertainties related to some material properties, such as the water-to-cement ratio or the cement content, on the variability of the model output is assessed by means of a sensitivity analysis (chapter 5 for thermo-chemical behaviour and chapter 6 for thermo-chemo-mechanical behaviour).

Generally, the sensitivity analysis' methods are divided into 3 groups: screening, local and global sensitivity analysis (Jacques, 2005). While screening methods are purely qualitative, local and global sensitivity analysis are quantitative, leading to the obtention of the so-called sensitivity indexes S_i. Anyway, all of the three groups of methods seek the same objective of establishing a hierarchy on the input variables based on the influence they have on the output variability (Jacques, 2005). This feature is recalled and demonstrated in chapter 5 of this thesis.

The main difference between a local and a global sensitivity analysis is that the former focuses on the output value (by changing each input parameter at each time giving the re-

maining their mean values), while the latter seeks its variability (by accounting for random input variables). Actually, an example of local sensitivity analysis are the parametric studies presented and discussed in chapter 4, on which several parameters are changed individually and the output of the model is analyzed given those changes. On the other hand, in chapters 5 and 6 the sensitivity indexes are evaluated by means of a global sensitivity analysis which focuses on the variability of the model output.

The results of a sensitivity analysis give then precious information about the influence of the input variables on the model output, being a useful tool either to evaluate the adequacy and efficiency of the model (by assessing that a given variable is too much important, while this fact is not proven physically, which may be due to the inability of the model to reproduce the desired phenomena (Jacques, 2005)), or to discard uncertainty that was *a priori* given to a variable (if the sensitivity analysis reveal that a certain random input variable does not contributes much to the output variability, then that variables could be considered as deterministic in future studies). Also in chapter 6, this time over the thermo-mechanical behaviour, some input uncertainties appear not to influence significantly the output of the model, being characterized by very low sensitivity indexes.

Saltelli et al. (2000) distinguish the following groups of global sensitivity methods: reliability methods of level I, like FORM or SORM, Bayesian methods, graphic methods and variance-based methods. In the present thesis global sensitivity analysis are performed by means of variance-based methods. In the present case, RBD-FAST analysis are used. The RBD-FAST is a sensitivity tests based on the Fourier amplitude sensitivity test (FAST), which will be briefly described in the following, before introducing its variant RBD-FAST. Firstly, an introduction to the sensitivity indexes and Sobol method is done.

B.1.1 Sensitivity index - Sobol method

Let's take a certain model output Y which can be described by a polynomial form of equation B.1 (Mara, 2006), consisting on a particular form of the so-called High Dimensional Model Representation (HDMR), where x_i are standardized factors, Y_0 is the base simulation output, β_i is the first-order regression coefficient, β_{ij} the second-order one, and forward.

$$Y(x) = Y_0 + \sum_{i=1}^{p} \beta_i x_i + \sum_{i=1}^{p}\sum_{j=1}^{p} \beta_{ij} x_i x_j + \sum_{i=1}^{p}\sum_{j=1}^{p} \ldots \sum_{n=1}^{p} \beta_{ij\ldots n} x_i x_j \ldots x_n + \ldots \tag{B.1}$$

If no hypothesis are made over the model and if the input variables are considered to be independent, the sensitivity index S_i is given by equation B.2, which traduces the sensitivity of the model output Y to the variability of the input X_i. In equation B.2, $V(Y)$ is the total variance, given in equation B.3, where $E[Y|X_i]$ is the mean of the model output, given X_i. $E[Y|X_i]$ will be lower if the model output Y is not sensitive to the variations of X_i (Jacques, 2005). On the other hand, its variance, $V(E[Y|X_i])$ will traduce the sensitivity of the model, presenting greater values for the most important random input variables X_i.

$$S_i = \frac{V(E[Y|X_i])}{V(Y)} \quad , \quad Y = f(X_1, \ldots, X_p) \tag{B.2}$$

$$V(Y) = V(E[Y|X_i]) + E[V(Y|X_i)] \tag{B.3}$$

Sobol (1993) defines S_i as the first-order sensitivity index by decomposing $f(X_1, \ldots, X_i)$ in a sum of increasing order functions, commonly called the Sobol decomposition, given by equation B.4, where $f_0 = E[Y]$ (E being the mean), $f_0 + f_i(X_i) = E[Y|X_i]$ ($E[.|.]$ being the conditioned mean), $f_0 + f_i(X_i) + f_j(X_j) + f_{ij}(X_i, X_j) = E[Y|X_i, X_j]$, and so on...

In the Sobol method, not only the model output $Y = f(X_1, \ldots, X_p)$ is decomposed, but also its variance (equation B.5). This method allows the evaluation of the first-order sensitivity index via equation B.2, as well as higher-order sensitivity indexes, S_{ij} (equation B.6). Therefore, not only the influence of each input random variable is assessed, but also the influence of their interactions is assessed as well.

$$Y(X) = f_0 + \sum_{i=1}^{p} f_i(X_i) + \sum_{j>i}^{p} f_{ij}(X_i, X_j) + \ldots + f_{12\ldots p}(X_1, X_2, \ldots, X_p) \tag{B.4}$$

$$V(Y) = \sum_{i=1}^{p} V_i + \sum_{j>i}^{p} V_{ij} + \ldots + V_{12\ldots p} \tag{B.5}$$

$$1 = \sum_{i=1}^{p} S_i + \sum_{i=1}^{p}\sum_{j>i}^{p} S_{ij} + \ldots + S_{12\ldots p} \tag{B.6}$$

The problem with the Sobol method is the exponentially increasing number of computations with the number of input random variables needed to perform the analysis, which becomes

rapidly numerically non-affordable.

B.1.2 FAST

The FAST method was initially proposed by Cukier et al. (1973) and relies on the Fourier transform to decompose the variance of a model output Y, such as achieved with the Sobol decomposition method.

Let's take the model defined by equation B.7

$$f(x) = f(x_1 \ldots, x_p) \qquad x \in [0,1]^p \tag{B.7}$$

In FAST, each independent random variable (r.v.) is generated from a periodic search function. In the present thesis, equation B.8 from Saltelli et al. (1999) was adopted, on which each r.v. is assigned a characteristic integer frequency w_i (Xu and Gertner, 2008). Those frequencies shall be chosen in such a way that they avoid interferences between the outputs on those frequencies and their higher-order harmonics $\{w_i, 2w_i, \ldots, Mw_{max}\}$ (Tarantola, 2006). In equation B.8, x_i is one realization of the r.v. and F^{-1} is the inverse cumulative distribution function over x_i. S is the sample defined by $S = [s_1, \ldots, s_j, s_N]$, where s_j is given by B.9, being N the sample size.

$$x_i = F_i^{-1}\left(\frac{1}{2} + \frac{1}{\pi}\arcsin(\sin(w_i s))\right), \; -\pi \leq s \leq \pi \tag{B.8}$$

$$s_j = -\pi + \frac{\pi}{N} + \frac{2\pi(j-1)}{N}, \; \forall j = 1, 2, \ldots, N \tag{B.9}$$

Such as pointed out in Xu and Gertner (2008), the search function B.8 will allow the sampling of each random variable according to an expected probability density function. Each random variable will oscillate periodically at its corresponding frequency w_i and therefore, the model output will be a periodic function and a Fourier analysis can then be performed over it.

Expanding the model output with a Fourier series (equation B.10), the Fourier coefficients A_j and B_j may then be determined (equations B.12 and B.13, where f is the model output) and used to compute the total (V) and partial (V_i) variances of the model output. The first order sensitivity indices are finally obtained by equation B.15.

$$Y = f(x_1, \ldots, x_p) = f(s) = A_0 + \sum_{j=1}^{+\infty}\{A_j \cdot \cos(js) + B_j \cdot \sin(js)\} \tag{B.10}$$

$$V \approx 2\sum_{j=1}^{+\infty}\left(A_j^2 + B_j^2\right) \tag{B.11}$$

$$A_j = \frac{1}{2\pi}\int_{-\pi}^{\pi} f(x(s)) \cdot \cos(js)ds \tag{B.12}$$

$$B_j = \frac{1}{2\pi}\int_{-\pi}^{\pi} f(x(s)) \cdot \sin(js)ds \tag{B.13}$$

$$V_i = 2\sum_{p=1}^{+\infty}\left(A_{pw_i}^2 + B_{pwi}^2\right) \tag{B.14}$$

$$S_i = \frac{V_i}{V} \tag{B.15}$$

The number of simulations N needed in FAST may be found by means of equation B.16 (Saltelli et al., 1999; Xu and Gertner, 2008; Mara, 2009), let $M = 4$ and $w_{max} = 35$ in this work.

$$N = (2 \cdot M \cdot w_{max} + 1) \cdot 2 \tag{B.16}$$

Such as reported in the work of Jacques (2005), one of the advantages of the FAST method when compared to the Sobol one is that the sensitivity indexes corresponding to each input random variable may be calculated from one single sample set, while for Sobol would need two sample sets. However, in FAST the obtained S_i will be deterministic and functions of the chosen frequency series, while with Sobol a confidence interval is also obtained for the sensitivity indexes (Jacques, 2005). Anyway, and as previously pointed out, the Sobol method is numerically expensive, and for the case under study, on which a coupled thermo-chemo-mechanical analysis of an RCC dam during construction is performed, and for the number of adopted random variables, the Sobol method would lead to enormous computation time. Another limitation of the FAST method and that shall not be ignored is the fact that it can only account for independent random variables, not allowing, at least in its original version, the account for correlation between input random variables.

B.1.3 RBD-FAST

To overcome some limitations of FAST method, the RBD-FAST was proposed by Tarantola (2006) by using a sampling technique based on Satterthwaite's random balance designs (Satterthwaite, 1959; Tissot and Prieur, 2012). In their work, Xu and Gertner (2008) propose to ally random balance design and reordering to overcome the two most evident limitations of FAST:

the aliasing effect between the input variables due to the use of integer frequencies (which leads to the need of a bigger sample size) and the limitation of independency of the random variables, not allowing the account for correlation between them. In the present thesis, all of the random variables are considered to be independent. Therefore, only the first part of those achievements are applied in the present thesis and explained hereafter.

The advantage of RBD-FAST is that each random variable may be sampled from a periodic search function considering a single frequency w_i for all random variables, which will lead to a reduction on the number of simulations N. This is possible thanks to a randomization procedure used in RBD-FAST method (Tarantola et al., 2006; Xu and Gertner, 2008; Mara, 2009). The randomization procedure consists of randomly permuting the set of samples for each random variable, run the model using those permuted sets of random variables, and finally reorder the model output according to the input permutation for each random variable. Then, for each reordered set of output the single frequency w_i is restored and the sensitivity indices may be evaluated using the same procedure as in FAST. The disadvantage of RBD-FAST is that it does not allow the computation of the total sensitivity indexes.

B.1.4 Example, FAST vs. RBD-FAST

As an example, is here firstly performed a FAST analysis over the problem described by equation B.17 from Mara (2009). Then, RBD-FAST is performed over the same model and the solutions are compared. In equation B.17, X_1 and X_2 are independent variables, characterized by a uniform distribution $[-1, 1]$, as depicted in Figure B.1.

$$Y = X_1 + X_2 + 2 \cdot X_1 X_2 \tag{B.17}$$

The Fourier spectrum is calculated over the model output Y, as well as the power spectrum, here plotted in Figure B.2. In Figure B.2 are identified the adopted frequencies for the variables X_1 and X_2, which are of 11 and 35 respectively, as well as their interactions at frequencies 24 and 46.

In order to better understand and illustrate the randomization procedure applied in RBD-FAST, the same example is taken, but only randomizing each variable at a time. In Figure B.3a the frequency 35 is correctly identified for the periodical variable X_2, while the noise is due to the random variable X_1 and its interactions. On the other hand, while randomizing X_2,

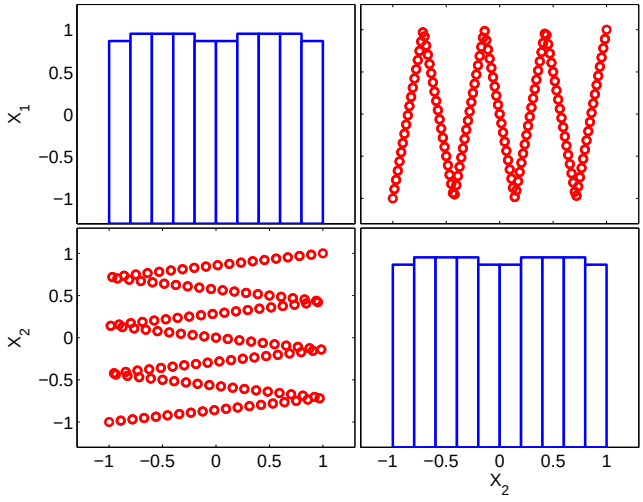

Figure B.1: Statistics of X_1 and X_2

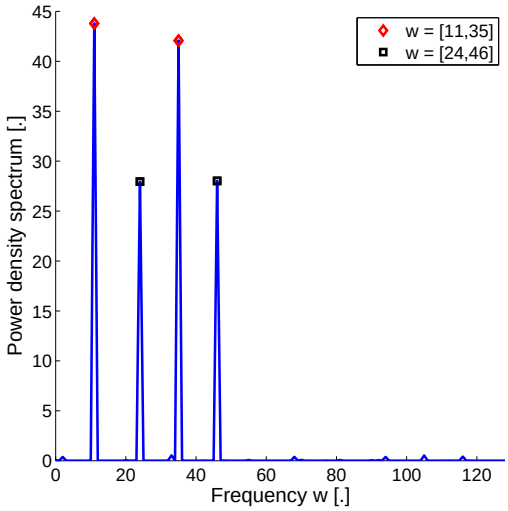

Figure B.2: Power spectrum of Y for FAST

the frequency of 11 of the periodical variable X_1 is identified in Figure B.3b. For more details please refer to Mara (2009), from which this example was extracted.

The first-order sensitivity indexes found using both procedures are described in Table B.1. The indexes found with both procedures are very similar.

Table B.1: Fist-order sensitivity indexes

	S_{i,X_1}	S_{i,X_2}
FAST	0.31	0.29
RBD-FAST	0.31	0.32

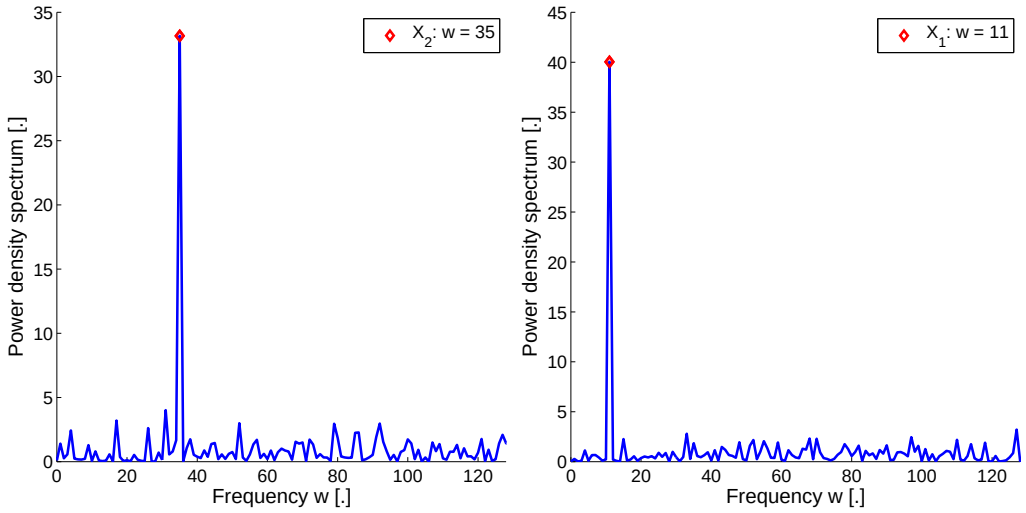

(a) (b)

Figure B.3: Power spectrum of Y applying randomization procedure: a) Randomization over X_1; b) Randomization over X_2.

B.2 Random fields approach

Here is described with more detail the random field approach used in the present thesis. Random field theory has been applied in several research domains, such as in structural engineering (e.g. Liu et al., 2001) and in geotechnical engineering (e.g. Vanmarcke (1977) and more recently Griffiths and Fenton (2004), Popescu et al. (2005), Lopez-Caballero and Modaressi-Farahmand-Razavi (2010), Caro et al. (2011), among others).

A random field is defined by a joint probability distribution such as in equation B.18 (Baecher and Christian, 2003). It may therefore be characterized by its mean (equation B.19), variance (equation B.20) and covariance (equation B.21).

$$F_{x_1,\ldots,x_n}(z_1,\ldots,z_n) = P\{z(x_1) \leq z_1,\ldots,z(x_n) \leq z_n\} \tag{B.18}$$

$$E[z(\mathbf{x})] = \mu(\mathbf{x}) \tag{B.19}$$

$$Var[z(\mathbf{x})] = \sigma^2(\mathbf{x}) \tag{B.20}$$

$$Cov[z(\mathbf{x}_i), z(\mathbf{x}_j)] = E[(z(\mathbf{x}_i) - \mu(\mathbf{x}_i)) \cdot (z(\mathbf{x}_j) - \mu(\mathbf{x}_j))] \tag{B.21}$$

A random field is generally characterized by its stationarity (or non-stationarity). A random field is considered stationary if the joint probability functions are independent of the absolute location, if the mean value is of $E[z(\mathbf{x})] = \mu\,, \forall \mathbf{x}$ and if the covariance only depends on the relative location between each couple of points discretized over the domain: $Cov[z(\mathbf{x}_i, \mathbf{x}_j)] =$

$C_z(\mathbf{x}_i - \mathbf{x}_j)$, where C_z is the autocovariance function (Baecher and Christian, 2003). In the present thesis the applied random fields are stationary (or homogeneous).

B.2.1 Gaussian random fields

In this thesis, the applied random fields are Gaussian, described by the probability density function of equation B.22, where μ is the mean vector and Σ is the covariance matrix (Baecher and Christian, 2003).

$$f_z(\mathbf{z}) = (2\pi)^{-n/2}|\Sigma|^{-1/2}\exp\{-\frac{1}{2}(\mathbf{z}-\mu)'\Sigma^{-1}(\mathbf{z}-\mu)\} \tag{B.22}$$

$$\Sigma_{ij} = \{Cov[z_i(\mathbf{x}), z_j(\mathbf{x})]\} \tag{B.23}$$

Adler (1981) have described the following properties of Gaussian random fields: they are fully characterized by the mean and autocovariance function; any subset of variables is also Gaussian; the conditional probability distributions of any two variables is Gaussian; if two variables are bi-variate Gaussian and their covariance is zero, then they are independent.

B.2.2 Autocorrelation functions

The autocorrelation function defines the correlation between the values of adjacent cells of the model and may be represented by equation B.24, being G_i and G_j two locations of the random field.

$$R(G_i, G_j) = \frac{Cov[Z(G_i), G(G_j)]}{\sqrt{Var[Z(G_i)] \cdot Var[Z(G_j)]}} \tag{B.24}$$

In a homogenous/stationary random field, the autocorrelation function only depends on the distance between the two locations G_i and G_j and it can be fully defined by its mean, variance and autocorrelation function (Huyse and Walters, 2001). There are several widely applied models to describe the autocorrelation function, such as: exponential (equation B.25), squared exponential (equation B.26), triangular (equation B.27) and damped sinusoidal (equation B.28) (Huyse and Walters, 2001). In these equations, $\hat{\rho}$ is the autocorrelation function, G_i and G_j are two locations and l_c is the correlation length. By definition, a larger correlation length will lead to a slower varying random field, and therefore the variation between two locations will increase by decreasing l_c.

$$\hat{\rho}_{G_i,G_j} = \exp\left(-\frac{|G_i - G_j|}{l_c}\right) \tag{B.25}$$

$$\hat{\rho}_{G_i,G_j} = \exp\left[-\left(\frac{G_i - G_j}{l_c}\right)^2\right] \tag{B.26}$$

$$\hat{\rho}_{G_i,G_j} = \begin{cases} 1 - \frac{|G_i - G_j|}{l_c} & \text{if} \quad |G_i - G_j| \leq l_c \\ 0 \quad \text{if} \quad |G_i - G_j| > l_c \end{cases} \tag{B.27}$$

$$\hat{\rho}_{G_i,G_j} = \frac{\sin(\pi|G_i - G_j|/l_c)}{\pi|G_i - G_j|/l_c} \tag{B.28}$$

Because of the lack of field data about the parameters' spatial variation, a squared exponential autocorrelation function of the form of equation B.29 was assumed to be well adapted in this thesis. The applied random field is bidimensional (2D) and two autocorrelation functions are given, one in each direction, characterized by two different correlation lengths: θ_x and θ_y.

$$\hat{\rho}_{G_i,G_j} = \exp\left[-\pi\left[\left(\frac{d_x}{\theta_x}\right)^2 + \left(\frac{d_y}{\theta_y}\right)^2\right]\right] \tag{B.29}$$

In equation B.29, $\hat{\rho}$ is the correlation coefficient between points G_i and G_j, d_x and d_y being the horizontal and vertical distances between those two points.

B.2.3 Random fields generation

There exist several methods available to discretize a random field, such as the midpoint method (used in this work), the spatial average method, the shape function method and series expansion-based methods such as Karhunen-Loève or Newman (Huyse and Walters, 2001; Phoon, 2008). In the midpoint method, the model is sub-divided into several cells, each one being assigned a random value of the parameter of interest, constant within that cell.

Then, the generation of those random fields may be done by several processes. In the case of midpoint random fields such as the ones applied in this thesis, their generation may be done by: auto-regressive processes, covariance decomposition and spectral representation. For more details about these methods please refer to Huyse and Walters (2001).

In the present thesis, the stationary Gaussian random fields are discretized by the midpoint method and have been generated via Monte Carlo sampling method, based on the covariance matrix decomposition technique (Lopez-Caballero and Modaressi-Farahmand-Razavi, 2010; Davis, 1987), used in the work of Caro et al. (2011) and proposed by El-Kadi and Williams

(2000).

Based on principal components analysis, the correlated random field P is obtained by equation B.30, where B is the matrix of the eigenvectors of the correlation matrix R (obtained via equation B.29 for each pair of points), Λ is the diagonal matrix of the square root of the eigenvalues of R and C is the matrix of the Gaussian uncorrelated random variables. The variables of the random field P are Gaussian $N[0,1]$ and correlated following the R matrix.

$$[P] = [B] * [\Lambda] * [C] \tag{B.30}$$

Afterwards, the Gaussian correlated field P is transformed into a non-Gaussian random field by using the *inverse CDF* (cumulative distribution function) method:

$$f_B(x) = F_B^{-1}\left[F_G[f_P(x)]\right] \tag{B.31}$$

where F_B and F_G are the CDFs of the non-Gaussian and Gaussian random field respectively. For further details about this method please refer to Lopez-Caballero and Modaressi-Farahmand-Razavi (2010).

Bibliography

Abdo, F. Y. (November 2008). Roller-compacted-concrete dams: Design and construction trends. *Hydro Review, HCI Publications*.

Adler, R. J. (1981). *The Geometry of Random Fields*. SIAM.

Alexandersson, J. (1972). Strength losses in heat cured concrete. *Swedish Cement and Concrete Research Institute, Handl*, 43:135p.

Altarejos-García, L. (2009). *Contribution to the estimation of the probability of failure of concrete gravity dams in the risk analysis context.* Ph.D. thesis, Universidad Politécnica de Valencia.

Altarejos-García, L., Escuder-Bueno, I., Serrano-Lombillo, A., and Gómez-Membrillera-Ortuño, M. (2012). Methodology for estimating the probability of failure by sliding in concrete gravity dams in the context of risk analysis. *Structural Safety*, 36-37(1):1–13.

Andriolo, F. R. (1998). *The use of Roller Compacted Concrete.* Oficina de Textos.

Aubry, D., Chouvet, D., Modaressi, A., and Modaressi, H. (1986). GEFDyn: Logiciel d'analyse de comportement mécanique des sols par éléments finis avec prise en compte du couplage sol-eau-air. Manuel scientifique, LMSS-Mat, Ecole Centrale Paris.

Aurich, M. (2008). *Simulação computacional do comportamento do concreto nas primeiras idades.* Ph.D. thesis, Escola Politécnica da Universidade de São Paulo.

Azenha, M. (2009). *Numerical simulation of the structural behaviour of concrete since its early ages*. Ph.D. thesis, Faculdade de Engenharia, Universidade do Porto.

Azenha, M., Faria, R., and Ferreira, D. (2008). Monitorização e simulação numérica do processo construtivo de uma barragem gravidade de betão. In *Encontro Nacional de Betão Estrutural,*

Guimarães. Paulo B. Lourenço 1967-ed. lit., Grupo Português de Betão Estrutural, Universidade do Minho, Escola de Engenharia.

Azenha, M., Faria, R., Magalhães, F., Ramos, L., and Cunha, A. (2010). Measurement of concrete E-modulus evolution since casting: A novel method based on ambient vibration. *Cement and Concrete Research*, 40(7):1096–1105.

Azenha, M., Faria, R., Magalhães, F., Ramos, L., and Cunha, A. (2011). Measurement of the E-modulus of cement pastes and mortars since casting, using a vibration based technique. *Materials and Structures*, 45(1-2):81–92.

BaCaRa (1996). *Projet National BaCaRa 1988-1996, Le Béton Compacté au Rouleau, Les barrages en BCR*. Presses de l'Ecole Nationale des Ponts et Chaussées.

Baecher, G. B. and Christian, J. T. (2003). *Reliability and Statistics in Geotechnical Engineering*. John Wiley & Sons.

Ballim, Y. and Graham, P. C. (2003). A maturity approach to the rate of heat evolution in concrete. *Magazine of Concrete Research*, 55(3):249–256.

Bastida-Arteaga, E., Chateauneuf, A., Sánchez-Silva, M., Bressolette, P., and Schoefs, F. (2010). Influence of weather and global warming in chloride ingress into concrete: A stochastic approach. *Structural Safety*, 32(1):238–249.

Bastida-Arteaga, E., Chateauneuf, A., Sánchez-Silva, M., Bressolette, P., and Schoefs, F. (2011). A comprehensive probabilistic model of chloride ingress in unsaturated concrete. *Engineering Structures*, 33(1):720–730.

Bažant, Z. and Osman, E. (1976). Double power law for basic creep of concrete. *Materials and Structures, Research and Testing*, 6(49):3–11.

Bažant, Z. P. (1988). *Mathematical modeling of creep and shrinkage of concrete*. John Wiley and Sons.

Bažant, Z. P. and Prasannan, S. (1989). Solidification theory for concrete creep. I: Formulation. *Journal of Engineering Mechanics*, 115(8):1691–1703.

Bayes, T. and Price, R. (1763). An essay towards solving a problem in the doctrine of chance. By the late Rev. Mr. Bayes, communicated by Mr. Price, in a letter to John Canton, A. M. F. R. S. *Philosophical Transactions of the Royal Society of London*, 53(0):370–418.

Benboudjema, F. and Torrenti, J. (2008). Early-age behaviour of concrete nuclear containments. *Nuclear Engineering and Design*, 238(1):2495–2506.

Bentz, D. P., Waller, V., and de Larrard, F. (1998). Prediction of adiabatic temperature rise in conventional and high-performance concretes using a 3-D microstructural model. *Cement and Concrete Research*, 28(2):285–297.

Berga, L., Buil, J. M., Jofré, C., and Chonggang, S. (2003). Proceedings of the International Symposium on Roller Compacted Concrete Dams. In *November 17th-19th, Madrid, Spain, ISBN 90 5809 564*, pages 215–225. A. A. Balkema.

Bertagnoli, G., Mancini, G., and Tondolo, F. (2008). Numerical modelling of early-age concrete hardening. *Magazine of Concrete Research*, 60.

Bettencourt Ribeiro, A. C. and de Almeida, I. R. (2000). Study on high performance roller compacted concrete. *Materials and Structures*, 33(1):398–402.

Bettencourt Ribeiro, A. C., Díez-Cascón, J., and Gonçalves, A. F. (2001). Roller compacted concrete - tensile strength of horizontal joints. *Materials and Structures*, 34(1):413–417.

Boutillon, L., Linger, L., Kolani, B., and Meyer, E. (2012). Effects of sun irradiation on the temperature and early age stress distribution in outdoor concrete structures. In *Crack Control of Mass Concrete and Related Issues concerning Early-Age of Concrete Structures, Proceedings of the RILEM-JCI International Workshop ConCrack3*, pages 181–192. RILEM.

Bowles, D. S. (2012). Tolerable risk guidelines for dams: Principles and applications. In *Risk Analysis, Dam Safety, Dam Security and Critical Infrastructure Management*, pages 215–225. I. Escuder-Bueno, E. Matheu, L. Altarejos-García, J. T. Castillo-Rodríguez, CRC Press, Taylor & Francis Group.

Bowles, D. S., Giuliani, F. L., Hartford, D. N. D., Janssen, J. P. F. M., McGrath, S., Poupart, M., Stewart, D., and Zielinski, P. A. (2007). ICOLD bulletin on dam safety management. In *IPENZ Proceedings of Technical Groups 33/2 (LD)*. IPENZ.

Buffo-Lacarrière, L. (2007). *Prévision et évaluation de la fissuration précoce des ouvrages en béton.* Ph.D. thesis, Laboratoire de Matériaux et Durabilité des Constructions, INSA-UPS, Toulouse, France.

Byfors, J. (1980). Plain concrete at early ages. CBI research report 3:80, 344p., Swedish Cement and Concrete Research Institute, Stockholm.

Caldeira, L. (2008). *Análises de risco em geotecnia. Aplicação a barragens de aterro.* Programas de Investigação e de Pós-graduação elaborados no Laboratório Nacional de Engenharia Civil em 2005 para obtenção do título de Habilitado para o Exercício das Funções de Coordenação Científica, LNEC, Lisboa, Portugal.

Calmon, J. L., Murcia, J., Botassi dos Santos, S., Gambale, E., and da Silva, C. J. (2003). Numerical modelling of thermal stress in RCC dams using 2-D finite element method - case study. In *Roller Compacted Concrete Dams*, pages 569–578. A. A. Balkema.

Cannon, R. W. (1974). Concrete Dam Construction Using Earth Compaction Methods. *Economical Construction of Concrete Dams, ASCE, New York*, pages 143–152.

Carino, N. J. (1982). Maturity functions for concrete. In *International Conference on Concrete at Early Ages (Paris), Ecole Nationale des Ponts et Chaussées, Paris*, pages 123–128. RILEM, Vol. I.

Carino, N. J. (1984). The maturity method: Theory and application. *Journal of Cement, Concrete and Aggregates (ASTM)*, 6(2):61–73.

Carino, N. J. and Lew, H. S. (2001). The maturity method: from theory to application. In *Structures Congress & Exposition, Washington D. C.* ASCE, Reston, Virginia, Peter C. Chang.

Caro, S., Masad, E., M.Sánchez-Silva, and Little, D. (2011). Stochastic micromechanical model of the deterioration of asphalt mixtures subject to moisture diffusion processes. *International journal for numerical and analytical methods in geomechanics*, 35(1):1079–1097.

Carol, I. and Bažant, Z. P. (1997). Viscoelasticity with aging caused by solidification of nonaging constituent. *Journal of Engineering Mechanics, ASCE*, 119(11):2252–2269.

Castro, A. T. (1998). *Métodos de retroanálise na interpretação do comportamento de barragens de betão.* Ph.D. thesis, IST, Lisboa, Portugal.

CEN (2004a). En 1992-1-1, Eurocode 2, Design of Concrete Structures. Part 1-1: General Rules and rules for buildings. Technical report, European Committee for Standardization, Brussels.

CEN (2004b). En 1997-1, eurocode 7: Geotechnical Design. part 1: General Rules. Technical report, European Committee for Standardization, Brussels.

Cervera, M., Faria, R., Oliver, J., and Prato, T. (2002). Numerical modelling of concrete curing, regarding hydration and temperature phenomena. *Computers and Structures*, 80(1):1511–1521.

Cervera, M. and García-Soriano, J. (2002). Simulación numérica del comportamiento termo-mecánico de presas de HCR. Parte II: Aplicación a la presa de Rialb. *Revista Internacional de Métodos para Cálculo y Diseño en Ingeniería*, 18(1):95–110.

Cervera, M., Oliver, J., and Prato, T. (1999a). Thermo-chemo-mechanical model for concrete. I: Hydration and aging. *Journal of Engineering Mechanics*, 125(9):1018–1027.

Cervera, M., Oliver, J., and Prato, T. (1999b). Thermo-chemo-mechanical model for concrete. II: Damage and creep. *Journal of Engineering Mechanics*, 125(9):1028–1039.

Cervera, M., Oliver, J., and Prato, T. (2000a). Simulation of construction of RCC dams. I: Temperature and Aging. *Journal of Structural Engineering*, 126(9):1053–1061.

Cervera, M., Oliver, J., and Prato, T. (2000b). Simulation of construction of RCC dams. II: Stress and Damage. *Journal of Structural Engineering*, 126(9):1062–1069.

Cervera, M., Oliver, J., Prato, T., and García, J. (2001). Simulación numérica del comportamiento termo-mecánico de presas de HCR. Parte I: Modelización y calibración. *Revista Internacional de Métodos para Cálculo y Diseño en Ingeniería*, 17(4):491–504.

Chateauneuf, A. M., Raphael, W. E., and Pitti, R. J. B. M. (2013). Reliability of prestressed concrete structures considering creep models. In *Structure and* I*nfrastructure* E*ngineering:* M*aintenance,* M*anagement,* L*ife-*C*ycle* D*esign and* P*erformance*. Taylor and Francis.

Conrad, M. (2006). *A contribution to the thermal stress behaviour of roller-compacted-concrete (RCC) gravity dams : field and numerical investigations*. Ph.D. thesis, Technischen Universitat Munchen.

Conrad, M., Aufleger, M., and Maikawi, A. (2003). Investigations on the modulus of elasticity of young RCC. In *Proceedings of the fourth international symposium on roller compacted concrete (RCC) dams.*, pages 729–733.

Cornell, C. A. (1967). *Bounds on the Reliability of Structural Systems*. Proc. Amer. Soc. Civil Eng., N. Y., 93(ST1).

Cornell, C. A. and Krawinkler, H. (2000). Progress and chalanges in seismic performance assessment. *PEER Center News*, 3(2).

Coussy, O. (1996). *Mechanics and Physics of Porous Solids*. J. Wiley & Sons.

Cukier, R. I., Fortuin, C. M., Shuler, K. E., Petschek, A. G., and Schaibly, J. H. (1973). Study of the sensitivity of coupled reaction systems to uncertainties in rate coefficients - theory. *Journal Chemical Physics*, 59(1):3873–3878.

Davis, M. W. (1987). Production of conditional simulations via the LU triangular decomposition of the covariance matrix. *Mathematical Geology*, 19(2):91–98.

de Araújo, J. M. and Awruch, A. M. (1998a). Cracking safety evaluation on gravity concrete dams during the construction phase. *Computers and Structures*, 66(1):93–104.

de Araújo, J. M. and Awruch, A. M. (1998b). Probabilistic finite element analysis of concrete gravity dams. *Advances in Engineering Software*, 29(2):97–104.

De Borst, R. and Van den Boogaard, A. (1994). Finite-element modeling of deformation and cracking in early-age concrete. *Journal of Engineering Mechanics, Div ASCE*, 120(12):2519–2534.

De Schutter, G. (2002). Finite element simulation of thermal cracking in massive hardening concrete elements using degree of hydration based material laws. *Computers and Structures*, 80(1):2035–2042.

De Schutter, G. (2004). Applicability of degree of hydration concept and maturity method for thermo-visco-elastic behaviour of early age concrete. *Cement and Concrete Composites*, 26(1):437–443.

De Schutter, G. and Taerwe, L. (1995). General hydration model for Portland cement and blast furnace slag cement. *Cement and Concrete Research*, 25(3):593–604.

De Schutter, G. and Taerwe, L. (1996). Degree of hydration-based description of mechanical properties of early age concrete. *Materials and Structures*, 29(1):335–344.

De Schutter, G. and Taerwe, L. (2000). Fictitious degree of hydration method for the basic creep of early age concrete. *Materials and Structures*, 33(1):370–380.

El-Kadi, A. and Williams, S. (2000). Generating two-dimensional fields of autocorrelated, normally distributed parameters by the matrix decomposition technique. *Ground water*, 38(4):530–532.

Emborg, M. (1986). Thermal stresses in massive concrete structures calculated with a linear creep law of integral type. In *Fourth RILEM International Symposium on Creep and Shrinkage of Concrete: Mathematical Modelling*. Evanston.

Emborg, M. (1998). Models and methods for computation of thermal stresses. In: Prevention of thermal cracking in concrete at early ages. Report 15, R. Springenschmid, E&FN Spon.

Escuder-Bueno, I., Matheu, E., Altarejos-García, L., and Castillo-Rodríguez, J. T. (2012). *Risk Analysis, Dam Safety, Dam Security and Critical Infrastructure Management*. CRC Press, Taylor & Francis Group.

Faria, R., Azenha, M., and Figueiras, J. A. (2006). Modelling of concrete at early ages: Application to an externally restrained slab. *Cement and Concrete Composites*, 28(1):572–585.

Favre, J.-L. (2004). *Sécurité des ouvrages, Risques. Modélisation de l'incertain, fiabilité, analyse des risques.* Ellipses.

Ferry-Borges, J. (1982). Quality assurance and reliability of concrete structures. Technical report, CEB Bulletin d'information, N.147.

Gaspar, A., Lopez-Caballero, F., Modaressi, A., and Gomes-Correia, A. (2014). Methodology for a probabilistic analysis of an RCC gravity dam construction. Modelling of temperature, hydration degree and ageing degree fields. *Engineering Structures*, 65(1):99–110.

Giesecke, J., Qin, M., and Marx, W. (2002). Realistic and computational efficient evaluation of temperature and stress development in large RCC dams. *DTK - Deutsches TalsperrenKomitee*.

Grieve, G. (1991). *The Influence of Two South African Fly Ashes on the Engineering Properties of Concrete*. Ph.D. thesis, University of Witwatersrand, Johannesburg.

Griffiths, D. and Fenton, G. (2004). Probabilistic slope stability analysis by finite element. *Journal of Geotechnical and Geoenvironmental Engineering*, 130(5):507–18.

Haldar, A. and Mahadevan, S. (2000). *Reliability Assessment Using Stochastic Finite Element Analysis*. John Wiley & Sons, Inc.

Hansen, K. D. and Forbes, B. A. (2012). Thermal induced cracking performance of RCC dams. In *6th International Sysposium on Roller Compacted Concrete (RCC) Dams*. SPANCOLD, CHINCOLD.

Hansen, K. D. and Reinhardt, W. G. (1991). *Roller-Compacted Concrete Dams*. McGraw-Hill, New York.

Hansen, P. F. and Pedersen, J. (1977). Maturity computer for controlled curing and hardening of concrete. *Nordisk Betong*, 1:19–34.

Harr, M. E. (1987). *Reliability Based Design in Civil Engineering*. McGraw-Hill, New York.

Hassan, J. E., Bressolette, P., Chateauneuf, A., and Tawil, K. E. (2010). Reliability-based assessment of the effect of climatic conditions on the corrosion of RC structures subject to chloride ingress. *Engineering Structures*, 32(1):3279–3287.

Helton, J. C., Johnson, J. D., and Storlie, C. B. (2006). Survey of sampling-based methods for uncertainty and sensitivity analysis. *Reliability Engineering and System safety*, 91(9-10):1175–1209.

Huyse, L. and Walters, R. W. (2001). Random field solutions including boundary conditions uncertainty for the steady-state generalized Burgers equation. Report n.2001-35, National Aeronautics and Space Administration.

ICOLD (2003). Bulletin on risk assessment in dam safety management. ICOLD.

Jaafar, M. S., Bayagoob, K. H., Noorzaei, J., and Thanoon, W. A. M. (2007). Development of finite element computer code for thermal analysis of roller compacted concrete dams. *Advances in Engineering Software*, 38(1):886–895.

Jacques, J. (2005). *Contributions à l'analyse de sensibilité et à l'analyse discriminante généralisé*. Ph.D. thesis, Université Joseph Fourier, Grenoble.

JCI (2012). JCI guidelines for control of cracking of mass concrete. In CONCRACK 3*, Paris, France*.

Ji, G. (2008). *Cracking risk of concrete structures in the hardening phase: Experiments, material modeling and finite element analysis*. Ph.D. thesis, Department of Structural Engineering, The Norwegian University of Science and Technology, Trondheim, Norway.

Keitel, H. and Dimmig-Osburg, A. (2010). Development of finite element computer code for thermal analysis of roller compacted concrete dams. *Engineering Structures*, 1(32):3758–3767.

Khan, N. A. (2011). *Thermo-Mechanical Analysis of Roller Compacted Concrete Dams*. Ms.C. thesis, Department of Civil Engineering, University of Engineering and Technology, Lahore, Pakistan.

Kim, J.-K., Moon, Y.-H., and Eo, S.-H. (1998). Compressive strength development of concrete with different curing time and temperature. *Cement and Concrete Research*, 28(12):1761–1773.

Lackner, R. and Mang, H. A. (2004). Chemoplastic material model for the simulation of early-age cracking: From the constitutive law to numerical analyses of massive concrete structures. *Cement and Concrete Composites*, 26(1):551–562.

Lancieri, M. and Zollo, A. (2008). A bayesian approach to the real-time estimation of magnitude from the early P and S wave displacement peaks. *Journal of Geophysical Research*, 113(1):112–147.

Laplante, P. (1993). *Propriétés mécaniques des bétons durcissants, analyse comparée des bétons classiques et à très hautes performances.* Ph.D. thesis, LCPC.

Leitão, N. A. S. (2011). Environmental thermal actions - thermal analysis of Alto Lindoso dam. In *6th International Conference on Dam Engineering, Lisbon, Portugal*, pages 687–697. C. Pina, E. Portela, J. Gomes (ed.).

Leitão, N. A. S., Batista, A. L., and Castro, A. T. (2007). Análise termo-mecânica de estruturas maciças de betão. Aplicação a barragens de betão compactado com cilindros. In *CMNE/CILAMNCE*. José César de Sá, Raimundo Delgado, Abel D. Santos, António Rodríguez-Ferran, Javier Oliver, Paulo R. M. Lyra, José L. D. Alves (Eds.).

Liu, N., Hu, B., and Yu, Z. W. (2001). Stochastic finite element method for random temperature in concrete structures. *International journal of solids and structures*, 1(38):6965–6983.

Lopez-Caballero, F., Gaspar, A. P. T., and Gomes-Correia, A. (2011). Uncertainty and sensitivity analysis of FWD test. In *2011 GeoHunan International Conference, Changsha, China*. ASCE.

Lopez-Caballero, F. and Modaressi-Farahmand-Razavi, A. (2010). Assessment of variability and uncertainties effects on the seismic response of a liquefiable soil profile. *Soil Dynamics and Earthquake Engineering*, 30(1):600–613.

Luna, R. and Wu, Y. (2000). Simulation of temperature and stress fields during rcc dam construction. *Journal of Construction Engineering and Management*, 126(5):381–388.

Lura, P. and Van Breugel, K. (2001). Thermal properties of concrete: sensitivity studies. Report BE96-3843/2001:15-X, Improved Production of Advanced Concrete Structures - IPACS, Lulea University of Techanilogy, ISBN 91-89580-15-X.

Malika, V. (2009). *Condition indicators for the assessment of local and spatial deterioration of concrete structures*. Ph.D. thesis, Institute of Structural Engineering, Swiss Federal Institute of Technilogy, ETH Zurich.

Malkawi, A. I. H., Mutasher, S. A., and Qiu, T. J. (2003). Thermal-structural modeling and temperature control of roller compacted concrete gravity dam. *Journal of performance of constructed facilities, ASCE*, 17(4):177–187.

Mara, T. A. (2002-2006). *Développement et Applications d'Outils d'Aide à la Vérification, la Calibration, l'Analyse de Sensitiblité et d'Incertitude de Modèles*. Rapport d'activités, Laboratoire de Physique du Bâtiment et des Systèmes, Université de la Réunion.

Mara, T. A. (2009). Extension of the RBD-FAST method to the computation of global sensitivity indices. *Reliability Engineering and System Safety*, 94(1):1274–1281.

Marques, T. A. S. (2008). *Estudo de um betão compactado com cilindros*. Ms.C. thesis, Faculdade de Ciências e Tecnologia da Universidade Nova de Lisboa.

Mata, J. T. C., Portela, E. T. A., and Dias, J. L. R. (2007). Application of neural networks to dam safety control. In *5th International Conference of Dam Engineering, LNEC, Lisbon, Portugal*, pages 315–324.

Miranda, M. P., Moura, G. M., Antunes, N. S., and Monteiro, P. J. (2000). Aproveitamento de pedrógão. aspectos principais do projecto da barragem. In *1° Congresso sobre Aproveitamentos e Gestão de Recursos Hídricos em Países de Idioma Português*. Rio de Janeiro.

Moncada, C. (2009). *Evaluation probabiliste de la sécurité structurale des barrages-poids*. Ph.D. thesis, Université Blaise Pascal - Clermont II, France.

Nisar, A., Dollar, D., Jacob, P., Chu, D., Logie, C., and Li, G. (2008). Nonlinear incremental thermal stress-strain analysis for Portugues dam, an RCC gravity arch dam. In *28th United States Society of Dams Annual Meeting and Conference*.

Noorzaei, J., Bayagoob, K. H., Thanoon, W. A., and Jaafar, M. S. (2006). Thermal and stress analysis of Kinta RCC dam. *Engineering Structures*, 28(1):1795–1802.

Nurse, R. W. (1949). Steam curing of concrete. *Magazine of Concrete Research*, 1(2):79–88.

Ortega, F., Bastos, C., and Alves, P. (2003). Pedrógão dam: first RCC experience in portugal. In *Roller Compacted Concrete Dams, Berga et al.(eds)*, pages 319–328. Swets & Zeitlinger.

Pantazopoulo, S. J. and Mills, R. H. (1995). Microstructural aspects of the mechanical response of plain concrete. *ACI Materials Journal*, 92(6):605–616.

Paté-Cornell, M. E. (1996). Uncertainties in risk analysis: six levels of treatment. *Reliaiblity Engineering and System Safety*, 54:95–111.

Phoon, K.-K. (2008). *Reliability-Based Design in Geotechnical Engineering*. Taylor & Francis Group.

Pimenta, L. (2009). *Abordagens de riscos em barragens de aterro*. Ph.D. thesis, Universidade Técnica de Lisboa, LNEC, Lisboa, Portugal.

Pimentel-Torres-Gaspar, A. (2010). *Performance evaluation and numerical modeling of an ISAC embankment and its comparison with a traditional soil embankment.* Ms.C. Thesis, Universidade do Minho, Escola de Engenharia.

Pinto, R. C. A. and Hover, K. C. (1999). Application of maturity approach to setting times. *ACI Materials Journal*, 96(6):686–691.

Popescu, R., Deodatis, G., and Nobahar, A. (2005). Effects of soil heterogeneity on bearing capacity. *Probabilistic Engineering Mechanics*, 20(4):324–341.

Prato, T., Cervera, M., and Oliver, J. (1997). Modelo termo-químico de hidratación del hormigón. *Mecánica Computacional*, 18(1):205–218.

Raphael, J. M. (1971). The Optimum Gravity Dam. *Rapid Construction of Concrete Dams, ASCE, New York*, pages 221–247.

Rastrup, E. (1954). Heat of Hydration in Concrete. *Magazine of Concrete Research*, 6(17):1–14.

Riahi, H., Bressolette, P., and Chateauneuf, A. (2010). Random fatigue crack growth in mixed mode by stochastic collocation method. *Engineering Fracture Mechanics*, 77(1):3292–3309.

Riahi, H., Bressolette, P., Chateauneuf, A., Bouraoui, C., and Fathallah, R. (2013). Reliability analysis and inspection updating by stochastic response surface of fatigue cracks in mixed mode. *Engineering Structures*, 33(1):3392–3401.

Rocha, M. and Serafim, J. L. (1958). Determination of thermal stresses in arch dams by means of models. In *VI Congress on Large Dams, New York, USA*.

Sabbagh-Yazdi, S. R., Mastorakis, N. E., and Bagheri, A. R. (2007). Galerkin finite volume solution of heat generation and transfer in RCC dams. *International Journal of Mathematical Models and Methods in Applied Sciences*, 1(4):261–268.

Sain, T. and Kishen, C. (2008). Probabilistic assessment of fatigue crack growth in concrete. *International Journal of Fatigue*, 30(12):2156–2164.

Saltelli, A., Tarantola, S., and Camolongo, F. (2000). Sensitivity analysis as an ingredient of modeling. *Statistical Science*, 15(4):377–395.

Saltelli, A., Tarantola, S., and Chan, K.-S. (1999). A quantitative model-independent method for global sensitivity analysis of model output. *Technometrics*, 41(1):39–56.

Santana, T. (1996). *Barragens de betão compactado com cilindros*. Ph.D. thesis, Universidade Nova de Lisboa, Lisbon, Portugal.

Satterthwaite, F. E. (1959). Random balance experimentation. *Technometrics*, 1(2):111–137.

Saul, A. G. A. (1951). Principles underlying the steam curing of concrete at atmospheric pressure. *Magazine of Concrete Research*, 2(6):127–140.

Schrader, E. K. (2008). Roller-compacted concrete. In *Concrete Construction Engineering Handbook*, pages 20.1–20.74. CRC Press, Taylor & Francis Group.

Shaw, Q.H.W.. (2010). *A New Understanding of the Early Behaviour of Roller Compacted Concrete in Large Dams*. Ph.D. thesis, University of Pretoria, viewed 10/09/2013 < http://upetd.up.ac.za/thesis/available/etd-06062011-221345/ >.

Silveira, A. (1961). *Temperatures variations in dams (in portuguese)*. Memória n.177, LNEC, Lisbon, Portugal.

Sobol, I. (1993). Sensitivity estimates for nonlinear methematical models. *Mathematical Modeling and Computational Experiment*, 1(4):407–414.

SPANCOLD (2013). Risk analysis applied to management of dam safety. Technical guides on dam safety. technical guide on operation of dams and reservoirs. vol. 1., Professional association of civil engineers and Spanish National Committee on Large Dams.

Springenschmid, R. and Breitenbucher, R. (1998). Influence of constituents, mix proportions and temperature on cracking sensitivity of concrete. In: Prevention of thermal cracking in concrete at early ages. Report 15, R. Springenschmid, E&FN Spon.

Tanabe, T., Kawasumi, M., and Yamashita, M. (1985). Thermal stress analysis of massive concrete. *Proc. The Seminar for Finite Element Analysis of Reinforced Concrete Structures*.

Tarantola, A. (2006). Popper, Bayes and the inverse problem. *Nature physics*, 2(1).

Tarantola, S., Gatelli, D., and Mara, T. A. (2006). Random balance designs for the estimation of first order global sensitivity indices. *Reliability Engineering and System Safety*, 91(6):717–727.

Teixeira, A. (2012). *Reliability and cost models of axial pile foundations*. Ph.D. thesis, Universidade do Minho, Escola de Engenharia, Guimarães, Portugal.

ACI Committee 207 (1999). Roller-Compacted Mass Concrete. ACI 207.5R-99, ACI Committee 207 Report, American Concrete Institute, Farmington Hills, Michigan.

Tissot, J.-Y. and Prieur, C. (2012). Bias correction for the estimation of sensitivity indices based on random balance designs. *Reliability Engineering and System Safety*, 107(1):205–213.

Ulm, F.-J. and Coussy, O. (1996). Strength growth as chemo-plastic hardening in early age concrete. *Journal of Engineering Mechanics*, 122(12):1123–1132.

USACE, U. (1995). Seismic design provisions for roller compated concrete dams. Pamphlet 1110-2-12, Department of the Army U.S. Army Corps of Engineers.

van Breugel, K. (1991). *Simulation of hydration and formation of structure in hardening cement-based materials.* Ph.D. thesis, Delft University of Technilogy, Delft, The Netherlands.

Vanmarcke, E. (1977). Probabilistic modeling of soil profiles. *Journal of Geotechnical Engineering*, 103(11):1227–46.

Venkovic, N., Sorelli, L., Sudret, B., Yalamas, T., and Gagné, R. (2013). Probabilistic slope stability analysis by finite element. *Probabilistic Engineering Mechanics*, 1(32):5–20.

Verbeck, G. J. and Helmuth, R. H. (1968). Structural and physical properties of cement paste. In *Fifth International Symposium on the Chemistry of Cement, Tokyo*, pages 1–32.

Waller, V. (1999). *Rélations entre composition des bétons, exothermie en cours de prise et résistance en compression.* Ph.D. thesis, École Nationale des Ponts et Chaussées, France.

Wang, X.-Y. and Lee, H.-S. (2012). Evaluation of the mechanical properties of concrete considering the effects of temperature and aging. *Construction and Building Materials*, 29(1):581–590.

Westberg, M. (2009). *Reliability-based assessment of concrete dam stability.* Ph.D. thesis, Lund University, Sweden.

Xu, C. and Gertner, G. (2008). A general first-order global sensitivity analysis method. *Reliability Engineering and System Safety*, 93(7):1060–1071.

Yang, I. (2007). Uncertainty and sensitivity analysis of time-dependent effects in concrete structures. *Engineering Structures*, 1(29):1366–1374.


POPH
QUALIFICAR É CRESCER.


QUADRO
DE REFERÊNCIA
ESTRATÉGICO
NACIONAL
PORTUGAL 2007.2013


GOVERNO DA REPÚBLICA
PORTUGUESA


UNIÃO EUROPEIA
Fundo Social Europeu